

Uranium isotopic analysis of terrestrial and extraterrestrial samples

Angela Kaltenbach

A thesis submitted for the degree of
Doctor of Philosophy
University of Otago, Dunedin, New Zealand

October 2012

Abstract

For several decades, an invariable $^{238}\text{U}/^{235}\text{U}$ ratio of 137.88 was assumed throughout the solar system, including Earth, due to uranium's heavy mass. However, recent studies have shown surprisingly variable $^{238}\text{U}/^{235}\text{U}$ values in terrestrial and extraterrestrial environments, including both low- and high-temperature settings. This has profound implications for both the accuracy of the U-Pb chronometer and understanding isotopic fractionation of the heavy elements. Isotope fractionation between ^{238}U and ^{235}U is controlled by both mass-dependent, and nuclear volume-dependent fractionation mechanisms during geochemical reactions. Mass-dependent effects preferentially remove the lighter ^{235}U isotope from the residue, while volume-dependent fractionation preferentially removes the heavier ^{238}U isotope, leaving the residue isotopically lighter.

In this study, $^{238}\text{U}/^{235}\text{U}$ was determined with high analytical precision on samples from a range of terrestrial and extraterrestrial environments, utilizing a ^{233}U - ^{236}U double spike procedure and multiple collector ICP-MS. A terrestrial $^{238}\text{U}/^{235}\text{U}$ reference value for 'Bulk Silicate Earth' of 137.795 ± 0.008 was determined, revoking the previously assumed value of 137.88. Additional uranium isotopic measurements of a wide range of low-temperature environments provide key insights into the mechanisms driving uranium isotopic shifts. To this end, uranium isotopic fractionation controlled by volume-dependent effects of 0.36‰ were observed at the redox interface of an anoxic basin. Most likely, this mechanism is induced by microbially-mediated uranium reduction, which preferentially removes isotopically heavy U(IV) from the water column. This process is in agreement

with Rayleigh fractionation in a closed system, corresponding to a fractionation factor of α of 0.9985 between the aqueous (oxidized) and solid (reduced) phase. In contrast, a $^{238}\text{U}/^{235}\text{U}$ fractionation of 0.35‰ heavier isotopic compositions was observed in the aqueous phase of an aquifer, following mass-dependent fractionation caused by adsorption processes.

Equally significant results were obtained from extraterrestrial meteorites. Samples of different meteorite groups, namely angrites, eucrites and chondrites, show homogeneous uranium isotope compositions between groups, but variations between single samples within the groups. The investigations of low-temperature samples indicate that these variations are likely caused by redox related fractionation during accretion processes, aqueous alteration, or thermal metamorphism, although no direct evidence of these processes was found.

Fractionation mechanisms aside, the $^{238}\text{U}/^{235}\text{U}$ ratios of the angrites analyzed result in revised absolute Pb-Pb ages for this important group of achondrites that are ~1 Myr younger than previously assumed. This reconciles previously reported deviations between absolute Pb-Pb ages and those obtained utilizing different extinct short-lived chronometers. Revised Pb-Pb ages of the carbonaceous chondrite Allende, including chondrules and a calcium-aluminium rich inclusion extracted from it, combined with other recent data [Connelly et al., 2012] give rise to a CAI formation age of 4567.30 ± 0.30 Myr, representing a revised age for the beginning of the solar system and an extended interval of chondrule formation of ~3 Myr. These new uranium isotopic data also have implications for the ^{247}Cm - ^{235}U short-lived chronometer, yielding an initial $^{247}\text{Cm}/^{235}\text{U}$ at the beginning of solar system formation of 2.9×10^{-4} - 1.5×10^{-3} , using Nd and Th as proxies for the extinct Cm. The resulting time interval of free decay between the last r-process event and solar system formation corresponds to 140-195 Myr, in very good agreement with previously published data.

Acknowledgements

I would like to thank all the people who supported me throughout the years of my PhD. It was an amazing experience living and working in New Zealand, meeting so many wonderful people and traveling over the islands.

First thanks go to my supervisor, Dr. Claudine Stirling, for her support, patience, and guidance throughout this project. Thanks also go to my advisors Dr. Malcolm Reid and Dr. Russell Frew for their support.

Many thanks to the FILTER members Dr. Melanie East, Dr. Mihoko Numata, and Dr. Martine Poffet for making many long hours in the clean lab more fun, for their help and encouragement, and many procrastinated hours at the Staff Club. All of you have become very good friend, and I don't think I would ever have finished without you. Thanks also to our newest member Phillip Nasemann, whose various attempts to make me keep my sanity were highly appreciated. Special thanks go to Melanie for being a native english speaker...

Special thanks go to Dr. Candace Martin for letting me use her clean lab in the Geology Department whenever I needed it, and many encouraging conversations.

Thanks to all old and new members of Waterworld, especially Dr. Imelda Velasquez, Dr. Linn Hoffmann, Dr. Eike Breitbarth, Birthe Kortner, Afroza Bulbul and Dr. Katie

Jones for their friendship, encouragement and many coffee breaks, beer Fridays, BBQs and other procrastinations.

Thanks to Dave Barr for many hours spent in front of the q-ICPMS for me and all the technical and administration staff at the Chemistry Department that helped me during the work for this thesis.

Special appreciation go to Dr. Yuri Amelin (ANU) for all his advice and support, including inviting me to spend several weeks at ANU, and fruitful comments on my thesis. Thanks also to Dr. Yuri Amelin and Dr. Tony Irving (University of Washington) for the supply of meteorite samples and Dr. Don Porcelli (University of Oxford) for the supply of water samples and ongoing support.

Thanks to the Marsden Fund, University of Otago, Department of Chemistry, Division of Science and the Geological Society New Zealand for the financial support of my work and making it possible to attend several conferences.

My final thanks go to my family and friends in Germany for all their encouragement, open ears and support throughout my years of studying far far away.

Contents

Abstract	i
Acknowledgements	iii
1 Introduction	1
1.1 Objectives	1
1.2 Origin of the solar system	1
1.2.1 Origin of the elements	2
1.3 Meteorite classification	8
1.3.1 Chondrites	9
1.3.2 Achondrites	11
1.3.3 Other meteorites	12
1.3.4 Inclusions in chondrites	12
1.4 Dating the solar system	14
1.4.1 Introduction	14
1.4.2 Short-lived nuclide chronometers	15
1.4.3 The long-lived nuclide chronometer	18
1.5 The collapse of the presolar cloud	22
1.5.1 Supernova / shockwave model	22
1.5.2 AGB star model	23
1.5.3 X-Wind model	24
1.6 The uranium redox system	25

<i>CONTENTS</i>	vi
1.6.1 Theory	27
1.6.2 Previous work	29
1.7 History of uranium isotopic analysis of $^{238}\text{U}/^{235}\text{U}$	32
1.8 Significance of this study	34
2 Samples and methods	38
2.1 Introduction	38
2.2 Samples	39
2.2.1 Meteorites and rock standards	39
2.2.2 Water samples	41
2.3 Sample preparation	42
2.3.1 Pre-cleaning and grinding of meteoritic samples	42
2.3.2 Digestion	43
2.3.2.1 Meteorites	43
2.3.2.2 Water samples	44
2.3.3 Co-precipitation of water samples	45
2.3.4 Ion exchange column chemistry	46
2.3.4.1 Uranium isotopes	46
2.3.4.2 Uranium-lead isotopes	47
2.4 Analysis	49
2.4.1 q-ICP-MS	51
2.4.2 Double spike	52
2.4.3 MC-ICPMS	53
2.4.4 TIMS	57
3 Results I: Isotopic fractionation mechanisms	58
3.1 Terrestrial reference	60
3.2 Anoxic aquatic conditions: Framvaren Fjord (Norway) and an Oxygen Minimum Zone (Peru)	63

3.2.1	Framvaren Fjord	63
3.2.1.1	Previous work	65
3.2.1.2	Results and discussion	69
3.2.2	Oxygen Minimum Zone: Peru	74
3.2.2.1	Results and discussion	76
3.3	Estuaries: Amazon River and Lena River	78
3.3.1	Amazon River	78
3.3.2	Lena River	79
3.3.3	Results and discussion	80
3.4	Aquifer: Mojave Desert	85
3.4.1	Results and discussion	86
3.5	Conclusions	90
4	Results II: Angrites	94
4.1	Introduction	94
4.2	Results and discussion	96
4.2.1	Rare Earth Elements	96
4.2.2	Uranium data	98
4.2.3	Implications for the timeline of the early solar system	99
4.3	Conclusions	105
5	Results III: Chondrites and eucrites	107
5.1	Introduction	107
5.2	Chondrites	108
5.2.1	Ordinary chondrites	108
5.2.2	Carbonaceous chondrites	118
5.2.3	Enstatite chondrites	122
5.2.4	Rare earth element patterns of bulk chondrites	123
5.2.5	Chronology of the oldest solids in the solar system	125

<i>CONTENTS</i>	viii
5.3 Eucrites	129
5.4 Implications for the ^{247}Cm chronometer	131
5.5 Conclusions	135
6 Conclusions and future work	137
6.1 Summary and conclusions	137
6.2 Future work	142
References	144
Appendix A: Cleaning procedures	163
Appendix B: Chemicals	167
Appendix C: REE data for meteoritic samples	168
Appendix D: q-ICP-MS instrument settings	173

List of Tables

1.1	Short-lived chronometers of extinct parent-daughter isotope systems. . . .	16
2.1	Protocol for iron co-precipitation for a sample size of 1000 ml	46
2.2	Two step ion exchange column protocol for the purification of uranium . .	49
2.3	Purification procedure for uranium-lead dating	50
3.1	Uranium isotope data for 12 igneous rock standards. Averages are weighted depending on ng U used per analysis (reflected by intensity and length of analysis).	61
3.2	Uranium, oxygen, hydrogen sulfide and salinity data of the Framvaren Fjord	70
3.3	Uranium, oxygen and salinity data for an Oxygen Minimum Zone profile off Peru	77
3.4	Uranium and salinity data of the Amazon and the Lena estuaries	82
3.5	Uranium data for two flowpaths of an aquifer in the Mojave Desert	88
4.1	Age differences of angrites after adjusting the $^{238}\text{U}/^{235}\text{U}$ ratios from 137.88 to the data of this study. Uncertainties on the newly calculated Pb-Pb ages are errors of the $^{238}\text{U}/^{235}\text{U}$ measurements only, or, in brackets, of the uranium isotopic measurements and the published Pb-Pb ages.	100
5.1	Uranium isotope and concentration data for bulk samples of 21 ordinary chondrites. Averages are weighted depending on ng U used per analysis (reflected in intensity and length of analysis). Subsamples of the same meteorite are marked as sample name + a, b, c, averages of which are weighted over all single measurements of the subsamples.	111
5.2	Uranium isotope and concentration data for 13 carbonaceous chondrites. Averages are weighted depending on ng U used per analysis (reflected by intensity and length of analysis). Subsamples of the same meteorite are marked as sample name + a-e, averages of which are weighted over all single measurements of the subsamples.	120

5.3	Uranium isotopic composition and concentration data for three enstatite chondrites. Averages are weighted depending on ng U used per analysis (reflected by intensity and length of analysis).	122
5.4	Uranium isotope and concentration data for bulk samples of five eucrites and the ungrouped achondrite NWA 5400. Averages are weighted depending on ng U used per analysis (reflected by intensity and length of analysis). Subsamples are marked as sample name + a, b, averages of which are weighted over all measurements of the subsamples.	129
1	PFA cleaning	164
2	Column cleaning	164
3	Resin cleaning	165
4	HDPE bottle cleaning	166
5	Chemicals used during this project	167
6	REE data from La to Lu, normalized to CI values by Barrat et al. [2012], and Th concentrations in ppb for meteoritic samples. The raw data can be found in the electronic appendix.	169
7	q-ICP-MS instrument settings	173
8	Internal standard concentrations	173
9	q-ICP-MS: Isotopes and integration times.	174

List of Figures

1.1	Hertzsprung-Russell Diagram, after R. Hollow, CSIRO, Australia, with kind permission.	2
1.2	Stellar evolution of a high mass star, starting with hydrogen burning and ultimately ending in an iron core surrounded by burning shells.	5
1.3	N (neutron) versus Z (proton) diagram, showing the nucleosynthetic paths of the s- and r-processes. The s-process forms only certain elements step by step up to the mass of Bi, shown by the red line, while the r-process is capable of rapidly synthesizing elements throughout all masses (dashed regions), figure from White [2009].	6
1.4	Element abundance pattern of the solar system. Figure from Truran, Jr. and Heger [2003].	7
1.5	Concordia diagram for U-Pb dating, created with Isoplot-Ex 4.13 [Ludwig, 2003]. The red line represents concordia (with ages), while the blue line symbolizes an example of discordia, generated using two random data points. The intercept of the two curves at the higher age depicts the date the system closed, while the intercept at the lower age represents the time of the last metamorphic event the sample was exposed to, during which Pb leaked out of the system.	19
1.6	A typical 'inverse' lead isochron. The intercept with the y-axis is used to calculate the age of the sample, in this example utilizing a measured $^{238}\text{U}/^{235}\text{U}$ ratio. Each ellipse equals a data point with 2SD ($= 2\sigma$) errors of a different leachate of the same sample. MSWD represents the mean square weighted deviation of the age calculation, from Amelin et al. [2010].	20
1.7	Age bias of a sample with the true age of 4567 Myr according to the excess of ^{235}U from the decay of ^{247}Cm	21
1.8	Shockwave model, from Krot et al. [2009]	23
1.9	X-Wind model from Shu et al. [1997]	25

1.10	Box model of uranium fractionation in the open ocean cycle. Figure published by Weyer et al. [2008].	30
1.11	Summary of $^{238}\text{U}/^{235}\text{U}$ ratios of a wide variety of samples, taken off Hiess et al. [2012].	32
2.1	Sampled slices of (a) the eucrite Millbillillie and (b) the L3.3 ordinary chondrite Dhofar 008	40
2.2	Samples of (a) a whole rock sample and CAI of the CV3 chondrite Northwest Africa (NWA) 4502 and (b) a slice of the ungrouped C3 chondrite Dar al Gani (DaG) 430	41
2.3	Elution curve of a basalt sample (BCR-2) using TRU resin. Every eluant is one ml eluted from the column.	48
2.4	Elution curve of a basalt sample (BCR-2) using UTEVA resin. Every eluant is one ml eluted from the column.	48
2.5	The instrument schematic for a Nu Plasma MC-ICPMS as used in this study.	53
2.6	Standard measurements of the uranium metal standard CRM145 over one day of meteorite sample analysis. The solid line represents the average $^{238}\text{U}/^{235}\text{U}$ ratio of all measurements, while the dashed blue lines are the 2SD/2SE errors of the average.	55
3.1	Uranium isotopic ratios for 12 terrestrial rocks, six volcanic rocks (blue dots) and six plutonic rocks (red squares).	62
3.2	Framvaren Fjord, Norway: a) Overview figure, published by Skei [1983]; b) Profile of the Framvaren Fjord and adjacent fjords. Reproduced after Skei [1988].	64
3.3	(A) The $\delta^{34}\text{S}_{\text{VCDT}}$ (crosses) and $\delta^{18}\text{O}_{\text{VSMOW}}$ (open circles) isotope compositions of sulfate throughout the water column. (B) as (A) but focused around the redox interface region. The dashed line represents a depth of 20 m at which sulfide is first detected. VCDT and VSMOW are the sulfur and oxygen standards used as references, with VCDT standing for 'Vienna Canon Diabolo Troilite' and VSMOW representing 'Vienna Standard Mean Ocean Water'. From Mandernack et al. [2003].	66
3.4	Metal concentrations for Mn, Fe and Co throughout the water column of Framvaren Fjord. Figure from Jacobs et al. [1985].	67
3.5	Uranium concentration profiles for Framvaren Fjord after Todd et al. [1988] (red circles), McKee and Todd [1993] (green squares) and Swarzenski et al. [1999] (blue triangles).	68

3.6	Left: Uranium concentration (blue triangles) and uranium isotope ratios with 2SE uncertainties (black dots) from this study. Right: Oxygen concentration (green diamonds), hydrogen sulfide concentration (red squares) and salinities (black crosses), after data from McKee and Todd [1993].	69
3.7	Rayleigh fractionation for the Framvaren Fjord profile. Closed circles and red regression line represent depth from 18 - 40 m and the dashed lines are the 95% interval of the regression.	73
3.8	Working area and cruise track of Meteor M77/3. The coordinates for the profile analyzed in this study are marked with a red dot and arrow.	75
3.9	Profile of the OMZ off Peru. Left: Uranium isotope ratios (black dots) and uranium concentrations (blue triangles). Right: Oxygen concentrations (green diamonds) and salinities (black crosses).	76
3.10	The shelf of the Amazon River, including the sample station locations of the AmasSeds cruise, after Swarzenski et al. [1995].	78
3.11	Setting of the Lena River in the Laptev Sea of the Arctic Ocean. Blue dots represent the sampling sites for this study, figure after Hölemann et al. [2005].	80
3.12	Estuaries of (a) the Amazon River and (b) the Lena River: Uranium concentrations (blue triangles), uranium isotopic ratios (black dots) with uncertainties according to their salinities and the modeled mixing lines of riverine and oceanic waters. Blue lines are concentration mixing lines, while black solid lines represent $^{238}\text{U}/^{235}\text{U}$ mixing lines (with uncertainties shown as dashed lines).	81
3.13	Location of the Mojave River Basin. a) Regional map including the study area. b) Location of the sampled boreholes (this study: blue dots). The direction of groundwater flow is indicated by black arrows, the blue lines show the northern and southern flowpaths. Dotted lines represent ^{14}C ages and solid lines show the piezometric surface contours. After Kulongoski et al. [2003].	85
3.14	Mojave Desert: Uranium isotope ratios (black circles) and uranium concentrations (blue triangles) according to their ^{14}C -age (ages from Kulongoski et al. [2003]). Data points of the northern flowpath of the aquifer are plotted as filled symbols, data from the southern flowpath as open symbols and the starting points of both flowpaths are the red symbols.	87

3.15	A summary of all water samples analyzed in this study, Framvaren Fjord (green squares), Oxygen Minimum Zone offshore from Peru (yellow upwards triangles), Amazon River estuary (red dots), Lena River estuary (blue diamonds) and Mojave River Basin aquifer (pink downwards triangles).	92
4.1	Rare Earth Element (REE) data for the different groups of angrites, normalized to CI values [Barrat et al., 2012]. Red lines represent the plutonic angrites, blue lines the quenched angrites and the green line represents the metaclastic angrite NWA 2999.	96
4.2	Comparison of uranium isotopic data of this study (red squares) and values reported by Brennecka and Wadhwa [2012] (blue circles).	99
4.3	Comparison of Pb-Pb ages of angrites. Red squares are data from this study, green triangles represent data from Brennecka and Wadhwa [2012] and the blue diamonds represent literature data (^a Amelin [2008b], ^b Amelin and Irving [2007], ^c Amelin et al. [2010], ^d Amelin [2008a], ^e Connelly et al. [2008], ^f Amelin and Irving [2011])	101
4.4	Comparison between the absolute Pb-Pb ages and the relative ¹⁸² Hf- ¹⁸² W, ⁵³ Mn- ⁵³ Cr and ²⁶ Al- ²⁶ Mg ages of angrites. Pb-Pb ages are from this study and previously published (see Table 4.1), while all relative ages are anchored to the Pb-Pb age of D'Orbigny (4563.60 Myr), using data of Kleine et al. [2012] (Hf-W), Sugiura et al. [2005] (D'Orbigny, SAH 99555, Mn-Cr), Shukolyukov and Lugmair [2008] (NWA 4801, Mn-Cr), Shukolyukov et al. [2009] (NWA 2999, Mn-Cr) and Schiller et al. [2010a] (Al-Mg). Uncertainties of Pb-Pb ages of this study represent total errors of uranium isotopic data and published Pb-Pb ages, uncertainties of relative chronometers are published uncertainties and do not take the Pb-Pb age uncertainty of D'Orbigny into account.	103
4.5	Comparison of published (in red) and revised (in blue) ¹⁸² Hf- ¹⁸² W and Pb-Pb ages. Published ¹⁸² Hf- ¹⁸² W ages are anchored to the CAI Pb-Pb age of 4567.1 ± 0.2 Myr Amelin et al. [2006], revised ¹⁸² Hf- ¹⁸² W ages are anchored to the CAI SJ101 (of the CV3 Allende) Pb-Pb age of 4567.2 ± 0.5 Myr from this study. Solid lines are linear regression lines and dashed lines represent the corresponding 95% confidence intervals.	104
5.1	Comparison of ²³⁸ U/ ²³⁵ U values and U concentrations of ordinary chondrites. The dataset includes all subsamples of the present study, but excludes the 'anomalous' ordinary chondrites.	109

5.2	$^{238}\text{U}/^{235}\text{U}$ data for ordinary chondrites. Samples analyzed as several subsamples are plotted with their average values only. Filled symbols represent 'finds', open symbols 'falls'. Note that values with very unusual uranium isotopic ratios are not part of this figure (see text).	112
5.3	Bulk subsamples and subsamples of high magnetic susceptibility of the ordinary chondrites Krymka and Elenovka.	113
5.4	$^{238}\text{U}/^{235}\text{U}$ data for carbonaceous chondrites. Samples analyzed as several subsamples are plotted with their average values only. Filled symbols represent 'finds', open symbols 'falls'. The mean average and 2SE errors are calculated excluding the values for the inclusions.	119
5.5	Comparison of $^{238}\text{U}/^{235}\text{U}$ values and U concentrations of carbonaceous chondrites. The dataset includes all subsamples of the present study, bulk samples are plotted as blue circles, inclusions as red squares.	121
5.6	Rare earth element patterns for chondrites.	124
5.7	Rare earth element patterns for the CV3 chondrites Allende and NWA 4502 and their inclusions.	126
5.8	Uranium isotopic data for the carbonaceous chondrites Allende and NWA 4502 and their inclusions. Allende average and 2SE lines (in blue) are for bulk Allende a-e samples only, BSE values (with 2SE lines, in green) are discussed earlier (Chapter 3.1).	127
5.9	$^{238}\text{U}/^{235}\text{U}$ ratios for the eucrites and the ungrouped achondrite NWA 5400. Filled symbols represent 'finds', open symbols 'falls'.	130
5.10	REE patterns for eucrites.	131
5.11	$^{144}\text{Nd}/^{238}\text{U}$ against $^{235}\text{U}/^{238}\text{U}$, the linear regression line (solid dark blue) gives the slope and the interception point for the calculations of the initial abundance of ^{247}Cm at $t+\Delta$. The dashed lines represent the 95% confidence intervals of the linear regression. Error bars on the x-axis represent 2% uncertainties of Nd, in agreement with the q-ICP-MS measurements of this element.	133
5.12	$^{232}\text{Th}/^{238}\text{U}$ ratios plotted against $^{235}\text{U}/^{238}\text{U}$, the linear regression line (solid dark blue) gives the slope and the interception point for the calculations of the initial abundance of ^{247}Cm at $t+\Delta$. The dashed lines represent the 95% confidence intervals of the linear regression. Error bars on the x-axis represent 10% uncertainties of Th, in agreement with the q-ICP-MS measurements for this element.	134

- 5.13 Summary of the average $^{238}\text{U}/^{235}\text{U}$ ratios of all meteorite groups analyzed in this study, in comparison with the terrestrial reference of this study. The dark blue solid line represents the mean of all meteorite groups, the dashed lines the 2SE uncertainty of this average. 135
- 6.1 Comparison of averaged $^{238}\text{U}/^{235}\text{U}$ values, with their 2SE errors, of the different datasets analyzed in this study. Chondrite data are plotted in blue, achondrite data in green and terrestrial aqueous data in red. The grey bar represents the BSE value, including its 2SE errors. 141

List of Abbreviations

AdoR	Angra dos Reis
AGB	Asymptotic Giant Branch
AOA	Amoeboid olivine aggregates
APB	Angrite parent body
ATP	Adenosine triphosphate
BSE	Bulk Silicate Earth
CAI	Calcium-aluminium rich inclusion
CCRMP	Canadian Certified Reference Materials Project
DaG	Dar al Gani
DOC	Dissolved organic carbon
DSN	Desolvating nebuliser (system)
GSJ	Geological Survey Japan
HED group	Group of meteorites, consisting of howardites, eucrites and diogenites
HRD	Hertzsprung-Russell Diagram
ISM	Interstellar medium
ISO	International Organization for Standardization
M_{\odot}	Solar mass, 1.99×10^{30} kg
MC-ICPMS	Multiple-collector inductively coupled plasma mass spectrometer
Myr	Million years

NWA	Northwest Africa
OAE	Oceanic anoxic event
OMZ	Oxygen Minimum Zone
PFA	perfluoroalkoxy
PTFE	polytetrafluoroethylene (Teflon)
q-ICP-MS	quadrupole inductively coupled plasma mass spectrometry
R/V	Research Vessel
REE	Rare earth element, lanthanides
SABS	South African Bureau of Standards
SAH	Sahara
SD	Standard deviation
SE	Standard error
TIMS	Thermal ionization mass spectrometry
TSM	Total suspended matter
USGS	United States Geological Survey

Chapter 1

Introduction

1.1 Objectives

This project utilizes new developments in uranium isotope geochemistry, involving the high-precision analysis of $^{238}\text{U}/^{235}\text{U}$, and is divided into two main objectives. The main goal was to find evidence for the event that triggered the formation of the solar system and to re-evaluate the timescale of events in the early solar system by revising the U-Pb chronometer. The second aim of this project focused on the behaviour of uranium and its isotopes in aqueous environments, especially under anoxic or changing redox conditions. These low temperature samples give insight into the control mechanisms of uranium isotope fractionation and explore the natural variability of $^{238}\text{U}/^{235}\text{U}$ outside of the possible influences by the decay of ^{247}Cm .

This chapter focuses on the theory behind the project. It includes a discussion of the possible events that triggered the formation of the solar system and how uranium isotopes can be utilized to determine the likelihood of each event and to redefine the U-Pb chronometer used for dating the events that took place in the early solar system. An overview of the classification scheme of the sampled meteorites is given as well as an introduction into the theory of the uranium redox system. This chapter closes with an overview of the history of uranium isotope analysis, the significance of this study, and a brief description of the chapters to follow.

1.2 Origin of the solar system

Most matter in our solar system is inherited from different stellar sources throughout the galaxy. It was part of the interstellar medium (ISM) that the sun and the solar system

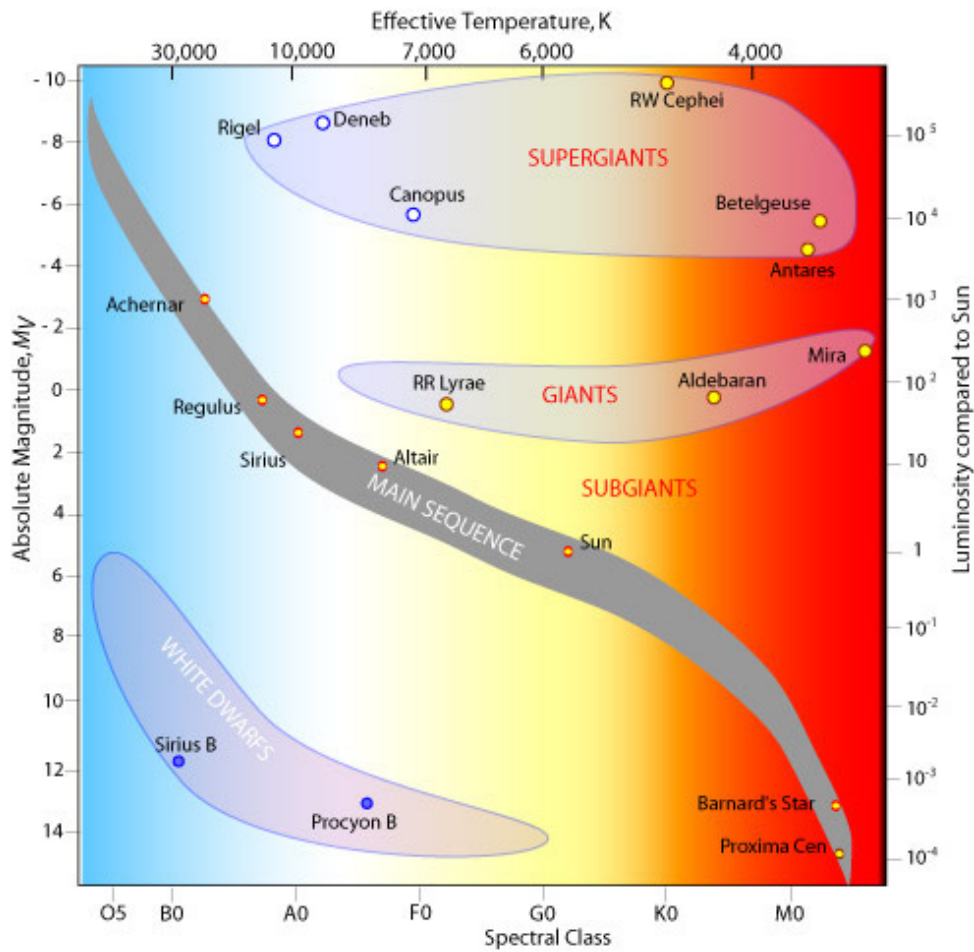


Figure 1.1: Hertzsprung-Russell Diagram, after R. Hollow, CSIRO, Australia, with kind permission.

were born out of during the collapse of a molecular cloud over 4.6 billion years ago [e.g. Zinner, 1998]. Meteorites and their parent bodies are representatives of the physical and chemical conditions in the matter of the presolar cloud and their composition depends largely on the evolutionary processes during the formation of the solar system. To fully understand the implications of uranium isotopic compositions in meteorites it is essential to first comprehend the formation of the elements and the processes that possibly triggered the collapse of the molecular cloud, leading to the formation of the solar system and meteorites.

1.2.1 Origin of the elements

Star formation Stars are formed during the collapse of dense molecular clouds of dust and gas. The possible events that might have triggered the initiation of this collapse are

described later, in section 1.5. This event causes an elevated density of matter in some regions of the presolar cloud, thereby increasing the gravitational energy between particles and leading to a build up in the amount of collisions between them. This, in turn, increases the temperature of these high-density regions of the molecular cloud and if the inwards gravitational energy is larger than the outwards radiation pressure the cloud will collapse. Following this, the density of the gas in the collapsing sections of the cloud will intensify and form a so-called protostar. When the outward radiation pressure of the protosun finally equals the inward gravitational force hydrostatic equilibrium is reached and the protostar has entered the first evolution stage of a star [Chrysostomou and Lucas, 2005, Busso, 2011].

Stars can produce elements to a certain mass depending on their own mass and stage of evolution [Truran, Jr. and Heger, 2003]. The Hertzsprung-Russell Diagram (HRD) is commonly used to characterize stars according to their luminosity, which equals the radiation energy emitted by the star, and effective temperature as a measure of the surface temperature of a star. Both of these parameters are indicators for the current evolution stage of a star. Fig. 1.1 shows an example of an HRD with the effective temperature and spectral classes on the x-axis and the absolute magnitudes and luminosities on the y-axis. The spectral classes range from type O, the hottest blue stars with effective temperatures of $>33,000$ K, to type M, the coolest red stars with effective temperatures of $<3,500$ K. The absolute magnitude of a star is defined as the brightness, or flux of light in W/m^2 , the star would have if placed at a distance of 10 parsecs¹ from Earth. About 90% of all stars lie on the main sequence of the HRD [Truran, 1984]. As shown in Fig. 1.1 as a comparison, our Sun is a spectral class G star with a surface temperature of ~ 6000 K, and a luminosity of one.

Elements lighter than iron primarily form during thermonuclear fusion within stars [Truran, Jr. and Heger, 2003]. The mass of the heaviest element reached during this process then depends on the mass of the star, and therefore on its gravity and fuel. The thermonuclear fusion of a star begins with the fusion of He out of H-atoms, the so-called hydrogen burning phase [Truran, 1984]. During this early stage in the evolution of a star it is situated on the main sequence of the HRD (Fig. 1.1).

The heavier helium produced during this process then starts to sink, accumulating and forming a core. At this stage, the further evolution of the star depends on its mass.

¹ 1 parsec (pc) = 3.26 lightyears = 3.09×10^{13} km

Low mass stars If a star has a mass of $<8 M_{\odot}$ ² it will run out of hydrogen, consequently lose its hydrostatic equilibrium and begin to contract. At this point it leaves the main sequence of the HRD and evolves into a giant branch star, also called a red giant ('Giants' on the HRD, Fig. 1.1). The contraction compresses enough of the left-over H around the He core to restart the H-burning in a thin layer, which is forced to expand due to its radiation pressure. At the time all hydrogen is consumed, the star contracts again until the He-burning is initiated, synthesizing carbon and oxygen in its core but not reaching high enough core temperatures to ignite the carbon. When all fuel is used up and the star has ejected its cooled down H and He shells, a white dwarf remnant is left (Fig. 1.1, left lower corner) [Lugaro and Chieffi, 2011].

High mass stars If a star has a mass $\geq 8 M_{\odot}$ higher core temperatures are possible due to a higher pressure in the core of the star, caused by its ongoing contraction. This ignites the He, and He-burning begins to form C and O [Truran, Jr. and Heger, 2003]. At this point, the H has formed a shell around the He core, the hydrogen burning shell (Fig. 1.2). As the star gains in mass, the pressure, and therefore the temperature in the core, rises and heavier elements are formed. The main reactions of these nuclear burning stages, starting from the outermost shell down to the core of a high mass star, are

$H \longrightarrow He \longrightarrow C \text{ (also forms O)} \longrightarrow Ne \longrightarrow O \longrightarrow Si \xrightarrow{\text{forms}} Fe \text{ core}$ (Fig. 1.2).

Each successive burning stage begins in the core and then moves outwards into the next shell, leaving the core to the next heavier burning stage as soon as the core temperatures are high enough to ignite the heavier element [e.g. Rauscher, 2004]. During these stages the star evolves horizontally onto the supergiant branch star of the HRD ('Supergiants', Fig. 1.1). Finally, an iron core forms, which becomes unstable as soon as it reaches the so-called Chandrasekhar limit of $1.4 M_{\odot}$, being too heavy to hold its hydrostatic equilibrium [Thielemann et al., 2011]. The core then collapses to explode in a core-collapse supernova and finally leaves a neutron star or a black hole as a remnant [e.g. Heger et al., 2003].

Core-collapse supernovae During the formation of the iron core of a star the gravity pressure, and therefore the temperature of the core, increases further and the electrons inside the core become degenerate³. The Fe nuclei begin to photodisintegrate⁴, releasing gamma photons, protons and He nuclei. This process absorbs energy rather than releasing it and the outward pressure of the core decreases [Thielemann et al., 2011]. When the energy inside the core is sufficiently high, the protons released during the photodisintegration begin to react with the degenerate electrons. This process decreases the outward

² M_{\odot} = Solar mass of our Sun = 1.99×10^{30} kg

³Degeneracy is a form of extremely high density, emitting an outward pressure.

⁴Photodisintegration is defined as a proton or neutron being knocked out of the nucleus by a gamma ray.

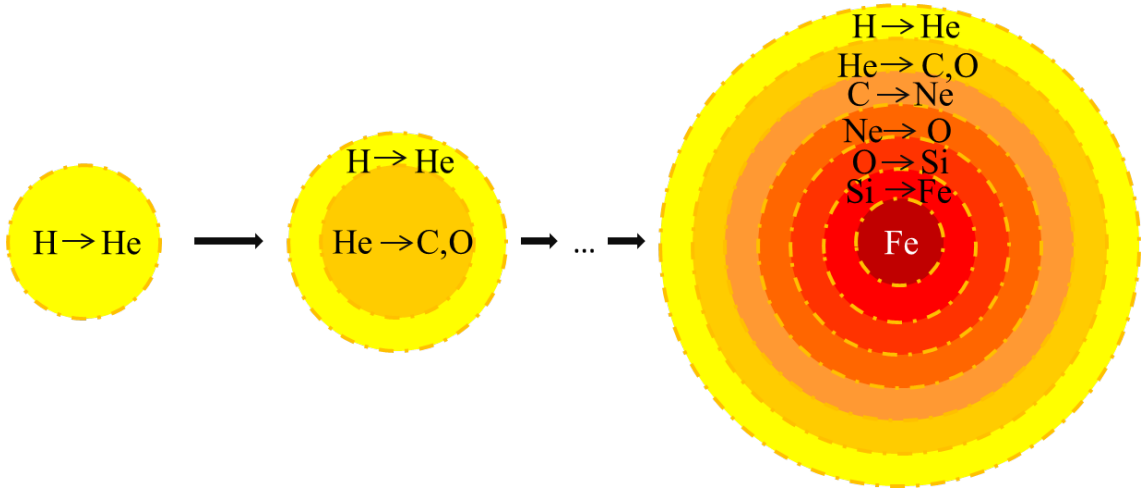


Figure 1.2: Stellar evolution of a high mass star, starting with hydrogen burning and ultimately ending in an iron core surrounded by burning shells.

pressure due to the loss of degeneracy energy, causing the further collapse of the core. At a temperature of $\sim 10^{12}$ K neutron degeneracy commences. The outward neutron degeneracy pressure halts the collapse of the core, but the surrounding material, synthesized during the thermonuclear burning, still collapses inwards. Once this material reaches the core it recoils, forming a neutron shockwave and ripping the star apart.

In this final stage of the supernova the iron core will photodisintegrate completely, forming neutrons and finally neutron degenerate matter. Depending on the mass of the star the neutron degeneracy pressure of the core will either halt the inner core collapse, turning the star into a neutron star, or, if the mass of the star is too high, the left-over material of the supernova will further collapse inwards, creating a black hole [Thielemann et al., 2011, and references therein].

S-Process Several processes can form elements heavier than iron. In low and intermediate mass stars with masses $\leq 10 M_{\odot}$ this process is the slow neutron capture, or s-process. This process is defined as slow, as the relative lifetime for the neutron capture is shorter than the relative lifetime for the electron decays. The s-process occurs during the so-called Asymptotic Giant Branch (AGB) star phase, which represents the final evolution stage of stars progressing on the giant branch on the HRD. This final phase consists of a complicated evolution, accompanied by a significant mass loss and convection between the burning shells [Truran, Jr. and Heger, 2003, Herwig, 2005].

The nucleosynthesis path of the s-process, as shown in Fig. 1.3, is simple, as the nucleus captures only one neutron at a time, raising its mass by one until it becomes unstable and decays to a new element of the same mass but with an atomic number elevated by one.

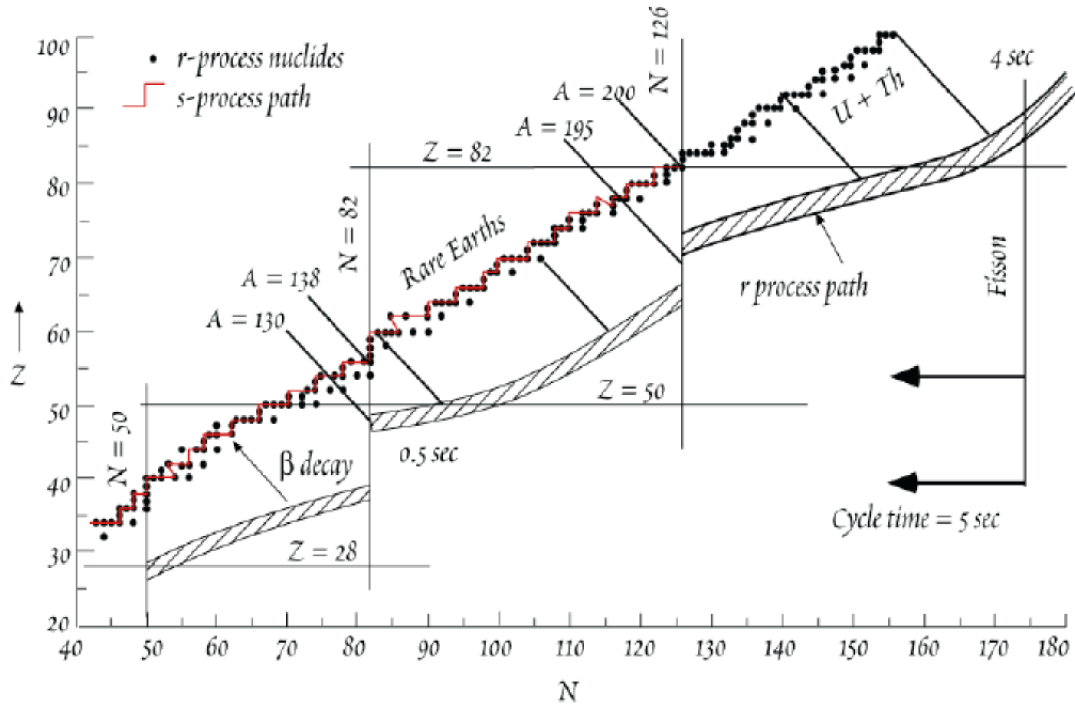


Figure 1.3: N (neutron) versus Z (proton) diagram, showing the nucleosynthetic paths of the s - and r -processes. The s -process forms only certain elements step by step up to the mass of Bi, shown by the red line, while the r -process is capable of rapidly synthesizing elements throughout all masses (dashed regions), figure from White [2009].

Consequently, this process cannot bridge nuclear instabilities. Most of this process takes place during the stable nuclear burning stages of stars [Truran, Jr. and Heger, 2003] and it can form elements up to the mass of ^{209}Bi (Fig. 1.3).

R- and p-processes In massive stars ($M \geq 10 M_{\odot}$) r - and p -processes are possible. The rapid neutron capture (r -process) forms elements in the environment of massive stars up to supernovae explosions. The lighter nuclei with masses < 130 -140 can be produced during the heavier burning stages of stars, while the heavy elements of masses to ~ 270 are only associated with r -processes initiated by explosive nucleosynthesis like a core-collapse supernova. The core-collapse forms a highly energetic, neutron-rich environment, where neutrons are captured by nuclei more rapidly than during the s -process. This allows the nuclei to bridge instabilities before they decay, forming elements throughout all masses, but with a tendency to form heavier, and therefore neutron rich, isotopes of a given element [Thielemann et al., 2011].

The proton capture process (p -process) synthesizes proton rich isotopes of heavy nuclei with masses between ^{74}Se and ^{196}Hg and is responsible for the lighter isotopes of any

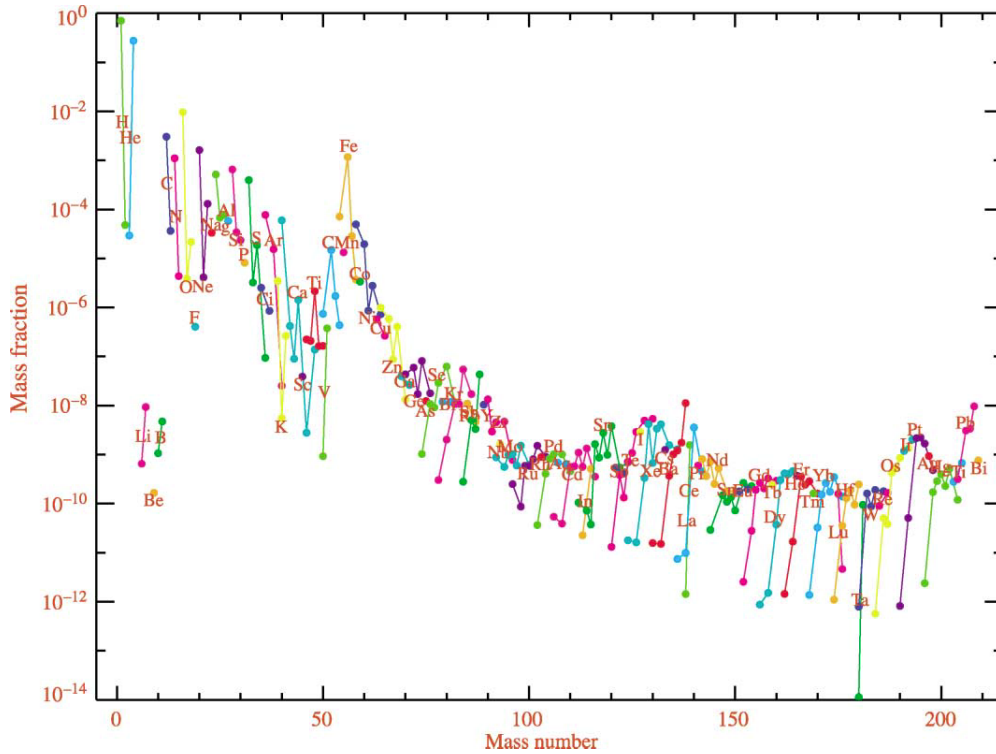


Figure 1.4: Element abundance pattern of the solar system. Figure from Truran, Jr. and Heger [2003].

given element. It is now understood that this process can either be a γ -process, which involves the photodisintegration of heavy elements, or a less likely ν -process, where a neutrino flux either converts a neutron into a proton or knocks out a nucleon [Truran, Jr. and Heger, 2003]. Proton capture alone is not sufficient.

The abundance of elements varies according to the different formation paths they take. For example, H and He are most abundant, as they form during all stages of nuclear burning, and display the largest peaks in Fig. 1.4. Further peaks correspond to the masses of C and O, the products of He burning and end-products of intermediate stars. Fe has a high abundance, as it is the end-product of nuclear burning in massive stars and defines the nuclear statistical equilibrium of element abundances. In the high mass region abundance peaks are found at the elements with filled outer neutron shells (Zr, Ba and Pb) (Fig. 1.4).

1.3 Meteorite classification

Elemental and isotopic compositions of meteorites and their inclusions vary depending on their formation history. This includes condensation and evaporation processes during their accretion, cooling rates of parent bodies, partial melting and crystallization of the asteroidal bodies, the impact of cosmic rays, differentiation mechanisms, metamorphic alterations, and impacts of smaller bodies. Many of these processes depend on the region of the protosolar nebula in which a meteorite parent body was formed.

The ratio of parent to daughter isotopes of short-lived nuclides, with half-lives of only a few million years, are commonly used as chronometers to define the time between certain events in the early stages of solar system formation (see also section 1.4). These short-lived nuclides were formed during nucleosynthesis events close enough in time to the cloud collapse to be mixed into it before the parent isotope had decayed to extinction [e.g. Busso, 2011]. The first solids, now found in meteorites as refractory inclusions, whose chemical and physical properties have been stable since their formation in a high temperature environment, were formed during transient heating events inside the protosolar cloud [Krot et al., 2009].

The general classification used in this study is widely accepted and described in Krot et al. [2003, and references therein]. Meteorites are generally divided into chondritic (chondrule bearing) and non-chondritic meteorites.

Chondrites consist mainly of chondrules, Fe-Ni metal, refractory inclusions, and a fine grained matrix [Krot et al., 2003]. They are separated into carbonaceous chondrites, ordinary chondrites, and enstatite chondrites. Further subgroups are defined based on their assumed formation history, as well as the Rumuruti-like and Kakangari-like chondrites.

Non-chondritic meteorites do not contain chondrules. They formed during heating and melting of their parent bodies [Bevan, 2007] and are classified as differentiated⁵ achondrites (planetary or asteroidal), primitive achondrites, iron meteorites, and stony iron meteorites. Both achondrite groups can be further divided according to the parent bodies their members are believed to have formed on.

Meteorites that do not fit into any of these groups are called anomalous or ungrouped meteorites. Further classification can be done according to the shock stage⁶ [Stöffler et al., 1991] and/or petrologic (metamorphic) types [van Schmus and Wood, 1967] of the meteorites. For the latter, types 1 and 2 represent aqueous alterations at $T < 300^\circ\text{C}$ and types

⁵Differentiated in the context of planetary differentiation means that the asteroidal or planetary body is separated into core, mantle and crust layers, initiated by major melting events causing the denser material (containing mostly metals) to sink and form the core, and lighter material to rise in the melt, forming the mantle and the crust.

⁶The shock stage of a meteorite is a measure of impact metamorphism produced by collisions between bodies.

3-6 are representative of the sequence of thermal metamorphism at temperatures ranging from 500°C to >1000°C.

Different chemical compositions of meteorite groups are generally associated with different locations within the meteorite forming region. Subgroups reflect different parent bodies and although one subgroup can contain meteorites from several parent bodies, the same parent body cannot be represented in different subgroups.

1.3.1 Chondrites

Carbonaceous chondrites Carbonaceous chondrites are currently divided into eight subgroups, representing a redox sequence with increasing oxidation states from CB, CH, CR, CO, CV, CK, CM to CI. Samples of four of these subgroups (CR, CV, CM and CI) were analyzed in this study.

These subgroups are mainly named after their first analyzed member, with B in CB standing for Bencubbin, R for Renazzo, O for Ornans, V for Vigarano, K for Karoonda, M for Mighei and I for Ivuna. The CH group is the only exception, with H representing the 'high-metal abundance' of this subgroup and the main member being ALH85085.

Despite the name 'carbonaceous' chondrites, only the CI, CM and CR chondrites are actually enriched in carbon [Krot et al., 2003].

The elemental composition of the CI group is used as a reference for the average solar system abundance, as they represent the most primitive meteorites with compositions close to those of the bulk solar system [Anders and Grevesse, 1989, Barrat et al., 2012]. CI chondrites contain presolar grains, but despite their name contain no chondrules. All carbonaceous chondrites belong to petrologic type 1 and have undergone extensive, multistage aqueous alteration.

Carbonaceous chondrites generally contain calcium-aluminium rich inclusions (CAIs, see section 1.3.4 for further explanations), are enriched in lithophile⁷ elements, depleted in volatile elements, are highly oxidized, contain hydrous minerals and high amounts of the mineral magnetite. Although their metamorphic degrees range from petrologic types 1-6, most groups only contain meteorites of types 1, 2 and 3, with two exceptions: CM, ranging from type 1-2, and CK, ranging from type 4-6.

Ordinary chondrites Ordinary chondrites are the most common meteorite class, with >80% of all recovered meteorites belonging to it. They are divided into three chemical classes: H, L and LL. These can be further classified depending on petrological types, forming a metamorphic sequence from 3 to 6, which represent the increasing degree of

⁷Lithophile elements predominantly bond with oxygen and are concentrated in crust and mantle regions of differentiated meteorites. They have closed (filled) outer electron shell configurations.

chemical equilibration and textural recrystallization of these chondrites.

The ordinary chondrites are mainly grouped according to their iron concentration from H (high total Fe) and L (low total Fe) to LL (low total Fe and low metallic Fe / total Fe ratio). Their oxidation states increase accordingly from H to LL. Chondrule sizes grow from 300-570 μm [Rubin, 2005] and siderophile element⁸ abundances decrease. The composition of ordinary chondrites is enriched in refractory lithophile elements relative to the abundances in CI chondrites.

They also contain high amounts of iron, have intermediate Mg/Si ratios, show a high variability in secondary metamorphic alterations and scarcely contain calcium-aluminium rich inclusions [Bevan, 2007].

It is assumed that the ordinary chondrites originate from at least three different parent bodies [Kallemeyn et al., 1989].

Enstatite chondrites Enstatite chondrites are only divided into two groups: EH, which contains high amounts of iron, and EL, with low iron concentrations. They consist of highly reduced material, have low Mg/Si ratios and high abundances of the name-giving mineral Enstatite (MgSiO_3). They can, like the ordinary chondrites, be subdivided into petrologic types, ranging from 3 to 6.

Enstatite chondrites rarely contain CAIs and are reduced in refractory lithophile elements. Their oxygen composition is close to that of the bulk Earth composition and their noble gases have near solar compositions, establishing enstatite chondrites and the Earth as part of the same group of solar system materials [e.g. Javoy et al., 2010]. Their highly reduced composition also distinguishes them from the other chondrite groups, showing that they most likely formed under different redox conditions in another region of the stellar disk than carbonaceous and ordinary chondrites.

R (Rumuruti-like) and K (Kakangari-like) These chondrites do not clearly belong to one of the major chondrite groups and differ in their chemical compositions, oxygen isotope compositions and matrix abundances. As such, they are considered to represent their own groups with 116 (R) and only 3 (K) members, respectively.

Both are enriched in lithophile and refractory elements but have characteristics of all chondrite classes combined. For example, K chondrites have matrix abundances like carbonaceous chondrites, metal abundances like H chondrites, oxidation states between H and enstatite chondrites, and lithophile element abundances like ordinary chondrites [Krot et al., 2003]. R chondrites have high oxidation states, are metamorphosed and

⁸Siderophile elements are concentrated in the metal phase like the core region of differentiated asteroidal bodies.

brecciated, and rarely contain calcium-aluminium rich inclusions.

1.3.2 Achondrites

Of the large amount of non-chondrite groups discussed in turn below only angrites and eucrites were sampled during this study.

Primitive achondrites Primitive achondrites include acapulcoites, lodranites, winonaites, and some iron meteorites. Acapulcoites and lodranites are not clearly distinguished, with acapulcoites generally being finer grained than lodranites. Their low cosmic-ray exposure ages indicate an origin from a single impact on the same parent body [McCoy et al., 1997]. Winonaites have chondritic compositions but achondritic textures. All primitive achondrites are mostly equigranular, highly metamorphic, contain relics of chondrules, and have undergone partial melting.

Differentiated achondrites Differentiated achondrites consist of aubrites, brachinites, ureilites, angrites, eucrites, mesosiderites, and pallasites.

Aubrites are also known as enstatite achondrites, are brecciated and mainly consist of enstatite. Their mineral composition is therefore close to that of enstatite chondrites, although originating from a different parent body. Brachinites are medium- to coarse-grained, consisting mainly of olivine, and their different petrologic and geochemical features suggest different formation scenarios. The ultramafic ureilites have high carbon contents, magmatic inclusions throughout and are believed to originate from partial melt residues. Mesosiderites are breccias, divided into petrological classes depending on their orthopyroxene content and silicate textures, reflecting metamorphic grades. Pallasites are grouped into main-group pallasites, eagle station pallasites and pyroxene-pallasites, depending on their olivine content and composition [Krot et al., 2003].

Angrites The small achondritic group of angrites currently consists of only 20 medium- to coarse-grained igneous rocks. This group is named after their most famous member, Angra dos Reis (AdoR), which was the first angrite found but is nowadays seen as the most unusual and petrologically different specimen of this group.

The angrites belong to the oldest known rocks of our solar system and are well preserved, with low metamorphism and shock effects. This makes them well suited as anchors and for intercalibration of the different isotopic systems used in extinct short-lived nuclide chronology (see also section 1.4).

Like all achondrite groups, angrites are considered to originate from only one differentiated planetesimal parent body and do not contain chondrules. They are basaltic achon-

drites that are enriched in refractory elements and formed during several melting stages of their parent body. The angrites can be further divided according to their textures, which resembles either quenched (fine grained) or plutonic (coarse grained) features.

HED group The HED group consists of howardites, eucrites, and diogenites. They are linked to the asteroid 4-Vesta as their parent body, with different meteorites resulting from impact ejecta [e.g. Misawa et al., 2005, Tera et al., 1997, Drake, 2001].

Howardites consist of lithified regoliths from the surface of 4-Vesta, containing impact-melt clasts, breccia fragments and high abundances of noble gases from solar winds [Suess et al., 1964, Metzler et al., 1995]. Diogenites are coarse-grained cumulate rocks, originating from the deepest impact layer of their parent body and mainly consist of orthopyroxenite [Metzler et al., 1995].

Eucrites are divided into basaltic (non-cumulate) eucrites, polymict brecciated eucrites and cumulate eucrites and vary in age, texture, degree of metamorphism and degree of volatile depletion [Tera et al., 1997, Nyquist et al., 1986]. Non-cumulate eucrites are divided into unequilibrated and ordinary eucrites. Unequilibrated eucrites originate from rapidly cooled surface lava flows and have undergone only minor metamorphism while ordinary (equilibrated) eucrites are highly metamorphic basalts. Cumulate eucrites are gabbros originating from deeper layers of the parent body. Their composition is close to that of terrestrial basalts. Eucrites are believed to contain some of the oldest basalts in the solar system [Nyquist et al., 1986], making them an important group to study.

1.3.3 Other meteorites

Iron meteorites are divided into 13 chemical groups depending on logarithmic plots of their trace element versus nickel abundances. They are also separated into structural groups depending on their metallic phase structure.

Martian meteorites are volcanic or plutonic rocks. Their fractionated isotopic compositions indicate that they originate from Mars.

Lunar meteorites originating from the Earth's moon are hard to classify, as they cover a wide spectrum of rock types from basalts to different breccias.

1.3.4 Inclusions in chondrites

Chondrules Chondrules represent the most abundant component of chondrites, with abundances ranging from having no preserved chondrules at all in CI type chondrites to

up to 80% by volume in enstatite and ordinary chondrites [Brearley and Jones, 1998]. Chondrules are millimeter-sized spherules believed to have formed from crystallized melt droplets in the earliest stages of the solar system, with variable shapes, textures and compositions [Zanda, 2004]. To date, there is no unifying model that explains the origin of chondrules, but there is evidence that their formation involved rapid heating, slower cooling, evaporation, condensation and redox processes. The two formation models that recently received attention are the so-called 'X-wind' model [Shu et al., 1997] and the nebula shockwave model [Desch and Connolly, 2002, Ciesla and Hood, 2002], which are explained in detail in section 1.5.

Calcium-aluminium rich inclusions Ca-Al-rich inclusions (CAIs) are refractory inclusions of <millimeter - centimeter size. They are the oldest known solids of the solar system with a complex history in the solar nebula and in the meteorites that became their parent bodies.

They condensed at very high temperatures ($>1200^{\circ}\text{C}$) at a very early stage of evolution of the solar system and are therefore of particular interest for gaining insight into the first events of the formation of the solar system. In fact, the ages of the oldest CAIs are often used as 'time zero', defining the beginning of the formation of the solar system, and as anchors for short-lived isotope chronometers [e.g. Nyquist et al., 2009, and many other references]. It is well established that CAI formation started 0-3 Myr (million years) before chondrule formation. This was determined using the absolute U-Pb chronometer [Amelin et al., 2010, Connelly et al., 2012] and several extinct nuclide chronometers, consisting of the parent-daughter nuclide systems ^{26}Al - ^{26}Mg [Villeneuve et al., 2009], ^{182}Hf - ^{182}W [Kleine et al., 2009], ^{129}I - ^{129}Xe [Swindle et al., 1996] and ^{53}Mn - ^{53}Cr [Yin et al., 2007].

There is evidence from all groups of chondrites that CAIs formed in only one nebula region and were distributed throughout the nebula after their formation period had ended [e.g. Guan et al., 2000].

Amoeboid olivine aggregates Amoeboid olivine aggregates (AOAs) are inclusions that condensed and aggregated with refractory objects from the same region of the solar nebula as CAIs, but at slightly lower temperatures of 900 - 1100°C [Fagan et al., 2004, Scott and Krot, 2003]. They are commonly found in chondrites and they consist mainly of fine-grained olivine, Fe-Ni metal and aluminium-diopside. They vary in size, shape, abundance and mineralogy.

1.4 Dating the solar system

1.4.1 Introduction

To fully understand the formation of the solar system and the meteorites recording its evolutionary history it is essential to create a timescale of early solar system events. Chronometers are used to determine the time between events that took place during the first few million years of the formation of the solar system. They are based on the decay of parent nuclides into daughter nuclides during a certain timeframe determined by the decay rates of the parent isotopes. The ages determined by these isotopic chronometers are always defined as the time of isotopic closure of a mineral, which is the time when a mineral ceases to exchange isotopes with its surroundings. Consequently, if a rock (or meteorite) undergoes melting or metamorphic processes after its initial formation, it is possible that the 'clock resets', meaning that the ages calculated represent the last time of alteration instead of the initial formation the rock. Also, minerals and isotopic systems can deviate in their isotopic closure times. This is especially important in slowly cooled rocks, as their closure times might vary, giving deviating ages depending on the minerals analyzed and the isotopic chronometer utilized.

The basic equation used for all isotopic chronometer calculations is

$$\frac{dN}{dt} = -\lambda N \quad (1.1)$$

which can be integrated and rearranged to give

$$D = D_0 + N * (e^{\lambda t} - 1) \quad (1.2)$$

where D = number of atoms of the daughter isotope in the sample; D_0 = original number of atoms of the daughter isotope; N = number of atoms of the parent isotope; λ = decay constant ($= \ln(2)/\text{half-life}$) of the parent isotope and t = time since isotopic closure.

For the actual isotopic calculations D , D_0 and N are divided by a common isotope, usually a stable isotope of the same element as the daughter isotope, for example ^{204}Pb for the ^{207}Pb - ^{235}U system. It is then possible to analyze these ratios in a sample to determine the time of isotopic closure.

For a parent-daughter system to be useful as an early solar system chronometer its nuclides have to be homogeneously distributed throughout the solar nebula at the time of their fractionation during the geological processes that led to the isotopic closure of the system. The precision of the radiometric ages determined increase with larger fractionation of the parent and daughter nuclides.

Equation 1.2 shows that isotope chronometers are strongly dependent on the parent-daughter isotope ratio and on the decay constants of the parent nuclide, and therefore the half-lives of the parent nuclides of the system. Depending on these half-lives the nuclide systems are divided into long-lived and short-lived isotope chronometers. In the case of the solar system only the U-Pb chronometer has a resolution high enough to be considered as a long-lived chronometer (<1 Myr). It is the only long-lived double isotope system and therefore any disturbances in the system can be recognized and used. The parent half-lives are also long enough (4.47 billion and 704 million years for ^{238}U and ^{235}U , respectively) to give absolute ages. All shorter-lived chronometers give relative ages, i.e. the timespan between two processes, and have to be anchored onto an absolute age given by the U-Pb chronometer.

What exactly triggered the formation of the solar system is still unclear, but the consensus is that a stellar nucleosynthetic event triggered the dense molecular cloud core to collapse, resulting in the protosun and solar nebula [e.g. Cameron and Truran, 1977].

Two important questions relate to the beginning of the formation of the solar system: what sequence of events occurred to form the present element and isotope compositions and were they distributed homogeneously in the protoplanetary disk? Answers to both questions depend on the nucleosynthetic environments from which the elements and their isotopes originated [e.g. Leya et al., 2003, Gounelle and Russell, 2005].

1.4.2 Short-lived nuclide chronometers

The first evidence for the former existence of many short-lived isotopes was found by elevated abundances of their daughter isotopes in comparison to other isotopes of the same elements in meteorites. These could not be explained by the nucleosynthetic events in the early solar system. One of the first extinct nuclides proven to have existed in the early stages of the solar system was ^{129}I , found by Reynolds [1960a,b], followed by many other isotopes throughout the periodic table from ^{10}Be to ^{244}Pu and the most recent suggestion of ^{247}Cm [Brennecka et al., 2010b].

The most commonly used parent-daughter isotope pairs used as early solar system chronometers are the ^{26}Al - ^{26}Mg [first evidence by Lee et al., 1976], ^{53}Mn - ^{53}Cr [first published by Birck and Allègre, 1985] and ^{182}Hf - ^{182}W [e.g. Lee and Halliday, 1995] systems (see Table 1.1).

^{26}Al and all Mg-isotopes, ^{24}Mg , ^{25}Mg and ^{26}Mg , can be synthesized during the thermonuclear fusion of a massive star and during explosive nucleosynthesis events like supernovae. Additionally, ^{26}Al decays in ~ 0.73 Myr to ^{26}Mg . This short half-life of the parent nuclide makes the ^{26}Al - ^{26}Mg system a high-resolution isotopic chronometer for the first

Table 1.1: Short-lived chronometers of extinct parent-daughter isotope systems.

Parent nuclide	Daughter nuclide	Half-life [Myr]	Estimated initial solar system abundance	Found in
^{26}Al	^{26}Mg	0.73	$^{26}\text{Al}/^{27}\text{Al} = 5.2 \times 10^{-5}$ ^a	CAIs, chondrules, achondrites
^{53}Mn	^{53}Cr	3.7	$^{53}\text{Mn}/^{55}\text{Mn} = 6.3 \times 10^{-6}$ ^b	CAIs, chondrules, carbonates, achondrites
^{182}Hf	^{182}W	8.9	$^{182}\text{Hf}/^{180}\text{Hf} = 9.7 \times 10^{-5}$ ^c	planetary differentiates
^{247}Cm	^{235}U	15.6	$^{247}\text{Cm}/^{235}\text{U} < 1.1 \times 10^{-4}$ ^d	CAIs, chondrules, achondrites

^aSchiller et al. [2010b]
^bTrinquier et al. [2008]
^cBurkhardt et al. [2008]
^dBrennecka et al. [2010b]

~5 Myr of the solar system. It is therefore particularly well suited to date the oldest solids in the solar system, such as CAIs, chondrules and achondrites. Also, the decay of ^{26}Al is a possible heat source for the melting processes that differentiated the achondrites [Kleine et al., 2012].

Both ^{53}Mn and ^{53}Cr are formed during explosive nucleosynthetic events, as are all other naturally occurring Cr-isotopes - ^{50}Cr , ^{52}Cr and ^{54}Cr . The half-life of ~3.7 Myr of ^{53}Mn , decaying to ^{53}Cr , allows us to date the events of the first ~20 Myr of the formation of the solar system including chondrite formation [Scott and Sanders, 2009]. The ^{53}Mn - ^{53}Cr isotopic system is somewhat unique, as both elements are depleted in CAIs due to their high volatilities, excluding the CAIs as possible anchors for this system. Therefore, this particular short-lived nuclide chronometer is generally anchored to Pb-Pb ages of the angrites instead.

The ^{182}Hf - ^{182}W isotope chronometer is the most important chronometer to evaluate accretion models and differentiation processes of asteroidal bodies in the early solar system. Due to a half-life of 8.9 Myr for ^{182}Hf it can be used to date events of the first ~60 Myr of the solar system [Kleine et al., 2009]. Moreover, both elements, Hf and W, are highly refractory and therefore unaffected by most high-temperature processes. Also, the lithophile Hf is strongly fractionated from the moderately siderophile W during differentiation processes in asteroidal bodies [Vockenhuber et al., 2004]. During this process all Hf is retained in the mantle while most of the incompatible W is distributed into the metal core. ^{182}Hf is believed to be primarily synthesized by r-processes during explosive nucleosynthesis, while the naturally occurring W-isotopes, ^{180}W , ^{182}W , ^{183}W , ^{184}W and ^{186}W , are formed during s-processes. However, a ‘fast’ s-process and a second r-process event have also been proposed as possible additional sources for ^{182}Hf , as its abundance, compared to the abundance of ^{129}I , cannot be explained by a uniform production model [Meyer and Clayton, 2000, Vockenhuber et al., 2004, and references therein].

The ^{247}Cm - ^{235}U short-lived nuclide chronometer investigated in this study is distinct from the other short-lived chronometers, as both the parent and the daughter isotopes can only be synthesized in r-processes. Therefore, if an increased abundance of ^{235}U can be definitely proven, the ^{247}Cm - ^{235}U isotopic system could be used to date the timeframe between the last r-process event effecting the solar nebula and the formation of the first solids. Also, the addition of ^{235}U from the decay of ^{247}Cm would challenge the validity of the absolute U-Pb chronometer, as ^{235}U decays to ^{207}Pb (see section 1.4.3). Specifically, the presence of ^{235}U derived from ^{247}Cm decay in early solar system solids would give rise to Pb-Pb ages that are systematically older than the true age calculated assuming no initial ^{247}Cm was present in the sample. To use the ^{247}Cm - ^{235}U system as a chronometer, Cm and U would have to be chemically fractionated either before or at the time of the forma-

tion of these first solids. As all isotopes of Cm are extinct the magnitude of this possible fractionation has to be determined using a chemical proxy for Cm. The light rare earth elements, including Pr, Nd and Sm, and the actinide Th are potentially useful as reference nuclides due to their similar volatilities, valence states and ionic radii [e.g. Lugmair and Marti, 1977, Jones and Burnett, 1987, Stirling et al., 2005, 2006].

Blake and Schramm [1973] first discussed the possibility of using the ^{247}Cm - ^{235}U isotopic system as a short-lived chronometer. They calculated that potential $^{238}\text{U}/^{235}\text{U}$ variations up to percentage levels should be present in early solar system condensates. First evidence for the existence of ‘live’ ^{247}Cm in the early solar system was reported by Arden [1977], measuring an ^{235}U excess of up to 30% in some bulk meteorites. Tatsumoto and Shimamura [1980] observed an excess of ^{235}U of up to 19% in mineral phases extracted from the CV3 chondrite Allende but also analyzed ^{235}U depletions of up to -35%. However, studies with higher precision by Chen and Wasserburg [1980, 1981] and Shimamura and Lugmair [1981, 1984] yielded unresolvable $^{238}\text{U}/^{235}\text{U}$ values based on samples including some of the bulk meteorites analyzed by Arden [1977] and mineral phases of Allende similar to those examined by Tatsumoto and Shimamura [1980]. The discussion around the ^{247}Cm - ^{235}U isotopic system and its application as a short-lived r-process chronometer was restarted with high-precision measurements of $^{238}\text{U}/^{235}\text{U}$ in bulk chondrites and eucrites reported by Stirling et al. [2005, 2006]. Although no resolvable differences in $^{238}\text{U}/^{235}\text{U}$ were measured in these bulk meteorites, Stirling et al. [2005, 2006] showed that a significant fractionation of these isotopes can be achieved during chemical leaching processes. The first high-precision measurements yielding resolvable $^{238}\text{U}/^{235}\text{U}$ variations and corresponding fractionations of ^{232}Th (^{144}Nd) and ^{238}U in CAIs extracted from the CV3 chondrite Allende were reported by Brennecka et al. [2010b]. To date, only the studies of Amelin et al. [2010] and Connelly et al. [2012] reported combined measurements of $^{238}\text{U}/^{235}\text{U}$ and Pb-Pb ages of the same set of samples. The variations in the $^{238}\text{U}/^{235}\text{U}$ ratios of CAIs analyzed in these studies correspond to very similar Pb-Pb ages of these samples. The implications of the above-mentioned studies will be discussed in detail in combination with findings of the present study in Chapter 5.4.

1.4.3 The long-lived nuclide chronometer

The lead isotopes ^{206}Pb and ^{207}Pb are used in U-Pb dating that provides the only absolute chronometers for dating events that occurred as long ago as the formation of the solar system. As lead forms from the decay of uranium, the uranium isotopic composition of $^{238}\text{U}/^{235}\text{U}$ is an important input parameter in U-Pb dating. All three natural occurring uranium isotopes, ^{238}U , ^{235}U and ^{234}U , form part of the radioactive decay chains that end

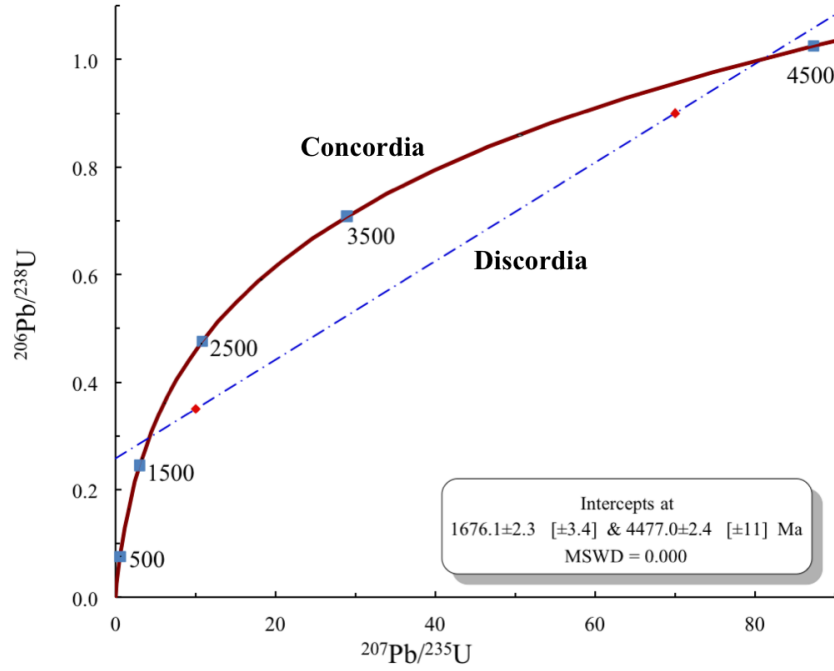
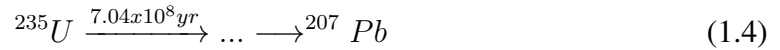
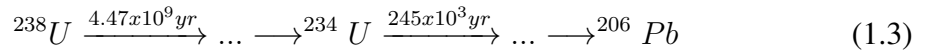


Figure 1.5: Concordia diagram for U-Pb dating, created with Isoplot-Ex 4.13 [Ludwig, 2003]. The red line represents concordia (with ages), while the blue line symbolizes an example of discordia, generated using two random data points. The intercept of the two curves at the higher age depicts the date the system closed, while the intercept at the lower age represents the time of the last metamorphic event the sample was exposed to, during which Pb leaked out of the system.

in the stable lead isotopes ^{206}Pb and ^{207}Pb , following equations 1.3 and 1.4:



These decay chains can be utilized to determine Pb-Pb ages using a traditional ($^{206}\text{Pb}/^{204}\text{Pb}$ over $^{207}\text{Pb}/^{204}\text{Pb}$) isochron and to calculate U-Pb ages using a concordia diagram (Fig. 1.5). The U-Pb concordia diagram is derived from equations 1.5 and 1.6. The following abbreviations apply for all of the following equations: p = present-day ratios, i = initial ratios, $\lambda_{235(238)}$ = decay constant of $^{235(238)}\text{U}$, t = time since isotopic closure and $^{206(207)}\text{Pb}^*$ = radiogenic lead.

$$\frac{^{206}\text{Pb}^*}{^{238}\text{U}} = \frac{(^{206}\text{Pb}/^{204}\text{Pb})_p - (^{206}\text{Pb}/^{204}\text{Pb})_i}{(^{238}\text{U}/^{204}\text{Pb})_p} = e^{\lambda_{238}t} - 1 \quad (1.5)$$

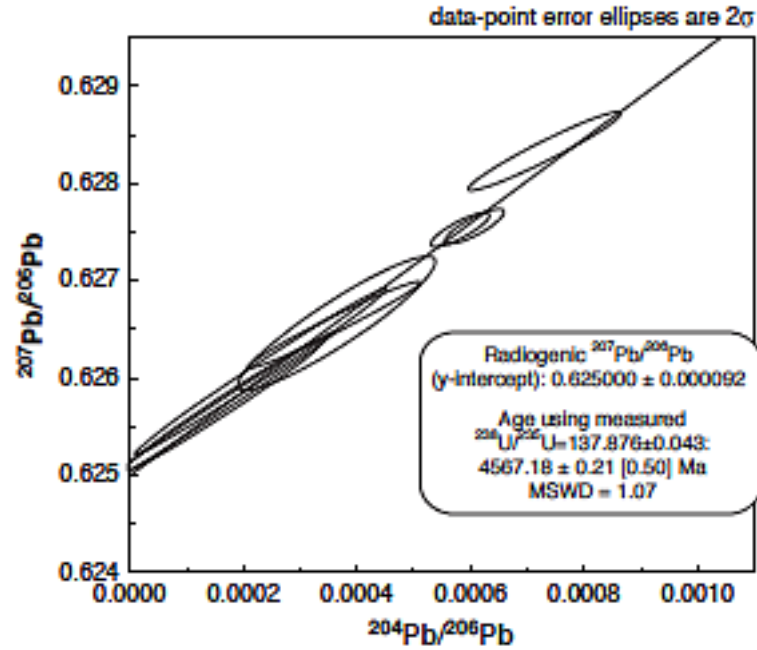


Figure 1.6: A typical 'inverse' lead isochron. The intercept with the y-axis is used to calculate the age of the sample, in this example utilizing a measured $^{238}\text{U}/^{235}\text{U}$ ratio. Each ellipse equals a data point with 2SD ($= 2\sigma$) errors of a different leachate of the same sample. MSWD represents the mean square weighted deviation of the age calculation, from Amelin et al. [2010].

$$\frac{{}^{207}\text{Pb}^*}{{}^{238}\text{U}} = \frac{({}^{207}\text{Pb}/{}^{204}\text{Pb})_p - ({}^{207}\text{Pb}/{}^{204}\text{Pb})_i}{({}^{235}\text{U}/{}^{204}\text{Pb})_p} = e^{\lambda_{235}t} - 1 \quad (1.6)$$

Concordia diagrams are especially useful for dating systems which were metamorphically disturbed and lost a certain amount of Pb in the process. Assuming that ^{206}Pb and ^{207}Pb do not fractionate during metamorphism and that $^{238}\text{U}/^{235}\text{U}$ is constant throughout the bulk silicate Earth all samples will plot on the discordia-line, depending on the amount of Pb loss. The interception point at the higher age of the concordia plot equals the real age of the sample, while the lower age represents the time of Pb loss.

The equation for Pb-Pb isochron dating is derived from both U-Pb decay equations (Eq. 1.7 and Eq. 1.8) and is shown in equation 1.9. Currently, an 'inverse' Pb-Pb isochron is often used instead of the traditional isochron mentioned above (Fig. 1.6), with $^{204}\text{Pb}/^{206}\text{Pb}$ used as the x-axis and $^{207}\text{Pb}/^{206}\text{Pb}$ used as the y-axis. One way to utilize an isochron like this is to plot several measurements of different leachates of a sample, including their 2SD uncertainties, and determine the intercept of the linear regression line and the y-axis. This intercept is then used to calculate the age of the sample. Alternatively, a range of related rock samples or mineral separates can be used for age determination.

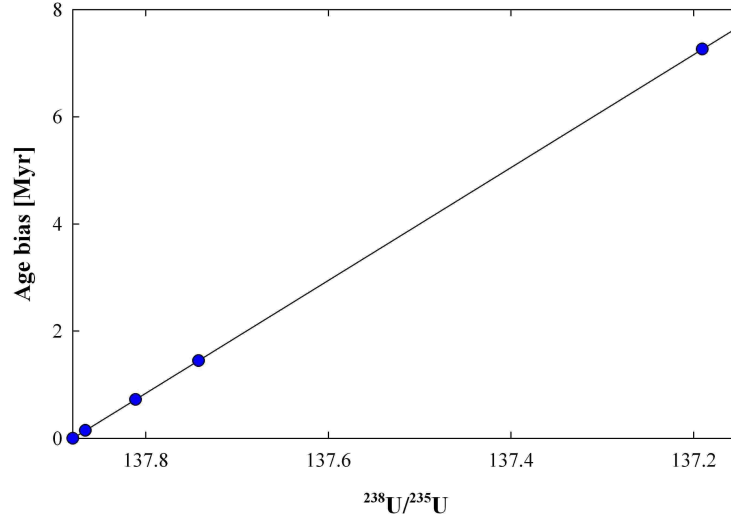


Figure 1.7: Age bias of a sample with the true age of 4567 Myr according to the excess of ^{235}U from the decay of ^{247}Cm .

$$\left(\frac{^{207}\text{Pb}}{^{204}\text{Pb}}\right)_p = \left(\frac{^{207}\text{Pb}}{^{204}\text{Pb}}\right)_i + \left(\frac{^{235}\text{U}}{^{204}\text{Pb}}\right) (e^{\lambda_{235}t} - 1) \quad (1.7)$$

$$\left(\frac{^{206}\text{Pb}}{^{204}\text{Pb}}\right)_p = \left(\frac{^{206}\text{Pb}}{^{204}\text{Pb}}\right)_i + \left(\frac{^{238}\text{U}}{^{204}\text{Pb}}\right) (e^{\lambda_{238}t} - 1) \quad (1.8)$$

$$\frac{(^{207}\text{Pb}/^{204}\text{Pb})_p - (^{207}\text{Pb}/^{204}\text{Pb})_i}{(^{206}\text{Pb}/^{204}\text{Pb})_p - (^{206}\text{Pb}/^{204}\text{Pb})_i} = \left(\frac{^{207}\text{Pb}}{^{206}\text{Pb}}\right)^* = \left(\frac{^{235}\text{U}}{^{238}\text{U}}\right) \left(\frac{e^{\lambda_{235}t} - 1}{e^{\lambda_{238}t} - 1}\right) \quad (1.9)$$

As can be seen in the equations above the U-Pb dating systems are easily disturbed if the true $^{238}\text{U}/^{235}\text{U}$ value deviates from the value used. For example, Fig. 1.7 shows the age bias of a sample with a true age of 4567 Myr if the assumed $^{238}\text{U}/^{235}\text{U}$ ratio of 137.88 [Steiger and Jäger, 1977] is adjusted to lighter values. After several decades of adopting a constant $^{238}\text{U}/^{235}\text{U}$ value of 137.88 across the entire solar system it is now recognized that considerable $^{238}\text{U}/^{235}\text{U}$ variability exists in nature [e.g. Stirling et al., 2007, Weyer et al., 2008, Bopp et al., 2009, Amelin et al., 2010, Brennecka et al., 2010b, Connelly et al., 2012]. Therefore, the uranium isotopic ratios of each sample should be analyzed before attempting to determine Pb-ages. As indicated above, the Pb-Pb ages of CAIs or Angrites are commonly used as anchors for the extinct short-lived nuclide chronometers. In practice this involves linking the absolute Pb-Pb age of a CAI or Angrite to the measured parent-daughter isotopic ratio of a short-lived nuclide system. Then other samples can be dated by analyzing only the isotopic ratio of the short-lived chronometer used in comparison with the composition of the sample used as a chronological anchor. Therefore, if the

Pb-Pb age is not correct, all relative ages anchored to it will have the same offset. Recently, several authors have reported discrepancies between the ages derived via different chronometers, especially between absolute and relative ages [e.g. Amelin et al., 2002, Jacobsen et al., 2008, Amelin et al., 2009, Spivak-Birndorf et al., 2009, Wadhwa et al., 2009]. For example, Wadhwa et al. [2009] reported an absolute Pb-Pb age for the achondrite Asuka 881394 of 4566.5 ± 0.2 Myr, about 1 Myr older than the corresponding ^{26}Al - ^{26}Mg and ^{53}Mn - ^{53}Cr ages of 4565.4 ± 0.2 Myr and 4565.5 ± 0.4 Myr. The differences in these age calculations most likely result from inaccurate assumptions of the initial isotopic abundances of parent and daughter nuclides (Table 1.1) and the presumption of a homogeneous distribution of these nuclides throughout the presolar cloud. By analyzing the uranium isotopic ratios of several meteorite groups this project will hence significantly contribute to the intercalibration of these absolute and the relative chronometers.

1.5 The collapse of the presolar cloud

The source(s) for the isotopes used as chronometer systems and their homogeneous distribution throughout the molecular cloud are dependent on the mechanism that triggered the collapse of the presolar cloud. The three main events that might have caused this collapse will be discussed in the following section.

1.5.1 Supernova / shockwave model

One possible source for homogeneously distributed short-lived isotopes are supernovae explosions close to the molecular cloud that later became the solar system, first proposed by Cameron and Truran [1977]. In this model material was distributed throughout the protoplanetary disk by shockwaves that caused heating events [Krot et al., 2009] during which chondrules and CAIs were formed (see Fig. 1.8). Ouellette et al. [2007] proposed that a supernova occurred after the protoplanetary disk was already formed and the radioactive material was injected straight into the disk.

There are two isotopes that strongly suggest a supernova as the source for short-lived nuclides: ^{247}Cm and ^{60}Fe . ^{247}Cm can only form during an r-process, while ^{60}Fe can be formed in an r- or an s-process. If the highly variable $^{238}\text{U}/^{235}\text{U}$ values in CAIs measured by Brennecka et al. [2010b] can be reproduced this will be strong evidence for the presence of the short-lived isotope ^{247}Cm (half-life 15.6 Myr) in the early solar system. This would indicate that an r-process took place close to the beginning of the formation of the solar system and may even have triggered its formation.

The high abundance of the short-lived ^{60}Fe (half-life 1.5 Myr) in the early solar system

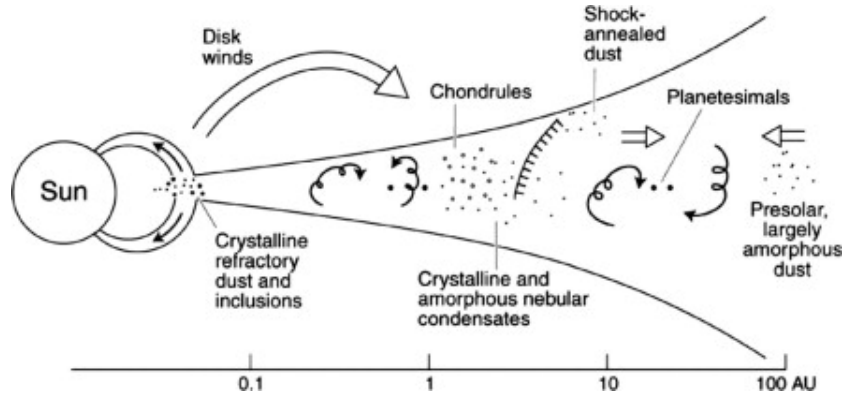


Figure 1.8: Shockwave model, from Krot et al. [2009]

can only be explained with a stellar source for nucleosynthesis. A supernova seems more likely to do so than an AGB star, which is not commonly associated with star forming regions and yields lower abundances of ^{60}Fe than supernovae [Ouellette et al., 2005, Goswami et al., 2005, Ouellette et al., 2007]. The inheritance from the interstellar medium can be ruled out due to the high abundances of ^{60}Fe found in meteorites and the short half-life of ^{60}Fe , which would have decayed before they could be incorporated into the molecular cloud [e.g. Ouellette et al., 2007].

An r-process strong enough to form ^{60}Fe and ^{247}Cm is most likely to occur in core collapse supernovae [Qian et al., 1998]. The r-process takes place in the outgoing neutron-rich shock wave, which is also distributing the left-over ashes and newly formed elements of the nuclear burning stages of the star into the surrounding areas.

This model is probably the most plausible as it can explain the formation of short-lived nuclides and the collapse of the molecular cloud. Also, supernovae are a common feature of star-forming regions and this model does not depend on a large amount of the elements being inherited from the ISM to be coherent. It would also allow the former existence of ^{247}Cm and therefore a higher variability in the $^{238}\text{U}/^{235}\text{U}$ ratio, as ^{247}Cm is the parent isotope of ^{235}U .

1.5.2 AGB star model

This model provides another possibility of a homogeneous distribution of short-lived isotopes in the nebula disk. AGB stars are intermediate mass stars in the final stage of their evolution, with masses $1 M_{\odot} \leq M \leq 10 M_{\odot}$. They consist of three layers: an electron degenerate C-O-core, a helium rich intershell, and a hydrogen rich mantle. AGB stars

induce strong stellar winds⁹ that increase as the star evolves and are caused by pulsation of the two outer layers. These layers alternate switching their nuclear burning on and off and by radiation pressure forcing the dust forming around the star to move [Lugaro and Chieffi, 2011, and references therein]. As mentioned above, AGB stars do not have a high enough mass to produce sufficient heat and pressure in their core to ignite the carbon within it. During their burning stages they undergo s-process nucleosynthesis, forming isotopes with masses up to ^{209}Bi and distributing them to their surroundings.

If an AGB star crossed through the nebula disk it would have passed on its isotopic signature to the early solar system. However, it is statistically unlikely that a late stellar stage object like an AGB star will spatially and temporarily overlap with the region of a forming star [e.g. Kastner and Myers, 1994]. Further, an AGB star might not be able to form ^{60}Fe in the high abundances needed to match the observed average abundances in the solar system [Tachibana et al., 2006]. It would also be unlikely to form high-mass elements like U or Cm. Therefore, this model seems less feasible than the supernova model.

This model would imply that no ^{247}Cm was formed in the early stages of the solar system. Therefore, uranium would have been inherited from the ISM and should not show variations in its isotopic signature caused by the decay of ^{247}Cm .

Similar limitations are encountered by other models involving nova or Wolf-Rayet stars¹⁰.

1.5.3 X-Wind model

The X-Wind model is the only accepted model that does not need the presence of stellar nucleosynthesis. In this scenario short-lived nuclides with masses from ^7Be to ^{93}Nb are produced by irradiation near the protosun. This model was first proposed by Shu et al. [1997] and presents the only mechanism that heterogeneously distributes short-lived nuclides throughout the protoplanetary disk. These nuclides would therefore not be useable for early solar system chronology.

CAIs and chondrules were formed in or near the X-region (see Fig. 1.9) [Shu et al., 2001, Leya et al., 2003] and were shielded from irradiation to different degrees. CAIs underwent a longer period of irradiation in the reconnection ring than chondrules, before both solids were simultaneously distributed by the X-wind [Krot et al., 2009]. The magnetised X-wind itself is formed by interactions of the stellar coronal wind and winds from the inner edge of the accretion disk [Busso, 2011, and references therein].

The X-wind is capable of transporting solids from the disk into solar flares, transporting them into other parts of the disk. Evidence for these processes were first found during the

⁹Stellar winds are the continuous ejecta of matter from a star.

¹⁰Wolf-Rayet stars are massive stars which rapidly lose mass due to strong stellar winds. They either evolve into supernovae or collapse into black holes.

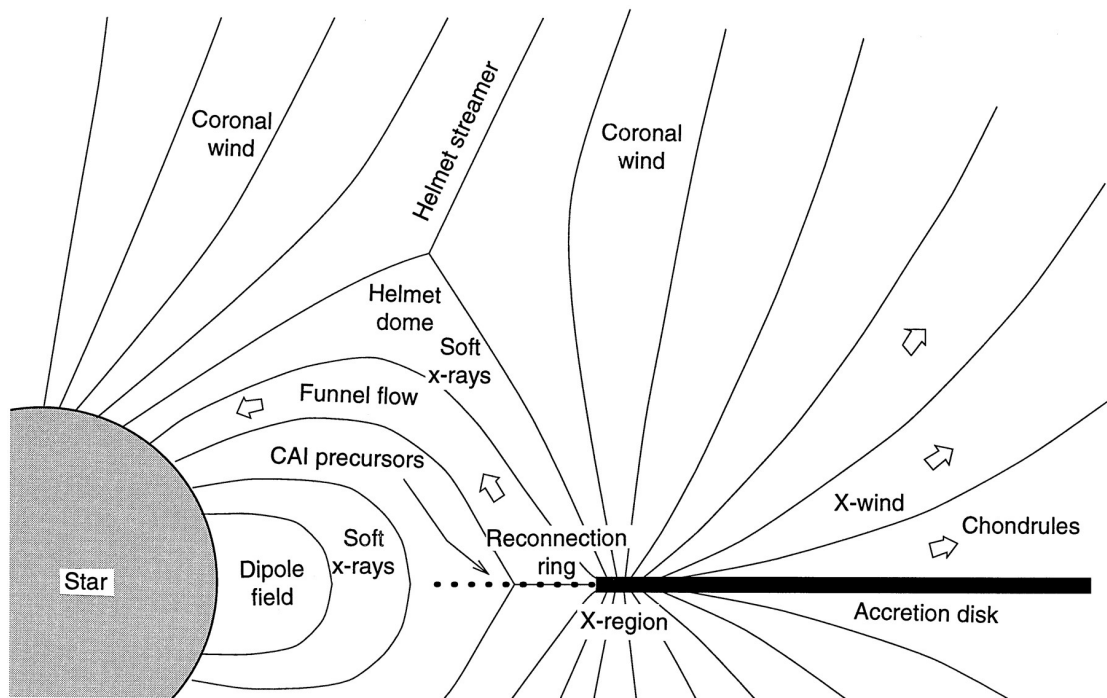


Figure 1.9: X-Wind model from Shu et al. [1997]

STARDUST mission of the NASA Discovery program [Brownlee et al., 2006].

However, one major limitation of this model is that it does not explain the former existence of ^{60}Fe or short-lived nuclides of masses higher than ^{93}Nb . Instead, those isotopes must have been produced by another nearby source or been inherited from the interstellar medium. This is unlikely, as, due to the short half-lives of those nuclides, they would have decayed before being incorporated into the presolar disk. This also implies that ^{247}Cm could not have been formed due to the lack of nucleosynthesis. The uranium isotope signature could, however, have been altered during the formation of CAIs and chondrules and heterogeneously distributed via the X-wind.

1.6 The uranium redox system

There are an increasing number of studies reporting significant $^{238}\text{U}/^{235}\text{U}$ variations in meteorites that cannot be related to the decay of ^{247}Cm , as they report depletions in ^{235}U rather than excesses [Amelin et al., 2010, Connelly et al., 2012]. Additionally, there is evidence of sizable $^{238}\text{U}/^{235}\text{U}$ fractionation in high-temperature terrestrial systems [Hiess et al., 2012]. This is despite previous expectations that U ‘stable’ isotope fractionation should not be resolvable in these environments. Therefore, further efforts are required to

elucidate the exact mechanism controlling $^{238}\text{U}/^{235}\text{U}$ isotope fractionation in meteorites over and above the isotopic shifts of possible ^{247}Cm decay. To this end, a large section of this thesis is dedicated to the uranium isotopic fractionation of ^{238}U and ^{235}U in low-temperature aquatic environments. To date, the largest isotopic shifts in $^{238}\text{U}/^{235}\text{U}$ ratios have been documented in these environments [Bopp et al., 2009, Brennecka et al., 2010a, Murphy et al., 2012]. This study will therefore improve our general understanding of the possible fractionation mechanisms controlling uranium isotopes. Some of these processes are likely to be extrapolated to meteoritic processes, including the accretion of chondrites and aqueous alterations in meteorites under both low- and high-temperature conditions. In terrestrial low-temperature environments possible fractionation mechanisms include aggregation/disaggregation and adsorption/desorption of U onto/from particles, weathering reactions, precipitation processes, the biological uptake of dissolved U(VI), back-reactions with porewaters in sediments, and, perhaps of the most relevance, the chemical or microbiological reduction of highly soluble U(VI) to insoluble U(IV) [e.g. Swarzenski et al., 1995, 1999, Porcelli and Swarzenski, 2003, and references therein]. Redox mechanisms in particular have been shown to change the isotopic signature of many geological systems, involving both low- and high-temperature mechanisms.

Another possible fractionation mechanism is given by natural fission and neutron capture reactions of uranium. These would result in $^{238}\text{U}/^{235}\text{U}$ that is depleted in ^{235}U . The only known natural fission reactors on Earth are the Oklo and Bangombé reactor in the Franceville basin, Gabon, showing uranium isotopic compositions that are highly depleted in ^{235}U [e.g. Lancelot et al., 1975, Kikuchi et al., 2010, Horie et al., 2004]. However, these natural reactors require high grade uranium ores with an uranium abundance of 10-20% [Gauthier-Lafaye et al., 1996], which do not occur in any of the meteorites analyzed in this study.

Uranium has four oxidation states, U(III)-U(VI), of which only U(IV) and U(VI) are commonly present. The oxidized, hexavalent condition, U(VI), is the most common species observed on the surface of present-day Earth. It exists in form of uranyl ions (UO_2^{2+}), which form soluble, non-reactive complexes with carbonates, primarily as $(\text{UO}_2)(\text{CO}_3)_3^{4-}$ [Langmuir, 1978]. If the redox conditions change, uranium can be reduced to tetravalent U(IV) and forms immobile minerals with hydroxides, fluorides and phosphates that precipitate out of the water column. It is very likely that isotopic fractionation of uranium takes place during this process. An analogous redox transformation is likely to occur in high-temperature environments, such as igneous melts and evaporation/condensation processes, on Earth and in extraterrestrial environments. For the ^{238}U - ^{234}U system, these fractionation mechanisms are well understood and have been applied to aquatic systems throughout the past several decades. Fractionation of ^{238}U and ^{234}U is based on the pref-

erential release of ^{234}U over ^{238}U during weathering. This is a consequence of α -recoil¹¹ and the relatively short half-life of ^{234}U and its precursor nuclide ^{234}Th of 245,000 years and 24 days, respectively. However, the mechanisms controlling ^{238}U - ^{235}U fractionation are not well understood. Both ^{238}U and ^{235}U are strongly lattice-bound and not affected by α -recoil. Fractionation between ^{238}U and ^{235}U appears to be controlled by stable isotope effects. This has been observed for other metal isotope systems, such as iron [Anbar, 2004], zinc and copper [Maréchal and Albarède, 2002]. However, mass-dependent mechanisms causing the preferential removal of the lighter isotope over the heavier isotope are not expected for uranium due to its heavy mass. Instead, so-called volume-dependent effects of the opposite signature to those expected from mass-dependent fractionation have been observed in uranium [Weyer et al., 2008, Bopp et al., 2010, Brennecka et al., 2011b, Murphy et al., 2012].

Since ^{238}U and ^{235}U both have extremely long half-lives of $\sim 4.47 \times 10^9$ yr and $\sim 0.7 \times 10^9$ yr, respectively, they are considered 'stable' in the context of redox behaviour in aquatic systems where the time frames of processes are much shorter.

1.6.1 Theory

Mass-dependent isotopic fractionation between two isotopes is proportional to their mass difference. Mass-dependent isotopic shifts can be caused by kinetic or equilibrium reactions. The latter represents the effect created by differences in the vibrational zero-point energy of these isotopes [Young et al., 2002], which is given by their lowest energy states. If the vibrational frequencies of two isotopes deviate, so does the strength of their bonds with other atoms in the molecule. Therefore, the isotope with the weaker bond is preferentially removed from the substrate. Heavier isotopes have lower zero-point energies and, hence, a higher energy is needed to break their bonds within a molecule and the lighter isotope is preferentially removed. Kinetic isotope fractionation characterizing, for example, evaporation and condensation processes, biological uptake or many redox reactions, is a function of the deviating reaction rates of isotopes with different masses. Specifically, the lighter isotopes have faster reaction rates, as their chemical bonds are more easily broken, and are preferentially removed. Kinetic fractionations depend largely on the reaction mechanisms and the amount of back-reactions involved, while equilibrium reactions are purely based on the energy differences between the isotopes.

Recent publications have observed that the volume-dependent nuclear field shift effects can cause isotopic fractionation of ^{238}U and ^{235}U up to three times stronger than the mass-dependent effects [Bigeleisen, 1996, Bopp et al., 2010, Weyer et al., 2008, Schauble,

¹¹An α -recoil is a displacement of a radiogenic daughter isotope in the crystal lattice, caused by the radioactive decay of the parent isotope.

2007]. These effects preferentially remove heavier isotopes from the substrate during reduction processes of U(VI) to U(IV). This fractionation behaviour is caused by two effects. First, nuclear radii of isotopes with odd neutron numbers tend to be smaller in size than isotopes with even neutron numbers. Therefore, the nuclear volume effect does not scale in proportion to the mass difference between the fractionating isotopes, particularly when both odd- and even-numbered isotopes are compared [Schauble, 2007]. This is the case for ^{235}U , comprising 143 neutrons, and ^{238}U , containing 146 neutrons. Secondly, differences in the orbital structures of molecules cause smaller isotopes to have a larger density of electrons at their nuclei than larger isotopes. This causes a displacement of the atomic ground electronic energy, producing lower electronic energy levels for the smaller isotope, ^{235}U , than for the larger isotope, ^{238}U [Bigeleisen, 1996, Fujii et al., 2006]. As mentioned before, a higher energy is needed to break the bonds of isotopes with lower electronic energy. Hence, the nuclear volume effect causes the heavier isotope to be preferentially removed. Bigeleisen [1996] also showed that the nuclear spin effect, resulting from the different spins of each nucleus, is negligible compared with the nuclear field shift for uranium isotopes, as it is a magnitude smaller at equilibrium. The uranyl ion, U(VI), has a larger electron density at its nucleus than the complexed U(IV) ion, leading to a preference for ^{238}U in the reduced U(IV) species [Bigeleisen, 1996].

The contributions to the fractionation factor¹² of the ^{238}U - ^{235}U isotope system during the U(VI)-U(IV) equilibrium exchange reaction at $T = 308 \text{ K}$ are $\ln \alpha_0 = -7.56 \times 10^{-4}$ for the mass-dependent vibrational effects (whereby the lighter isotope is preferred over the heavier isotope) and $\ln K_{fs} = 20.56 \times 10^{-4}$ for the volume-dependent nuclear field shift effects (whereby the heavier isotope is preferred over the lighter isotope). This gives a total $\ln \alpha = \ln \alpha_0 + \ln K_{fs} = 13.00 \times 10^{-4}$ [Bigeleisen, 1996]. This corresponds to an enrichment factor of the product, U(IV), of $\alpha = 1.0013$ and a fractionation factor for the oxidized, U(VI) rich residue of $\alpha = 0.9987$.

Fractionation factors decrease with temperature, scaling $1/T$ for nuclear field shift and $1/T^2$ for zero-point energy effects (Eq. 1.10 and Eq. 1.11) [Bigeleisen, 1996, Schauble, 2007]. This means that both effects are reduced with higher temperatures, but the mass-

¹²The fractionation factor α is defined as

$$\ln \alpha = \left(\frac{hc}{kT} \right) f_s * A + \frac{1}{24} * \left(\frac{h}{2\pi kT} \right)^2 \frac{\delta m}{mm'} * B \quad (1.10)$$

where k = Boltzmann constant, h = Planck constant, m', m = masses of the light and heavy isotopes, $\delta m = m - m'$, T = temperature, f_s = field shift, c = velocity of flight and A, B are adjustable constants.

As the field shift is proportional to the isotopic difference in the nuclear charge radius, $\delta \langle r^2 \rangle$, this equation can be simplified to give

$$\ln \alpha = \delta \langle r^2 \rangle_{m,m'} * a + \frac{\delta m}{mm'} * b \quad (1.11)$$

where a, b are adjustable coefficients and functions of $1/T$ and $1/T^2$, respectively [Fujii et al., 2006].

dependent effect is reduced faster than the nuclear field shift effect. Therefore, $\ln \alpha$ will always stay positive and ^{238}U should always be preferentially removed over ^{235}U . For low-temperature samples with a very small temperature range, like the water samples analyzed in this study, the effect of this scaling is negligible. For high-temperature magmatic samples, like differentiated meteorites, the scaling effect has a higher importance, as it generally means that the ability of ^{238}U and ^{235}U to fractionate should decrease with increasing closure temperature of the isotopic system.

1.6.2 Previous work

There are several applications for the study of isotopic fractionation of uranium in terrestrial samples. These include, for example, the remediation of contaminated groundwater, following U exploration and mining, uranium ore formation processes for economic geology and using uranium stable isotopes as a proxy for paleo-redox conditions to constrain the underlying causes of past environmental changes. These observations have been underpinned by the following recent observations of ^{238}U - ^{235}U isotope fractionation.

Field studies involving the controlled microbial reduction of U(VI) to U(IV) and the consequent removal of uranium from contaminated groundwater at mining sites leads to lower $^{238}\text{U}/^{235}\text{U}$ ratios in the remaining aqueous phase, consistent with the nuclear field shift effect [Bopp et al., 2010]. Uranium reducing bacteria are an efficient way of removing uranium from contaminated groundwater and soil, especially at mining sites, to prevent it from migrating through the aquifer [Abdelouas et al., 2000, Luo et al., 2007, Komlos et al., 2008, Bopp et al., 2010]. The magnitude of uranium isotope fractionation might therefore be used to identify the progress of bioremediation and assess the long-term re-oxidation and remobilization of uranium in aquifers [Bopp et al., 2010].

In contrast to the finding of Bopp et al. [2010], laboratory controlled microbial reduction experiments of Rademacher et al. [2006] show mass-dependent fractionation with the lighter ^{235}U preferentially removed from the water column under reducing conditions. Chemically induced uranium reduction driven by Fe^0 [Rademacher et al., 2006] and Zn^0 [Stirling et al., 2007] did not produce an isotopic shift between ^{238}U and ^{235}U , but the possibility exists that reaction rates were too fast to induce $^{238}\text{U}/^{235}\text{U}$ fractionation. It may also indicate that biological processes are required to mediate uranium reduction, as microbes are present in almost all the natural environments where uranium reduction occurs.

In terms of field-based measurements for natural systems, Stirling et al. [2007] found that uranium isotope fractionation in low-temperature terrestrial samples can follow both mass-dependent and volume-dependent pathways. However, they did not find direct evidence that the reduction of uranium caused the observed $^{238}\text{U}/^{235}\text{U}$ shifts of $>1\%$.

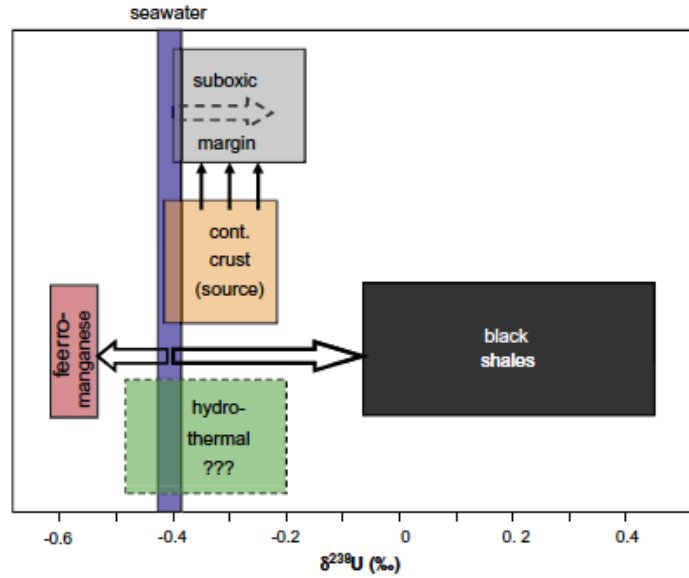


Figure 1.10: Box model of uranium fractionation in the open ocean cycle. Figure published by Weyer et al. [2008].

Weyer et al. [2008] argued that processes resulting in nuclear field shift effects are linked to the reduction of U(VI) to U(IV), while the formation of ferromanganese oxides and adsorption of uranium results in much smaller fractionation in the opposite direction when analyzing natural samples. This is in agreement with Brennecka et al. [2011b], who found that ^{235}U is favourably adsorbed onto Mn-oxyhydroxides with a fractionation factor of 0.2‰ under laboratory controlled conditions. By reproducing the less precise data of Cowan and Adler [1976], Bopp et al. [2009] observed 1‰ ^{238}U - ^{235}U fractionations in redox-controlled aquifer settings, between precipitates from reducing groundwaters (sandstones) and hydrothermally or magmatically derived rocks in ore deposits. Additionally, Murphy et al. [2012] reported large $^{238}\text{U}/^{235}\text{U}$ isotopic shifts up to 5‰ in reducing groundwaters and sandstone-hosted uranium deposits in an active, redox-controlled aquifer. Again, both datasets follow the nuclear field shift theory, showing heavier $^{238}\text{U}/^{235}\text{U}$ compositions in the reduced U(IV) phase.

Weyer et al. [2008] also published a preliminary box model showing the different directions of U isotope fractionation, characterizing the sinks and sources of U in the open oceans according to their uranium isotopic compositions (Fig. 1.10)¹³.

Noordmann et al. [2009, 2010] report that neither weathering and transport in rivers nor

¹³

$$\delta^{238}\text{U} = \left[\frac{(^{238}\text{U}/^{235}\text{U})_{\text{sample}}}{(^{238}\text{U}/^{235}\text{U})_{\text{standard}}} - 1 \right] * 1000 \quad (1.12)$$

hydrothermal processes influence the uranium budget of the oceans enough to significantly alter its uranium isotopic composition. In contrast, Stirling et al. [2007], Weyer et al. [2008] document a slight enrichment of ^{235}U in seawater. Based on leaching experiments it is proposed that this is caused by the preferential leaching of ^{235}U from exposed crustal rocks during weathering processes [Stirling et al., 2007, Hiess et al., 2012]. This is possibly due to the slightly weaker bonds of ^{235}U in the crystal lattice compared to ^{238}U , and is in agreement with the mass-dependent equilibrium effect described above.

On the basis of these datasets, which show consistency in their U isotopic behaviour during U reduction, it has recently been suggested that the ^{238}U - ^{235}U isotope system offers significant potential as a paleo-redox proxy. This proxy can be utilized to quantify the changing redox conditions during past Oceanic Anoxic Events (OAE's, first defined by Schlanger and Jenkyns [1976]) that occurred during the warm 'super-greenhouse' conditions of the Mesozoic¹⁴ [Montoya-Pino et al., 2010]. Oceanic Anoxic Events might have caused the largest mass extinctions on Earth. They were accompanied by elevated mean surface temperatures, resulting in changes of the ocean currents and lowered dissolved oxygen levels in the oceans [e.g. Wignall and Twitchett, 1996, Brenneke et al., 2011a]. These unusual anoxic conditions preserved high amounts of organic matter, which is nowadays found in form of major oil and gas reserves. Determining the timeframe and extent of OAEs is a crucial tool to finding these worldwide reserves.

In terms of high-temperature environments, Hiess et al. [2012] defined a new average $^{238}\text{U}/^{235}\text{U}$ ratio of 137.818 ± 0.050 for the composition of 'Bulk Silicate Earth' (BSE), supported by the analyses of 44 zircons. This new ratio is significantly lower than the previously assumed uniform $^{238}\text{U}/^{235}\text{U}$ value of 137.88. The new value would result in a significant decrease of ^{207}Pb - ^{206}Pb ages of about one million years for 100 Myr old samples and about 700,000 years for samples that are four billion years old. Hiess et al. [2012] further note that based on all published data to date near-surface environments show a wider range of uranium isotope ratios than magmatic samples (see Fig. 1.11), implicating a better homogenization of uranium isotopes in magmatic systems than in low-temperature processes. Andersen and Elliott [2011] are currently exploring the influence of recycled uranium on $^{238}\text{U}/^{235}\text{U}$ ratios by analyzing ocean water, ocean island basalts and mid-ocean ridge basalts with ultra-high precision levels.

¹⁴The Mesozoic is a geological era, lasting from 261.0-65.5 Ma ago. It started with the largest mass extinction event in the Earth's history and ended with the mass extinction of the dinosaurs and other species.

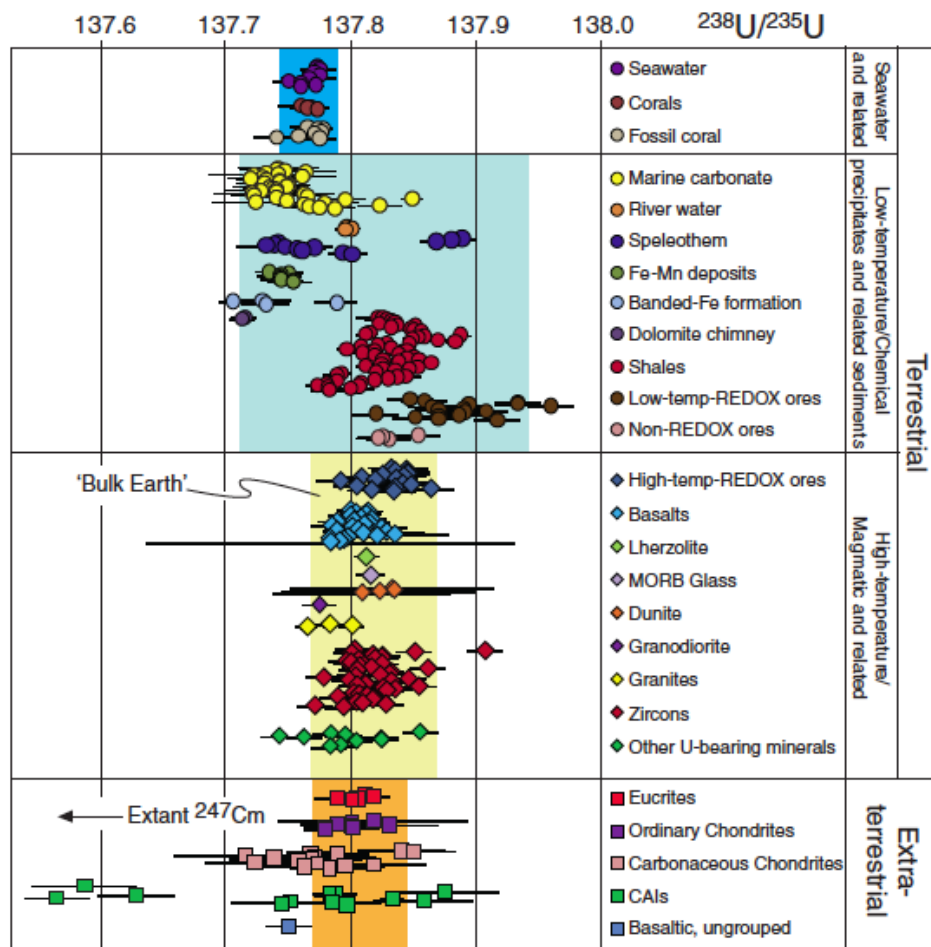


Figure 1.11: Summary of $^{238}\text{U}/^{235}\text{U}$ ratios of a wide variety of samples, taken off Hiess et al. [2012].

1.7 History of uranium isotopic analysis of $^{238}\text{U}/^{235}\text{U}$

Nier [1939] was the first to report a value for the present $^{238}\text{U}/^{235}\text{U}$ ratio of $139 \pm 1\%$, based on a compilation of analyzed uranium isotopic ratios ranging from 135.3-142.3 in natural samples, utilizing an early mass spectrometer. The implications of uranium isotope ratios for geochronology using U-Pb-dating was shown by Kuroda [1955], but uranium isotope fractionation could not be confirmed for terrestrial samples. Instead a new $^{238}\text{U}/^{235}\text{U}$ average of 137.7 ± 0.3 was introduced [e.g. Senftle et al., 1957], which was changed to 137.8 with the introduction of the U-Pb concordia diagram [Wetherill, 1956] and its first applications [Ulrych, 1967, Russell et al., 1967] (see also Fig. 1.5). However, other ratios were still widely applied [e.g. Hamilton, 1967].

Dietz et al. [1962] first applied a ^{233}U - ^{236}U isotope tracer to $^{238}\text{U}/^{235}\text{U}$ measurements, using Thermal Ionization Mass Spectrometry (TIMS).

The discussion about variations in uranium isotope ratios was re-opened when fractionation in Precambrian ore deposits were found [Cowan and Adler, 1976, and references therein], using gas spectrometry.

Blake and Schramm [1973] first mentioned the possibility of using the extinct, short-lived isotope ^{247}Cm to gain new insights into r-process nucleosynthesis and to use it as a short-lived chronometer for early solar system processes. Arden [1977] reported wide variations in chondritic meteorites with average $^{238}\text{U}/^{235}\text{U}$ ratios ranging from 106.8-137.5 and single measurements of acid-etched residues of as low as 40.23 ± 0.73 . However, the decay of ^{247}Cm was only considered as one possible explanation for these variable $^{238}\text{U}/^{235}\text{U}$ compositions. Tatsumoto and Shimamura [1980] first claimed to have found evidence for the former existence of ^{247}Cm in inclusions of Allende and variations in the meteoritic uranium isotope ratio to values both higher and lower than the terrestrial value of 137.88 published by Steiger and Jäger [1977]. Shortly after, both findings were negated by Chen and Wasserburg [1980, 1981], who could not detect a discrepancy between terrestrial and extraterrestrial uranium isotope ratios outside 0.6% for bulk meteorites and 2% for Allende inclusions.

Rokop et al. [1982], still using TIMS, was the first study to report a method to analyze $^{238}\text{U}/^{235}\text{U}$ ratios with accuracies of $<1\%$ but still with blanks of up to 400 pg U for natural samples. This was shortly followed by Donohue et al. [1984], using Resonance Ionization Mass Spectrometry (RIMS). At this point it had become standard practice to analyze the uranium isotopic compositions of samples by adding an enriched spike made of one or two uranium isotopes to correct for drifting instrumental mass fractionation behaviour. Still, different spike isotopes were used, usually either ^{235}U , ^{236}U , or a double spike (Chapter 2.4.2) of ^{233}U and ^{236}U .

Developments in multiple collector inductively coupled mass spectrometry (MC-ICPMS) [Halliday et al., 1995, 1998] made it possible to ionize the samples efficiently enough to simultaneously analyze several isotopes on a Faraday cup array. These advancements finally lead to the present high precision measurements of $^{238}\text{U}/^{235}\text{U}$ isotopes using MC-ICPMS [e.g. Stirling et al., 2005, 2006, Weyer et al., 2008, Brennecka et al., 2010b, Amelin et al., 2010, Montoya-Pino et al., 2010], which will be further discussed in Chapters 3 to 5, where the results of this study are presented.

The development of a gravimetrically calibrated ^{233}U - ^{236}U double spike by the Institute for Reference Materials and Measurements (IRMM) and the new absolute values for several commonly used uranium standards published by Richter et al. [2010] and Condon et al. [2010] finally made it possible to define and compare sample values between laboratories and to significantly increase the accuracy of $^{238}\text{U}/^{235}\text{U}$ measurements, leading to the recent compilation of data presented by Hiess et al. [2012].

1.8 Significance of this study

The significance of the $^{238}\text{U}/^{235}\text{U}$ system in terms of defining the timescale of events leading to the formation of the solar system is two-fold.

Firstly, uranium is the heaviest naturally occurring element and is part of the actinide group, together with naturally occurring actinium, thorium and protactinium and other, synthetic, elements of which only curium (mass 247) has importance to this study.

Because uranium is such a heavy element it can only be synthesized by primary neutron capture that is faster than β -decay during r-process nucleosynthesis. The only known natural r-process source is core-collapse supernovae (Type II supernovae) (for further explanation see Section 1.2). In this scenario ^{235}U has six progenitors, including ^{247}Cm , and ^{238}U has three.

As ^{247}Cm decays to ^{235}U , the ratio of $^{238}\text{U}/^{235}\text{U}$ in the very first solids formed in the solar system should be lower than the ratios in later produced solids. To confirm the former existence of ^{247}Cm the excess of ^{235}U has to be linked to the Cm/U ratios of each sample. As all isotopes of Cm are extinct, Nd or other light lanthanides are commonly used as proxies when measuring the Cm/U (then Nd/U) ratio, as they have near identical geochemical properties such as valence states, volatilities and ionic radii. If evidence for Cm is found the Cm-U chronometer could be used as a short-lived chronometer of the events in the very early solar system, as $^{247}\text{Cm} \xrightarrow{15.6\text{Myr}} ^{235}\text{U}$ [Blake and Schramm, 1973]. Confirmation or refutation of the former existence of ^{247}Cm can also be used to confirm or confute possible events that triggered the collapse of the molecular cloud prior to the formation of the solar system.

Secondly, the U-Pb chronometer is critically dependent on the accuracy of the $^{238}\text{U}/^{235}\text{U}$ isotopic ratio.

It is easy to see from equations 1.5, 1.6 and 1.9 that the U-Pb chronometer is dependent on the correct ratio of $^{238}\text{U}/^{235}\text{U}$. This ratio was considered to be invariant and equal to 137.88 [Steiger and Jäger, 1977] until recent discoveries showed variability in both meteorites [Amelin et al., 2010, Amelin and Irving, 2011, Brennecka et al., 2010b] and terrestrial samples [Stirling et al., 2007, Weyer et al., 2008, Bopp et al., 2009, Brennecka et al., 2010a, Hiess et al., 2012], making it crucial to analyze and apply the correct uranium isotope ratio for each sample when calculating Pb-Pb ages. This may not only lead to corrected Pb-Pb ages of meteorites but might also reduce or solve inconsistencies between absolute Pb-Pb ages and the associated relative chronometer ages. Also, the deviations between the uranium isotope ratios of different meteorite groups can be used as evidence for the event that triggered the formation of the solar system.

Recent studies have shown that $^{238}\text{U}/^{235}\text{U}$ variations are pervasive in meteorites and the early solar system as well as in terrestrial environments. Not all of the reported meteoritic variations can be attributed to the former decay of extinct ^{247}Cm . Stable isotope fractionation effects during, for example, redox processes and aqueous alterations may also lead to isotopic shifts in $^{238}\text{U}/^{235}\text{U}$. To date, only a few studies have considered a link between the ratio of $^{238}\text{U}/^{235}\text{U}$ and the U(VI)-U(IV) redox transformation. If a link between the redox conditions of water samples and the $^{238}\text{U}/^{235}\text{U}$ ratios can be proven, this data can be used to gain better insight into the redox behaviour and the fractionation mechanisms of uranium in terrestrial and extraterrestrial environments. The ^{238}U - ^{235}U system could then be applied as a paleo-proxy for OAE's [Montoya-Pino et al., 2010], add to the knowledge about the biogeochemical paths uranium can undertake, and enhance the understanding of bioremediation in uranium contaminated water [e.g. Luo et al., 2007, Abdelouas et al., 2000, Bopp et al., 2010]. It will ultimately advance the knowledge about possible fractionation mechanisms controlling higher temperature magmatic and meteoritic systems.

The chapters of this thesis are categorized as follows:

Chapter 2 includes a brief description of the meteorite and water samples analyzed, an overview of the sample preparation and purification procedures of uranium and lead samples, as well as a description of the analytical methods used to measure uranium isotopic compositions, lead isotopic compositions and uranium, lead, trace and major element concentrations.

Chapter 3 begins with the analyses of terrestrial rock standards, giving rise to a terrestrial reference value of $^{238}\text{U}/^{235}\text{U}$ representing the composition of BSE. This is later used as a tool to compare samples within and between datasets.

This chapter also consolidates the findings of the analyses of water samples of several different aquatic systems and their implications of the fractionation behaviour of uranium isotopes during redox and biogeochemical processes. Two suboxic and anoxic aquatic systems, an anoxic basin and an Oxygen Minimum Zone, were examined for the influence of changing redox conditions on the uranium behaviour in these environments. This is followed by an investigation of two estuaries undergoing U flocculation and adsorption during mixing processes of water masses and the influence of these processes on their uranium content and isotopic composition. Lastly, groundwaters from a large scale

aquifer were examined for their uranium isotope systematics, providing an example of an environment which only contains freshwater.

Chapter 4 discusses the influence of individually analyzed $^{238}\text{U}/^{235}\text{U}$ ratios in angrites on their previously published Pb-Pb ages. This is followed by the analysis of the implications that follow for the consistency of absolute and relative chronometers after the Pb-Pb ages were revised according to their real uranium isotopic composition.

Chapter 5 describes the findings of the analyses of chondrite and eucrite samples and discusses their implications for the homogeneous distribution of uranium in the pre-solar disk, the possible events that triggered the collapse of the presolar cloud, the former existence of nowadays extinct ^{247}Cm , and the use of the short-lived nuclide ^{247}Cm - ^{235}U chronometer to constrain the timeframe between the last r-process and the formation of the solar system.

Chapter 6 summarizes the major conclusions reached by this project and their impact on the existing knowledge of uranium isotope behaviour in aquatic systems, and timing and sequence of events in the early solar system. A comparison of the uranium isotopic composition of all environments analyzed throughout this study and a suggestion of future work is also included in this chapter.

Two publications were co-authored during the time of this study:

- Amelin et al. [2010] discusses the timeframe of early events in the solar system. It is the first study reporting a combined analysis of uranium and lead isotopic compositions of the same samples.
- Murphy et al. [2012] explores the uranium isotopic fractionation mechanisms in groundwaters in sandstone-hosted uranium ore deposits.

Also, several presentations were given at conferences:

- The findings on the possible uranium isotopic fractionation mechanisms in Framvaren Fjord and an aquifer in the Mojave desert were presented in poster form during the American Geophysical Union (AGU) Fall Meeting, 13-17 December, 2010 [Kaltenbach et al., 2010].
- The $^{238}\text{U}/^{235}\text{U}$ compositions of angrites and their application to the U-Pb chronometer were presented in oral presentations at the Goldschmidt conference 2011 [Kaltenbach et al., 2011] and the Lunar and Planetary Science Conferences 2011 [Amelin et al., 2011].

- $^{238}\text{U}/^{235}\text{U}$ compositions of carbonaceous chondrites have been partly presented in an oral presentation at the Australian Space Science Conference 2009 [Kaltenbach et al., 2009] and as poster presentation at the Lunar and Planetary Science Conference 2012 [Kaltenbach et al., 2012].

Chapter 2

Samples and methods

2.1 Introduction

The following chapter starts with a brief description of the meteorite and water samples analyzed (Chapter 2.2). This is followed by an overview of the sample preparation and purification procedures used prior to analysis of their uranium isotope composition, lead isotope composition, and trace and major element abundances. Due to the very different nature of the samples, most of this section (section 2.3) is divided between meteoritic and water samples. The chapter closes with a description of the analytical methods utilizing quadrupole inductively plasma coupled mass spectrometry (q-ICP-MS), multiple-collector ICPMS (MC-ICPMS) and thermal ionization mass spectrometry (TIMS) (section 2.4). The objectives of this study required the analysis of $^{238}\text{U}/^{235}\text{U}$ isotope ratios in meteoritic and water samples. Uranium isotopes have been analyzed since the 1930s [Nier, 1939] but the chemical purification and analytical methods have only recently become precise and accurate enough to allow $<1\%$ variations in $^{238}\text{U}/^{235}\text{U}$ to be detected (see Chapter 1.7 and Stirling et al. [2005, 2006, 2007], Weyer et al. [2008], Brennecka et al. [2010b], Amelin et al. [2010], Richter et al. [2010], Montoya-Pino et al. [2010]).

In this study, one of the difficulties that had to be overcome included sample sizes that were limited to <5 ng of uranium. This increased the importance of achieving a high analytical yield with negligible contamination during sample preparation. To achieve high precision during analysis an absolute purification of uranium to prevent interferences was necessary. Preparation was complicated by the various types of sample matrices from meteorites comprising different rock types and organic compound abundances to water samples with varying salinities. Another challenging factor was the diversity of sample sizes, ranging from tens of mg of powdered rock to 1000 ml of water. The processing of these samples required a complex chemical preparation procedure to adequately cope

with their diversity.

2.2 Samples

2.2.1 Meteorites and rock standards

Meteoritic samples were either purchased from commercial sources or provided by collaborators, primarily Dr. Yuri Amelin (Australian National University) and also Dr. Tony Irving (University of Washington). A complete list of meteorites and rock standards can be found in Appendix E1 (meteorites) and E2 (rock standards), including their group distinctions and amounts used.

A total of 79 meteoritic samples from 50 different specimens (see Fig. 2.1 and 2.2 for examples) were analyzed for their uranium isotopic composition and concentration, as well as their rare earth element (REE) and major element compositions. Samples include several bulk sub-samples of the same specimen, samples received as fragmental samples or prepared as a fine powder, separated mineral fractions of different magnetic susceptibility, as well as one sample of chondrules and two CAIs extracted from CV3 chondrites. Thirteen different terrestrial rock standards were either purchased from the United States Geological Survey (USGS, 3 samples) or provided by the Department of Geology, University of Otago (9 samples, from different standard authorities) and analyzed for their uranium isotopic compositions and concentrations. All terrestrial rock standards are of igneous origin and should therefore closely represent the elemental compositions of different meteorite classes, as well as provide a terrestrial reference $^{238}\text{U}/^{235}\text{U}$ value for ‘Bulk Silicate Earth’ (BSE).

The following terrestrial rock standards and meteorites representing the following groups were analyzed in this study:

- terrestrial rock standards
 1. volcanic rocks
 - (a) basalts (4 samples)
 - (b) andesite (one sample)
 - (c) rhyolite (one sample)
 2. plutonic rocks



(a) Millbillillie



(b) Dhofar 008

Figure 2.1: Sampled slices of (a) the eucrite Millbillillie and (b) the L3.3 ordinary chondrite Dhofar 008

- (a) pyroxenite (one sample)
 - (b) dunite (one sample)
 - (c) diabase (one sample)
 - (d) syenite (one sample)
 - (e) nepheline syenite (one sample)
 - (f) granite (one sample)
- non-chondrites
 - 1. angrites (7 samples)
 - 2. ungrouped achondrite (one sample)
 - 3. eucrites (5 samples, Fig. 2.1a)
 - chondrites
 - 1. carbonaceous chondrites
 - (a) CI (one sample)
 - (b) CM (one sample)
 - (c) CR (3 samples)
 - (d) CV (7 samples, Fig. 2.2)
 - (e) ungrouped C3 (one sample)
 - 2. ordinary chondrites

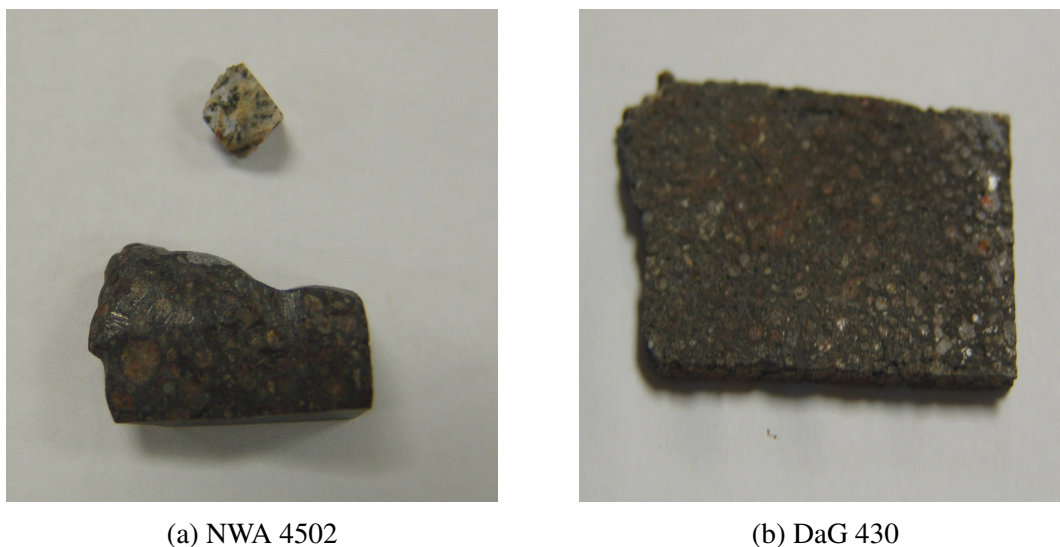


Figure 2.2: Samples of (a) a whole rock sample and CAI of the CV3 chondrite Northwest Africa (NWA) 4502 and (b) a slice of the ungrouped C3 chondrite Dar al Gani (DaG) 430

- (a) H (9 samples)
 - (b) L (9 samples, Fig. 2.1b)
 - (c) LL (3 samples)
3. enstatite chondrites
- (a) EH (3 samples)

In total, these samples provide a wide variety of petrologic types of meteorites according to their alteration and history (for meteorite classification see Chapter 1.3).

Total sample sizes for the MC-ICPMS analysis of meteorites varied widely between <100 mg and 2 g. Uranium contents varied from 3-560 ng. Trace and major elements were analyzed using q-ICP-MS, utilizing 5-20 mg of sample.

2.2.2 Water samples

Water samples were kindly provided by Dr. Donald Porcelli (University of Oxford). A complete list of all water samples and amounts used can be found in Appendix E2.

A total of 40 water samples from five different aquatic environments were analyzed for their uranium isotopic composition and concentration, and some for their REE composition. The samples consist of:

- a depth profile of the Framvaren Fjord, Norway (10 samples)
- a flow path profile of an aquifer in the Mojave Desert, USA (10 samples)

- an oceanic depth profile taken off the coast of Peru during the IFM-GEOMAR cruise no. M77, Leg 3, of the research vessel (R/V) METEOR (6 samples)
- samples of different salinities from the estuary of the Amazon River in Brazil (6 samples)
- samples from varying depths and locations from the estuary of the Lena River in the Arctic Ocean (7 samples)

If sample volumes were <200 ml they were directly evaporated to dryness prior to purification. Larger sample volumes were pre-concentrated using iron co-precipitation prior to further chemical processing.

Water samples for uranium isotope analysis were 125-1000 ml, resulting in a total uranium content of several hundred ng each. 1-2 ml of each sample were used for trace element analysis by q-ICP-MS.

2.3 Sample preparation

After the removing of fusion crust of meteorite samples all chemical preparation for uranium isotopic analysis by MC-ICPMS and elemental composition analysis by q-ICP-MS took place in an ISO Class 4 laminar flow bench in an ISO Class 5 clean laboratory, housed in the Centre for Trace Element Analysis at the University of Otago, New Zealand. All chemical preparations for lead isotopic analysis by TIMS took place in an ISO class 5 laminar flow bench in an ISO class 7 clean laboratory at the Research School of Earth Sciences, Australian National University, Australia.

2.3.1 Pre-cleaning and grinding of meteoritic samples

Many meteoritic samples were provided in powdered form, making any treatment prior to digestion unnecessary.

Samples that were provided as fragments were cleaned by sonicating them in alternate baths of Milli-Q water and teflon-distilled ethanol until both fluids appeared clean of particulates. Whole rock samples and slices were sonicated the same way before and after removing the fusion crust. The latter process took place in a regular (non-clean) laboratory facility in a fume hood that had been wiped out with Milli-Q water and covered in aluminium foil. A Dremel® rotary tool equipped with a new diamond cutting wheel was used to remove the fusion crust and was cleaned after each sample using Milli-Q water and distilled ethanol.

The cleaned sample pieces were ground and homogenized in an agate mortar, which was

cleaned after each sample by repeatedly grinding small amounts of trace metal clean quartz-sand (Alfa Aesar, 99.99% metal based). This ensured that any leftover sample powder in the small fissures of the mortar was replaced by trace metal clean quartz-sand. After each grinding step the mortar and pestle were rinsed several times with Milli-Q water and distilled ethanol before air drying.

2.3.2 Digestion

2.3.2.1 Meteorites

Uranium analysis All powdered meteoritic and standard rock samples were weighed into acid cleaned Savillex PFA vials on a Mettler Toledo AB265-S DualRange balance with a precision of 0.1 or 0.01 mg, depending on sample type and size. Large samples required larger digestion vials, reducing the precision of the balance. An appropriate volume of the ^{233}U - ^{236}U double spike (see Chapter 2.4.2) was then weighed into the vials prior to digestion, ensuring that any chemical reaction during sample processing effect the natural and the spike uranium simultaneously. The double spike allows for instrumental mass fractionation during analysis.

All acids other than the ultra-high purity H_2O_2 (Ultrapur [Merck] and Optima [Fisher Scientific]) and HClO_4 (Optima [Fisher Scientific]) used for digestion were double-distilled prior to usage, using either a 'fast' quartz still (ca. 400 ml in 8 hours) and a 'slow' teflon still (ca. 80 ml in 44 hours) for HNO_3 and HCl or one fast and one slow teflon still for HF .

The sample digestion started with a 10:1 mixture of HF - HNO_3 (4-5 days, 160°C), followed by 6 M HCl (overnight, 140°C), 7 M HNO_3 (overnight, 140°C) and finalized with about 36 hours of a 1:1 mixture of 7 M HNO_3 and concentrated H_2O_2 at 120°C to break down any residual organic compounds. If residual organic matter was still present after the hydrogen peroxide treatment, samples were also treated with conc. HClO_4 . For this treatment, the vial was wrapped in aluminium foil, 50 μl of concentrated HClO_4 and up to 1ml of concentrated HNO_3 were added. The mixture was then refluxed for up to one hour and dried on a hotplate held at 200 - 220°C . The samples were then redissolved in 5-15 ml of 1.5 M HNO_3 and refluxed for a minimum of one hour at 120°C in preparation for the ion exchange column chemistry procedure.

Lead analysis Precise U-Pb dating is achieved by analyzing the lead isotopic compositions of several progressive leaching steps of the sample. As every step extracts Pb from different reservoirs within the sample, each fraction contains an increasing amount of radiogenic lead. This makes it possible to identify and remove contamination of terrestrial

lead during the data analysis using an isochron approach (see Chapter 1.4 for an explanation of the isochron method).

The leachate method for U-Pb analysis was published in detail in the supplementary material of the co-authored journal article by Amelin et al. [2010].

In brief, a total of three washes, each representing several leaching steps, and one residue were obtained per sample. The first wash included leachates of 4-5 steps of 0.5 M HNO₃ washes in an ultrasonic bath for 10 min each. The second wash incorporated up to two leachates using 7 M HNO₃ and two leachates using 6 M HCl, each held on a hotplate at 110-120°C for 60-90 min. This was followed by the third wash, a 14 hour long wash using 9 M HBr. The remaining residue was then digested using a 2:1 mixture of 25 M HF and 12 M HNO₃.

All subsamples were spiked with a ²⁰²Pb-²⁰⁵Pb-²²⁹Th-²³³U-²³⁶U tracer, used for instrumental fractionation corrections during analysis, before being evaporated to dryness at 110°C. The washes were first dissolved in 6 M HCl, dried at 70°C overnight, redissolved in 9 M HBr, evaporated at 80°C, then finally dissolved in 0.3 M HBr and centrifuged to remove any undigested particles. The dried residues were dissolved in 12 M HNO₃, dried at 110°C, redissolved again in 12 M HNO₃, sonicated for 30 min, refluxed at 120°C for one hour, evaporated and refluxed in 6 M HCl at 120°C, refluxed in 9 M HBr, then finally taken up in 0.3 M HBr and centrifuged prior to the ion exchange column chemistry.

2.3.2.2 Water samples

To determine their uranium concentrations one ml of each sample was taken directly from the Nalgene HDPE sample bottles. This aliquot was evaporated, taken up in 2% HNO₃ and analyzed using q-ICP-MS. Depending on the total uranium content of the sample one of two protocols were followed:

1. For sample sizes <200 ml, a suitable volume of ²³³U-²³⁶U spike was weighed into an acid cleaned PFA vial. Then an appropriate amount of sample was added to the spike and the mixture was evaporated, while adding more sample to it if necessary. Each HDPE bottle was weighed prior to and after adding the sample to the spike to determine the exact amount of water used.
2. For sample sizes >200 ml, the required amount of spike was weighed directly into the HDPE bottle containing the sample. Then the mixture was allowed to equilibrate for three days prior to co-precipitation (see section 2.3.3). Following the co-precipitation procedure the precipitate was cleaned and evaporated.

Following this the samples were dried down at 100°C, digested in 6 M HCl at 100°C, evaporated to dryness, then re-dissolved in 1.5 M HNO₃. The sample and spike mixture

was left to equilibrate at 110°C for three days prior to ion exchange chemistry.

2.3.3 Co-precipitation of water samples

Co-precipitation of Fe and U is widely used to pre-concentrate uranium in water samples [e.g. Ku et al., 1977, Chou and Moffatt, 2000, Hubert et al., 2006]. Changing the pH of the sample to reducing conditions (pH 2) reduces all uranium to U(IV) and all iron to Fe(II). By adjusting the solution to oxidizing conditions (pH 9) the redox states of the ions change from U(IV) to U(VI) and from Fe(II) to Fe(III). Fe(OH)₃ then forms a precipitate building hydroxide complexes and adsorbs U(VI) onto its surface [Bruno et al., 1995, Duff et al., 2002].

The co-precipitation method was tested on 1 l-water samples of different salinities before using it on the samples described in this study. Milli-Q water was used as a blank and given the same treatment as the test samples. The test samples consisted of a fresh water sample of the Leith River, Dunedin, two samples of Dunedin harbour water, regarded as equivalents to brackish water, and saline seawater samples of from St. Clair Beach, Dunedin¹. All samples were filtered using a glass fibre filter prior to the co-precipitation procedure.

The supernatants recovered at each step and the final precipitates of all test samples were analyzed for Fe, Cu, Zn, Cd, Pb, Th and U as indicators for the yield of the co-precipitation procedure, although only Fe and U are of interest to the present study. Yields of Fe and U were >99.9% for all samples. Thorium concentrations of all test samples were below the detection limit of the q-ICP-MS and could therefore not be assessed further. Blank concentrations of uranium were below the analytical detection limit, while the Fe yield after co-precipitation was near 100%. As uranium loss and U blank contributions following iron co-precipitation was found to be negligible and uranium yields were near 100% this procedure was considered suitable to apply to all other water samples.

Samples had been received acidified to different pHs for preservation. The initial pH of the samples was determined and samples with pH>2 were acidified to a pH of 2 using 6 M HCl. As mentioned in section 2.3.2.2 the uranium double-spike was added and equilibrated prior to the co-precipitation procedure to ensure that no unaccounted isotopic fractionation could occur during co-precipitation. After adding pre-cleaned FeCl₃ (10%) to the sample solution to obtain a 50 ppm Fe solution the pH was raised to 9 using NH₃ (aq, 20%), which initiated iron precipitation. The solution was then left to settle,

¹Fresh water is defined as water with low salinities (<0.5‰ dissolved salts), brackish water is a mixture of stream and ocean waters and saline water has high salinities of 30-50‰ dissolved salts.

Table 2.1: Protocol for iron co-precipitation for a sample size of 1000 ml

Step	Details	Outcome
1	add 400 μ l FeCl_3 (10%) to the sample	50 ppm Fe solution
2	shake bottle for one minute, let stand for one hour	equilibration
3	add approximately 2 ml NH_3 (20%)	pH = 9
4	shake bottle for one minute, let sit for one hour, repeat five times	equilibration
5	let the precipitate settle overnight	co-precipitation
6	decant the supernatant	isolate the precipitate
7	transfer the precipitate into centrifuge tubes, rinse HDPE bottles with Milli-Q water to transfer residual precipitate	
8	centrifuge for 20 min at 1500 G, decant supernatant	isolate the precipitate
9	add 10 ml Milli-Q water, shake, centrifuge again	remove NH_3
10	decant the supernatant, re-dissolve the precipitate in 2% HNO_3	conc. metal solution

the supernatant was removed and the precipitate was redissolved in 2% HNO_3 . The exact method utilized in this study can be found in Table 2.1. The co-precipitation was conducted directly in the sample bottles.

2.3.4 Ion exchange column chemistry

Ion exchange column chemistry was used to isolate and purify uranium or lead from the samples. The resins used consist of chromatographic materials, which reversibly exchange ions depending on the type and strength of the acid added. Different elements can be separated and purified by utilizing this behaviour.

2.3.4.1 Uranium isotopes

For uranium purification a two-step separation procedure was adapted from Luo et al. [1997] and Potter et al. [2005]. Double distilled acids were used throughout. Each column contained about 700 μ l of resin. It is assumed that all uranium present in the samples is oxidized to U(VI) during the digestion process.

Both separation steps were tested with different multi-element standard mixtures, containing progressively more matrix elements in the solutions. The first multi-element standard

was comprised of U-Th-Sm-Nd. Thorium is the main source for interferences across the uranium mass range during MC-ICPMS analysis. It is also the most difficult element to separate from uranium. Samarium and neodymium are later used as proxies for extinct curium and also serve as proxies for other lanthanides during the ion exchange purification process. The last test was conducted using rock standard digests of BCR-2, DTS-2 and BHVO-2 (USGS). The matrices in these standards can be regarded as chemical and mineralogical analogues to those of meteorites. For tests conducted on standard material, every milliliter eluted from the columns was collected and the matrix element concentrations were analyzed by q-ICP-MS. The rock standards were additionally analyzed for their uranium isotopic ratios using MC-ICPMS. Elution curves for a sample of the basalt BCR-2 are shown in Fig. 2.3 (first step, TRU resin) and Fig. 2.4 (second step, UTEVA resin).

The exact purification method applied can be seen in Table 2.2. The first stage column was filled with TRU resin (Eichrom Technologies, USA, particle size 100-150 μm), a resin known for its high retention capacity of tetravalent actinides, making it an easy way to separate nearly all elements from uranium. However, TRU resin is insufficient in completely separating thorium and uranium if these are present in a complex matrix, especially if the sample contains organic complexes. The final eluants were dried down over night, refluxed in a 1:1 mixture of 7 M HNO_3 and conc. H_2O_2 at 120°C for 24 hours to break down any organic compounds derived from the TRU resin. They were then dried again and refluxed for at least one hour in 3 ml 3 M HNO_3 prior to the second stage column chemistry based on UTEVA resin (Eichrom Technologies, USA, particle size 100-150 μm). This resin is specifically designed to separate actinides from one another, especially uranium and thorium, and ensures near complete purification of uranium. The purified samples were either treated again with the previously described HNO_3 - H_2O_2 or HClO_4 treatments to break down any inherited organic compounds derived from the ion exchange chemistry by oxidizing the samples.

2.3.4.2 Uranium-lead isotopes

All lead isotopic data mentioned in this project were analyzed by Y. Amelin at the Australian National University. I was present to study the method [e.g. Manhès et al., 1978, Amelin et al., 1996, 2005, 2010] during a several week long visit that resulted in the publication of Amelin et al. [2010]. Uranium and lead were separated and purified using a three stage ion exchange column protocol. The first two stages consisted of a double pass through 50 μl AG1x8 200-400 mesh (Eichrom) resin. Between the two passes 60 μl of 9 M HBr were added and the aliquot was refluxed for 60 min at 80°C, dried and taken up

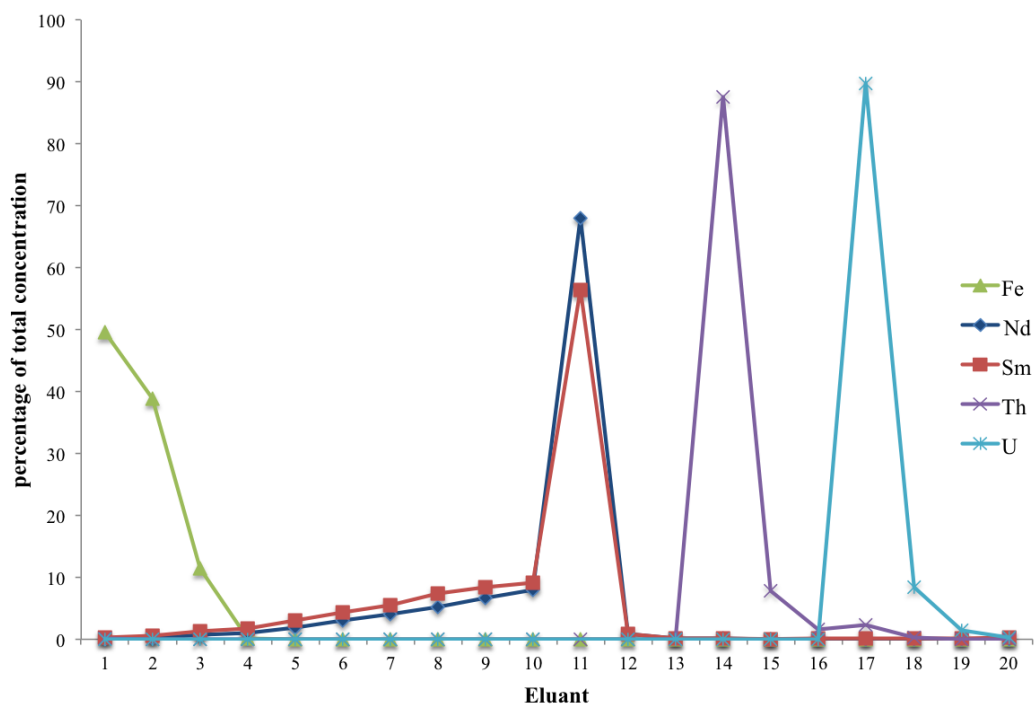


Figure 2.3: Elution curve of a basalt sample (BCR-2) using TRU resin. Every eluant is one ml eluted from the column.

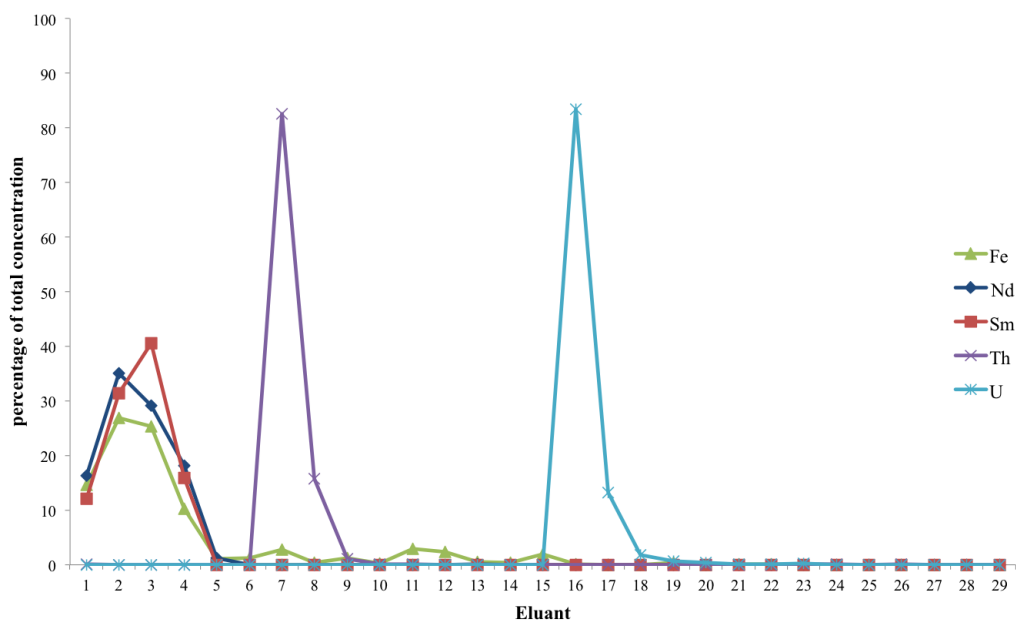


Figure 2.4: Elution curve of a basalt sample (BCR-2) using UTEVA resin. Every eluant is one ml eluted from the column.

Table 2.2: Two step ion exchange column protocol for the purification of uranium

Step	Details	Eluted
Resin	TRU 100-150 μm	
Cleaning	9 ml 0.2 M HCl	
	9 ml 0.1 M HCl - 0.3 M HF	
Conditioning	9 ml 1.5 M HNO_3	
Loading	5-15 ml 1.5 M HNO_3	Matrix elements
Purification	12 ml 1.5 M HNO_3	Matrix elements
	3 ml 3 M HCl	Matrix elements, REEs
	6 ml 0.2 M HCl	Thorium
Collection	9 ml 0.1 M HCl - 0.3 M HF	Uranium
Evaporate U fraction, treat with H_2O_2 , take up in 3 M HNO_3		
Resin	UTEVA 100-150 μm	
Cleaning	9 ml 0.2 M HCl	
	9 ml 0.1 M HCl - 0.3 M HF	
Conditioning	9 ml 3 M HNO_3	
Loading	3 ml 3 M HNO_3	Matrix elements
Purification	5 ml 3 M HNO_3 - trace HF	Thorium
	2 ml 3 M HNO_3	Thorium
	2 ml 3 M HCl	Thorium
Collection	7 ml 0.2 M HCl	Uranium
	7 ml 0.1 M HCl - 0.3 M HF	Uranium

in 0.3 M HBr. All bulk washes eluted from the first two column chemistry stages were evaporated to dryness together before being redissolved in 2 M HNO_3 prior to the third step column using 50 μl UTEVA (Eichrom) resin with a particle size of 100-150 μm . The exact method can be found in Table 2.3.

2.4 Analysis

All uranium isotopic and elemental concentration analyses were conducted at the Centre for Trace Element Analysis at the University of Otago, New Zealand. Lead isotopic analyses were conducted at the Research School of Earth Sciences (RSES) at the Australian National University (ANU). Complete datasets with raw data of each q-ICP-MS and MC-ICPMS analysis are available in the electronic Appendix E1 (meteorites), Appendix E2 (water samples and rock standards), and Appendix E3 (BCR-2 and BHVO-2 repeated

Table 2.3: Purification procedure for uranium-lead dating

Step	Details	Eluted
Resin	AG1x8 200-400 μm	
Cleaning	full Milli-Q water full 8 M HCl full 0.5 M HNO_3	
Conditioning	2x 165 μl 0.3 M HBr	
Loading	1000 μl 0.3 M HBr	Matrix and uranium
Bulk Wash	2 x 165 μl 0.3 M HBr	Matrix and uranium
	330 μl 0.3 M HBr	Matrix and uranium
	1600 μl 0.3 M HBr	Matrix and uranium
	330 μl 2.5 M HCl	Matrix and uranium
Collection	100 μl 0.5 M HNO_3	Lead
	2 x 330 μl 0.5 M HNO_3	
Add 65 μl 9 M HBr to Pb fraction, reflux for 60 min at 80°C		
Resin	AG1x8 200-400 μm	
Cleaning	full Milli-Q water full 8 M HCl full 0.5 M HNO_3	
Conditioning	2 x 165 μl 0.3 M HBr	
Loading	1000 μl 0.3 M HBr	Matrix and uranium
Bulk Wash	2 x 165 μl 0.3 M HBr	Matrix and uranium
	330 μl 0.3 M HBr	Matrix and uranium
	1600 μl 0.3 M HBr	Matrix and uranium
	330 μl 2.5 M HCl	Matrix and uranium
Collection	100 μl 0.5 M HNO_3	Lead
	2 x 330 μl 0.5 M HNO_3	
Evaporate all bulk washes, take up in 2 M HNO_3		
Resin	UTEVA 100-150 μm	
Cleaning	full 0.02 M HNO_3 - 0.2 M HF full 0.02 M HNO_3	
Conditioning	2 x 330 μl 2 M HNO_3	
Loading	1000 μl 2 M HNO_3	Matrix elements
Purification	2 x 100 μl 2 M HNO_3	Matrix elements
	165 μl 2 M HNO_3	Matrix elements
	660 μl 2 M HNO_3	Matrix elements
Collection	165 μl 0.02 M HNO_3 - 0.2 M HF	U/Th
	500 μl 0.02 M HNO_3 - 0.2 M HF	U/Th

analyses).

2.4.1 q-ICP-MS

Lanthanide (REE), Th and major element concentrations were analyzed by q-ICP-MS in two separate runs using different dilutions and analytical routines. An Agilent 7500 cs/cc q-ICP-MS instrument (Agilent Technologies, USA) was utilized for these analyses. For meteorite analysis, either a ca. 5-60 mg aliquot of the powdered sample was digested independently or an aliquot resembling 20 ± 5 mg of sample was taken directly from the digest used for U isotopic analysis following the last 6 M HCl digestion step. Analysis on water samples were conducted on 1-2 ml of sample.

Before beginning sample analysis, the q-ICP-MS was calibrated by creating standard curves of different multiple-element solutions containing the elements to be analyzed across the range of expected concentrations.

For major element analysis samples were dissolved in the usual 2% HNO₃ acid with a dilution factor of 500 to stay within the analytical concentration limits, giving measured concentrations of several ppb for elements like Cu and Zn and several 1000 ppb for major elements like Fe and Mg. A multiple-element internal standard consisting of Be, Sc, Ge, Rh, In, Bi and Tb (the latter was not included for REE analysis) was added to each sample to monitor the instrumental performance and the recovery of elements. These elements are generally not expected to be present in the samples in measurable quantities.

For REE and Th quantification optimal performance could be achieved by dissolving the samples in 2% HCl, which makes the Th in the sample more soluble. Each sample was diluted approximately by a factor of 20 prior to analysis. This is the minimum dilution required to avoid peak suppression due to matrix contents that are too high and generally gave measured REE concentrations of 0.5-10 ppb.

Samples analyses were alternated with measurements of a basaltic standard (BCR-2) to ensure that the high concentration of matrix elements did not cause drifts in the concentration measurements. Several attempts were made to remove some of the highly concentrated metals like iron, zinc, nickel and copper from the matrix using Chelex (Bio-Rad) chelating ion exchange resin to allow the separated REEs to then be analyzed in higher concentrations, but developing this method was found to be too timely for this project.

Several measurements of BHVO-2 and BCR-2 rock standards as well as several replicate measurements of samples were used to monitor instrument performance and to assess the analytical errors associated with every element during each session (see Appendix E3 for details). For the basaltic rocks, standard errors associated with the majority of REE concentrations were <1%. The corresponding sample errors varied depending on the

composition of the sample matrix and the concentration of each element but were generally better than 2% for higher concentrations (>0.5 ppb) and up to 5% for concentrations nearing the detection limits of the instrument. Thorium measurements were found to be extremely difficult with average errors of $\sim 10\%$ and maximal errors up of to 20%. This was due to the adhesive nature of Th during the sample introduction process.

2.4.2 Double spike

An in-house ^{233}U - ^{236}U double spike was used to correct for any possible isotopic fractionation that might have occurred during sample preparation and to monitor the instrumental mass bias during analyses throughout this study. The exponential mass fractionation law (Eq. 2.1) was applied to correct for isotopic fractionation as described in Stirling et al. [2006, 2007]:

$$r = R * (M_2/M_1)^\beta. \quad (2.1)$$

In equation 2.1 r = true isotopic ratio, R = measured isotope ratio of isotopes with masses M_1 and M_2 , and β = instrumental mass fractionation factor.

Both spike isotopes are of purely synthetic origin and can only be found in nuclear reactions. These are in nuclear bomb sites or nuclear power plants, where ^{236}U and ^{233}U are formed as products of neutron irradiation of ^{235}U and ^{232}Th , respectively. In the early solar system all uranium isotopes would have formed during r-process nucleosynthesis, but due to their short half-lives of 2.4×10^7 yr and 1.6×10^5 yr, ^{236}U and ^{233}U are nowadays extinct and therefore not present in natural system. This makes calculations straightforward, as it can be assumed that none of the samples contain ^{233}U or ^{236}U . However, the spike contains small amounts of ^{235}U and ^{238}U , which is accounted for in the data reduction.

The main spike ratio was determined to be $^{236}\text{U}/^{233}\text{U} = 0.9569408 \pm 0.0000115$ (2SE). This is based on the iterative calculation of $^{236}\text{U}/^{233}\text{U}$ ratios from 116 analyses of several mixtures of the uranium metal standard CRM145 and ^{233}U - ^{236}U double spike. The CRM145 standard has a gravimetrically calibrated $^{238}\text{U}/^{235}\text{U}$ ratio of 137.840 ± 0.015 , derived using the weighted average values published by Richter et al. [2010] and Condon et al. [2010]. Ratios of minor abundances in the spike are $^{236}\text{U}/^{238}\text{U} = 633.3$ and $^{236}\text{U}/^{235}\text{U} = 1712.3$.

Depending on their total uranium concentration, different spike concentrations were added to the samples to minimize the weighing error. Spike concentrations were calibrated using isotope dilution against several gravimetrically diluted CRM145 metal standard solutions and are 0.669 ± 0.001 ppb (2SE), 1.114 ± 0.002 ppb (2SE) and 11.023 ± 0.041 ppb (2SE), respectively.

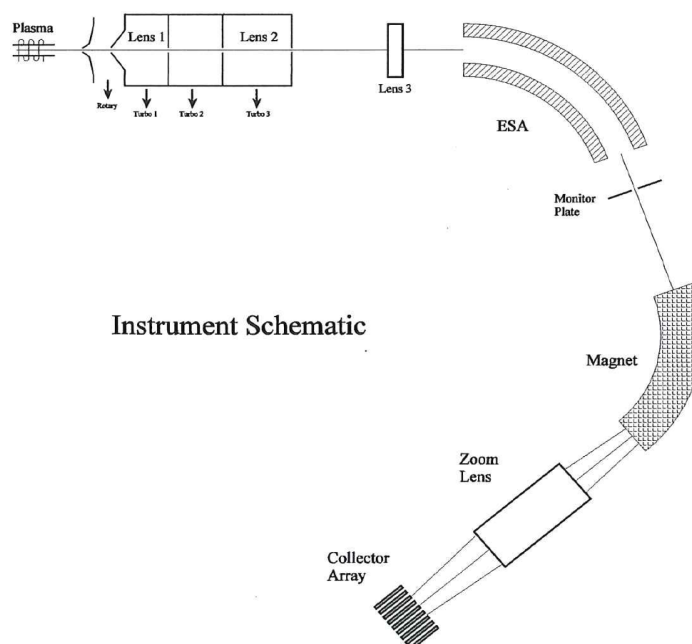


Figure 2.5: The instrument schematic for a Nu Plasma MC-ICPMS as used in this study.

2.4.3 MC-ICPMS

All uranium isotopic and concentration measurements were conducted using a Nu Instruments Nu Plasma MC-ICPMS coupled to a Nu Plasma DSN-100 desolvating nebuliser. The instrument schematic is shown in Fig. 2.5 [Nu-Instruments, 2005].

Analysis 100 μl aliquots, representing 0.7% and 1.1% of the sample U, were taken from the final TRU and UTEVA elutions of each sample. These aliquots were checked for uranium concentration via MC-ICPMS to allow an appropriate dilution of the remaining U fraction to be determined. Samples were then dissolved in a 0.24 M HCl - 0.06 M HF mixture with volumes varying from 60-1500 μl depending on the sample U concentration, and transferred into micro-centrifuge tubes when cooled. The samples were introduced into the DSN via a 60 ± 4 $\mu\text{l}/\text{min}$ PFA-nebuliser, where a dry aerosol is generated out of the sample droplets. This aerosol is then forwarded into the argon plasma using an argon carrier gas.

Uranium and thorium isotopes were analyzed simultaneously on static Faraday cups with 10^{11} Ω resistors and ion currents of 5.5×10^{-11} - 1.9×10^{-10} A (^{238}U), 8.9×10^{-13} - 1.2×10^{-11} A (^{236}U), 6.7×10^{-13} - 1.4×10^{-12} A (^{235}U) and 9.1×10^{-13} - 1.2×10^{-11} A (^{233}U), respectively. The transmission efficiency was 0.40-0.52%. ^{232}Th was monitored for possible ThH^+ interferences on mass ^{233}U but was, together with platinum argides that can potentially interfere over the entire range of uranium isotope masses, found to be

negligible due to the effectiveness of the uranium purification procedure. Any possible mass fractionation occurring during sample preparation and the instrumental mass bias of the MC-ICPMS were corrected for using the ^{233}U - ^{236}U double spike procedure described above.

The range of the pre-amplifiers was set to 20 V for the ^{238}U Faraday cup and to 10 V for all other cups.

Each meteorite sample was analyzed one to three times, depending on the individual sample size, with on-peak measurements of 17-180 seconds and an integration time of 0.2 seconds in time resolved mode using methods adapted from Stirling et al. [2006, 2007]. Before and after each measurement a 60 second baseline of the electronic amplifier noise was measured and subtracted from the results via linear interpolation.

Water samples were generally analyzed using a programmed analysis procedure consisting of 4 blocks, each with 100 seconds of on-peak analysis with 1 second integration times and 50 seconds of background noise measurements between each blocks. Backgrounds were then subtracted from the data of the following block.

The errors used throughout this study represent the larger error of (a) the two standard error of the sample measurements or (b) the two standard error of the sample measurements scaled to the standard analysis error of the session. The scaling was done using the following equations, where V = average voltage during measurement, s = on-peak data acquisition time in seconds, SD = standard deviation and SE = standard error. If

$$\frac{V_{\text{sample}} * s_{\text{sample}}}{V_{\text{standard}} * s_{\text{standard}}} > 1 \quad (2.2)$$

and

$$2SE_{\text{sample}} > 2SD_{\text{standard}} \quad (2.3)$$

then $2SE_{\text{sample}_{sc}} = 2SE_{\text{sample}}$, otherwise

$$2SE_{\text{sample}_{sc}} = \frac{2SD_{\text{standard}}}{2SE_{\text{standard}}} * 2SE_{\text{sample}}. \quad (2.4)$$

The total error is then determines by propagating the scaled 2SE uncertainties of the sample ($2SE_{\text{sample}_{sc}}$, see above) and the uranium metal standard throughout the session in quadrature as follows:

$$\sqrt{2SE_{\text{sample}_{sc}}^2 + 2SE_{\text{standard}}^2} \quad (2.5)$$

Total standard errors ranged from 0.02 - 0.20‰ (2SE) for water samples and 0.04 - 0.64‰ (2SE) for meteorite samples.

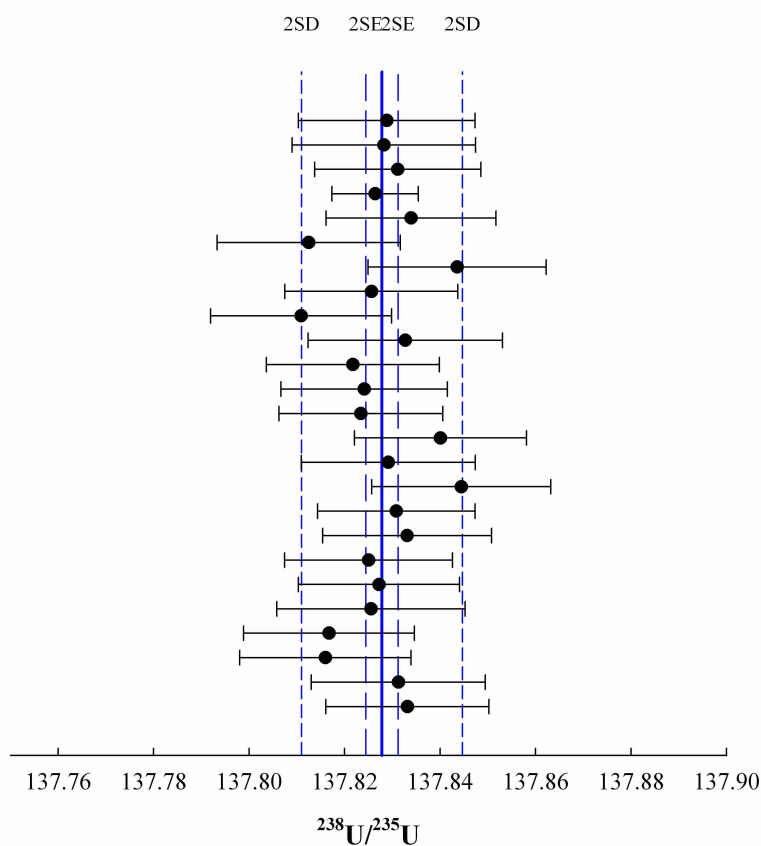


Figure 2.6: Standard measurements of the uranium metal standard CRM145 over one day of meteorite sample analysis. The solid line represents the average $^{238}\text{U}/^{235}\text{U}$ ratio of all measurements, while the dashed blue lines are the 2SD/2SE errors of the average.

Memory effects One type of interferences are memory effects. These occur when samples are not completely washed out of the nebuliser and/or the DSN. In this case uranium rich droplets can accumulate in the spray chamber or the desolvator system, causing systematic offsets in the measured uranium isotopic compositions. To ensure that memory effects were not disturbing sample measurements, washout sequences using 0.6 M HCl - 0.15 M HF followed by 0.24 M HCl - 0.06 M HF acids were applied. Sample measurements were additionally bracketed with measurements of the isotopically light CRM145 standard, using the same analytical procedure as for the sample. Typical standard measurements over one day of meteoritic sample analysis, using 90 second on-peak analysis times and two 60 second intervals of background measurement, can be seen in Fig. 2.6. If memory effects were present the measurements would drift in the direction of the lighter isotope and, in this case, produce measurements with an increased amount of ^{235}U , therefore lowering the $^{238}\text{U}/^{235}\text{U}$ ratio during the day. As Fig. 2.6 shows, all measurements are identical, within error, with the average composition and no systematic drift

in a specific direction is visible, demonstrating that memory effects are not problematic for the present study. Although daily averages of standard measurements are slightly drifting from day to day all of them are within uncertainty of the reference value of 137.840 ± 0.015 and no further adjustments were made to the obtained sample values.

Interferences Spectral interferences include isobaric and polyatomic interferences. Polyatomic interferences are caused by molecules with identical masses to uranium isotopes. On the uranium mass range these are mainly thorium hydrides ($^{232}\text{ThH}^+$) interfering on ^{233}U and platinum argides that may form with the plasma or nebuliser argon gas and cause interferences of $^{195}\text{Pt}^{38}\text{Ar}$ on ^{233}U , $^{195}\text{Pt}^{40}\text{Ar}$ on ^{235}U , $^{196}\text{Pt}^{40}\text{Ar}$ and $^{198}\text{Pt}^{38}\text{Ar}$ on ^{236}U and $^{198}\text{Pt}^{40}\text{Ar}$ on ^{238}U . Thorium was routinely monitored during analysis but was never found to be present in high enough concentrations to produce interferences that had to be taken into account during data reduction. This is evidence for the near complete separation of uranium and thorium during sample preparation. Standard rock samples were analyzed for their platinum contents but they were found to be below the detection limit of the q-ICP-MS. Therefore, interferences caused by platinum argides were deemed negligible. Isobaric interferences and doubly charged ion interferences cannot cause disturbances during the uranium isotopic measurements due to the high mass of uranium. The presence of larger polyatomic molecules interfering across the uranium range could not be detected following the treatment of all samples with highly oxidizing $\text{HNO}_3\text{-H}_2\text{O}_2$ or $\text{HNO}_3\text{-HClO}_4$ immediately prior to analysis.

Matrix effects can suppress the signal intensities by changing the ionization characteristics of the plasma and can lead to long term drifts in the signals. They can be caused by impure samples still containing matrix elements and by differences between acids used during analysis. These effects were minimized by the two-stage column chemistry procedure used to purify all uranium samples (see section 2.3.4), the use of double distilled acids throughout the sample processing, and the regular cleaning of instrument parts (this includes cones, torch, spray chamber, DSN, nebuliser and, on an annual basis, the lens stacks). Any residual effects were removed from the data as part of the double spike implementation used for correcting the instrumental mass fractionation.

The main source of instrumental mass fractionation is the so-called 'space charge effect'. The positively charged ions in the argon plasma repel each other resulting in lower mass ions being deflected to the outside of the ion beam, while heavier ions stay in the middle of the ion beam. As mainly the mid-section of the ion beam is extracted through the cones into the analyzer region of the instrument, the isotope ratios detected will always be heavier than they really are. The double spike method is used to mathematically compensate for this effect during data reduction (see section 2.4.2).

2.4.4 TIMS

U-Pb data were obtained using a Finnigan MAT-261 TIMS instrument by simultaneously analyzing the lead isotopes ^{202}Pb , ^{204}Pb to ^{208}Pb , and ^{238}U . Samples were taken up in one drop of silica gel, pipetted onto rhenium filaments, dried at a current of 1.0 A and heated up to a current of 2.2 A.

The evaporation and ionization temperatures of Pb are so close together that only a single filament per sample analysis is needed in the filament carousel. Analyses took place after building up a vacuum in the sample magazine overnight, resulting in vacuum of $<10^{-7}$ Torr.

Samples were analyzed by applying a 1.6-1.7 A ionization current on the filament. The measurements each consisted of 20 blocks comprising 10 cycles with 8 second integration times for on-peak analysis, by increasing the current applied with each block. Peak centering and 30 second background measurements were conducted after every third block. Pb was detected on Faraday cups while U was detected on an electron multiplier.

The only source of mass fractionation using TIMS is the so-called Rayleigh distillation, meaning that lighter isotopes which have a lower bond energy break at a lower temperature than heavier isotopes and are ionized faster. This results in increasingly heavier isotope ratios being measured during an analysis. A spike with a known $^{202}\text{Pb}/^{205}\text{Pb}$ ratio was used to correct for this effect. Instrument performance was tested using a NIST SRM-981 standard. Isoplot-Ex version 3.0 [Ludwig, 2003] was utilized to produce Pb-Pb isochrons, U-Pb concordia regressions, and model age calculations from the data obtained.

Chapter 3

Results I: Isotopic fractionation mechanisms

Several terrestrial systems were studied for their uranium isotopic fractionation mechanisms to investigate how $^{238}\text{U}/^{235}\text{U}$ varies with changing environmental conditions. This includes redox changes, the mixing of water masses, flocculation and aggregation, and adsorption onto particles.

The following chapter begins with a discussion of terrestrial igneous rock standards, as their compositional average can be used as an estimation for the 'Bulk Silicate Earth' (BSE) composition, which can then be utilized as a terrestrial reference to compare the different samples analyzed throughout this study. Unlike sediments and sedimentary rocks that originate from smaller reservoirs and can have highly fractionated $^{238}\text{U}/^{235}\text{U}$ ratios due to low-temperature geochemical processing [e.g. Stirling et al., 2007, Weyer et al., 2008, Hiess et al., 2012], igneous rocks are mainly derived from the well mixed mantle, with possible crustal influences. They are therefore unlikely to have fractionated uranium isotopic compositions, making them a far better estimate for defining a uranium isotopic terrestrial reference value than the value based on zircons published by Hiess et al. [2012].

The following three subchapters each have a different purpose in approving or rejecting possible mechanisms for the isotopic fractionation of ^{238}U and ^{235}U and uranium removal in aquatic systems. In these environments the uranium isotopes can be considered as 'stable' due to their long half-lives in comparison with the fast removal processes.

The first subchapter reviews the uranium behaviour of $^{238}\text{U}/^{235}\text{U}$ and uranium concentrations in two different anoxic settings, a permanently anoxic fjord, Framvaren Fjord (Norway), with a distinct, temporally and spatially stable redox interface [e.g. Skei, 1988],

and an Oxygen Minimum Zone¹ in the shelf region off the coast of Peru, which is stable but records seasonal changes in intensity and size [e.g. Chavez et al., 2008, Scholz et al., 2011]. Oxygen Minimum Zones in particular are associated with OAEs (Oceanic Anoxic Events) and can therefore be a useful tool for studying the redox evolution of the oceans during these events involving massive chemical changes [e.g. Schlanger and Jenkyns, 1976, Arthur et al., 1987, Brennecke et al., 2011a]. It is well known that uranium can be removed from the water column under reducing redox conditions [e.g. Langmuir, 1978]. However, most studies agree that a sudden valence change due to purely chemical reduction under changing redox conditions does not naturally occur in aquatic systems without a catalyst [Anderson et al., 1989, McKee and Todd, 1993, Swarzenski et al., 1999, and references therein].

Further possible explanations for uranium removal are scavenging by microorganisms followed by biologically induced reduction, uranium adsorption onto or complexation with organic and inorganic colloids and particles, formed mainly by humic and fulvic acids or redox sensitive elements like Fe and Mn, back-reactions with sediments, and interactions between U and dissolved organic carbon (DOC) [Swarzenski et al., 1999].

The second subchapter focuses on mechanisms that might influence uranium behaviour during the mixing processes between riverine and seawater. Two large estuaries were profiled for this purpose, namely the tropical Amazon River estuary (Brazil) and the arctic Lena River estuary (Siberia). Mixing processes of water masses induce physical and chemical transformations of dissolved and particulate materials, caused by salt-induced precipitation, aggregation, and adsorption processes [Swarzenski et al., 1995]. Understanding these transformations is crucial for interpreting the mass balance of uranium in the major oceans and also in smaller water systems. Most early studies of uranium behaviour in estuaries have concluded that it is possible for uranium to behave conservatively throughout the salinity gradient between sea- and freshwater [e.g. Martin et al., 1978, Toole et al., 1987], meaning that the studied estuaries are neither a source nor a sink for uranium. However, more recent studies have found that uranium can also behave non-conservatively, which is reportedly the case for the Amazon River [Swarzenski et al., 1995], the Kalix River [Andersson et al., 2001] and the Ganges-Brahmaputra mixing zone [Carroll and Moore, 1994], showing uranium removal in lower salinity regions and a possible excess of uranium in the higher salinity regions of the estuaries compared with expected concentrations during simple mixing between open ocean and riverine waters.

The third subchapter investigates the uranium behaviour following two flowpaths in an

¹Oxygen Minimum Zones occur in regions of the oceans where the upwelling of nutrient-rich water causes an increased biological activity in the surface water, creating an oxygen depletion during the microbial degradation process due to a lack of ventilation throughout the water column.

aquifer in the Mojave Desert (USA). Aquifers are ideal environments to study chemical changes in groundwater over a prolonged period of time, as the water moves very slowly through the system. Possible changes in the water chemistry can be caused by weathering reactions with the surrounding geological formations (mainly rock, sand and silt), radioactive decay of short-lived isotopes over their residence time in the groundwater system, aggregation and disaggregation of particles, adsorption/desorption onto/off the surrounding solids or particles in the water, and redox transformations if reductant sources are present in the system [e.g. Porcelli and Swarzenski, 2003].

3.1 Terrestrial reference

A total of 12 commercially available bulk igneous rock standards were analyzed for their uranium isotopic compositions and concentrations (Table 3.1 and Fig. 3.1). The rock standards adopted in this study are comprised of six volcanic rocks and six plutonic rocks, covering a wide range of lithologies, spanning the ultramafic (<45% silica content), mafic (45 - 55% silica content) and intermediate (55 - 65% silica content) to felsic (> 65% silica content) igneous rock types.

Commercial rock standards are made up of large (kg-sized) amounts of homogenized powdered bulk rocks, so that they are considered to be more representative of the host material than smaller, gram-sized bulk rock samples or individual milligram-sized minerals. Most reference materials were generously provided by Dr. C. E. Martin of the Geology Dpt., University of Otago. The basaltic reference materials of BCR-2 and BHVO-2 and the dunite reference material DTS-2b were also used to test the performance of the chemical preparation methods and analysis protocols, as their elemental composition and uranium concentrations make them well suited as chemical analogues of the range of meteorite samples analyzed in the present study. The uranium concentration of DTS-2b is, however, far lower than those of the other rock standards analyzed.

Fig. 3.1 shows that all analyzed rock standards have $^{238}\text{U}/^{235}\text{U}$ ratios varying from a minimum value of 137.772 ± 0.010 for the rhyolite standard JR-1 to a maximum value of 137.827 ± 0.013 for the dunite standard DTS-2b. Some of the standards have $^{238}\text{U}/^{235}\text{U}$ compositions that vary outside of the limits of their reported uncertainties. However, no specific trend according to silica content is visible and there is no resolvable isotopic difference between volcanic and plutonic rocks. The $^{238}\text{U}/^{235}\text{U}$ compositions for BCR-2 and BHVO-2 of 137.803 ± 0.014 and 137.791 ± 0.011 in this study are in agreement with published data of Weyer et al. [2008] for BCR-2 of 137.789 ± 0.010 and BHVO-1 of 137.795 ± 0.008 and 137.789 ± 0.007 (values transformed by Hiess et al. [2012] using a $^{238}\text{U}/^{235}\text{U}$ standard value of 137.829 ± 0.022 for the CRM112a standard).

Table 3.1: Uranium isotope data for 12 igneous rock standards. Averages are weighted depending on ng U used per analysis (reflected by intensity and length of analysis).

Sample	Rock type	Silica content	Institution	$^{238}\text{U}/^{235}\text{U}$	2SE	n	U conc. [ppm]
Volcanic rocks							
BCR-2	Basalt	mafic	USGS ^a	137.803	0.014	11	1.8
BHVO-2	Basalt	mafic	USGS	137.791	0.011	2	0.45
JB-1a	Basalt	mafic	GSJ ^b	137.797	0.011	7	1.6
JB-3	Basalt	mafic	GSJ	137.781	0.011	7	0.5
JA-3	Andesite	intermediate	GSJ	137.788	0.014	4	1.0
JR-1	Rhyolite	felsic	GSJ	137.772	0.010	6	8.8
Plutonic rocks							
NIM-P	Pyroxenite	ultramafic	SABS ^c	137.793	0.019	3	0.2
DTS-2b	Dunite	ultramafic	USGS	137.827	0.013	4	0.0019
W-1	Diabase	mafic	USGS	137.797	0.009	6	0.6
SY-3	Syenite	intermediate	CCMP ^d	137.796	0.011	11	750
STM-1	Nepheline Syenite	intermediate	USGS	137.784	0.017	7	8.8
G-1	Granite	felsic	USGS	137.814	0.017	7	3.9
Average				137.795	0.008	12	

^aUSGS: United States Geological Survey

^bGSJ: Geological Survey Japan

^cSABS: South African Bureau of Standards

^dCCRMP: Canadian Certified Reference Materials Project

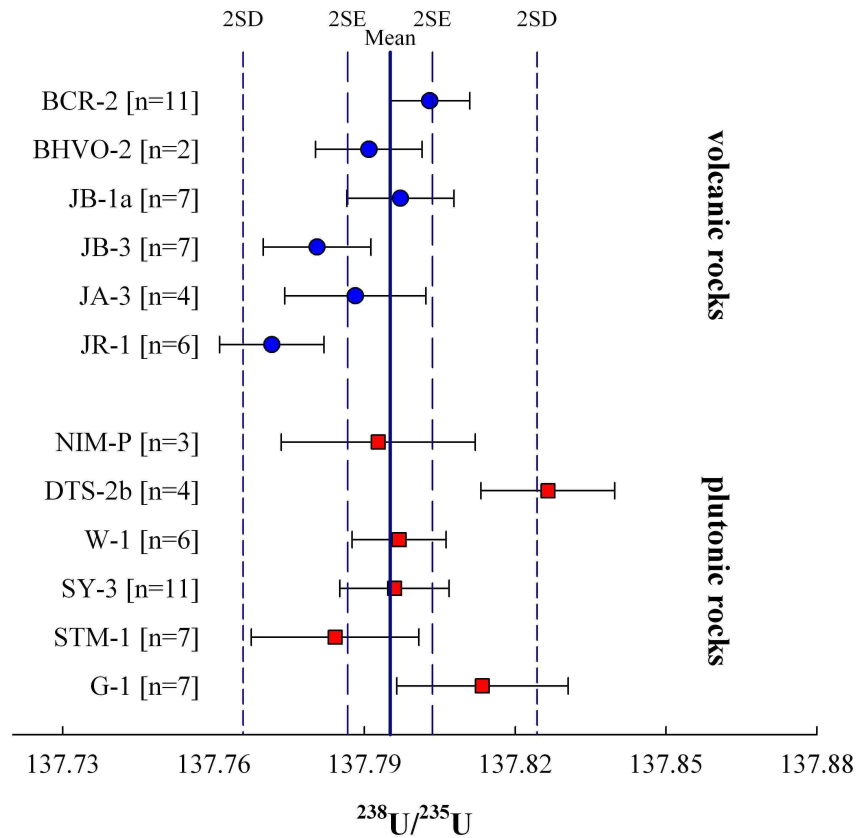


Figure 3.1: Uranium isotopic ratios for 12 terrestrial rocks, six volcanic rocks (blue dots) and six plutonic rocks (red squares).

The average $^{238}\text{U}/^{235}\text{U}$ ratio obtained from these standards is 137.795 ± 0.008 , which is used as the BSE value throughout this study. This value is in very good agreement with the average of $^{238}\text{U}/^{235}\text{U} = 137.802 \pm 0.010$ calculated using only the 37 measurements of 13 different bulk igneous rock samples published in Hiess et al. [2012, and references therein], which includes the uranium isotopic ratios for BCR-2, BHVO-2 and DTS-2b reported in this study and published in Amelin et al. [2010]. All data published by Hiess et al. [2012] is according to a reference value of 137.829 ± 0.022 for $^{238}\text{U}/^{235}\text{U}$ of the standard CRM112a. The published value is, however, lower than the proposed BSE ratio of 137.818 ± 0.007 of Hiess et al. [2012, and references therein], calculated using the measurements of the igneous rocks mentioned before combined with analyses of zircons and other U-bearing minerals. The latter approach is, however, not representative of the $^{238}\text{U}/^{235}\text{U}$ BSE ratio, as single minerals, including zircons, have been shown to undergo sizable, permil-level uranium isotope fractionation processes during their formation. Including results for these minerals in the compilation most likely skews the inferred BSE composition towards heavier values. It is therefore more suitable to use only homogenized

bulk rock samples when defining a BSE $^{238}\text{U}/^{235}\text{U}$ ratio, as reported here.

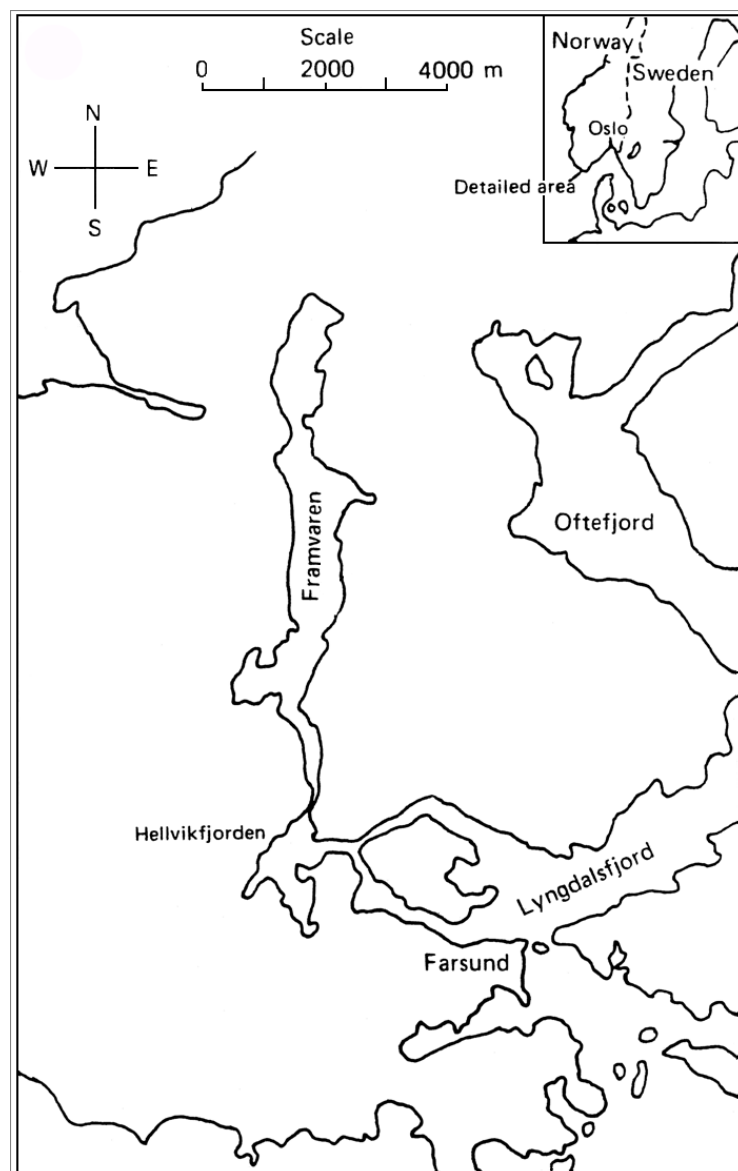
3.2 Anoxic aquatic conditions: Framvaren Fjord (Norway) and an Oxygen Minimum Zone (Peru)

3.2.1 Framvaren Fjord

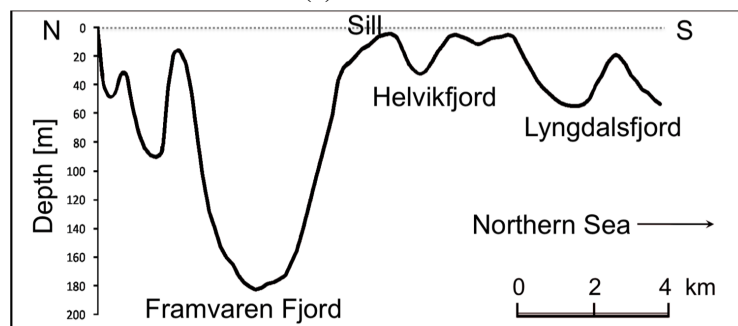
Framvaren Fjord is located in southern Norway, at $58^{\circ}10'\text{N}$, $6^{\circ}45'\text{E}$, has a surface area of 5.8 km^2 and a maximum depth of 183 m [McKee and Skei, 1999] (Fig. 3.2a). It was formed as a result of changing isostatic conditions during glaciation and deglaciation events of the area. Framvaren Fjord is separated from the Northern Sea by a 2.5 m deep sill to the Helvikfjord, which is in turn connected to the Lyngdalsfjord, which then discharges into the Northern Sea. The Framvaren Fjord itself contains another sill of 20 m depth which separates the main basin in the south from a shallower basin of 100 m depth in the northern part of the fjord (Fig. 3.2b, Skei [1988]). The major freshwater contributions are via the Lyngdals River, which enters the Lyngdalsfjord, and freshwater runoff of $1\text{--}2 \text{ m}^3 \text{ sec}^{-1}$ annual average from a catchment area of 31 km^2 [Skei, 1988].

The tidal amplitude of about 10 cm is extremely low and most of the water flowing into the Framvaren Fjord from the Helvikfjord is of low density and therefore only renews the upper 10–20 m of the Framvaren water column [Stigebrandt and Molvær, 1988], as the lower water layers are of higher density due to their increased salinity. Because of this low water renewal and the restricted water circulation, the water in the fjord is depleted in oxygen and permanently anoxic below a depth of 18 m, with the $\text{O}_2/\text{H}_2\text{S}$ redox boundary being spatially static within $\pm 1 \text{ m}$ and coinciding with the lower level of the euphotic zone [Swarzenski et al., 1999]. Sulfate levels in Framvaren Fjord, which provide an indicator for the scale of anoxicity, are 25 times greater than in the Black Sea [Skei, 1983], which is one of the most popular study areas for anoxic basins. The last deep water renewals in Framvaren Fjord occurred during the first excavation of the sill into the Helvikfjord in 1850 and during its modification in 1878 and in 1902, with Framvaren having been a meromictic lake before 1850 [Skei, 1983]. It is unknown how much water entered the fjord during these water renewal processes and if all bottom water was renewed at any of these times. However, it is certain that the Framvaren Fjord remained untouched by major water exchanges and human influences since the last excavation 110 years ago [Skei, 1988].

The water column of Framvaren Fjord can be divided into four stable layers, which, according to Skei [1988], are: 'the low salinity surface layer (0–2 m) above sill depth; the intermediate oxygenated layer down to $\sim 18 \text{ m}$; the deep water where steep gradients in



(a) Overview



(b) Profile

Figure 3.2: Framvaren Fjord, Norway: a) Overview figure, published by Skei [1983]; b) Profile of the Framvaren Fjord and adjacent fjords. Reproduced after Skei [1988].

the chemistry occur (18 to 80-100 m depth); and the bottom water below 100 m, where changes in salinity and chemistry are small', see also Fig. 3.6. The anoxic layer is therefore comprised of the deep and the bottom water layer.

The salinity and the associated density profiles portray the above described layers, with salinities of <10 in the surface layer, rising to a salinity of 20 at the redox boundary and then reaching near static salinity values of about 21-23 in the deep and bottom layers (Fig. 3.6). As a comparison, fresh water has zero salinity while the mean surface ocean water has a salinity of about 35.

3.2.1.1 Previous work

The biogeochemistry of Framvaren Fjord has been extensively studied in the last decades, as it is an undisturbed example of a permanently anoxic basin. The studies of Skei [1988] and Stigebrandt and Molvær [1988] describe the environmental setting and the water exchange of the Framvaren, as described above.

If a water mass, like Framvaren Fjord, has a low water exchange rate but a higher supply of organic matter, the decay of this organic material induces the hydrogen sulfide and the total carbonate concentrations to increase and the pH to decrease with depth [Anderson et al., 1988, Mandernack and Tebo, 1999]. The sulfur isotopic behaviour in Framvaren Fjord is consistent with the cumulative effects of dissimilatory sulfate reduction² by sulfate-reducing bacteria throughout the deep anoxic water column [Mandernack et al., 2003]. Specifically, the sulfide produced during sulfate reduction that is expelled back into the water column is very depleted in ³⁴S, giving rise to light $\delta^{34}\text{S}$ compositions relative to the reactant sulfate, as sulfate reducing bacteria preferentially metabolize ³²S over ³⁴S during the decomposition of organic matter. The produced HS⁻ can diffuse upwards and be re-oxidized in the suboxic and oxic layers of the fjord. However, sulfide oxidation only has a small isotopic effect on sulfur compared with sulfate reduction [Anderson et al., 1988, Mandernack et al., 2003]. At depths below 24 m $\delta^{34}\text{S}_{\text{SO}_4^{2-}}$ and $\delta^{18}\text{O}_{\text{SO}_4^{2-}}$ increase steadily with depth and sulfate reduction becomes the primary influence on the sulfur isotopic composition at depths below 40 m [Mandernack et al., 2003] (Fig. 3.3).

Sulfur concentration shows a very good correlation with sulfide isotopic composition at

²Bacteria utilizing dissimilatory sulfate reduction take up sulfate, use the reduction process to gain energy and expel the reduced sulfide.

$$\delta^{34}\text{S} = \left(\frac{(^{34}\text{S}/^{32}\text{S})_{\text{sample}}}{(^{34}\text{S}/^{32}\text{S})_{\text{standard}}} - 1 \right) * 1000 \quad (3.1)$$

4

$$\delta^{18}\text{O} = \left(\frac{(^{18}\text{O}/^{16}\text{O})_{\text{sample}}}{(^{18}\text{O}/^{16}\text{O})_{\text{standard}}} - 1 \right) * 1000 \quad (3.2)$$

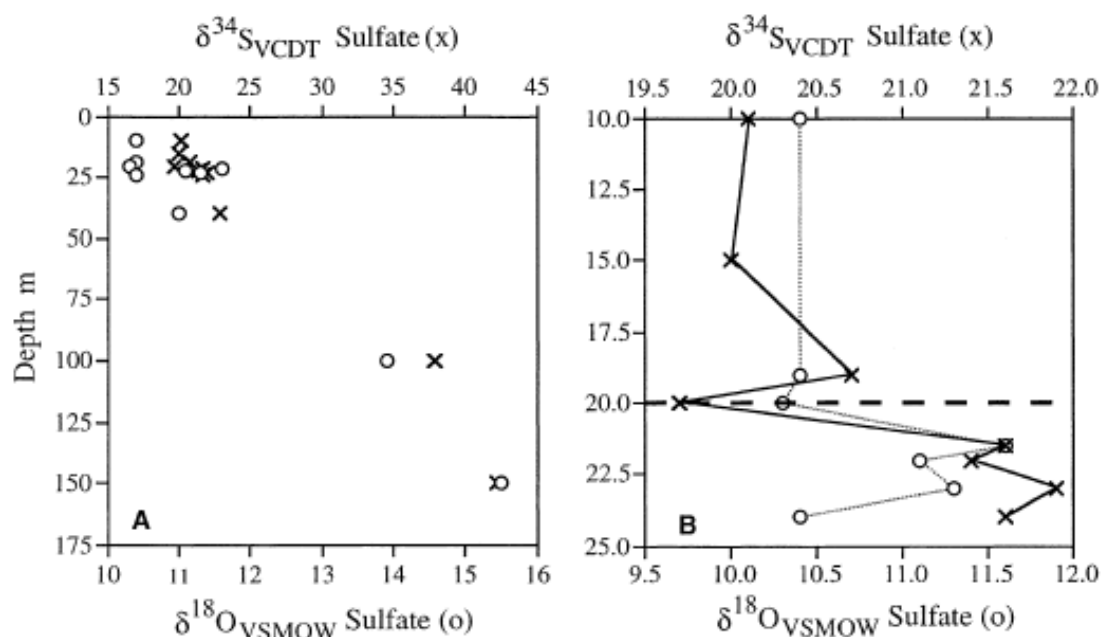


Figure 3.3: (A) The $\delta^{34}\text{S}_{\text{VCDT}}$ (crosses) and $\delta^{18}\text{O}_{\text{VSMOW}}$ (open circles) isotope compositions of sulfate throughout the water column. (B) as (A) but focused around the redox interface region. The dashed line represents a depth of 20 m at which sulfide is first detected. VCDT and VSMOW are the sulfur and oxygen standards used as references, with VCDT standing for 'Vienna Canon Diabolo Troilite' and VSMOW representing 'Vienna Standard Mean Ocean Water'. From Mandernack et al. [2003].

depths below 24 m, in agreement with a Rayleigh distillation model for closed systems [Mandernack et al., 2003].

Phytoplankton and phototrophic bacteria both show dense populations around the redox interface, which coincides with the lower euphotic zone. The bacterial layer is up to one meter lower than the photosynthetically active phytoplankton zone. Bacteria are reportedly responsible for changes in the isotopic signatures of nitrogen, oxygen, carbon and sulfur during their metabolism [Velinsky and Fogel, 1999, Mandernack et al., 2003]. For example, the uptake of ammonium in the interface region results in depleted $\delta^{15}\text{N}$ particulate nitrogen. Also, the isotopic composition of particulate organic carbon indicate the different pathways of carbon uptake, being low at the interface and high at the particulate carbon maximum. Bacteria can also cause a rapid decrease in molecular oxygen and nitrate from the surface to the redox interface at 18 m, where the highest count of active biomass (ATP) is observed [Ormerod, 1988].

Several publications address the distribution of trace metals in the water column according to their behaviour at the redox interface [Piper, 1971, Jacobs et al., 1985, Egeberg et al., 1988, Haraldsson and Westerlund, 1988, Skei, 1988]. These findings are all in

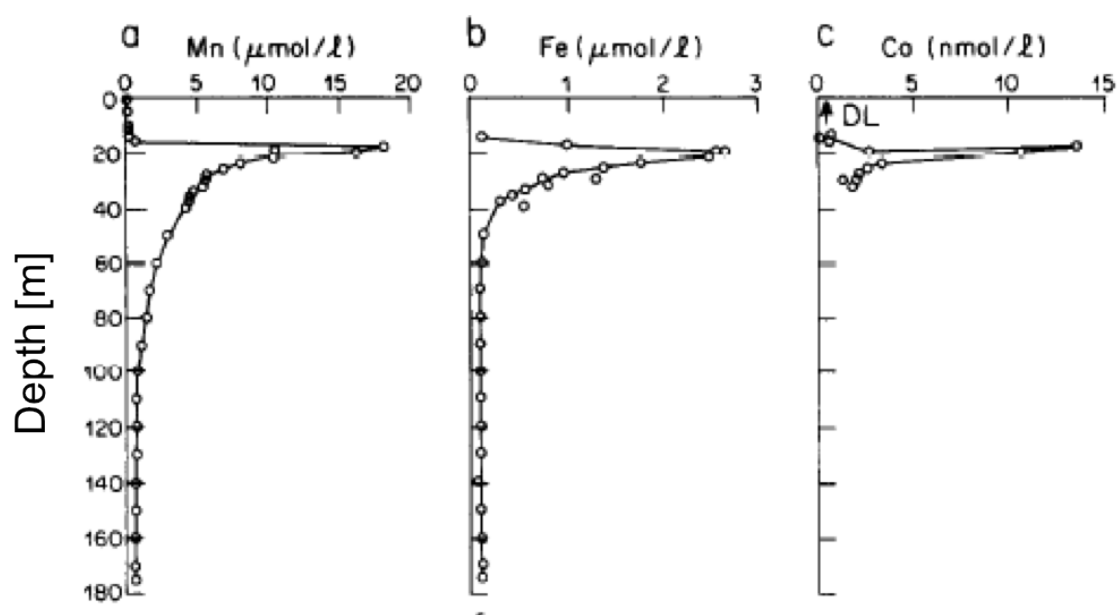


Figure 3.4: Metal concentrations for Mn, Fe and Co throughout the water column of Framvaren Fjord. Figure from Jacobs et al. [1985].

agreement with each other, stating that the Framvaren acts as an effective trap for trace metals introduced into the surface water. The transition metals Mn, Co, and Fe, have dissolved concentration maxima at or just below the interface at depth of 18 m (Mn, Co) and 20 m (Fe) [Jacobs et al., 1985] due to the increased solubility of the reduced species and the reductive dissolution of Fe-Mn-oxyhydroxides. The concentrations of these transition metals then decrease with depth until they reach their minimum levels in the deep water layer between water depths of 80 and 100 m (Fig. 3.4). This behaviour indicates that the transition metals and other elements are involved in metal oxide redox cycling around the redox interface as well as metal sulfide formation in the anoxic layer [e.g. Jacobs et al., 1985].

There are some data available on the uranium distribution in the Framvaren Fjord, summarized in Fig. 3.5. For example, both Todd et al. [1988] and McKee and Todd [1993], report a slight concentration maxima of dissolved $^{238}\text{U} = 1.20\text{--}1.22$ ppb just above the redox interface and a minima below the interface ($^{238}\text{U} = 0.47$ ppb) at 24 m. These excursions are superimposed on a general increase in uranium concentration from 0.87 ppb at 1 m depth to 1.48 ppb at 175 m depth [McKee and Todd, 1993, Todd et al., 1988]. Both concentration profiles display a positive linear relationship with the salinity increase above the anoxic layer, which has been interpreted to reflect simple two-component mixing between high salinity open-ocean water and lower saline freshwater, and the conservative behaviour of uranium in Framvaren Fjord by these workers. However, Swarzenski et al. [1999] argue instead that this interpretation is invalid, as their data shows that Fram-

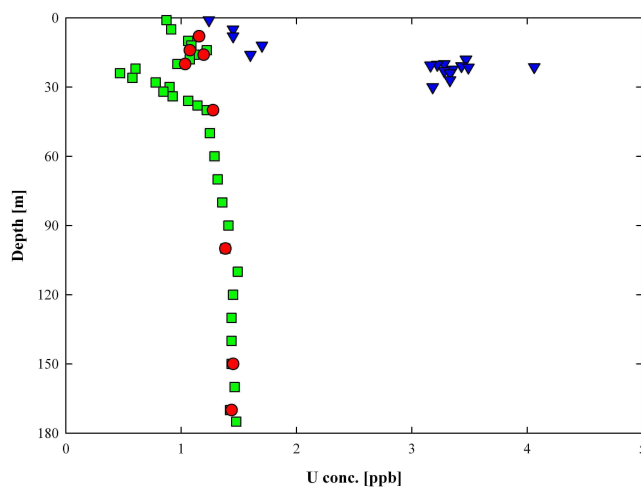


Figure 3.5: Uranium concentration profiles for Framvaren Fjord after Todd et al. [1988] (red circles), McKee and Todd [1993] (green squares) and Swarzenski et al. [1999] (blue triangles).

varen Fjord is a more complex system than described by a linear two-component mixing scenario. Contrary to the other studies, Swarzenski et al. [1999] report a massive concentration maximum of 4.06 ppb for dissolved uranium at the redox boundary and a small minimum of 1.60 ppb U. This behaviour is superimposed on a general increase of uranium concentration from 1.24 ppb at 1 m depth to 3.33 ppb at 27 m depth. McKee and Todd [1993] argue that their data indicate a non-conservative net loss of uranium throughout the anoxic layer of the fjord, probably influenced by the removal of uranium by bacteria at depths of 20 to 36 m, possibly involving the bacterially-mediated reduction of dissolved U(VI) to insoluble U(IV). However, Swarzenski et al. [1999] showed that uranium occurs primarily as soluble U(VI) on both sides of the redox transition zone. Despite these differences, probably due to changes in the water chemistry between years sampled, all three studies confirm that redox-controlled oxidation state transformation on its own cannot explain the observed uranium behaviour analyzed. According to these studies, a more suitable explanation for the observed uranium distribution patterns is given by biological processes involving active and passive uptake and release mechanisms, in which the reduction of oxidized U(VI) to reduced U(IV) is only one of several processes influencing the biogeochemistry of the fjord.

It has not yet been possible to isolate the main reaction(s) responsible for uranium removal in the Framvaren Fjord due to many different redox-, particle- and biologically reactive elements in and around the O_2/H_2S interface. This study of $^{238}U/^{235}U$ fractionation in addition to uranium concentration patterns will help to further understand the reactions controlling uranium cycling in this anoxic environment and their significance. This is be-

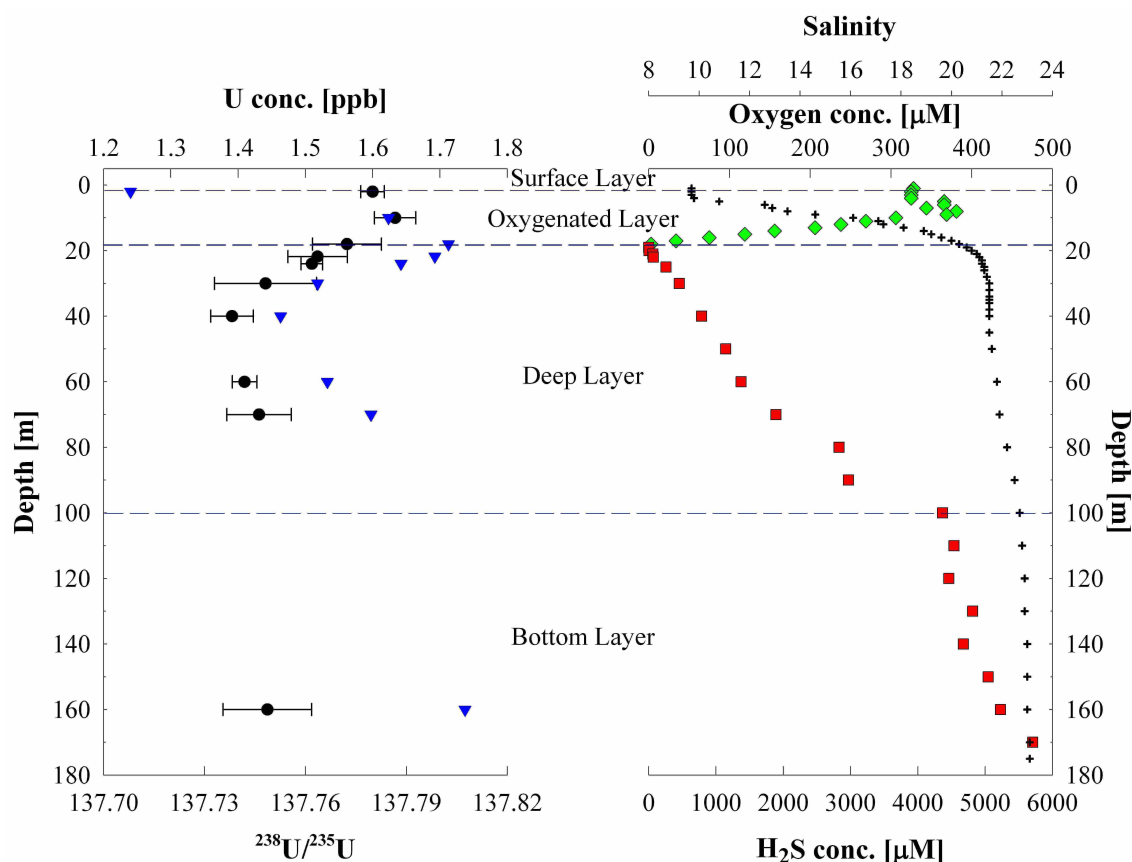


Figure 3.6: Left: Uranium concentration (blue triangles) and uranium isotope ratios with 2SE uncertainties (black dots) from this study. Right: Oxygen concentration (green diamonds), hydrogen sulfide concentration (red squares) and salinities (black crosses), after data from McKee and Todd [1993].

cause only certain processes, each displaying a unique isotopic signature, can fractionate uranium in a water column.

3.2.1.2 Results and discussion

Sampling for this study took place from 07.-11. August, 1998, at the deepest point of the main basin of Framvaren Fjord.

Uranium $^{238}\text{U}/^{235}\text{U}$ isotope ratio and uranium concentration profiles of Framvaren Fjord are reported in Fig. 3.6 and Table 3.2. The data show that uranium concentrations are low in the surface layer (1.2 ppb), rising to a maximum of 1.7 ppb at a depth of 18 m, where the redox interface is situated. Uranium concentrations systematically decrease below the interface, reaching a minimum of 1.5 ppb at 40 m, followed by progressively increasing concentrations with increasing depth, reaching the former maximum of 1.7 ppb again in

Table 3.2: Uranium, oxygen, hydrogen sulfide and salinity data of the Framvaren Fjord

Depth [m]	$^{238}\text{U}/^{235}\text{U}$	2SE	n	U conc. [ppb]	O [μM]	H ₂ S [μM]	Salinity
2.0	137.780	0.004	2	1.24	325	-	9.7
10.0	137.787	0.006	2	1.62	306	-	16.1
18.0	137.772	0.010	2	1.71	3	-	20.3
21.8	137.764	0.009	2	1.69	-	69	21.1
24.0	137.762	0.003	2	1.64	-	218	21.2
30.0	137.748	0.015	2	1.52	-	457	21.5
40.0	137.738	0.006	2	1.46	-	787	21.5
60.0	137.742	0.004	2	1.53	-	1372	21.8
70.0	137.746	0.010	2	1.60	-	1892	21.9
160.0	137.749	0.013	2	1.74	-	5228	23.0
Average	137.759	0.011		1.58			

the bottom layer. This behaviour is generally consistent with the previously published data mentioned above (Fig. 3.5).

The $^{238}\text{U}/^{235}\text{U}$ isotope ratio profile closely follows the general trend shown by the uranium concentration profile, becoming more depleted in ^{238}U relative to ^{235}U with decreasing uranium concentrations. Specifically, $^{238}\text{U}/^{235}\text{U}$ values of 137.780 ± 0.004 and 137.787 ± 0.005 at depth of 2 m and 10 m, respectively, are identical within error to the composition of BSE. A progressive decrease of the uranium isotopic composition then takes place just below the O₂/H₂S interface, in anoxic water conditions with rising H₂S concentrations, reaching its minimum value of $^{238}\text{U}/^{235}\text{U} = 137.738 \pm 0.006$ at 40 m depth, offset by 0.4‰ from the composition of BSE of 137.795 ± 0.008 . Below 40 m only a minor, unresolvable, increase of the uranium isotopic ratios is observed, reaching a value of 137.749 ± 0.013 in the bottom layer of the fjord. The fractionation of ^{238}U and ^{235}U follows the theory of the nuclear field shift effect, whereby the heavier isotopes are preferentially removed from the water column over the lighter isotopes, causing the $^{238}\text{U}/^{235}\text{U}$ ratio to decrease during the process.

At first glance, the observed uranium behaviour indicates that uranium is chemically reduced from U(VI) to the more particle reactive U(IV) at and below the redox interface at a water depth of about 18 m, coincident with the redox cycling of other reactive elements like Fe and Mn. However, this scenario is difficult to reconcile with the gradual increase in uranium abundance below 40 m depth, as, once precipitated, U(IV) should be completely removed from the water column and the uranium concentrations should remain consistently low in the deeper layers of the fjord. External sources of uranium other than

the inflow of surface water into Framvaren are considered to be insignificant [e.g. Skei, 1988], although a back-reaction between the bottom water and sedimentary porewater is possible. It is, however, unlikely that uranium from the sediment of Framvaren Fjord is transported more than 100 m up the water column to a depth of 40 m. Also, other studies such as Todd et al. [1988], McKee and Todd [1993] and Swarzenski et al. [1999] showed that the concentration maxima of uranium is in fact just above the redox interface, indicating the beginning of uranium removal before the development of anoxia (no sample of this depth was available for this study) and U(IV) concentrations are only slightly elevated below the transition zone compared with the oxygenated layer [Swarzenski et al., 1999]. Further, the chemical reduction of U(VI) and U(IV) during laboratory controlled experiments has, to date, shown no resolvable fractionation of $^{238}\text{U}/^{235}\text{U}$ [Rademacher et al., 2006, Stirling et al., 2007], although further experiments are needed to confirm this. Together, these observations imply that pure chemical reduction of uranium alone does not control the uranium behaviour in Framvaren Fjord.

Alternatively, it is possible that the uranium behaviour is controlled by the redox cycles of Fe and Mn. Both Fe and Mn are known to form oxyhydroxides at the redox interface, and uranium is known to adsorb onto these particles. The Fe(II) and Mn(II) maxima are found exactly at or below the redox interface [e.g. Jacobs et al., 1985] and the U and Mn maxima coincide with this depth. However, the uranium concentration profile of Framvaren Fjord shows a distinct minimum at 40 m, far below the interface region, while Fe and Mn concentrations decrease gradually (Fig. 3.4). This implies that adsorption of uranium onto inorganic colloids may control uranium behaviour near the interface at Framvaren Fjord, but does not control the cycling of uranium further down the water column. A minor influence of adsorption onto inorganic particles on the uranium concentration and isotopic composition around the redox interface cannot be excluded.

The most plausible explanation for the concentration profile and the deep situated minima at a depth of 40 m of both the uranium isotopic ratio and uranium concentration is given by microbially mediated uranium reduction involving sulfate reducing and possibly sulfide oxidizing bacteria. These bacteria can scavenge uranium and form a major sink for uranium, releasing at least parts of it again during the organic breakdown of bacterial remains in the deeper layers of the fjord. It is possible that only oxidized U(VI) adsorbed to bacterial cell walls or inorganic particles is released again, while the assimilated, isotopically shifted reduced U(IV) precipitates to sediment. This theory would explain the increase in uranium abundance in the deeper layers of the fjord while the isotopic composition of $^{238}\text{U}/^{235}\text{U}$ remains at a constantly low level. The bacterially-mediated reduction and consequent removal of uranium by sulfur-reducing bacteria in aquifers is well documented by bioremediation studies [Abdelouas et al., 2000, Komlos et al., 2008, Luo

et al., 2007] and can lead to the uranium isotopic fractionation behaviour observed in Framvaren Fjord. For example, Bopp et al. [2010] report a 1‰ decrease in $^{238}\text{U}/^{235}\text{U}$ with decreasing U(VI) in a contaminated groundwater aquifer after biostimulation with sulfate-reducing bacteria. The uranium concentration profile of this study is consistent with earlier studies at Framvaren Fjord, reporting intense uranium removal between 20 m and 36 m, with the main removal taking place just below the interface region [McKee and Todd, 1993]. Why the minimum concentration of dissolved uranium of this study is located at much lower depth than in other studies (40 m instead of reported 24 m by McKee and Todd [1993]) cannot be resolved, but the most likely explanations involve an increased bloom of sulfate reducing bacteria during the sampling period for this study and the larger filter sizes of $0.45\ \mu\text{m}$ used during this study compared with $0.22\ \mu\text{m}$ filter sizes used by McKee and Todd [1993] and Swarzenski et al. [1999], which might lead to a larger fraction of colloidal material in samples of this study. The relatively invariant but depleted uranium isotope ratios at water depths below 40 m centered about $^{238}\text{U}/^{235}\text{U}$ compositions of 137.744 indicates the release of uranium depleted in ^{238}U with respect to ^{235}U into the lower water column. This implies that some of the heavier ^{238}U has to be irreversibly removed from the water column, for example during biological uptake by assimilatory bacteria, which incorporate uranium in their cells, or by adsorption.

For most redox reactions isotopic exchange is kinetically driven and controlled by differing reaction rates between heavy and light isotope species. The observed systematic relationship between uranium concentration and $^{238}\text{U}/^{235}\text{U}$ composition in the anoxic waters of Framvaren Fjord between depths of 18 m and 40 m were therefore considered in relation to a closed-system Rayleigh fractionation model. This model requires uranium to be present as a finite pool without replenishment. It also assumes that the initial uranium is removed from the water column without a significant back-reaction or any other interactions between the dissolved uranium and solid uranium phases. The uranium behaviour in the water column can then be described by

$$R/R_0 = (c/c_0)^{1/\alpha-1}, \quad (3.3)$$

which can be rewritten as

$$\ln(R/R_0) = (1/\alpha - 1) * (c/c_0) \quad (3.4)$$

In these equations R equals the observed isotopic ratio $^{238}\text{U}/^{235}\text{U}$, R_0 defines the initial $^{238}\text{U}/^{235}\text{U}$ ratio, c equals the observed uranium concentration, c_0 represents the initial uranium concentration, and α equals the fractionation factor [Scott et al., 2004]. It can

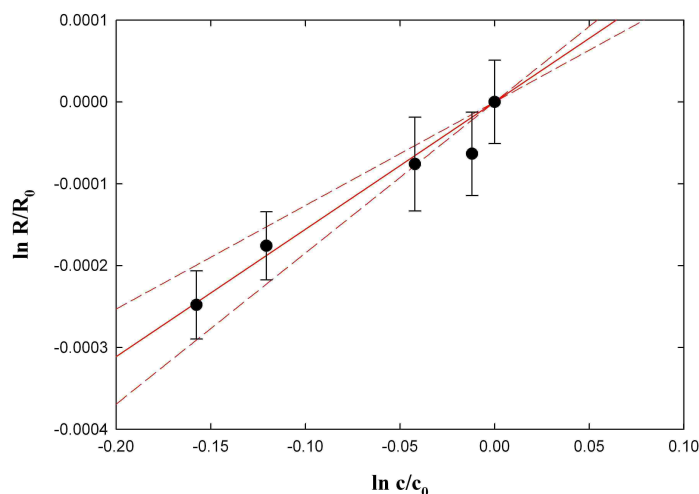


Figure 3.7: Rayleigh fractionation for the Framvaren Fjord profile. Closed circles and red regression line represent depth from 18 - 40 m and the dashed lines are the 95% interval of the regression.

be seen from Eq. 3.4 that the fractionation factors are calculated from the slope of the regression line of Fig. 3.7, being $\alpha^{-1}-1$. The Framvaren data obtained in this study correspond to $\alpha = 0.9985$ for depths of 18 m - 40 m. The fact that this value is below one shows that uranium fractionation of ^{238}U and ^{235}U follows the volume-dependent nuclear field shift effect, preferentially removing the heavier ^{238}U isotope from the water column and thereby enriching the lighter ^{235}U . This fractionation factor is in excellent agreement with the theoretically findings of Bigeleisen [1996], reporting a corresponding fractionation factor of $\alpha = 0.9987$ for the residual aqueous phase during the U(IV)-U(VI) equilibrium exchange reaction at 35°C. Furthermore, the very good fit of the observational data with the results of the Rayleigh fractionation model from 18-40 m shows that uranium removal predominantly occurs in a closed system. This is consistent with the physical oceanography of Framvaren Fjord, which is not replenished by freshwater or influenced by currents below a depth of 18 m. This is also in agreement with the closed-system behaviour of stable sulfur isotope data in the anoxic layer of Framvaren, as described above [Mandernack et al., 2003]. The fractionation factor for 18-40 m water depths of 0.9985 is significantly larger than the previously reported values of $\alpha = 0.9995$ -0.9997 for a natural aquifer in a sandstone-hosted uranium deposit by Murphy et al. [2012] and $\alpha = 0.99954$ for a biostimulation experiment in a contaminated groundwater system by Bopp et al. [2010]. This might be due to the high abundance of biomass around the redox interface of Framvaren Fjord causing a spatially confined bacterial layer in which most of the decomposition of biomass, and consequently the bacterially mediated uranium reduction, takes

place.

3.2.2 Oxygen Minimum Zone: Peru

There are only four large permanent Oxygen Minimum Zones (OMZs) in the world, one in the Arabian Sea, one in the Bay of Bengal, one in the eastern tropical North Pacific Ocean and the OMZ discussed in this study, located in the eastern tropical South Pacific Ocean. According to Paulmier and Ruiz-Pino [2009] the latter OMZ extends off the coasts of Chile (18-37°S, 70-82°W) and Peru (0-18°S, 80-90°W).

The Peruvian OMZ discussed here is part of the so-called Humboldt Current System and is caused by upwelling of cooler deep ocean water. This upwelling water contains a high abundance of nutrients which increases the biological productivity in the surface water. This, in turn, causes an oxygen depletion during the sinking and decay of organic material, which uses up the dissolved oxygen during the microbial degradation process. As most marine animals need ocean water to contain a certain amount of oxygen to survive, the Peruvian OMZ forms a natural respiratory barrier for most zooplankton and marine animals, making the surface water an ideal fishing ground.

The water column in this shelf region has a stable stratification, therefore allowing a shallow OMZ to form. The first 50 m of the water column in the area of the OMZ contains the euphotic zone, with the first 70 m being well mixed due to atmospheric influences [Ryabenko et al., 2012]. The OMZ itself begins at ~50 m and is disturbed by seasonal influences, El Niño, and other large scale climate effects including global warming [Chavez et al., 2008]. These influences make the OMZ temporally stable but not spatially static, as it can change in size and intensity and can be disturbed by lenses of more oxygenated water.

The nitrogen cycle in oceanic oxygen deficient water is generally considered to be of high importance due to its essential role in the global nitrogen cycle and its influence on the geochemistry and microbial ecology in the OMZ regions. Despite the presence of sulfate reducing bacteria, the sulfur cycle is regarded to be of little importance in the OMZs, as it is generally believed that the sulfur cycle becomes dominant only when no other electron acceptors are available in the water column. Therefore, one of the main research subjects around OMZs is understanding the mechanism controlling the anaerobic oxidation of ammonium with nitrite, referred to as the bacterial anammox process. This process occurs in the surface waters as well in the suboxic and anoxic waters of the core of the

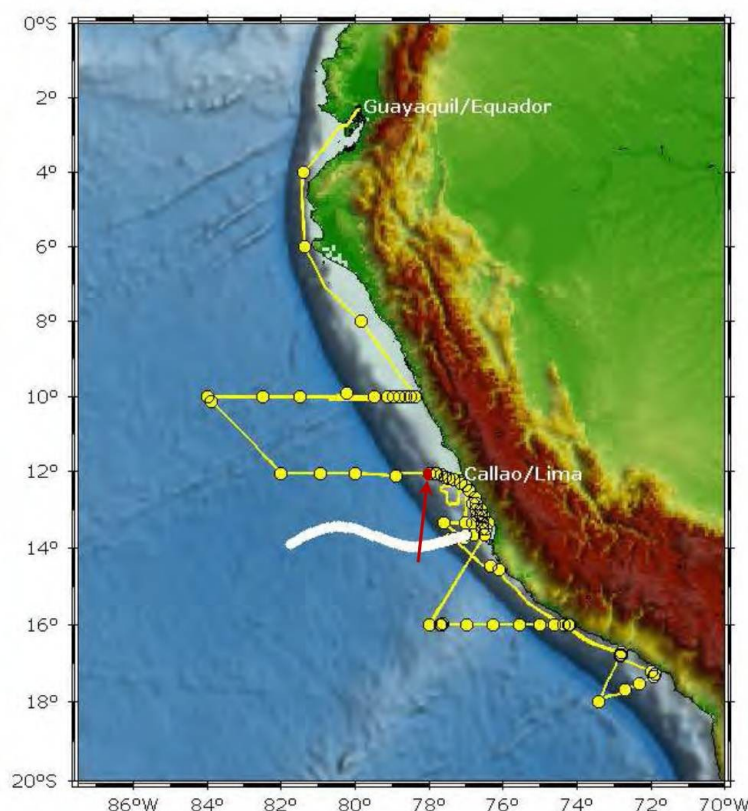


Figure 3.8: Working area and cruise track of Meteor M77/3. The coordinates for the profile analyzed in this study are marked with a red dot and arrow.

OMZ. The anaerobe, autotroph⁵ anammox and the heterotroph⁶ denitrification⁷ processes are the controlling mechanisms in the biogeochemical cycling of nitrogen in this environment [Ulloa and Pantoja, 2009, Ryabenko et al., 2012, and references therein].

For the present study, samples were retrieved on board the R/V Meteor, cruise number M77, leg 3 from December 27, 2008, to January 24, 2009, starting in Guayaquil (Ecuador) and finishing in Callao (Peru). The depth profile analyzed in this study was sampled on January 8, 2009, at station number 11-4, CTD-RO-35, located at 12°02,01'S, 78°00,00'W, in the shelf region off the coast of Peru (see Fig. 3.8). The maximum water depth at these coordinates is 1761 m, resulting in a profile consisting of six samples from the surface to 1500 m depth. A 0.45 μm polycarbonate filter was used to remove particulates from the samples.

⁵Autotroph bacteria metabolize carbon only in form of CO_2 .

⁶Heterotroph bacteria are able to use organic compounds as source of carbon for their metabolism.

⁷Denitrification is a bacterial process that converts NO_3^- into gaseous N_2 .

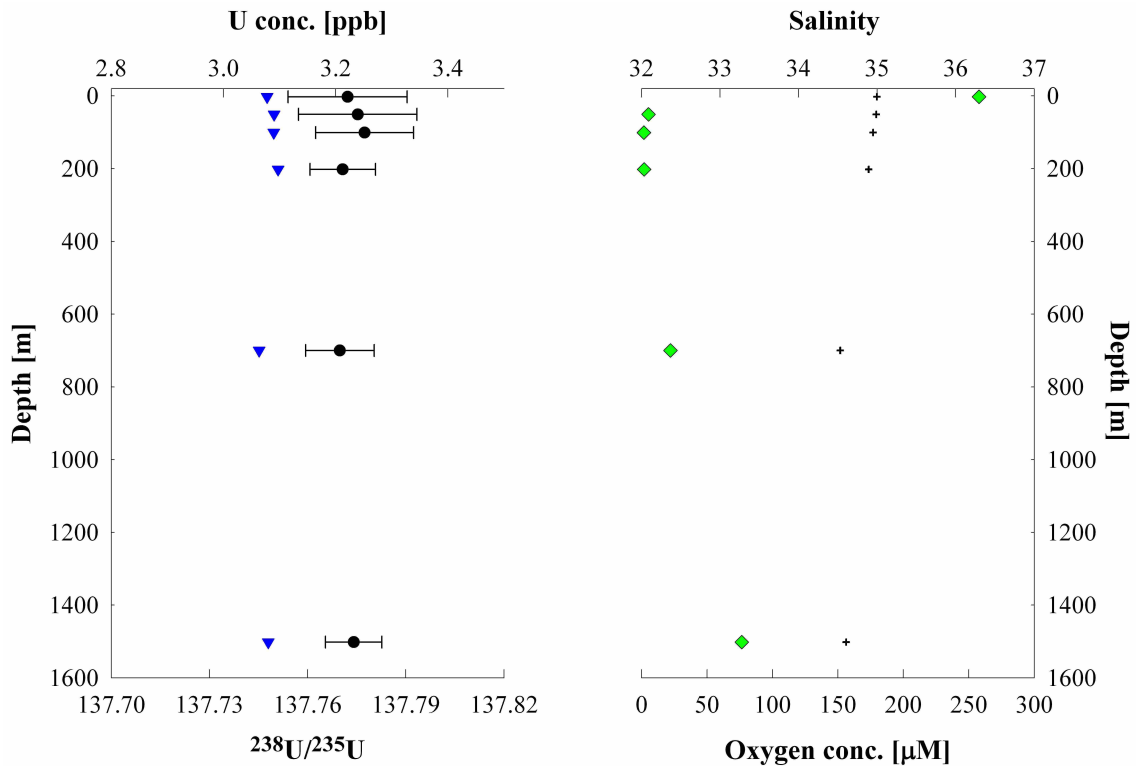


Figure 3.9: Profile of the OMZ off Peru. Left: Uranium isotope ratios (black dots) and uranium concentrations (blue triangles). Right: Oxygen concentrations (green diamonds) and salinities (black crosses).

3.2.2.1 Results and discussion

The sampled depth profile was analyzed for its uranium isotope behaviour and uranium concentrations. The results are shown in Fig. 3.9 and Table 3.3. The figure also shows salinity and dissolved oxygen profiles, data for which was kindly provided by Prof. Dr. M. Frank (GEOMAR, Kiel, Germany, personal communication). The oxygen data show that the OMZ has its core between 50 m and 700 m, with oxygen levels reaching suboxic levels at the stations located at 100 m and 200 m depth. However, the research community has not reached a consensus about the exact definition of OMZs and their cores according to their oxygen abundances, yet.

The uranium isotopic composition appears to be constant throughout the profile, giving an average $^{238}\text{U}/^{235}\text{U}$ ratio of 137.773 ± 0.002 (2SE), and the uranium concentrations are equally constant at 3.1 ppb over the depths sampled. The latter value is within error of the open ocean concentration 3.3 ± 0.2 ppb [Ku et al., 1977]. The uranium isotopic ratios reported here are in agreement, within uncertainty, with previous $^{238}\text{U}/^{235}\text{U}$ data for open ocean water of 137.768 ± 0.004 (2SE), published by Stirling et al. [2007] and Weyer et al. [2008] (data adjusted to a reference value for CRM112a of $^{238}\text{U}/^{235}\text{U} = 137.829 \pm$

Table 3.3: Uranium, oxygen and salinity data for an Oxygen Minimum Zone profile off Peru

Depth [m]	$^{238}\text{U}/^{235}\text{U}$	2SE	n	U conc. [ppb]	O [$\mu\text{mol/kg}$]	Salinity
2.6	137.772	0.018	3	3.1	257.9	34.99
51.0	137.775	0.018	3	3.1	5.3	34.99
100.7	137.777	0.015	4	3.1	1.9	34.95
201.0	137.771	0.010	3	3.1	2.1	34.89
699.9	137.770	0.010	4	3.1	22.1	34.53
1501.5	137.774	0.009	4	3.1	76.6	34.61
Average	137.773	0.002		3.1		

0.022 by Hiess et al. [2012]). The constant uranium concentration in this environment shows that uranium is not removed from the water column, for example by adsorption of uranium onto organic or anorganic particles. These must be present in the low oxygen layers, where biological degradation and redox processes take place. Also, denitrification and anammox processes in low and suboxic conditions do not appear to influence the geochemical behaviour of uranium. Together, these observations demonstrate that the biochemical cycling of uranium is not associated with the complex nitrogen cycle in the environment of the Peru OMZ.

The uranium isotopic results for Framvaren Fjord discussed above provide a basis for interpreting the uranium isotope systematics for the Peru OMZ. The data acquired in the present study can also provide constraints on whether the core of the OMZ is suboxic or anoxic. The dissolved oxygen data suggest that no sustained anoxia is achieved throughout the profile and only suboxic oxygen levels are reached. In the absence of reducing H_2S sulfur, sulfate reducing bacteria would not be present in the OMZ to scavenge and fractionate uranium, as suggested in the Framvaren Fjord dataset. This scenario is consistent with the invariant uranium isotopic and concentration data. However, as dissolved oxygen measurements have relatively high detection limits it is possible that anoxic conditions are indeed achieved in the core of the Peru OMZ, but are not detected. To this end, Thamdrup et al. [2012] report that no detectable oxygen is present in the core of the OMZ. Furthermore, Canfield et al. [2010] presents evidence that sulfate reducing bacteria are present in the anoxic core of the OMZ off the coast of Chile, with sulfide oxidizing bacteria being also present. The sulfur cycle seems to be actively coupled to the nitrogen cycle, as higher sulfide abundances enhance not only sulfide oxidation but also nitrate reduction, and sulfate reduction contributes to the ammonium requirements of the anam-

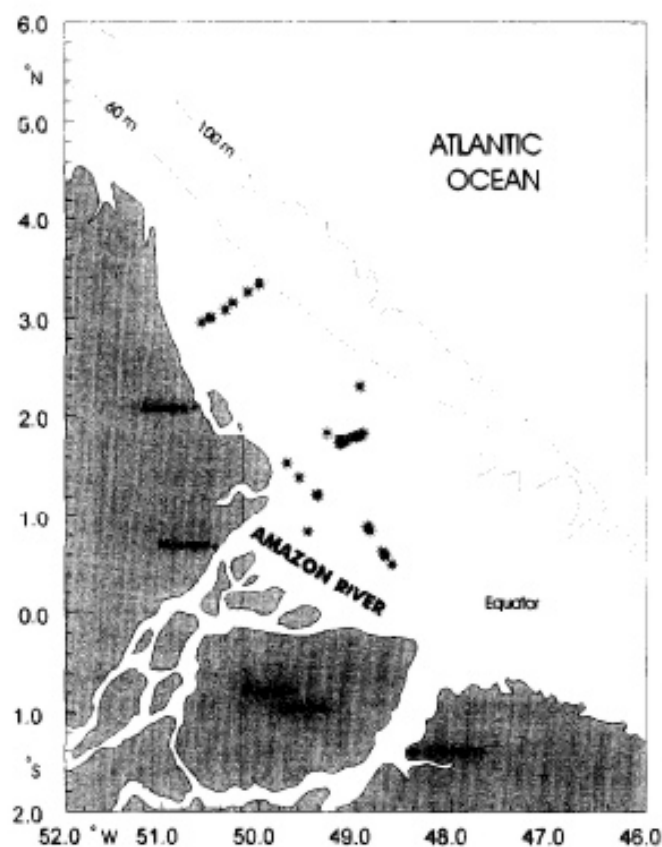


Figure 3.10: The shelf of the Amazon River, including the sample station locations of the AmasSeds cruise, after Swarzenski et al. [1995].

mox process. This suggests that any reduced sulfate is immediately reoxidized. In this case, any uranium scavenged by sulfate reducing bacteria would probably be released again as part of the oxidation process and not show any difference in the $^{238}\text{U}/^{235}\text{U}$ ratios or uranium concentrations.

3.3 Estuaries: Amazon River and Lena River

3.3.1 Amazon River

The Amazon River estuary is situated around the equator, with a large drainage basin extending from about 5°N to 15°S and across 3000 km of longitude, including the Andes Mountains. The estuary off the coast of Brazil (see Fig. 3.10) is defined by a highly energetic regime of tides, oceanic currents, and constant easterly trade winds. The Amazon River has a water discharge of 6×10^{15} L/yr, carrying 1.3×10^9 t of sediments into the Atlantic Ocean [McKee et al., 1987], which is the highest discharge of any of the world's

ivers and traces of fresh water can be detected thousands of kilometers from the river mouth. The Amazon is situated in a humid tropical region, defined by constantly high precipitation (> 60 mm/month), high temperatures ($> 20^{\circ}\text{C}$), and high solar radiation [Nittrover and DeMaster, 1996]. As in all rivers, the main fraction of suspended and dissolved metals in the Amazon River originates from physical and chemical weathering processes along its drainage basin.

Six surface samples along the estuary/shelf region of the Amazon River were collected in November 1991 as part of the multidisciplinary Amazon Shelf Sediment Study (AmasSeds) during a ten day cruise of the R/V C. Iselin between the equator and 4°N . Samples were collected during the month of November when discharge of the Amazon River is at its lowest. A $0.4\ \mu\text{m}$ filter was used to acquire the dissolved fraction of each sample. The samples cover a range of salinity values from zero to 15. This region is characterized by low biological activity and a high concentration of particulates, originating from the river itself and from the resuspension of the seabed [Swarzenski et al., 1995]. The uranium transported from the river is mainly (92%) bound in the highly reactive colloid fraction⁸ [Swarzenski et al., 1995]. All samples of the Amazon river profile represent the terrigenous zone. This is the area with <20 salinity, also defined by low biological activity and a high abundance of TSM (amount of Total Suspended Matter in the water column). The zone containing >20 salinity is defined as the intermediate to high salinity zone with high biological activity.

3.3.2 Lena River

The Arctic Ocean has a high influx of freshwater from several large rivers. Together, the discharge of these Arctic Rivers is similar to that of the Amazon River. However, the large influx into a relatively small ocean leads to its stratification, with a surface layer of reduced salinity (5-10 m deep, <20 salinity) and a highly saline bottom layer [Dittmar and Kattner, 2003, Hölemann et al., 2005].

The Lena River discharges into the Laptev Sea of the Arctic Ocean out of the Siberian tundra and taiga (Fig. 3.11). It has the second largest discharge into the Arctic Ocean after the Yenisey River, with a drainage basin of $2.49 \times 10^6\ \text{km}^2$ [Gordeev and Sidorov, 1993]. Before the Lena River discharges into the Arctic Ocean it branches off into several arms, which form a large delta of about $32,000\ \text{km}^2$ and a delta front of more than 400 km. This area is defined by low precipitation, permafrost, and high seasonal variability with respect to water temperatures throughout the Lena basin. The central part of the Lena

⁸Colloids are particles of $10000\ \text{nm}$ - $0.4\ \mu\text{m}$ size. They can be of organic nature, consisting of humic and fulvic acids or microorganisms, or of inorganic nature like Fe- and Mn oxyhydroxides, clays and precipitates.

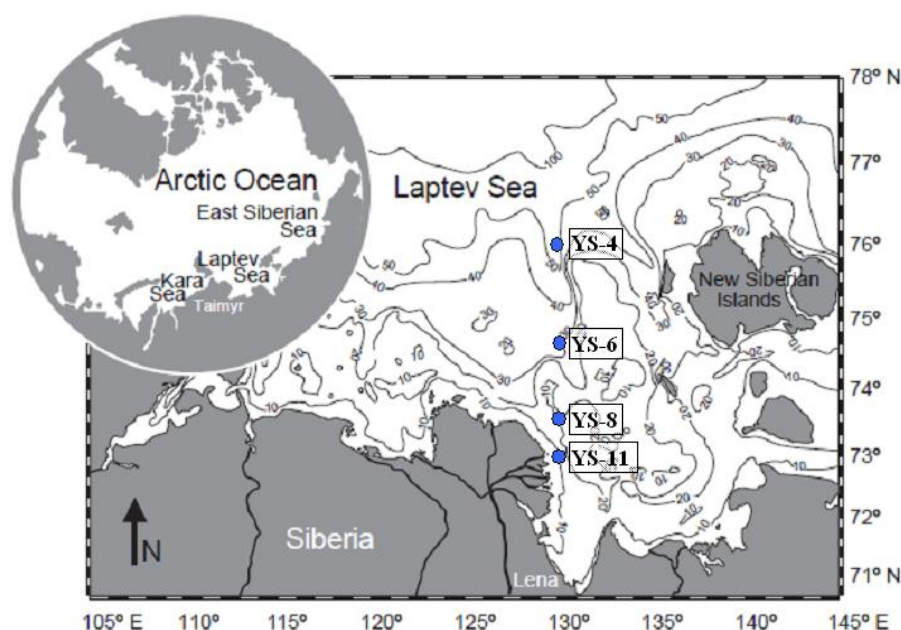


Figure 3.11: Setting of the Lena River in the Laptev Sea of the Arctic Ocean. Blue dots represent the sampling sites for this study, figure after Hölemann et al. [2005].

River basin is dominated by karst, containing carbonate, gypsum- and halogen-bearing rocks [Gordeev and Sidorov, 1993].

Water sampling took place on the shelf of the Lena river from 05.-08. August, 2008, just after the largest seasonal runoff during the annual ice melt in June and July. The samples are located along a salinity profile ranging from 2-32 salinity and originate from both the surface and the bottom layer of the Lena estuary. The surface water is generally frozen from October to July but is ice free and therefore highly oxygenated in August, with an oxygen saturation of up to 96% [Cauwet and Sidorov, 1996]. During the ice-free part of the year hydrocarbonates and calcium ions predominate the river water, primarily governed by the weathering of carbonate rocks and groundwater [Gordeev and Sidorov, 1993]. The riverine water is also characterized by high DOC and TSM concentrations but a very low nutrient abundance.

3.3.3 Results and discussion

Results of the uranium concentration and isotopic analyses for the Amazon River and Lena River estuaries are shown in Fig. 3.12a and 3.12b, respectively, and in Table 3.4. Given the wide-ranging salinity values for both the Amazon and Lena River samples, the data are considered in the context of a two-component mixing model with the follow-

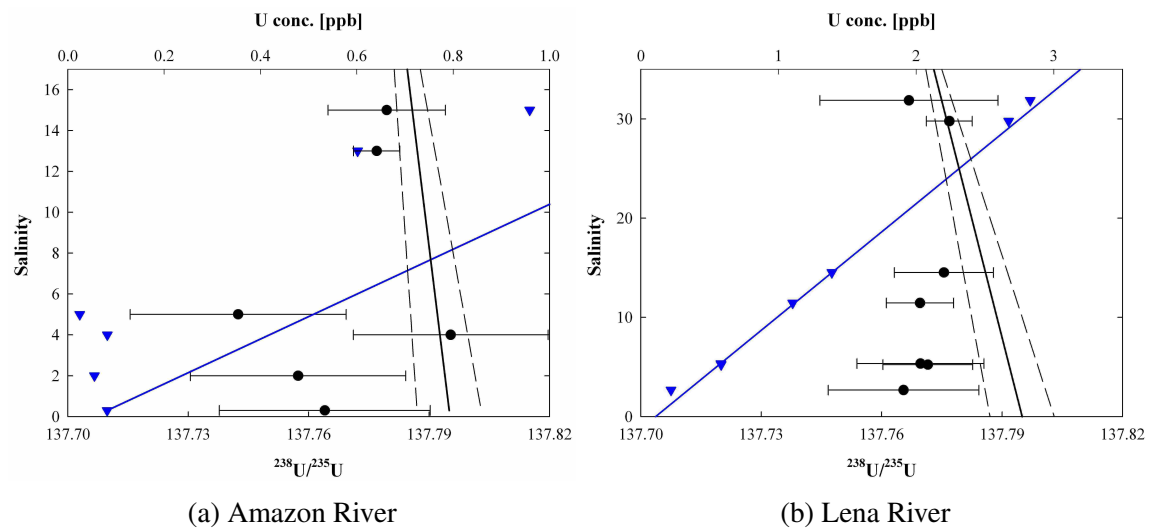


Figure 3.12: Estuaries of (a) the Amazon River and (b) the Lena River: Uranium concentrations (blue triangles), uranium isotopic ratios (black dots) with uncertainties according to their salinities and the modeled mixing lines of riverine and oceanic waters. Blue lines are concentration mixing lines, while black solid lines represent $^{238}\text{U}/^{235}\text{U}$ mixing lines (with uncertainties shown as dashed lines).

ing riverine and open ocean end-members: (1) 0.08 ppb of dissolved U and 0.3 salinity for the Amazon River (this study), and (2) 3.28 ppb dissolved U and 35.44 salinity for the Atlantic Ocean offshore from the Amazon River [Swarzenski et al., 1995], (3) 0.107 ppb dissolved U and zero salinity for the Lena River and (4) 3.19 ppb dissolved U and 34.95 salinity, measured at the deepest point of the Arctic Ocean [Andersen et al., 2007]. Modeled mixing lines over the range of observed uranium concentrations and the salinity gradients are shown in Fig. 3.12. Modeled mixing lines over the range of measured uranium isotopic ratios and the same salinity gradients are also shown, based on $^{238}\text{U}/^{235}\text{U} = 137.795 \pm 0.008$ for riverine water, representing the BSE average reported in this study (see section 3.1), and $^{238}\text{U}/^{235}\text{U} = 137.773 \pm 0.002$ for open ocean water, determined from the average ratio of Peruvian OMZ waters. Both uranium isotope end-members are in very good agreement with the reported values of Hiess et al. [2012, and references therein] for seawater of $^{238}\text{U}/^{235}\text{U} = 137.768 \pm 0.004$ and high-temperature terrestrial rocks of $^{238}\text{U}/^{235}\text{U} = 137.802 \pm 0.010$ (see also Fig. 1.11).

Neither estuary shows a significant variation in the $^{238}\text{U}/^{235}\text{U}$ isotopic composition despite significant changes in uranium concentrations along the salinity gradients. Specifically, $^{238}\text{U}/^{235}\text{U}$ varies from 137.742 ± 0.027 to 137.795 ± 0.024 in the Amazon River estuary, and has an average ratio of 137.769 ± 0.015 . The only resolvable fractionation away from the average uranium isotopic composition occurs in the high turbidity zone of the salinity

Table 3.4: Uranium and salinity data of the Amazon and the Lena estuaries

Salinity	$^{238}\text{U}/^{235}\text{U}$	2SE	n	U conc. [ppb]	Depth [m]	Sample No
Amazon River						
0.3	137.764	0.026	1	0.08	surface	
2	137.757	0.027	1	0.06	surface	
4	137.795	0.024	1	0.08	surface	
5	137.742	0.027	1	0.03	surface	
13	137.777	0.006	2	0.60	surface	
15	137.779	0.015	2	0.96	surface	
Average	137.769	0.015		0.30		
Lena River						
2.7	137.765	0.008	1	0.22	2	YS-11 ^s
5.2	137.772	0.022	2	0.58	3	YS-6 ^s
5.3	137.770	0.011	2	0.58	3	YS-8 ^s
11.4	137.770	0.006	3	1.10	3	YS-4 ^s
14.5	137.776	0.016	3	1.39	9	YS-8 ^b
29.8	137.777	0.012	2	2.67	20	YS-6 ^b
31.9	137.767	0.019	4	2.83	25	YS-4 ^b
Average	137.771	0.003		1.34		

^ssurface layer; ^bbottom layer

gradient, at 4-8 salinity. This zone reportedly has the highest TSM of the entire profile (up to 1500 mg/l) and is the result of massive salt-induced flocculation and aggregation processes of colloids and particles due to abrupt changes in their ionic strength. A second source of particles to this region is given by semidiurnal tidal currents and oceanic currents which induce the advection of sediments [Swarzenski et al., 1995, 2004]. This mechanism removes dissolved REEs and Fe in the low salinity region [Sholkovitz, 1993]. It also leads to reoxidation (for example of Fe and Mn) and remineralization of organic carbon in the upper part of the seabed [Nitttrouer and DeMaster, 1996]. Both, redox and mineralization processes can, in theory, change the $^{238}\text{U}/^{235}\text{U}$ isotopic signature of uranium if one isotope is favourably adsorbed or incorporated over the other. Although no evidence for significant uranium isotope fractionation is present in this data set, two data points of the high turbidity zone of the Amazon River estuary deviate just outside their uncertainties. The variation in $^{238}\text{U}/^{235}\text{U}$ compositions of 137.795 ± 0.024 at a salinity of 4 and 137.742 ± 0.027 at a salinity of 5 correlates with subtle changes in uranium concentration in the low

salinity zone of the Amazon River estuary, showing that the uranium isotopic ratio might be correlated to the rapid aggregation processes in this zone. However, a high-resolution profile is needed to confirm the isotopic fractionation of ^{238}U and ^{235}U and to specify the extent and direction of the fractionation. As uranium concentrations in the low salinity zone of the Amazon River estuary are particularly low at <0.1 ppb, large quantities of water would have to be utilized to achieve the resolution needed.

The uranium concentrations behave non-conservatively in the Amazon River estuary, meaning that they differ from the ideal mixing line between riverine and oceanic water. In fact, all uranium concentrations observed plot above the modeled mixing line and thus have lower uranium concentrations than would be expected for this environment (see Fig. 3.12a). These findings are in agreement with McKee et al. [1987], Swarzenski et al. [1995, 2004], who also found that the dissolved fraction of uranium only behaves in a conservative manner above salinity values of about 20.

Several samples have slightly lighter $^{238}\text{U}/^{235}\text{U}$ than the average value determined for BSE of 137.795 ± 0.008 . Reasons for this behaviour include the possibility that the uranium $^{238}\text{U}/^{235}\text{U}$ composition fractionated during aggregation and flocculation processes in the low salinity region. Alternatively, the inferred uranium isotopic composition end-members might be variable and thus not be representative of the BSE composition given by the magmatic rock samples, as assumed in the two-component mixing model. Also, Stirling et al. [2007], Hiess et al. [2012] and others proposed that ^{235}U might be preferentially released over ^{238}U during silicate weathering due to slightly weaker bonds in the crystal lattice, explaining the reportedly lighter uranium isotopic composition of seawater in comparison to terrestrial rocks. Consequently, as weathering processes are the primary source of uranium in riverine waters, this mechanism would also cause the $^{238}\text{U}/^{235}\text{U}$ compositions of river waters to be lighter than BSE. A release of uranium from the porewaters of the estuarine sediment during sediment advection is also possible. These porewaters might be isotopically lighter than BSE due to redox processes in the anoxic deeper sediment, reducing uranium.

In conclusion, uranium is removed from the water column at salinities below 20, with the strongest removal taking place in the high turbidity zone. Due to the lack of biological activity in the terrigenous zone, biological uptake cannot be responsible for the removal of uranium from the water column. Also, according to McKee et al. [1987], the redox potentials of estuarine waters are not low enough to reduce U(VI) to U(IV), excluding uranium reduction as a possible mechanism for uranium removal from the water column at these sites. The main reasons for the uranium removal lies therefore in the salt-induced aggregation of colloidal to particulate material and the adsorption of uranium onto these particles. However, this process does not lead to significant, resolvable changes in the

uranium isotopic ratio of ^{238}U and ^{235}U . Although Brennecka et al. [2011b] reports a shift in $^{238}\text{U}/^{235}\text{U}$ of 0.2‰ towards heavier ratios in the groundwaters during the removal of uranium by adsorption onto Mn-oxyhydroxides, these observations might not be relevant to the present study for several reasons: (a) the aggregation in estuaries is very rapid, while the experiment of Brennecka et al. [2011b] was conducted over 48 hours, (b) the redox potentials and other geochemical properties of seawater, riverine water and groundwater can differ from each other, (c) the primary uranium species differs between water masses, for example, uranium in seawater is dominated by uranyl carbonate complexes, while uranium hydroxy complexes become more prominent in groundwater, and (d) estuaries are highly energetic environments, while groundwater aquifers are not effected by tides, currents and/or winds. Adsorption may, however, be responsible for the apparent shift towards a heavier $^{238}\text{U}/^{235}\text{U}$ composition in the single sample with a salinity of 4.

Uranium isotope compositions in the Lena River are constant, giving rise to an average of $^{238}\text{U}/^{235}\text{U} = 137.771$ over the entire salinity range analyzed. The uranium isotopic compositions in the low salinity zone are slightly lighter than expected by the modeled mixing line between riverine and seawater (Fig. 3.12). As discussed above, the river water probably has a lighter $^{238}\text{U}/^{235}\text{U}$ composition than BSE, due to preferential leaching of ^{235}U during silicate and carbonate weathering processes.

The uranium concentrations follow the modeled mixing line defined by riverine and Arctic Ocean water, indicating that uranium displays conservative behaviour throughout the mixing process. This is especially interesting as Fe reportedly shows non-conservative behaviour in the Lena River estuary and is removed rapidly in the lower salinity zone, presumably caused by salt-induced coagulation of riverine colloids and precipitation of hydrated oxides [Martin et al., 1993, Guieu et al., 1996]. These mechanisms are identical to those responsible for the uranium removal in the Amazon River estuary. This indicates that uranium adsorption onto Fe-oxyhydroxides is not the primary mechanism for uranium removal in the Lena River estuary.

It is well established that uranium is associated with riverine colloids [Swarzenski et al., 1995, Porcelli et al., 1997, Andersson et al., 2001], but the colloidal fraction of uranium in the Lena River water is unknown. It can, however, be assumed that this fraction is equally high in the Lena River as in the Amazon River water, as both rivers are high in TSM and DOC. The DOC load in the Lena River has a reportedly high colloidal fraction (e.g. >55% in the river delta in September 1991 [Cauwet and Sidorov, 1996]) and the DOC concentrations behave conservatively throughout the mixing zone [Dittmar and Kattner, 2003], consistent with the uranium behaviour. The nature of the uranium-bearing colloids is of high importance, as colloids including humic substances do not necessarily aggreg-

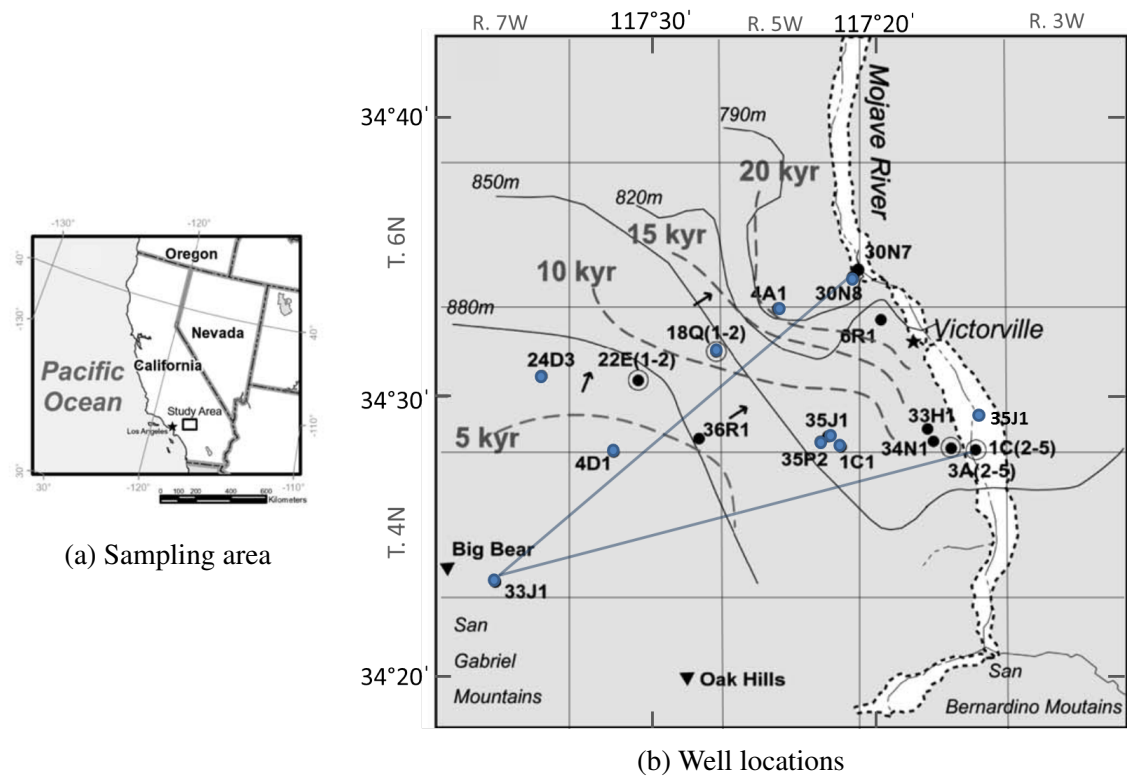


Figure 3.13: Location of the Mojave River Basin. a) Regional map including the study area. b) Location of the sampled boreholes (this study: blue dots). The direction of groundwater flow is indicated by black arrows, the blue lines show the northern and southern flowpaths. Dotted lines represent ^{14}C ages and solid lines show the piezometric surface contours. After Kulongoski et al. [2003].

ate as easily during the mixing process of riverine and seawater as colloids composed of Fe-oxyhydroxides [Andersson et al., 2001]. It is therefore possible that the uranium in the analyzed samples is associated with organic colloids such as humic substances, which might not aggregate to large enough particles to precipitate and are consequently not removed from the water column. Alternatively, it is also possible that some uranium removal occurs from the water column closer to the river in a region of very low salinity, as the first sampled water has a salinity of 2.7 and is therefore slightly brackish. However, this behaviour is not considered likely, as the zone with the highest turbidity and therefore highest coagulation rate is generally in the salinity zone of 4-8.

3.4 Aquifer: Mojave Desert

All samples were taken from boreholes along an aquifer flowing through alluvial deposits. These deposits can have several sources, the main source being sediments that eroded by weathering in mountain areas and are then redeposited in the surrounding plains. Other

sources of alluvium are sedimentary deposits of rivers and lakes. Rivers deposit, resuspend, and redeposit sediments wherever they flow, but when a river changes its flowpath the detached section dries out and deposits all of its load. These alluvial deposits are often used to track the previous flowpaths of rivers.

The study area of the Mojave River Basin is located in the Mojave Desert of southern California, about 130 km northeast of Los Angeles (Fig. 3.13a). The 3626 km² large basin stretches from the San Bernardino and San Gabriel Mountains in the south and southwest to the Mojave River in the east. The basin slopes gently to the north and east, with smaller basins separated from each other by hills, low mountains and geological faults. As the area is semi-arid, with low precipitation (<150 mm/year), low humidity and high summer temperatures, the main recharge occurs from the Mojave River during sporadic stormflows [Stamos et al., 2001].

The aquifer system consists of unconsolidated⁹ and moderately consolidated alluvial deposits of gravel, sand, silt and clay. The aquifer's two flowpaths of this study (Fig. 3.13b) are mainly filled with undifferentiated¹⁰ alluvium. However, a lens of older alluvium (Pliocene to Pleistocene, 5.332-0.0117 million years old) from the ancestral Mojave River surrounds the present-day riverbed of the southern flowpath (stretching westwards to borehole number 5N/5W-35J1). A far smaller lens of younger alluvium (Pleistocene to Holocene, 2.588 million years to present) is located directly around the present riverbed [Kulongoski et al., 2003]. The latter two alluvial deposits build the so-called floodplain, while the undifferentiated alluvium is known as the regional aquifer. The basin is situated above a bedrock of igneous and metamorphic rocks.

Sampling for the present study took place from 18.-20. January, 2005, lead by Dr. J. Kulongoski (USGS, USA), Dr. D. Hilton (Scripps Institution of Oceanography, USA) and Dr. D. Porcelli (University of Oxford, UK).

3.4.1 Results and discussion

The uranium isotopic compositions and concentration data for the Mojave aquifer samples are presented in Fig. 3.14 and Table 3.5.

The residence time of uranium in the Mojave aquifer is only ~10 years [D. Porcelli, personal communication]. Accordingly, the uranium concentrations and ²³⁸U/²³⁵U isotope compositions reflect very recent processes within the aquifer and not long-term processing according to their age. ¹⁴C, which is used for carbon dating in this aquifer, only forms in the atmosphere during interactions of nitrogen and cosmic rays. This implies that carbon has a by far longer residence time in this groundwater aquifer than uranium. This is prob-

⁹Unconsolidated means that the sediments are loose in contrary to cemented sedimentary rocks.

¹⁰Undifferentiated meaning unmodified, undisturbed throughout time.

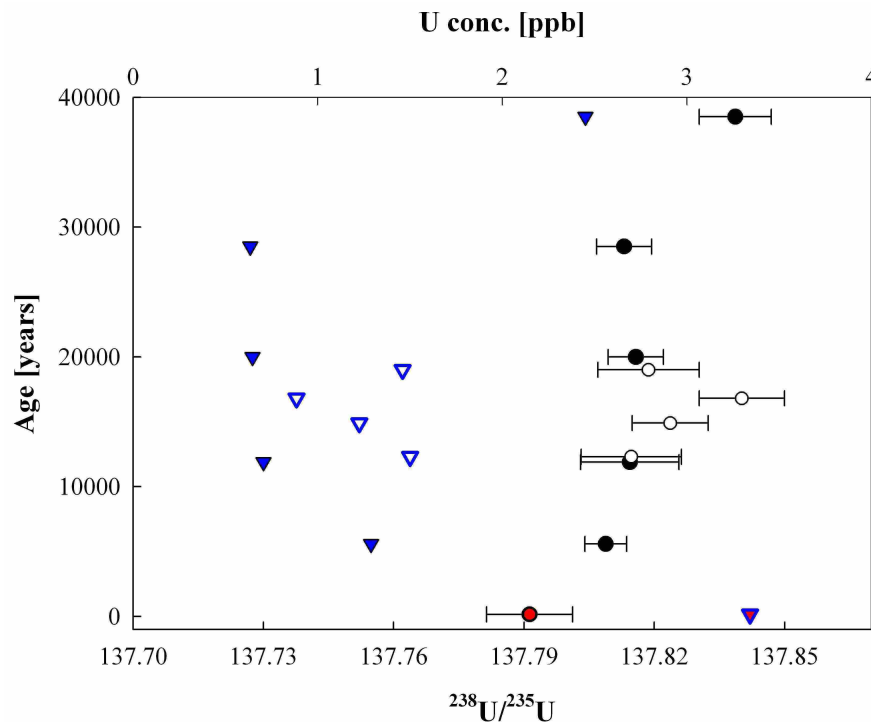


Figure 3.14: Mojave Desert: Uranium isotope ratios (black circles) and uranium concentrations (blue triangles) according to their ^{14}C -age (ages from Kulongoski et al. [2003]). Data points of the northern flowpath of the aquifer are plotted as filled symbols, data from the southern flowpath as open symbols and the starting points of both flowpaths are the red symbols.

ably due to a lower rate of interaction between the sediment and dissolved carbon in the groundwater.

The isotopic ratio of the youngest sample of 150 years of age ($^{238}\text{U}/^{235}\text{U} = 137.791 \pm 0.010$, Table 3.5) is identical, within the uncertainties, to the average of the magmatic material used as the BSE value of 137.795 ± 0.008 (see Chapter 3.1), and river waters published by Stirling et al. [2007]. It can therefore be assumed that this sample has not undergone significant geochemical processing since its formation.

The samples of the northern flowpath (Fig. 3.14) show a slight trend towards heavier isotopic compositions with increasing age but stabilize early on, with samples of 5580 to 28500 years of age being indistinguishable from each other, and give uranium isotopic ratios centered about 137.811 ± 0.008 , marginally heavier than the composition of the 150 year old sample. This shows that the weathering input in this part of the aquifer equals the precipitation output of uranium, and that the weathered material has the same $^{238}\text{U}/^{235}\text{U}$ composition throughout the host sediments. The oldest sample of the northern flowpath, aged 38,500 years, shows a fractionation towards an even heavier isotopic ratio of 137.839 ± 0.008 . The same samples show a massive removal of total uranium with

Table 3.5: Uranium data for two flowpaths of an aquifer in the Mojave Desert

Age [yr]	$^{238}\text{U}/^{235}\text{U}$	2SE	n	U conc. [ppb]	pH	Well No
Northern Flowpath						
150	137.791	0.010	5	3.34	7.3	4N/7W33J1
5580	137.801	0.005	4	1.29	8.0	4N/6W4D1
11880	137.814	0.011	3	0.71	8.4	5N/5W18Q1
19990	137.816	0.006	3	0.65	9.1	5N/7W24D3
28500	137.813	0.006	3	0.64	8.5	5N/5W4A1
38500	137.839	0.008	6	2.45	8.5	6N/4W30N8
Average	137.814	0.012		1.51		
Southern Flowpath						
150	137.791	0.010	5	3.34	7.3	4N/7W33J1
12300	137.815	0.012	4	1.50	8.4	4N/5W1C1
14890	137.824	0.009	4	1.23	-	5N/5W35J1
16800	137.840	0.010	4	0.89	-	5N/5W35P2
19000	137.819	0.012	4	1.46	-	5N/4W35J1
Average	137.818	0.016		1.68		

increasing age from 150 ($U_{conc} = 3.34$ ppb) to 11880 ($U_{conc} = 0.71$ ppb) years of age, when the concentration stabilizes, implying a higher precipitation output than weathering input of uranium at this stage. The oldest sample shows an increase in uranium to 2.45 ppb. Several explanations for this behaviour are possible. For example, a change in the sedimentary composition might release more uranium, consisting of a potentially different $^{238}\text{U}/^{235}\text{U}$ composition, due to an increased weathering rate. An unknown source of replenishment is unlikely as a source for increasing uranium concentration due to the age of this sample. A re-oxidation of reduced uranium in the aquifer can be ruled out as well, as there is no evidence supporting anoxic conditions at any point in the aquifer. A further study including sediment samples of each borehole would be necessary to investigate possible differences in the host sediment of the Mojave aquifer.

The $^{238}\text{U}/^{235}\text{U}$ isotopic ratios of the southern flowpath increase consistently from values for $^{238}\text{U}/^{235}\text{U}$ of 137.791 ± 0.010 at an age of 150 years to 137.840 ± 0.010 at 16,800 years of age. During the same period uranium concentrations gradually decrease from 3.34 ppb to 0.89 ppb. Both isotopic composition and abundance of uranium indicate a constantly slightly higher precipitation output than weathering input of uranium into the aquifer. The only outlier is the apparently oldest sample of this flowpath with an age of

19,000 years and a uranium isotopic composition of $^{238}\text{U}/^{235}\text{U}$ of 137.819 ± 0.012 , which is not resolvable from values for the other samples, and a uranium concentration of 1.46 ppb. This sample is, however, different from the others, as (a) the age is not analyzed but estimated from the regional pattern (shown in Fig. 3.13b) and (b) the sample was taken from a fish hatchery very close to the Mojave River on top of the floodplain (well 5N/4W35J1 in Fig. 3.13b). The fish hatchery uses groundwater as freshwater to circulate through their fishery ponds, with the effluent being discharged onto the floodplain. It is not known if this might lead to a contamination of the sample. Also, the floodplain aquifer is more permeable than the regional aquifer which overlies the aquifer further away from the present riverbed. This, together with the close proximity of the sampling station to the river, might result in a slow water recharge of the groundwater, in which case the age should be adjusted to a younger age. The uranium data alone would suggest that the actual age would be between the data points of 12,300 and 14,890 years. However, no further evidence for this is at hand at the present and the slight deviation in uranium isotopic composition and concentration can also easily be caused by differing mineral assemblages of the host rock or changes in the redox conditions in the aquifer at this location. With the exception of only one sample, namely the oldest sample from the northern flowpath, there is a striking inverse correlation between $^{238}\text{U}/^{235}\text{U}$ isotopic composition and uranium concentration. The samples displaying the lowest $^{238}\text{U}/^{235}\text{U}$ values show the highest uranium concentrations and vice versa.

Nuclide concentrations in groundwater systems are generally influenced by weathering processes, adsorption and aggregation processes. For some nuclides, such as the relatively short-lived ^{234}U with a half-life of 245,000 years, α -recoil can be of importance, but this is not the case for ^{238}U and ^{235}U , which are both tightly bound to the crystal lattice. Weathering of the alluvial material surrounding the water body alone should increase the uranium content with age but instead a clear decrease in uranium concentration is observed along both flowpaths of the Mojave River Basin. Uranium can be adsorbed onto sediment surfaces and particles and colloids in the water column, and this process is considered the primary mechanism for uranium removal in groundwater [e.g. Langmuir, 1978]. Under the neutral and alkaline conditions present in the Mojave aquifer (Table 3.5), uranyl carbonate and phosphate complexes are the predominant species. Uranyl is easily adsorbed onto the surface of minerals. Long-term precipitation of uranium-bearing minerals can irreversibly incorporate uranium into secondary phases during mineralization [Porcelli and Swarzenski, 2003]. The uranium data in this study likely reflect uranium adsorption processes and the preferential uptake of light ^{235}U over the heavier ^{238}U into the solid phase, causing a fractionation of up to 0.35‰ towards heavier uranium iso-

topic ratios in the aqueous phase, following a mass-dependent fractionation pattern. This would be consistent with the findings of Brennecke et al. [2011b], who observed a shift of $\sim 0.2\text{‰}$ towards heavier $^{238}\text{U}/^{235}\text{U}$ in the aqueous phase during uranium adsorption onto Mn-oxyhydroxides in groundwater. However, taking into account the possible preferential release of ^{235}U during weathering processes acting in addition, the reported uranium isotopic fractionation of 0.35‰ towards heavier $^{238}\text{U}/^{235}\text{U}$ in the groundwaters should be considered as a minimum value.

3.5 Conclusions

The uranium behaviour in Framvaren Fjord according to this study can be divided into three main layers of the water column:

- The oxygenated layer: the mixing of different water masses results in increasing salinity and uranium concentrations. The isotopic composition of uranium does not show resolvable differences. Nonetheless, uranium behaviour might be influenced by the scavenging of uranium by inorganic particles such as Fe- and Mn-oxyhydroxides and the appearance of bacteria below a depth of 10 m.
- The redox interface to 40 m depth: the removal of uranium from the water column results in lighter $^{238}\text{U}/^{235}\text{U}$ isotope ratios, following a Rayleigh fractionation model in direction of the nuclear field shift effect and with a fractionation factor of α of 0.9985 between the aqueous and solid phases. This isotopic fractionation behaviour is consistent with uranium removal within a closed system, as shown for the sulfur isotope system by Mandernack et al. [2003]. This indicates that the removal of uranium by sulfate reducing bacteria is the major mechanism controlling uranium behaviour in this part of the fjord. This provides more definitive support for the conclusion of McKee and Todd [1993] and Swarzenski et al. [1999], who speculated that uranium might be scavenged by dissolved organic carbon produced by microbes around the redox interface as well as being coupled to the Mn- and Fe-redox cycle.
- The deep layer below 40 m and the bottom layer: uranium concentrations increase to the previous maximum while the uranium isotopic ratios show no resolvable deviations. The increase in concentration can be explained by the subsequent release of uranium from bacteria or particles. The constantly low uranium isotope ratio might be explained by the presence of different pools of uranium in the solid phase and the subsequent release of uranium with depleted isotopic compositions back into the water column. This is in agreement with the overall depleted nature of

uranium in the fjord. Theoretically, at a salinity of 23, the water should contain ~2.2 ppb U, assuming a conservative mixing of freshwater and seawater. However, the Framvaren Fjord shows a maximum abundance of ~1.7 ppb U. Therefore, approximately 20% of the total U is removed from the water column. The different pools removing U from the water column could be different types of organic complexes, inorganic colloids, or alternatively different pools within microbes. For example, isotopically light uranium that has been adsorbed onto the cell walls of microbes might be released, while isotopically heavy assimilated uranium is mineralized and sinks to the bottom of the fjord. The systematically light uranium isotope ratios acquired throughout the water column might be reflected in the sediment, and in the underlying shales formed by cementation. If this is the case uranium isotopic compositions could be used as an indicator for oxygen depletion in the sedimentary rocks of Framvaren Fjord. This would also suggest that these sedimentary records could be a useful tool to research the extent of Oceanic Anoxic Events. However, an expanded study investigating the uranium behaviour in the bottom sediments of Framvaren Fjord would be necessary to confirm this hypothesis.

Both uranium concentration and uranium $^{238}\text{U}/^{235}\text{U}$ composition in the Peruvian OMZ are constant. This suggests that the biogeochemical behaviour of uranium is not affected by the complex nitrogen cycle or redox processes present in the OMZ. Data from the Framvaren Fjord and the OMZ together suggest that uranium fractionation of ^{238}U and ^{235}U only occurs under anoxic conditions, when other electron acceptors such as nitrate and nitrite are fully utilized and only sulfate reduction, but no reoxidation, is possible.

Uranium also participates in geochemical processes associated with the mixing of water masses. In estuarine environments it can behave conservatively or non-conservatively, but neither behaviour appears to fractionate ^{238}U and ^{235}U in a significant manner and both the Amazon River and the Lena River estuaries investigated in this study show very similar average $^{238}\text{U}/^{235}\text{U}$ compositions of 137.769 ± 0.015 and 137.771 ± 0.003 , respectively. However, second order uranium isotopic fractionation might occur in the non-conservative Amazon River estuary due to aggregation and flocculation processes. The analytical uncertainties associated with the measurements of the low salinity samples of the Amazon estuary were comparatively large and limited by very small sample sizes due to extremely low uranium concentrations in the water samples. Therefore it might be possible to investigate this non-conservative uranium profile with higher resolution using more accurate measurements, which can be achieved by using larger sample sizes. This could potentially lead to resolvable changes in the uranium isotopic composition. Also, a further investigation of riverine waters is necessary to confirm the influences of silicate

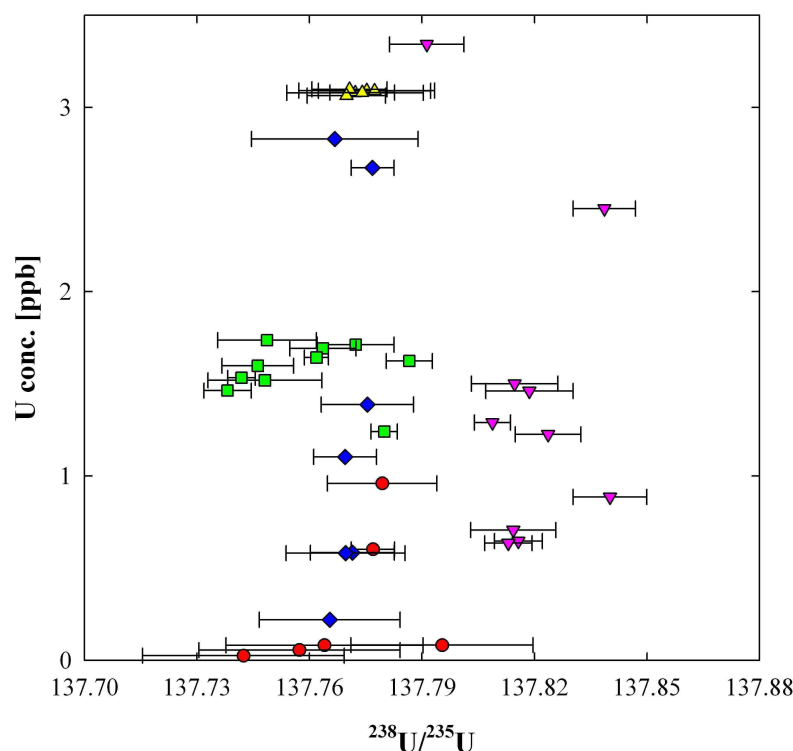


Figure 3.15: A summary of all water samples analyzed in this study, Framvaren Fjord (green squares), Oxygen Minimum Zone offshore from Peru (yellow upwards triangles), Amazon River estuary (red dots), Lena River estuary (blue diamonds) and Mojave River Basin aquifer (pink downwards triangles).

and carbonate weathering on the $^{238}\text{U}/^{235}\text{U}$ isotopic composition and the deviation of this composition from the assumed BSE isotopic composition.

The uranium isotopic composition in the Mojave aquifer is primarily influenced by adsorption processes, preferentially removing the heavier ^{238}U isotope over the lighter ^{235}U isotope from the water column. This behaviour is consistent with a mass-dependent fractionation caused by vibrational differences in the molecular bonds of ^{238}U and ^{235}U . As uranium concentration mirrors $^{238}\text{U}/^{235}\text{U}$ isotopic compositions a kinetic effect depending on the reaction rate of adsorption and amount of desorption is most likely.

Fig. 3.15 shows that all riverine and seawater (and the mixtures thereof) plot around the same value, the average being 137.768^{11} for the four systems studied (Framvaren Fjord, OMZ, Amazon River and Lena River). Only the groundwater samples of the Mojave

¹¹averaged from $^{238}\text{U}/^{235}\text{U} = 137.759$ (Framvaren Fjord), 137.771 (OMZ), 137.769 (Amazon) and 137.771 (Lena).

River Basin aquifer show a far heavier isotopic ratio averaging around 137.818.

In comparison with the data summarized by Hiess et al. [2012] (see Fig. 1.11), the average uranium ratios of all surface water samples are in compliance with published seawater uranium isotope ratios ($^{238}\text{U}/^{235}\text{U} = 137.768 \pm 0.015$ by Stirling et al. [2007] and Weyer et al. [2008]), but are isotopically lighter than the limited river water data available to date ($^{238}\text{U}/^{235}\text{U} = 137.798 \pm 0.005$ by Stirling et al. [2007]). As before, all data used for comparison is in accordance to the CRM112a reference value of $^{238}\text{U}/^{235}\text{U} = 137.829 \pm 0.022$.

The average uranium isotopic composition of the aquifer samples of $^{238}\text{U}/^{235}\text{U} = 137.818 \pm 0.016$ is similar to the values Hiess et al. [2012] reports for a suite of zircons, high-temperature redox ores and shales. Of these three rock types only shales are formed in a low-temperature environment. These sedimentary rocks are mainly composed of clay minerals, quartz, and calcite, formed by the compaction of sediments (e.g. alluvial deposits). This would be mineralogically analogous to the host rock of the Mojave River Basin aquifer.

Chapter 4

Results II: Angrites

4.1 Introduction

The small meteorite group of the angrites currently consists of 20 known specimens. They are planetary achondrites, probably originating from the same differentiated asteroidal body referred to as the angrite parent body (APB). Angrites are depleted in moderately volatile elements. They formed as partial melts from a primitive source material which cooled rapidly, explaining their igneous textures [Mittlefehldt et al., 2002]. They lack evidence for brecciation, metamorphism, and shock effects, which makes them some of the best preserved materials formed in the early stages of the solar system [Mittlefehldt et al., 2002, Weiss et al., 2008]. Angrites have unusual mineral assemblages compared with other meteorites, consisting mainly of Ca-Al-Ti-rich pyroxene, Ca-rich olivine, including kirschsteinite, and anorthite [Kurat et al., 2004]. The mineral phases of the angrites are out of equilibrium due to the rapid cooling of these rocks [Kurat et al., 2002]. They are enriched in refractory minerals [Floss et al., 2003] and have strong textural, mineralogical, and chemical similarities to CAIs [Kurat et al., 2004].

The group of angrite meteorites are divided into either two or, more recently, three subgroups: the coarser grained ‘plutonic’ angrites, as Angra dos Reis, the finer grained ‘quenched’ angrites, including D’Orbigny, and a third possible group of metaclastic angrites currently only consisting of the paired meteorites Northwest Africa (NWA) 2999 and Northwest Africa 4931. The differences between these subgroups show that the angrites originate from different melting events of the APB, but the mineral assemblages provide evidence that their melting and crystallization paths were similar. However, the metaclastic angrite NWA 2999 is interpreted to contain a few percent of chondritic material [Gellissen et al., 2007]. The different mineral sizes prove that the plutonic angrites cooled less rapidly than the quenched angrites. Although this implies that the quenched angrites are primary candidates to study different nuclide chronometers, as the closure

time for all isotopic systems should have been similar, it does not rule out the plutonic angrites from age comparisons.

Determining precise absolute ages for angrites leads to a better understanding of the accretion of the APB and the melting and differentiation processes that followed [Markowski et al., 2007, Kleine et al., 2012]. Several different chronometers can be used to define the timescale of early solar system events, but absolute dating with the high resolution needed is only possible with the long-lived Pb-Pb chronometer, which is the only nuclide system that gives absolute ages for events that occurred as far in the past as the formation of the solar system. The basis for this chronometer is the paired decay of ^{238}U to ^{206}Pb and ^{235}U to ^{207}Pb , with half-lives of ~ 4.5 billion years and ~ 0.7 billion years, respectively. Pb-Pb ages therefore form the cornerstone of all now extinct short-lived nuclide chronometers used, such as the ^{26}Al - ^{26}Mg , ^{53}Mn - ^{53}Cr and ^{182}Hf - ^{182}W isotopic systems with half-lives of only approximately 0.7, 3.7 and 8.9 million years, respectively.

The Pb-Pb ages of CAIs and angrites, both representing some of the oldest solids in the solar system, are commonly used as anchors for the relative chronometers mentioned above and for the intercalibration between them. In recent years reports of differences of several million years between early solar system events determined using the absolute and the relative chronometers have increased [Markowski et al., 2007, Connelly et al., 2008, Jacobsen et al., 2008, Nyquist et al., 2009], revealing a small but well resolved inconsistency of 1-1.5 Myr between the timescales of the formation of the solar system out of the nebular disc of the protosun.

Here we show how the direct measurement of their $^{238}\text{U}/^{235}\text{U}$ composition changes the accepted Pb-Pb ages of the angrites [Amelin, 2008b,a, Connelly et al., 2008, Amelin et al., 2010, Brennecka and Wadhwa, 2012] of 4,558.06 - 4,564.61 Myr by about one million years towards younger values of 4,557.00-4,563.61 Myr, helping to reconcile the reported age differences between the long-lived and short-lived nuclide chronometers [Connelly et al., 2008, Markowski et al., 2007, Nyquist et al., 2009, Jacobsen et al., 2008]. Finding precise and accurate absolute ages for the angrites has become essential with the enhancement of analytical techniques leading to a higher resolution of the early solar system timescales and an associated growing number of inconsistencies between the different chronometers. A better understanding of the accretion of the APB and the processes that followed are crucial for developing a consistent timescale of events in the early solar system. The degree of consistency of the timescale also has a direct impact on whether short-lived radionuclides like ^{26}Al were homogeneously distributed in the nebular disc or not, as a heterogeneous distribution of nuclides would cause a mismatch between the calculated ages for different early solar system events.

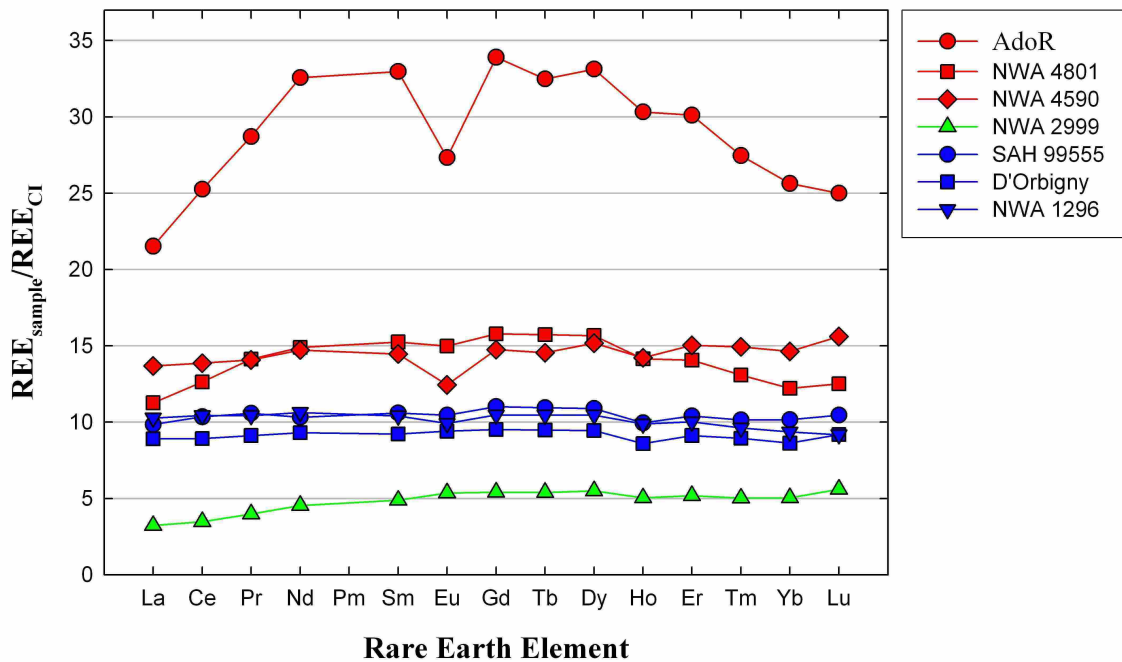


Figure 4.1: Rare Earth Element (REE) data for the different groups of angrites, normalized to CI values [Barrat et al., 2012]. Red lines represent the plutonic angrites, blue lines the quenched angrites and the green line represents the metaclastic angrite NWA 2999.

4.2 Results and discussion

A total of seven angrites were analyzed during this study: the quenched angrites D'Orbigny, Sahara (SAH) 99555 and Northwest Africa (NWA) 1296, the plutonic angrites NWA 4590, NWA 4801 and Angra dos Reis (AdoR) and the metaclastic angrite NWA 2999. These angrites were analyzed for their REE compositions, their uranium concentrations, and their $^{238}\text{U}/^{235}\text{U}$ ratios, as described in Chapter 2.

4.2.1 Rare Earth Elements

The REE data for bulk rock samples of the angrites characterize the three different angrite subgroups as well as the atypical mineralogical assemblage of AdoR. All of the reported data have been normalized relative to the abundances in CI chondrites, representing the approximate solar system composition, after Barrat et al. [2012] (Fig. 4.1, for the complete data set of REE composition in meteorites please refer to Appendix C). Consequently, a normalized REE ratio of one would be consistent with the CI carbonaceous chondrite group. Fig. 4.1 clearly shows that NWA 2999 (green line) with a

$\text{REE}_{\text{sample}}/\text{REE}_{\text{CI}}$ ratio of ~ 5 is closest to the solar value, followed by the quenched angrites (blue lines) with a ratio of ~ 10 and the plutonic angrites (red lines) with ratios of ~ 15 . AdoR clearly stands out with a negative europium anomaly and REE abundances that reflect the unusually high abundances of clinopyroxene in this meteorite. The REE abundance patterns of angrites are a reflection of their mineral phases. For example, the phosphate minerals contain very high REE abundances in percentage levels, reflected by enrichments in light REEs of up to several thousand times of the CI value in merrillite [Floss et al., 2003]. The coexisting apatite contains REE concentrations that are about a magnitude lower [Jolliff et al., 1993]. Clinopyroxenes show a light REE depletion [e.g. Sanborn and Wadhwa, 2010, and references therein].

These data indicate that at least AdoR must have formed during a different magmatic event than the other angrites in this study. With the exception of AdoR the members of the three subgroups most likely originate from partial melts followed by fractional crystallization of either the same, or identical or similar magmas and were formed at the same differentiation stage of the APB. AdoR, however, seems to have formed from a magma source with a different composition.

The declining $\text{REE}_{\text{sample}}/\text{REE}_{\text{CI}}$ ratios shown by the plutonic angrites to the quenched angrites and then to the metaclastic angrite NWA 2999 represent the different depletion stages of the refractory elements of their parent magma. The plutonic, slower cooled angrites probably crystallized in a deeper layer of the APB, while the quenched angrites crystallized at or near the surface of the APB. The generally flat REE patterns of the angrites demonstrate that no significant elemental fractionation occurred between the light, most incompatible (La, Ce, Pr) to the heavy, more compatible (Tm, Yb, Lu) REEs during the crystallization from the parent magma. The observation that the plutonic angrites show subtle variation in their REE patterns can either be caused by a slight depletion of light and heavy REEs during crystallization or alternatively it is possible that the sample sizes of < 20 mg of these coarser grained meteorites might not have been large enough to obtain a completely homogeneous sample, representative of the bulk meteorite. AdoR shows a high depletion in the light and the heavy REEs, indicating a different source region of its parent magma and a chemically heterogeneous mantle of the APB. It is, however, possible that AdoR could originate from a different parent body than the other angrites. Studies of oxygen and strontium isotopic compositions show strong similarities between all angrites, making this theory less likely to be true [Keil, 2012, and references therein].

4.2.2 Uranium data

Uranium isotopic composition and concentration data were analyzed using MC-ICPMS. The $^{238}\text{U}/^{235}\text{U}$ ratios range from 137.759 ± 0.038 to 137.802 ± 0.031 but are all within uncertainty of the average ratio of all angrite samples of 137.783 ± 0.011 (see Table 4.1). The uranium isotopic data is consistent within and between the subgroups of the angrites, including the compositionally unusual AdoR. This implies that no uranium isotopic fractionation took place between or during the different magmatic events during which the angrites formed, or during their crystallization process. The average $^{238}\text{U}/^{235}\text{U}$ ratio of the angrites is also within uncertainty of the BSE average of 137.795 ± 0.008 (see Chapter 3.1), showing the similarity between the differentiated APB and the (also differentiated) Earth. Neither the uranium data nor the REE data discussed above show any influence of weathering processes or terrestrial contamination, although only AdoR is considered a 'fall'¹ while all other angrites analyzed in this study are 'finds'².

The average uranium isotopic composition of $^{238}\text{U}/^{235}\text{U} = 137.783 \pm 0.029$ is 0.7‰ lower than the previously assumed constant ratio of 137.88. Adopting the individually analyzed $^{238}\text{U}/^{235}\text{U}$ compositions of the angrites of this study leads to age corrections of previously published Pb-Pb ages of -0.82 Myr for D'Orbigny to -1.28 Myr for NWA 4801. The revised angrite Pb-Pb ages are therefore an average of 1.02 Myr younger than previously assumed.

It should be noted that the errors on revised Pb-Pb ages in Table 4.1 are represented in two ways. The first uncertainties are the propagated errors of the uranium isotopic measurements only and the second errors, in brackets, contribute from the uncertainties of the published Pb-Pb ages and the uranium isotope measurements. Uncertainties on uranium and lead half-lives and the error on the uranium metal standard of 137.840 were not propagated through the calculations.

The revised Pb-Pb ages do not change the clear distinction shown between the three angrite subgroups, ranging from 4556.68 ± 0.22 , 4556.78 ± 0.22 and 4557.38 ± 0.31 Myr for the plutonic angrites, 4560.82 ± 0.25 Myr for the metaclastic angrite, and an average of 4563.42 ± 0.38 Myr for the quenched angrites. This trend reflects the timing of crystallization of the angrites from their parent magmas. The quenched angrites are the oldest and most rapid cooled angrites and the plutonic angrites are the youngest angrites and cooled slightly less rapidly. The metaclastic angrite NWA 2999 is different from the other angrites, as it has undergone thermal metamorphism, causing its age to reflect the time of the last metamorphism rather than the formation age.

¹'Fall' meteorites are defined as meteorites which were seen falling through the Earth's atmosphere and were collected shortly after. This implies that they were least exposed to the elements.

²'Find' meteorites were exposed to the elements for an unknown time before they were found and preserved. They might show more effects of terrestrial contamination and weathering than 'falls'.

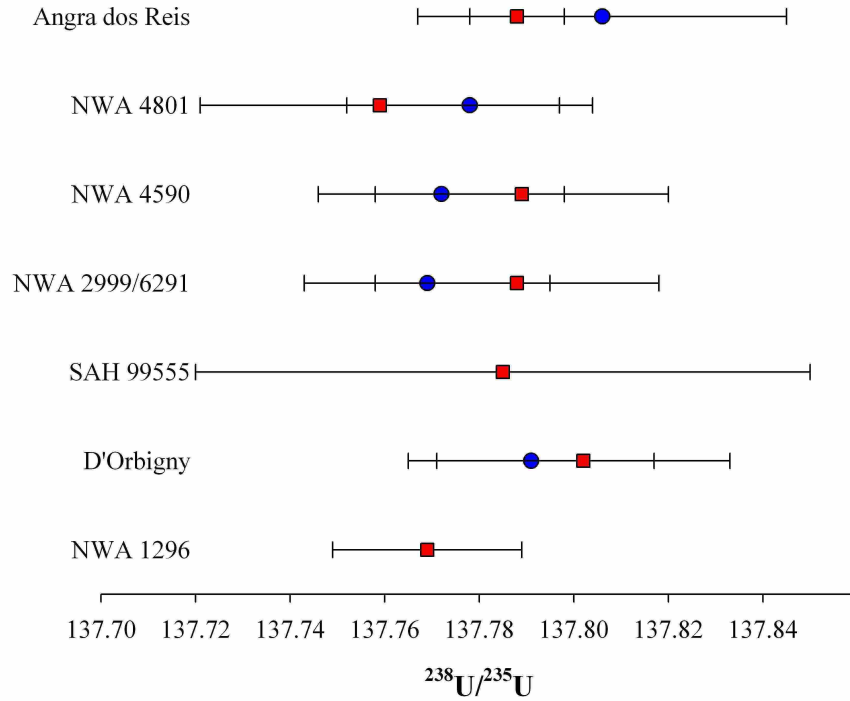


Figure 4.2: Comparison of uranium isotopic data of this study (red squares) and values reported by Brennecka and Wadhwa [2012] (blue circles).

As can be seen in Fig. 4.2 the uranium isotopic data of this study is in excellent agreement with recently published $^{238}\text{U}/^{235}\text{U}$ values by Brennecka and Wadhwa [2012]. This confirms the validity of methods utilized in both studies and allow a comparison between the two independent laboratories.

4.2.3 Implications for the timeline of the early solar system

As mentioned above, the ages of the quenched angrites and CAIs obtained from the long-lived Pb-Pb chronometer are commonly used as absolute anchors for the extinct short-lived nuclide chronometers. This is due to their short cooling period relative to the half-lives of the isotopes commonly used for chronometry, as it is a reasonable assumption that none of these isotope systems were disturbed before the time of closure. This makes angrites and CAIs crucial for the intercalibration between chronometers. A revision of the Pb-Pb ages of these anchors is therefore expected to have a significant impact on all other chronometers. Figure 4.3 shows the age differences between previously published literature values for the Pb-Pb ages of angrites (see Table 4.1) assuming a constant $^{238}\text{U}/^{235}\text{U}$ ratio of 137.88, and the newly calculated Pb-Pb ages of this study as well as

Table 4.1: Age differences of angrites after adjusting the $^{238}\text{U}/^{235}\text{U}$ ratios from 137.88 to the data of this study. Uncertainties on the newly calculated Pb-Pb ages are errors of the $^{238}\text{U}/^{235}\text{U}$ measurements only, or, in brackets, of the uranium isotopic measurements and the published Pb-Pb ages.

Angrite	find/ FALL	Uranium conc. [ppb]	Pb-Pb age [Myr] $^{238}\text{U}/^{235}\text{U} = 137.88$	Measured $^{238}\text{U}/^{235}\text{U}$	2SE $^{238}\text{U}/^{235}\text{U}$	n	New Pb-Pb age [Myr]	Δt
Angra dos Reis	FALL	197	4557.65 ± 0.13^a	137.788	± 0.010	3	$4556.68 \pm 0.22 (\pm 0.35)$	-0.97
NWA 4801	find	93	4558.06 ± 0.16^b	137.759	± 0.038	2	$4556.78 \pm 0.22 (\pm 0.38)$	-1.28
NWA 4590	find	210	4558.34 ± 0.07	137.789	± 0.031	2	$4557.38^c \pm 0.31 (\pm 0.38)$	-0.96
NWA 2999	find	114	4561.79 ± 0.42^d	137.788	± 0.030	3	$4560.82 \pm 0.25 (\pm 0.67)$	-0.97
SAH 99555	find	103	4564.61 ± 0.13^e	137.785	± 0.065	1	$4563.61 \pm 0.52 (\pm 0.65)$	-1.00
D'Orbigny	find	71	4564.42 ± 0.12^f	137.802	± 0.031	1	$4563.60 \pm 0.32 (\pm 0.44)$	-0.82
NWA 1296	find	67	4564.20 ± 0.45^g	137.769	± 0.020	1	$4563.04 \pm 0.26 (\pm 0.71)$	-1.17
Average		122	4561.30	137.783 ± 0.011			4560.27	-1.02 ± 0.03

^aAmelin [2008b]^bAmelin and Irving [2007]^cAmelin et al. [2010]^dAmelin and Irving [2007]^eAmelin [2008a], Connelly et al. [2008]^fAmelin [2008b]^gAmelin and Irving [2011]

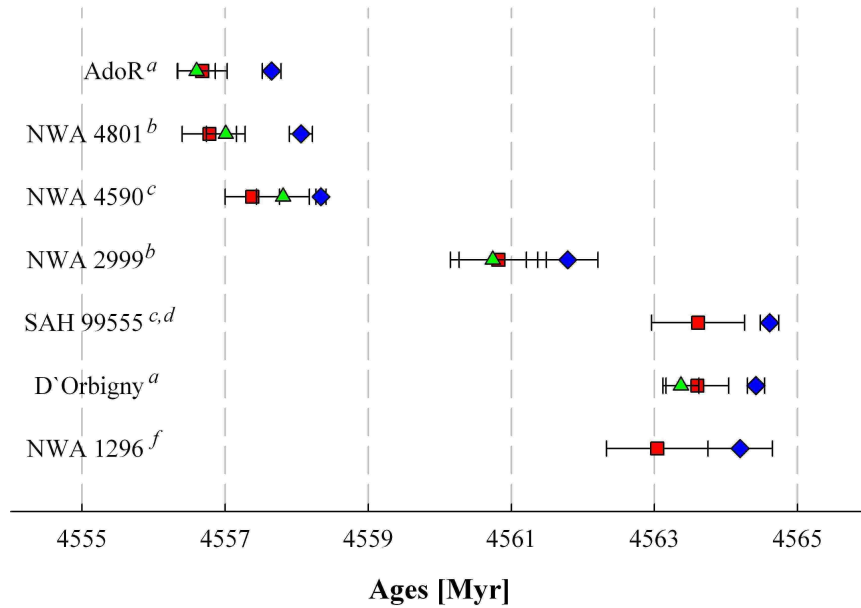


Figure 4.3: Comparison of Pb-Pb ages of angrites. Red squares are data from this study, green triangles represent data from Brennecka and Wadhwa [2012] and the blue diamonds represent literature data (^aAmelin [2008b], ^bAmelin and Irving [2007], ^cAmelin et al. [2010], ^dAmelin [2008a], ^eConnelly et al. [2008], ^fAmelin and Irving [2011])

new ages published by Brennecka and Wadhwa [2012], the latter using a reference value of the standard SRM950a of $^{238}\text{U}/^{235}\text{U} = 137.837 \pm 0.015$. Both revised ages have been re-calculated utilizing their individually analyzed uranium isotopic ratios. A difference between the previously published and the newly revised Pb-Pb ages of about one million years can clearly be seen, with the new ages being systematically younger than the previously published ages. It is again obvious that both of the newly revised data sets are within uncertainty of each other. This demonstrates the accuracy of the procedures applied for the uranium isotopic analysis at two independent laboratories, as well as the necessity of uranium isotopic analyses for Pb-Pb dating.

The most commonly used short-lived nuclide chronometers are the ^{26}Al - ^{26}Mg , ^{182}Hf - ^{182}W and ^{53}Mn - ^{53}Cr systems, described in detail in Chapter 1.4.

Due to the short half-life of ^{26}Al of ~ 0.7 Myr the ^{26}Al - ^{26}Mg system is a very precise, high-resolution chronometer for the first few million years of the accretion in the early solar system. It is ideally suited to date the oldest solids in the solar system, represented by CAIs and quenched angrites (D'Orbigny, SAH 99555 and NWA 1296 in this study). Recently questions have arisen about the homogeneity of the distribution of ^{26}Al throughout the solar nebula and the validity of assuming a spatially invariant initial ('canonical')

$^{26}\text{Al}/^{27}\text{Al}$ ratio of 5×10^{-5} [e.g. Spivak-Birndorf et al., 2009, Schiller et al., 2010b, Larsen et al., 2011]. If ^{26}Al was indeed heterogeneously distributed in the solar nebula, the ^{26}Al - ^{26}Mg dating method will have to be re-considered as a valid chronometer. In fact, the same case can be made for all relative chronometers, as all of them rely on the correctness of their initial parent-daughter isotope ratios in the solar system. It is especially important for the radionuclides that potentially originate from several nucleosynthetic sources. The exact values for these initial isotope ratios and the homogeneity or heterogeneity of their elemental and isotopic distributions in the presolar disc are therefore one of the most discussed problems in the cosmochemistry research community.

The ^{53}Mn - ^{53}Cr chronometer with a half-life for ^{53}Mn of ~ 3.7 Myr has a wider dating range of about 20 Myr but, in contrast to all other short-lived nuclide systems, cannot be anchored to CAI ages. This is caused by the volatile nature of Mn and Cr resulting in CAIs being highly depleted. Instead, ^{53}Mn - ^{53}Cr data are linked to the Pb-Pb ages of angrites, mainly of Lewis Cliff (LEW) 86010 and AdoR. Although quite similar estimates of the initial $^{53}\text{Mn}/^{55}\text{Mn}$ ratio at the time of isotopic closure still varies from $3.24\text{--}8.5 \times 10^{-6}$ between studies [e.g. Glavin et al., 2004, Trinquier et al., 2008, Scott and Sanders, 2009].

Of the most commonly used short-lived chronometer systems the ^{182}Hf - ^{182}W system has the longest half-life with ~ 8.9 Myr for ^{182}Hf . This isotopic system is especially well suited to determine accretion, differentiation, and core formation processes. This is due to the fact that hafnium and tungsten are both refractory elements and the lithophile, more compatible Hf is mostly incorporated into silicates, while the siderophile W is mainly bound into metal cores, causing large fractionations between these two elements during differentiation processes.

Fig 4.4 shows that the revised Pb-Pb ages of angrites of this study are in excellent agreement with the ages derived using the short-lived relative chronometers, if the latter are anchored to the newly revised the Pb-Pb age for D'Orbigny of 4563.60 Myr of this study. It also shows the improvement between the previously published Pb-Pb ages and those from this study.

Few age constraints are available for angrites utilizing the ^{26}Al - ^{26}Mg chronometer. This chronometer can only be applied to age calculation of quenched angrites, as the other angrites are too young to have contained a sufficient abundance of ^{26}Al at the time of crystallization. Therefore data is limited to values for D'Orbigny and SAH 99555, which are nearly identical. As all short-lived nuclide ages are anchored to D'Orbigny, these data are insufficient to discuss whether Al was homogeneously or heterogeneously distributed in the solar nebula. In contrast, ^{182}Hf - ^{182}W data are available for all angrites analyzed in

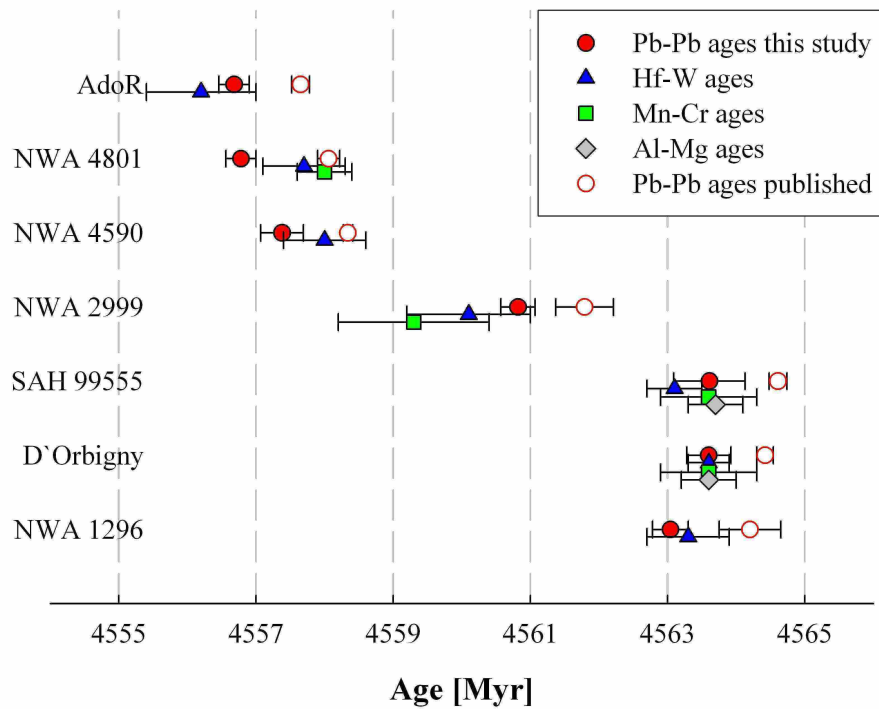


Figure 4.4: Comparison between the absolute Pb-Pb ages and the relative ^{182}Hf - ^{182}W , ^{53}Mn - ^{53}Cr and ^{26}Al - ^{26}Mg ages of angrites. Pb-Pb ages are from this study and previously published (see Table 4.1), while all relative ages are anchored to the Pb-Pb age of D'Orbigny (4563.60 Myr), using data of Kleine et al. [2012] (Hf-W), Sugiura et al. [2005] (D'Orbigny, SAH 99555, Mn-Cr), Shukolyukov and Lugmair [2008] (NWA 4801, Mn-Cr), Shukolyukov et al. [2009] (NWA 2999, Mn-Cr) and Schiller et al. [2010a] (Al-Mg). Uncertainties of Pb-Pb ages of this study represent total errors of uranium isotopic data and published Pb-Pb ages, uncertainties of relative chronometers are published uncertainties and do not take the Pb-Pb age uncertainty of D'Orbigny into account.

this study, showing a very good agreement with the revised Pb-Pb ages.

The ^{53}Mn - ^{53}Cr ages and Pb-Pb ages of this study are in far better agreement than with the previously reported Pb-Pb ages. This is particularly true for the quenched and metaclastic angrites of this study. However, the NWA 4801 ages obtained using the ^{53}Mn - ^{53}Cr short-lived nuclide chronometer are in better accordance with the previously published Pb-Pb age than with the newly re-calculated Pb-Pb age of this study. This might be due to the volatile nature of Mn and Cr, which might have depleted during the prolonged crystallization process of the plutonic angrites in comparison with the metaclastic and quenched angrites. Also, different closure times of the ^{53}Mn - ^{53}Cr and the U-Pb isotopic systems might cause deviations in the calculated ages. The slower the parent magma of a rock cools, the larger these deviations might become. Unfortunately, to date NWA 4801 is the only plutonic angrite with a published ^{53}Mn - ^{53}Cr age. Although a heterogeneous abundance of $^{53}\text{Mn}/^{55}\text{Mn}$ can probably be ruled out between meteorites originating from the

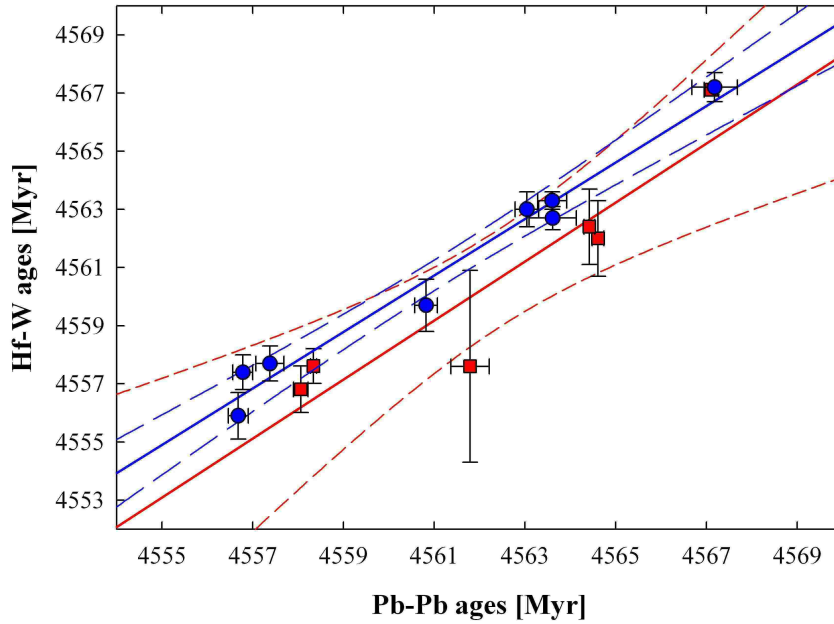


Figure 4.5: Comparison of published (in red) and revised (in blue) ^{182}Hf - ^{182}W and Pb-Pb ages. Published ^{182}Hf - ^{182}W ages are anchored to the CAI Pb-Pb age of 4567.1 ± 0.2 Myr Amelin et al. [2006], revised ^{182}Hf - ^{182}W ages are anchored to the CAI SJ101 (of the CV3 Allende) Pb-Pb age of 4567.2 ± 0.5 Myr from this study. Solid lines are linear regression lines and dashed lines represent the corresponding 95% confidence intervals.

same parent body, the varying initial $^{53}\text{Mn}/^{55}\text{Mn}$ used by different authors might cause shifts in the obtained ^{53}Mn - ^{53}Cr ages. A comparison of revised Pb-Pb ages and ^{53}Mn - ^{53}Cr ages of AdoR, NWA 4590 or other plutonic angrites might give further insight into the solution of this problem.

The ^{182}Hf - ^{182}W and Pb-Pb ages of angrites allow us to compare previously published datasets of these two chronometers and the dataset of this study in more detail. As can be seen in Fig. 4.5, the revised Pb-Pb ages of the angrites and the Allende CAI SJ101 of this study show a much better correlation with the ^{182}Hf - ^{182}W ages for the same samples when the latter are recalculated by anchoring them to the CAI SJ101 Pb-Pb age of 4567.2 ± 0.5 (see Chapter 5.2.2 for discussion), compared to previous data. Literature data comprise the Pb-Pb ages for the angrites as shown in Table 4.1 and the ^{182}Hf - ^{182}W data are from Markowski et al. [2007] and Kleine et al. [2009]. The linear regressions represent coefficients of determination of $R^2 = 0.86$ for the unrevised data, which is dramatically improved to $R^2 = 0.97$ for the revised data. The significant improvement shown by the revised dataset reiterates again the necessity to revise all previously published Pb-Pb ages

according to the true $^{238}\text{U}/^{235}\text{U}$ values, based on absolute measurements of individual samples instead of adopting a constant uranium isotopic composition of 137.88.

4.3 Conclusions

The Hf-W compositions of angrites show that accretion and differentiation of the mantle and the core of the APB had been completed within ~ 2 Myr of CAI formation [Kleine et al., 2012] and before the first angrites formed. The quenched angrites are the oldest angrite group with a revised Pb-Pb age of 4563.42 ± 0.38 Myr. This age gives the oldest possible age for the completion of the APB accretion and the start of the first melting event within the APB. The revised CAI Pb-Pb age of 4567.30 ± 0.16^3 then gives a maximum age difference of 3.88 ± 0.54 Myr between the timing of the CAI formation and the completion of the APB accretion.

The REE data shows that the angrites originate from at least two different magmatic events. These were probably caused by partial melting of the APB mantle followed by fractional crystallization at different depths within the asteroidal parent body. These melting processes could have been caused by the decay of ^{26}Al and other short-lived nuclides acting as a massive heat source [Kleine et al., 2012]. This explanation is plausible due to the above-mentioned early accretion of the APB, whereby the first melting events in the APB occurred in the time interval before the extinction of ^{26}Al and other nowadays extinct short-lived nuclides. However, to date no reasonably constrained quantitative thermal model is available to confirm this hypothesis. The primary reason for this is that the size of the APB is unknown, preventing the calculation of thermal energy that was necessary to produce the partial melts.

Utilizing the absolute $^{238}\text{U}/^{235}\text{U}$ ratios obtained in this study has lead to an adjustment of the Pb-Pb ages of the individual angrite samples to values that are on average about one million years younger than those previously reported. Absolute ages range from 4556.68 ± 0.22 Myr to 4563.61 ± 0.52 Myr. This approach has also been effective in resolving some crucial inconsistencies between the absolute U-Pb chronometer and the short-lived nuclide relative chronometers, leading to a better inter-calibration between these nuclide systems and one step closer to the overall goal of providing a consistent timescale for the events of the early solar system.

The differences in uranium isotopic ratios between the analyzed angrites is not resolvable, giving an average $^{238}\text{U}/^{235}\text{U}$ value of 137.783 ± 0.029 . This raises the possibility of

³This age is based on measurements of the CAI SJ101 extracted from the Allende CV3 chondrite in combination with data reported by Connelly et al. [2012]. The reader is referred to Chapter 5.2.2 for the discussion.

utilizing a single average $^{238}\text{U}/^{235}\text{U}$ ratio for all Pb-Pb age calculations of angrites instead of analyzing every sample individually, although there is no consensus on this issue at the present time. However, it is possible that improvements in the resolution of Pb-Pb ages and uranium isotopic values will result in resolvable deviations.

Chapter 5

Results III: Chondrites and eucrites

5.1 Introduction

Chondrites are the only meteorite group that contains CAIs, the oldest known solids of the solar system. The elemental abundances of chondrites have been derived from the solar nebula [e.g. Rubin, 2005]. As mentioned before the carbonaceous CI-chondrite composition is used as a reference for the normalization of REE abundances, as their elemental composition closely approximates the composition of our bulk solar system [Anders and Grevesse, 1989, Barrat et al., 2012]. Chondrites originate from diverse undifferentiated parent bodies that, although having undergone metamorphism, have never been molten. They therefore have the best preserved chemical evidence for processes that took place during the initial formation and accretion stages of the early solar system. This makes the chondrites the best meteorite group to study the origin of the solar system [Scott and Krot, 2003].

As discussed in Chapter 1.3.1 chondrites are divided into the subgroups of ordinary, carbonaceous and enstatite chondrites, which will be discussed individually in this chapter. Ordinary chondrites are the most common meteorites found on Earth (>80%). They have the highest concentration of chondrules, rarely contain CAIs, and have experienced the widest range of metamorphic conditions of all chondrites [Scott and Krot, 2003]. The primary parameter to distinguish the H, L and LL subgroups are their total and metallic Fe concentrations, and their increasing oxidation states from H-L-LL [e.g. Kallemeyn et al., 1989, Rubin, 2005].

Carbonaceous chondrites are the compositionally most diverse group of chondrites. They consist of a variety of sedimentary rocks and originate from different parent bodies [Scott and Sanders, 2009]. Carbonaceous chondrites contain the highest abundance of CAIs, making them an important geochemical tool for understanding the first chemical and physical processes that occurred during the formation of the solar system and for dat-

ing events in the early solar system [Scott and Krot, 2003, Scott and Sanders, 2009]. Enstatite chondrites were formed under the most reducing conditions of all chondrites [Weeks and Sears, 1985, Kallemeyn and Wasson, 1986]. They can contain high abundances of chondrules but have very low abundances of CAIs [Scott and Krot, 2003]. Some enstatite chondrites have undergone at least partial melting [Krot et al., 2003, and references therein]. All of their elements investigated so far (O, N, Ru, Os, Cr, Ti) have an identical isotopic signature to the Earth's mantle [Javoy et al., 2010, and references therein].

Section 5.3 discusses the uranium isotopic composition and concentration of eucrites. Eucrites form part of the achondrite HED group, probably originating from the same differentiated parent body, most likely the asteroid 4-Vesta [Binzel and Xu, 1993]. Due to the melting processes on their parent body eucrites are igneous rocks and are often brecciated, displaying variable stages of metamorphism caused by impact. Due to the differentiation process of their parent body eucrites show elemental compositions that are highly fractionated with respect to the compositions of the undifferentiated chondrites [Yamaguchi et al., 2009]. They provide insight into the consequences of internal and impact melting of parent bodies and might give evidence for the heat source(s) present in the early solar system [Shukolyukov and Lugmair, 1993]. Some meteorites, for example Ibitira, are mineralogically identical with eucrites but according to the oxygen isotope evidence originate from a different parent body. These meteorites are referred to as 'eucrite-like' meteorites. This subchapter also includes data of the ungrouped achondrite NWA 5400.

5.2 Chondrites

5.2.1 Ordinary chondrites

A total of 21 ordinary chondrites were analyzed for their uranium isotopic composition, uranium concentration and REE content. The ordinary chondrites in the present study comprise nine H-chondrites, eight L-chondrites, and four LL-chondrites. All ordinary chondrites have undergone thermal metamorphism, expressed by their petrological types, ranging from 3-6 [Scott and Krot, 2003]. Type 3 chondrites are commonly referred to as 'unequilibrated', although strictly speaking only the chondrites showing the least secondary processes throughout their lifetime are unequilibrated. Therefore, type 3 chondrites can be further divided on a finer scale, for example 3.05. Type 4-6 chondrites are considered to be 'equilibrated', meaning that the thermal metamorphism in the chondrite parent body reached temperatures in which all minerals are subject to alteration (up to

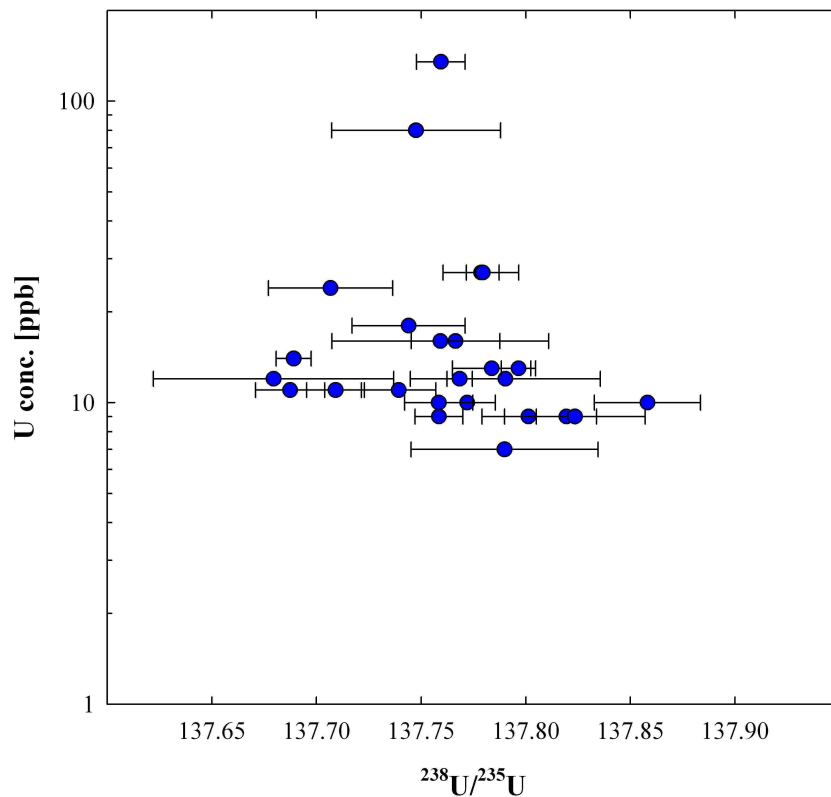


Figure 5.1: Comparison of $^{238}\text{U}/^{235}\text{U}$ values and U concentrations of ordinary chondrites. The dataset includes all subsamples of the present study, but excludes the ‘anomalous’ ordinary chondrites.

1000°C).

The bulk ordinary chondrites of this study show a wide range of uranium concentrations, varying from 9 ppb to 135 ppb, which are not correlated to variations in $^{238}\text{U}/^{235}\text{U}$ (Fig. 5.1). Similar variations in uranium concentration are observed between different subsamples of the same meteorite. For example, the two subsamples of NWA 267 show differences in U concentrations ranging from 24 ppb to 135 ppb, possibly due to varying mineralogical assemblages. The primary reason for this is probably that type 5 and 6 chondrites contain rare but large phosphate grains, containing a higher abundance of U than bulk chondrites. The same subsamples show deviating uranium isotopic compositions of 137.759 ± 0.012 and 137.707 ± 0.030 . This indicates that different samples and subsamples, each characterized by slightly varying abundances of uranium bearing minerals, might also have deviating uranium isotopic compositions due to metamorphic effects. The other chondrites whereby multiple subsamples were analyzed, NWA 869 (a, b), Saratov (a, c) and Krymka (a, b), show similar uranium concentrations and also

identical uranium isotopic compositions.

The majority of $^{238}\text{U}/^{235}\text{U}$ values of the ordinary chondrites vary around an average value of 137.763 ± 0.005 (2SE) (Table 5.1 and Fig. 5.2). This is slightly lower than the composition of BSE of 137.795 ± 0.008 reported here, and the average chondritic ratio previously reported by Stirling et al. [2005] of 137.799 ± 0.013 (2SE), after recalculation of the latter data to the notation used here. However, several samples in the present study have uranium isotopic ratios that deviate greatly from this average towards both heavier and lighter compositions. This anomalous group constitutes the ordinary chondrites Orlovka (H5), Estacado, Mount Browne (both H6 chondrites) and two out of the three subsamples of Saratov (L4), with $^{238}\text{U}/^{235}\text{U}$ values of 142.417 ± 0.006 , 135.354 ± 0.006 , 137.523 ± 0.006 and 138.607 ± 0.026 , respectively. These unusual samples, showing deviations of up to 3.4% away from the average chondritic value, will be discussed later in the text. The following discussion focuses on the majority of the ordinary chondrite samples displaying 'normal' uranium isotopic compositions.

As can be seen in Fig. 5.2, most of the ordinary chondrites have $^{238}\text{U}/^{235}\text{U}$ compositions that are identical within the 2SE error limits of their average composition. However, several chondrites have values that deviate outside of their uncertainties. These are Kunashak (H5), QUE 90218.4 (L5), Krymka (LL3.1) and EET 85744.4 (LL4). Slight differences in the uranium isotopic compositions of ordinary chondrites can potentially be explained by secondary uranium 'stable' isotope effects. These are caused by the influence of different metamorphic processes on this chondrite group, like redox processes and thermal metamorphism, which are possibly able to change the isotopic compositions between minerals. A terrestrial contamination can be eliminated as cause for these fractionations, as Kunashak and Krymka are considered 'falls', while QUE 90218.4 and EET 85744.4 were found in the cold desert of Antarctica.

The isotopic composition of ordinary chondrites in this study ranges over $\sim 0.8\%$, in agreement with reported $^{238}\text{U}/^{235}\text{U}$ variations in high-temperature and low-temperature environments. Hiess et al. [2012] reports ranges of uranium isotopic composition in a suite of uranium-bearing accessory minerals of 5.4% , and in zircons of $\sim 1\%$. However, one of the zircons shows an extreme variation of 0.34% from the $^{238}\text{U}/^{235}\text{U}$ zircon uranium isotopic average. This study, Bopp et al. [2009], Brennecka et al. [2011b] and Murphy et al. [2012] report $^{238}\text{U}/^{235}\text{U}$ compositions spanning $0.1\text{-}0.5\%$ in low-temperature environments.

Considering the different chondrite classes in more detail, the $^{238}\text{U}/^{235}\text{U}$ compositions of the three different ordinary chondrite groups range from 137.772 ± 0.026 (H chondrites, $n=6$), 137.761 ± 0.017 (L chondrites, $n=9$) and 137.751 ± 0.065 (LL chondrites, $n=3$).

Table 5.1: Uranium isotope and concentration data for bulk samples of 21 ordinary chondrites. Averages are weighted depending on ng U used per analysis (reflected in intensity and length of analysis). Subsamples of the same meteorite are marked as sample name + a, b, c, averages of which are weighted over all single measurements of the subsamples.

Sample	Type	find/FALL	$^{238}\text{U}/^{235}\text{U}$	2SE	n	U conc. [ppb]
Tulia(a)	H3-4	find	137.766	0.021	2	16
NWA 267 a	H4	find	137.759	0.012	3	135
NWA 267 b	H4	find	137.707	0.030	1	24
NWA 267 av.	H4	<i>find</i>	<i>137.752</i>	<i>0.037</i>	4	
Kunashak	H5	FALL	137.819	0.014	3	80
Orlovka	H5	find	142.417	0.006	2	20
Richardton	H5	FALL	137.748	0.040	1	9
Estacado	H6	find	135.354	0.006	2	50
Great Bend	H6	find	137.801	0.022	1	19
Kidairat	H6	FALL	137.744	0.027	1	9
Mount Browne	H6	FALL	137.523	0.006	2	18
Dhofar 008	L3.3	find	137.784	0.019	1	13
Bjurböle	L4	FALL	137.759	0.052	1	16
NWA 869 a	L4	find	137.779	0.018	2	27
NWA 869 b	L4	find	137.780	0.008	2	27
NWA 869 av.	L4	<i>find</i>	<i>137.779</i>	<i>0.010</i>	4	
Saratov a	L4	FALL	138.610	0.016	2	20
Saratov c	L4	FALL	138.604	0.030	2	19
Saratov a,c av.	L4	<i>FALL</i>	<i>138.607</i>	<i>0.026</i>	4	
Saratov b	L4	FALL	137.772	0.013	1	10
Elenovka	L5	FALL	137.790	0.045	1	12
Elenovka IF0.2	L5	FALL	137.824	0.034	1	9
Elenovka IF0.3	L5	FALL	137.790	0.045	1	7
Elenovka IF0.4	L5	FALL	137.858	0.025	1	10
QUE 90201.5	L5	find	137.739	0.018	1	11
QUE 90218.4	L5	find	137.709	0.014	1	11
ALH 77927.4	L6	find	137.758	0.016	1	9
EET 87541.2	L6	find	137.759	0.011	1	10
Holbrook	L/LL6	FALL	137.768	0.006	2	12
Krymka a	LL3.2	FALL	137.689	0.008	2	14
Krymka b	LL3.2	FALL	137.680	0.057	1	14
Krymka IF0.2-0.4	LL3.2	FALL	137.687	0.017	1	11
Krymka av.	LL3.2	<i>FALL</i>	<i>137.688</i>	<i>0.012</i>	4	
EET 85744.4	LL4	find	137.797	0.008	2	13

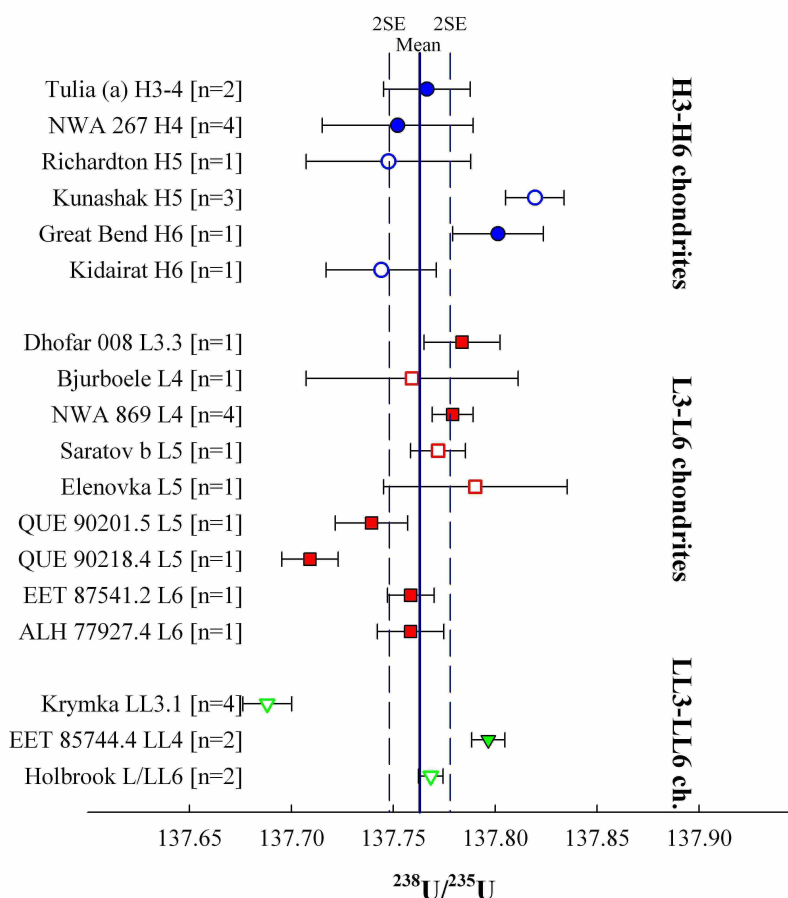


Figure 5.2: $^{238}\text{U}/^{235}\text{U}$ data for ordinary chondrites. Samples analyzed as several sub-samples are plotted with their average values only. Filled symbols represent 'finds', open symbols 'falls'. Note that values with very unusual uranium isotopic ratios are not part of this figure (see text).

All three values are identical within the limits of their uncertainties. It is therefore not possible to invoke a large-scale redox-related uranium isotopic fractionation. Having said that, each of the ordinary chondrite groups shows one or two 'outliers'. These show progressively lighter compositions from the more reduced H group to the more oxidized LL group, leaving the possibility that the isotopic shifts shown by individual samples may indeed be controlled by redox mechanisms during secondary mineral processing. As can be seen in Fig. 5.2 and Table 5.1 the distinction between 'finds' and 'falls' does not show any signs of uranium fractionation due to terrestrial contamination or weathering processes. Additionally, differences in the $^{238}\text{U}/^{235}\text{U}$ composition within each group are not related to the increasing metamorphic equilibration from geological chondrite types 3 to 6.

To further explore the possibility of deviating uranium isotopic compositions in miner-

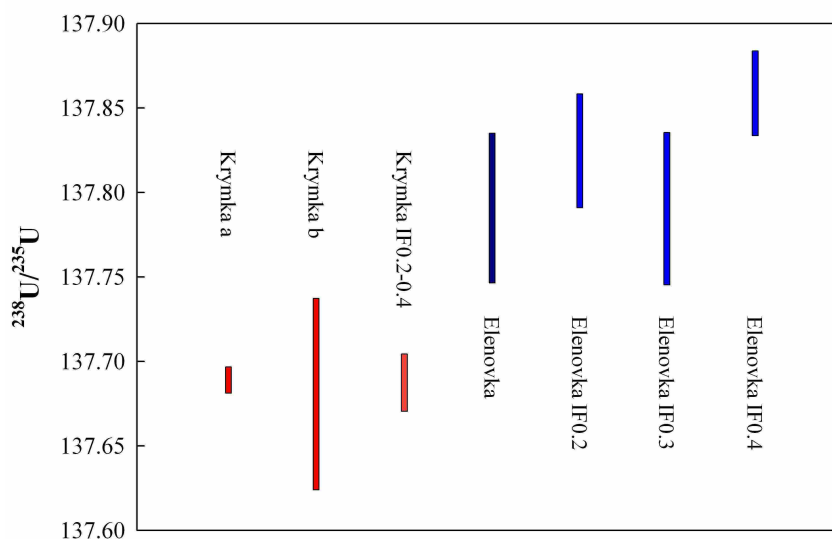


Figure 5.3: Bulk subsamples and subsamples of high magnetic susceptibility of the ordinary chondrites Krymka and Elenovka.

als two chondrites, Elenovka and Krymka, were subsampled using a Frantz isodynamic magnetic separator. This instrument separates the minerals of powdered rocks according to their magnetic susceptibility, usually after the ferromagnetic minerals are removed from the powder (a common magnet is sufficient for this). However, minerals in chondrites are closely intergrown and cannot be completely separated. Both Elenovka and Krymka are considered 'falls', therefore the possibility of any terrestrial contamination is reduced to a minimum. The subsamples of Elenovka, IF0.2¹, IF0.3 and IF0.4, and Krymka IF0.2-0.4 are representative of sample fractions containing a larger amount of pyroxenes, concentrated from the silico-phosphates, both of which are major uranium-bearing minerals. Pyroxenes are more commonly used for Pb-Pb dating than phosphates, as they give older ages. This might be caused either by an earlier closure time for the U-Pb system at higher temperatures in pyroxenes, or by a uranium isotopic fractionation during the migration of uranium into phosphates [e.g. Amelin et al., 2011]. It is therefore important to know if the uranium isotopic compositions between pyroxenes and bulk rock samples deviate.

There is no resolvable difference in the uranium isotopic composition between the separated mineral fractions and the bulk sample of Elenovka. Unfortunately, due to the very small sample sizes of only 2-7 ng U, the errors associated with these measurements are

¹IF is an abbreviation for isodynamic Frantz, 0.2-0.4 represent the currents in ampere applied to the magnetic field of the instrument.

relatively large (Fig. 5.3). In addition, there is no resolvable deviation in the $^{238}\text{U}/^{235}\text{U}$ ratios between both bulk samples and the IF0.2-0.4 subsample of the LL-chondrite Krymka. This shows that the uranium isotopic compositions of pyroxene minerals, at least of the two samples analyzed, are representative of the bulk meteorite samples. Therefore, it is more likely that differences in the Pb-Pb ages between the mentioned mineral phases represent different closure times for the U-Pb system of the minerals than being influenced by deviating uranium isotopic compositions.

The origin of the highly unusual anomalies towards heavier (Orlovka, Saratov a, c) and lighter (Estacado, Mount Browne) uranium isotopic compositions is not clearly understood. If the values are in fact real, these samples would have needed to have undergone a massive isotope fractionation, resulting in isotopic shifts of 3.3% and 0.6% for the isotopically heavier chondrites and -1.8% and -0.2% for the isotopically lighter chondrites. As a comparison, the uranium ‘stable’ isotope fractionations between ^{238}U and ^{235}U observed in the terrestrial water samples of this study are only 0.036% (Framvaren Fjord, Chapter 3.2.1.2) and 0.035% (Mojave aquifer, Chapter 3.4.1), although $^{238}\text{U}/^{235}\text{U}$ variations in redox-sensitive samples of 0.51% [Murphy et al., 2012], 0.10% [Bopp et al., 2009] and 0.12% [Brennecke et al., 2010a] and variations in a suite of uranium-bearing accessory minerals of 0.54% [Hiess et al., 2012] have been reported. All of these fractionations are still far lower than those seen in the chondrites of this study, which would therefore have needed some kind of extreme metamorphism or redox process capable of fractionating the uranium isotopes by up to six times larger than currently found on Earth. This would require large fractionation factors and orders of magnitude shifts in uranium concentrations.

A terrestrial influence can be ruled out as a cause for these isotope fractionations, as Saratov and Mount Browne are ‘falls’, Estacado was found in Texas, USA, and Orlovka in Siberia, Russia. The highest influence of weathering, however, occurs in meteorites that are found in hot deserts [Crozaz et al., 2003]. It would therefore be unlikely that meteorites found in hot deserts (e.g. NWA 267, Dhofar 008, NWA 869 and others) or cold deserts (e.g. QUE 90201.5, EET 85741.2, ALH 77927.4 and others) do not show any signs of terrestrial influences while the before mentioned ‘anomalous’ meteorites show large isotopic shifts in $^{238}\text{U}/^{235}\text{U}$.

However, the U concentration in certain phosphate-minerals of chondrites can be enriched up to the ppm-levels, since uranium migrates into these minerals during metamorphism. This provides the possible means to create uranium isotopic shifts. If a fractionation of uranium would occur during this process, and these minerals were over-represented in the ‘bulk’ chondrite samples, this might lead to the anomalous uranium isotopic compositions

measured. An argument in favour of this scenario is given by the uranium concentrations of the unusual chondrites, which are generally ~20-50 ppb and higher than most other ordinary chondrites. Although, other ordinary chondrites like NWA 267 and Kunashak show even higher uranium concentrations of 135 ppb and 80 ppb, without displaying unusual uranium isotopic compositions. However, two other lines of evidence make this scenario improbable. First, the sample sizes of the anomalous samples are ~0.35 g (Estacado) and ~1.0 g (Orlovka, Saratov b, Mount Browne), and are therefore sufficiently large, so that an over-representation of one mineral over another is unlikely. Second, merrillite, one of the main phosphate minerals in chondrites, is enriched in uranium as well as highly enriched in the REEs, with concentrations 50 to several hundred times the CI abundances [e.g. Ebihara and Honda, 1983, Crozaz et al., 1989]. The REE abundances in this study are <2.5 larger than the CI composition (Section 5.2.4), implying that the mineralogy of these samples was not dominated by U- and REE-enriched merrillite. However, if apatite is the primary phosphate mineral in the unusual ordinary chondrites uranium abundances might be elevated without an increase in REEs. It is also noteworthy that no other publication reports any unusual elemental or isotopic behaviour in these chondrites [e.g. Clayton et al., 1991, Amelin and Rotenberg, 2004, Kleine et al., 2008].

Another possible explanation for the anomalous uranium isotopic behaviour of some chondrites is that the fractionations are derived from the chemical processing of the sample prior to MC-ICPMS analysis. In this case, an incomplete digestion, the formation of fluoride complexes, or an incomplete equilibration of the sample with the spike tracer could have triggered the uranium isotope fractionation during the digestion and ion exchange column chemistry procedures, as suggested by Stirling et al. [2005]. Several attempts were made to duplicate the anomalous isotope fractionation during sample processing and analysis.

First, incomplete digestions of rock standard samples were produced, possibly causing an enrichment of certain minerals with potentially anomalous uranium isotopic compositions in the digest. Second, hydrogen peroxide was added to the rock standard samples between digestion and ion exchange column chemistry. This might cause an oxidizing reaction of the hydrogen peroxide with one of the ion exchange resins used during the purification process, disturbing the ion exchange properties of the resin in the process. Third, the possible presence of uranium oxides during mass spectrometry was examined. These oxides can create non-mass dependent isotope fractionations in the mass spectrometer, which are not accounted for during mass bias corrections applying an exponential mass fractionation law. For example, this effect was observed for Nd and Ce, producing isotope-dependent oxides close to the skimmer surface of the mass spectrometer [New-

man et al., 2009]. Fourth, elevated ^{232}Th concentrations can create $^{232}\text{ThH}^+$, causing interferences on the mass of ^{233}U during analysis. However, the mass of ^{232}Th was continuously monitored and no elevated concentrations were observed at any time. Lastly, the possible formation of colloids during the ion exchange procedure, or interferences from larger polyatomic molecules across the mass range, including residual organic molecules from the ion exchange resin. The presence of colloids or polyatomic molecules can possibly lead to matrix effects and non-exponential mass fractionation during MC-ICPMS analysis, as shown for cadmium isotopic analyses by Gault-Ringold and Stirling [2012]. None of these laboratory tests led to any result that might explain the anomalous uranium isotopic fractionation behaviour in the Orlovka, Saratov, Estacado and Mount Browne ordinary chondrites. It is hence considered unlikely that the observed anomalous isotopic compositions were inherited by laboratory artifacts incurred during chemical processing, although the possible presence of oxides and interferences from organic molecules cannot entirely be discounted. However, as all of the ‘anomalous’ chondrites were processed and analyzed concurrent with other, isotopically ‘normal’ meteorites, the fractionation mechanism would have to be specific to the ‘anomalous’ ordinary chondrites.

Contamination from anomalous sources of uranium prior to the samples being received at Otago for analysis was also considered as a potential explanation for the anomalous uranium isotopic compositions. Several samples that yielded high fractionation factors were initially prepared or stored at nuclear laboratories that handle anomalous sources of uranium, including both enriched and depleted uranium. While naturally occurring uranium contains only ~0.72% of ^{235}U , highly enriched uranium, as used for atomic weapons, can contain over 90% of ^{235}U . Depleted uranium may have abundances as low as 0.2% of ^{235}U . Enriched uranium possibly contains ^{233}U and/or ^{236}U as well, which would cause a change in the measured $^{233}\text{U}/^{236}\text{U}$ double spike ratio, therefore disturbing the calculation of the $^{238}\text{U}/^{235}\text{U}$ composition after correction for instrumental mass fractionation. Enriched uranium can have $^{238}\text{U}/^{235}\text{U}$ ratios as low as 0.1 while depleted uranium may have compositions of up to 500.

Importantly, only minute levels of contamination from anomalous U would be needed to explain the anomalous uranium isotopic behaviour observed here. Specifically, levels of 1.75% enriched uranium and 1.28% depleted uranium of the sample concentration would be needed to achieve the measured results for the anomalous uranium isotopic compositions. Assuming a typical sample size of 20 ng U, 0.36 ng highly enriched uranium would be necessary to change the uranium isotopic composition from an assumed 137.763, the average $^{238}\text{U}/^{235}\text{U}$ value of the ordinary chondrites, to the measured 135.354 of Estacado. On the other hand, 0.26 ng very depleted uranium would be necessary to increase the

average uranium isotopic composition to the measured $^{238}\text{U}/^{235}\text{U}$ ratio of Orlovka of 142.417. This kind of contamination could have occurred in the presence of material like weapon-grade uranium, containing U at percentage-levels. However, it would be difficult to explain the opposite directions of the alleged contaminations unless both enriched and depleted uranium were present in the laboratory. It is possible that the contamination did not occur by ^{238}U and ^{235}U , but instead by ^{233}U and/or ^{236}U . In this case a small contamination would result in a calculated high fractionation of $^{238}\text{U}/^{235}\text{U}$, as ^{233}U - ^{236}U spike concentrations in the samples are by a factor of 80-100 lower than ^{238}U concentrations. It is, however, improbable that such a contamination would occur without simultaneous ^{238}U and ^{235}U contamination.

Contamination during sample preparation is also considered highly unlikely as all highly fractionated samples were processed in the same facilities, in a laboratory that has handled only natural samples and a single ^{233}U - ^{236}U double spike. In addition, at most only one or two samples per processed batch show an anomalous uranium isotopic composition. The major question to be answered here is what causes specifically these ordinary chondrite samples to be affected by extreme uranium isotopic fractionation while none of the other meteorite groups show similarly anomalous compositions.

None of the above mechanisms can explain why two subsamples of the same ordinary chondrite, Saratov a and c, show nearly identical, heavier uranium isotopic compositions while a third subsample, Saratov b, shows a 'normal' composition. It is noteworthy that Saratov a was processed and analyzed at a different time than Saratov b and c. Additionally, each subsample was derived from different fragments of Saratov and sample sizes were sufficiently large at ~1.5 g for Saratov a and ~1.0 g for Saratov b and c. If all three subsamples have the same mineralogical composition they should have been either identically affected by the same fractionation mechanism, or the influences causing uranium isotopic fractionation should have been too random to result in two identical anomalous isotopic fractionations, leaving one subsample undisturbed. It is therefore even more doubtful that the anomalous uranium isotopic compositions were inherited from sample processing, interferences during analysis, or the influence of enriched uranium in the laboratory. Also, the subsamples Saratov a and c show uranium concentrations that are about doubled against the U concentration of Saratov b (19 and 20 ppb against 10 ppb). This is, in turn, an indication for the presence of different mineral assemblages in these subsamples, like the above mentioned elevated concentration of phosphates, causing the uranium concentration to increase.

In conclusion, a natural cause for the anomalous uranium isotopic behaviour of Orlovka,

Saratov, Estacado and Mount Browne, although unlikely, should be explored as a possible explanation for these highly metamorphic chondrites. However, anomalous isotopic shifts generated from large, polyatomic interferences cannot be entirely ruled out as an alternative possibility. Although beyond scope of the present study, subsamples of the main uranium-bearing minerals should be extracted and analyzed for their uranium concentrations and uranium isotopic compositions to address this issue. Although the analyses of subsamples containing concentrated pyroxenes, as explained earlier in this chapter, is the first step in this direction, more mineral phases should be analyzed to find possible sources of uranium with highly fractionated isotopic compositions. These tests should be conducted on the same samples that show unusual uranium isotopic compositions in bulk material analyzed in this study.

5.2.2 Carbonaceous chondrites

Carbonaceous chondrites are not influenced by high temperature thermal metamorphism like ordinary chondrites but are characterized by aqueous alterations, with geological types ranging from 1 to 3. This indicates low temperature alteration at $<300^{\circ}\text{C}$ and low degree thermal metamorphism at temperatures below 600°C [Keil, 2000]. Type 1 chondrites, like all CI chondrites, have undergone large scale aqueous alteration which erased all primary petrological and mineralogical characteristics. Type 2 chondrites also show signs of aqueous alteration but at a lesser scale, while type 3 chondrites have undergone the least amount of secondary processing.

Samples of 13 bulk carbonaceous chondrite samples spanning four subgroups (CR, CV, CM and CI), 2 CAIs extracted from the CV3 chondrites Allende and NWA 4502, and chondrules extracted from Allende were analyzed in this study.

The average of all carbonaceous chondrite bulk rock samples is $^{238}\text{U}/^{235}\text{U} = 137.778 \pm 0.016$, which is in agreement with the terrestrial reference value of 137.795 ± 0.008 . All of the analyzed carbonaceous chondrite samples, apart from the ungrouped C3 chondrite DaG 430 and both Allende inclusions, are identical within the 2SE uncertainty limits of their mean average value (Fig. 5.4 and Table 5.2). Subtle deviations in U isotopic compositions outside of their 2SE uncertainties are also observed between several carbonaceous chondrites, especially between bulk Allende and DaG 521, NWA 4502 and Mighei, as well as NWA 801 and NWA 4502, indicating that this chondrite group is not isotopically uniform in respect to $^{238}\text{U}/^{235}\text{U}$. In agreement with the ordinary chondrites, no difference is shown between the U isotopic composition of 'finds' and 'falls' of the carbonaceous chondrites that could be explained with terrestrial contamination or weathering processes (Fig. 5.4 and Tablecarbonaceous). In particular, Allende and Mighei are both 'falls' but their isotopic composition is not uniform. However, it should be noted that all 'finds' but

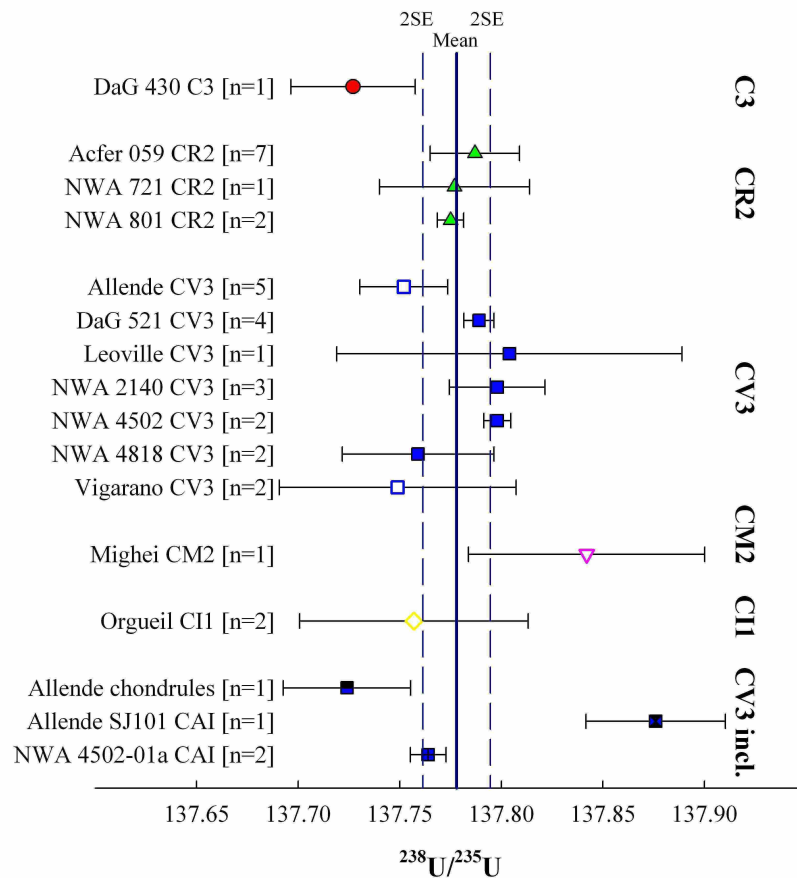


Figure 5.4: $^{238}\text{U}/^{235}\text{U}$ data for carbonaceous chondrites. Samples analyzed as several subsamples are plotted with their average values only. Filled symbols represent 'finds', open symbols 'falls'. The mean average and 2SE errors are calculated excluding the values for the inclusions.

Leoville (found in Kansas, USA) were found in hot deserts, giving at least the potential for weathering influences.

In the same manner to the ordinary chondrites, systematic variations are not resolvable between the different meteorite subgroups, indicating that increasing oxidation state (CR-CV-CM-CI) and varying abundances of refractory inclusions and volatile contents do not necessarily result in an increased fractionation of uranium isotopes. It is especially noteworthy that the $^{238}\text{U}/^{235}\text{U}$ value of Orgueil, the only analyzed member of the CI subgroup, does not show a resolvable deviation from the bulk average value. This is despite Orgueil probably being the only carbonaceous chondrite in this study that does not contain chondrules and being the chemically most primitive of the carbonaceous chondrites.

In agreement with the findings of the ordinary chondrites discussed above, neither deviations in uranium isotopic composition nor variations in uranium abundances are linked to the petrological types of the carbonaceous chondrites. It is however possible that the chon-

Table 5.2: Uranium isotope and concentration data for 13 carbonaceous chondrites. Averages are weighted depending on ng U used per analysis (reflected by intensity and length of analysis). Subsamples of the same meteorite are marked as sample name + a-e, averages of which are weighted over all single measurements of the subsamples.

Sample	Type	find/FALL	$^{238}/^{235}\text{U}$	2SE	n	U conc. [ppb]
DaG 430	C3 ungr., bulk	find	137.727	0.031	1	14
Acfer 059 a	CR2, bulk	find	137.794	0.025	4	247
Acfer 059 b	CR2, bulk	find	137.779	0.006	3	491
<i>Acfer 059 av.</i>	<i>CR2, bulk</i>	<i>find</i>	<i>137.787</i>	<i>0.022</i>	7	
NWA 721	CR2, bulk	find	137.777	0.037	1	69
NWA 801	CR2, bulk	find	137.775	0.006	2	103
Allende a	CV3, bulk	FALL	137.715	0.056	1	12
Allende b	CV3, bulk	FALL	137.771	0.050	1	13
Allende c	CV3, bulk	FALL	137.739	0.036	1	15
Allende d	CV3, bulk	FALL	137.769	0.041	1	12
Allende e	CV3, bulk	FALL	137.758	0.041	1	14
<i>Allende av.</i>	<i>CV3, bulk</i>	<i>FALL</i>	<i>137.752</i>	<i>0.022</i>	5	
Leoville	CV3, bulk	find	137.804	0.085	1	18
Vigarano a	CV3, bulk	FALL	137.785	0.046	1	16
Vigarano b	CV3, bulk	FALL	137.727	0.055	1	17
<i>Vigarano av.</i>	<i>CV3, bulk</i>	<i>FALL</i>	<i>137.758</i>	<i>0.058</i>	2	
DaG 521 a	CV3, bulk	find	137.790	0.012	2	417
DaG 521 b	CV3, bulk	find	137.787	0.009	2	441
<i>DaG 521 av.</i>	<i>CV3, bulk</i>	<i>find</i>	<i>137.789</i>	<i>0.007</i>	4	
NWA 2140	CV3, bulk	find	137.798	0.024	3	127
NWA 4818 a	CV3, bulk	find	137.769	0.022	1	13
NWA 4818 b	CV3, bulk	find	137.732	0.032	1	17
<i>NWA 4818 av.</i>	<i>CV3, bulk</i>	<i>find</i>	<i>137.758</i>	<i>0.037</i>	2	
NWA 4502	CV3, bulk	find	137.798	0.007	2	108
Mighei	CM2, bulk	FALL	137.842	0.058	1	14
Orgueil a	CI1, bulk	FALL	137.788	0.083	1	25
Orgueil b	CI1, bulk	FALL	137.732	0.069	1	23
<i>Orgueil av.</i>	<i>CI1, bulk</i>	<i>FALL</i>	<i>137.755</i>	<i>0.056</i>	2	
Bulk average			137.778	0.016		
NWA 4502	CAI	find	137.764	0.009	2	122
Allende	CAI SJ101	FALL	137.876	0.034	1	65
Allende	chondrules	FALL	137.724	0.031	1	26

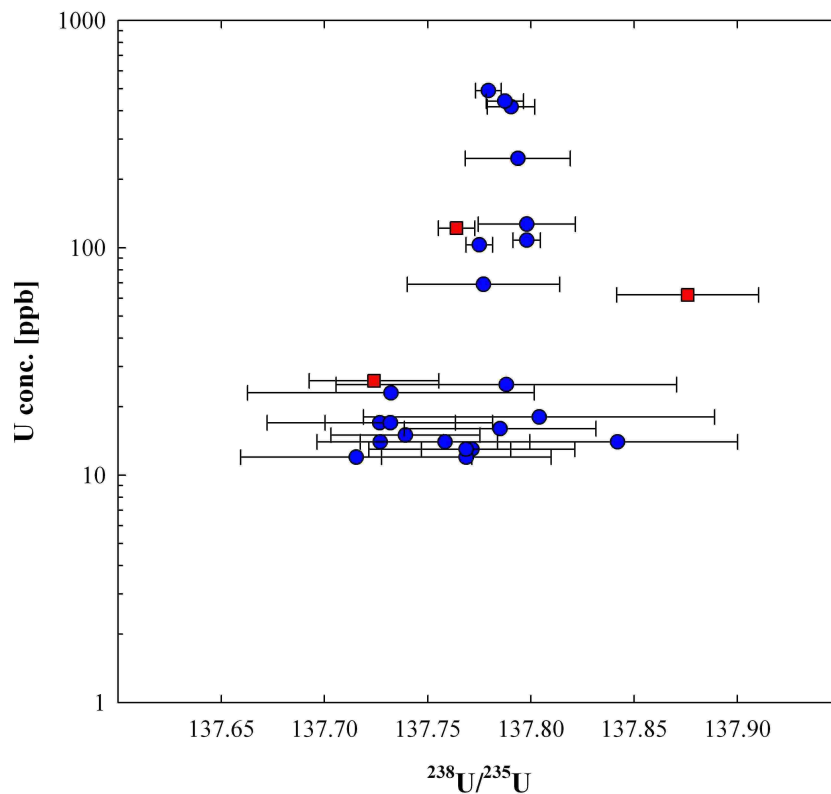


Figure 5.5: Comparison of $^{238}\text{U}/^{235}\text{U}$ values and U concentrations of carbonaceous chondrites. The dataset includes all subsamples of the present study, bulk samples are plotted as blue circles, inclusions as red squares.

chondrites with isotopically lighter uranium are influenced by an increased amount of chondrules in the bulk sample, given the light $^{238}\text{U}/^{235}\text{U}$ determined in this study for Allende chondrules in respect to the uranium isotopic composition of most other chondrites. As all petrological type 3 chondrites, here CV3 and C3, are mineralogically unequilibrated, a higher amount of chondrules might significantly lower the uranium isotopic composition of the bulk sample. This would also explain the deviations in the uranium composition of the five Allende subsamples, the heaviest of which show $^{238}\text{U}/^{235}\text{U}$ values of 137.771 ± 0.050 and 137.769 ± 0.041 , which is close to the carbonaceous chondrite average of 137.778 ± 0.016 . The higher abundance of ^{235}U in isotopically lighter chondrites might also be influenced by the former existence of ^{247}Cm , which decays to ^{235}U . This possibility will be further explored in section 5.4.

As shown in Fig. 5.5, the uranium concentrations of the carbonaceous chondrites in this study have a wide range from 12-491 ppb (Table 5.2). This heterogeneity is typically not reflected in the concentrations between different bulk subsamples of the same

Table 5.3: Uranium isotopic composition and concentration data for three enstatite chondrites. Averages are weighted depending on ng U used per analysis (reflected by intensity and length of analysis).

Sample	Type	find/FALL	$^{238}\text{U}/^{235}\text{U}$	2SE	n	U conc. [ppb]
SAH 97096	EH3	find	137.742	0.032	1	8
Abee	EH4	FALL	137.767	0.031	1	7
Indarch	EH4	FALL	137.767	0.039	1	8
Average			137.759	0.017		

carbonaceous chondrite, apart from the two subsamples of Acfer 059. This possibly indicates that the different carbonaceous chondrites originate from parent bodies with deviating bulk compositions rather than showing different mineral assemblages between subsamples, unlike discussed in the ordinary chondrites. The uranium isotopic composition does not correlate with the uranium concentration, as both the isotopically lightest sample (DaG 430) and the isotopically heaviest sample (Mighei) have identical uranium abundances of 14 ppb. Instead, all carbonaceous chondrites yielding high uranium abundances of >100 ppb, namely Acfer 059, NWA 801, DaG 521, NWA 2140 and NWA 4502, show uranium isotopic compositions that are in very close agreement with the carbonaceous chondrite average of this study, ranging from $^{238}\text{U}/^{235}\text{U} = 137.775 \pm 0.006$ to 137.798 ± 0.007 (Fig. 5.5). If heterogeneity in uranium concentration is not caused by fractionation processes during mineralogical alterations it has to be inherited from the parent bodies of the carbonaceous chondrites. On the basis of the data of this study it is not possible to infer whether this is caused by heterogeneity in the solar nebula during the time of accretion of the parent bodies, implying that the different parent bodies of the carbonaceous chondrites have different uranium abundances, or heterogeneity in the composition of the parent bodies themselves.

5.2.3 Enstatite chondrites

The three enstatite chondrites analyzed during this project, namely Sahara (SAH) 97096, Abee and Indarch, experienced only moderate levels of thermal metamorphism, being classified as petrologic types 3 (SAH 97096) and 4 (Indarch, Abee). The samples are of the subgroup EH, indicating high abundances of iron and were formed in a highly reducing environment.

All three $^{238}\text{U}/^{235}\text{U}$ compositions are identical within the limits of their 2SE uncertainties, with ratios of 137.742 ± 0.032 (SAH 97096), 137.767 ± 0.031 (Abee) and 137.767 ± 0.039 (Indarch). The uranium concentrations of these samples of 7-8 ppb are also very similar.

These isotopic ratios have an average $^{238}\text{U}/^{235}\text{U}$ of 137.759 ± 0.017 , agreeing, within error, with the carbonaceous chondrite average of 137.778 ± 0.016 . It is also similar to the $^{238}\text{U}/^{235}\text{U}$ average of the ordinary chondrites of 137.763 ± 0.005 , if the highly fractionated 'unusual' ordinary chondrites are disregarded. This supports the findings of the ordinary and carbonaceous chondrites which neither showed any correlation between their $^{238}\text{U}/^{235}\text{U}$ values and the redox state of the meteorite groups. This clearly shows that changing redox conditions in the solar nebula during the accretion processes of the chondrite parent bodies do not result in a resolvable isotopic fractionation of uranium.

The average $^{238}\text{U}/^{235}\text{U}$ ratio of the enstatite chondrites deviates, outside error, from the BSE average of 137.795 ± 0.008 . This is of particular interest, as the overall isotopic composition of enstatite chondrites and BSE are generally very similar.

5.2.4 Rare earth element patterns of bulk chondrites

The patterns of the REE concentrations, normalized to CI concentrations [Barrat et al., 2012], in chondrites can be used as indicators for the degree of evaporation or condensation experienced in the cooling solar nebula according to the condensation theory [Boyn-ton, 1984]. During the evaporation process the lighter elements are enriched in the gas. Consequently, the residue becomes more refractory and shows an enrichment in the heavy REEs. Hence, the initial condensates of this gas will be enriched in the light REEs as well. On the other hand, if condensation takes place at a late stage of evaporation the REE pattern formed during condensation will be enriched in the heavy REEs, if the condensate is removed from the gas before the condensation is complete [Boyn-ton, 1975]. As uranium is a refractory element it should be removed from the gas together with the heavy REEs. The degree of evaporation or condensation inferred from the REE patterns also provides an indication for the extent of isotopic fractionation that can be expected in a sample. Additionally, REE patterns of chondrites are influenced by metamorphic processes as REEs, like U, migrate into phosphates during metamorphism [Murrell and Burnett, 1983].

For the chondritic meteorites analyzed in this study nearly all REE patterns from lanthanum to lutetium are roughly equal to the CI (= solar system) average. Sample to CI ratios range from 0.5 and 2.5 and do not show any significant fractionation between the REEs. These abundances are in agreement with differing REE abundances throughout the solar nebula.

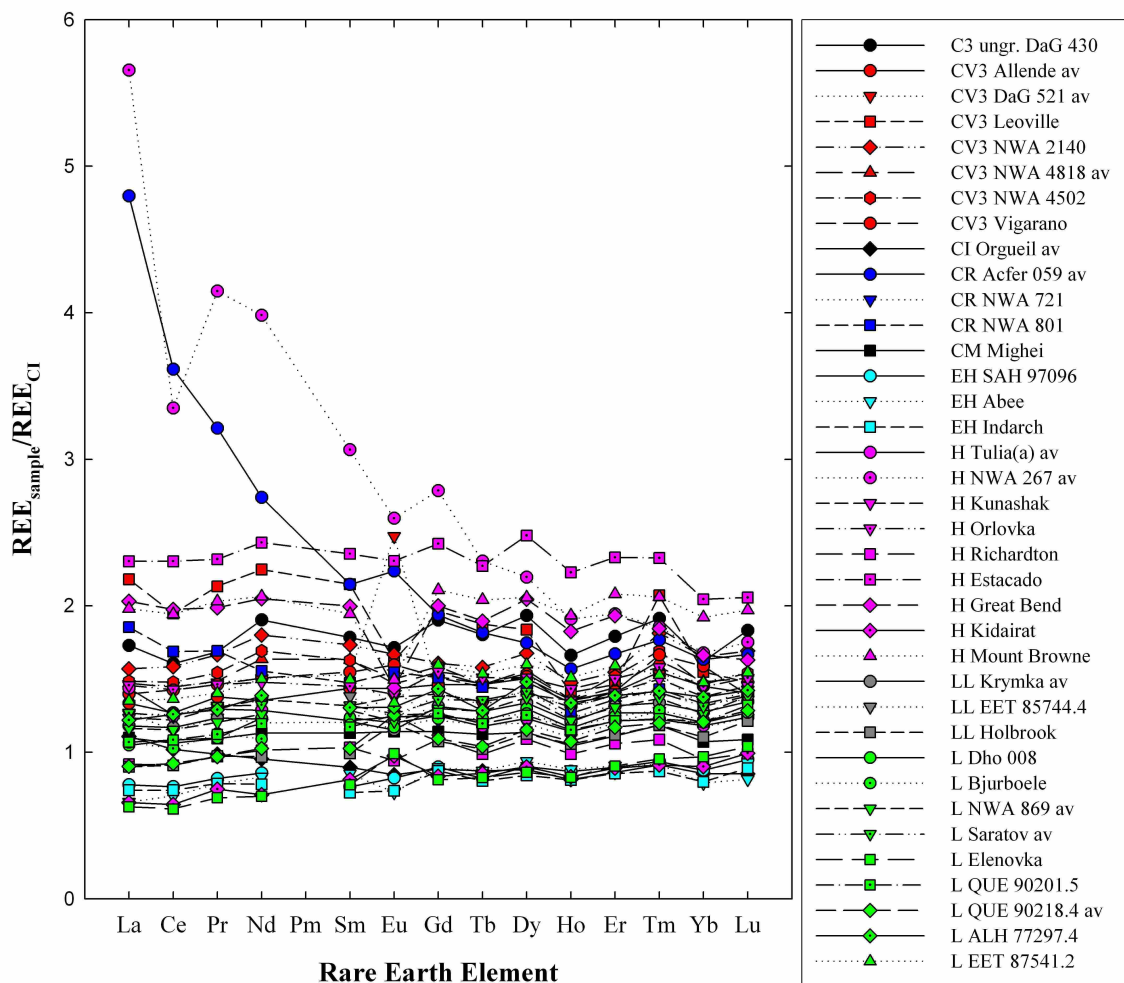


Figure 5.6: Rare earth element patterns for chondrites.

Several chondrites contain small europium anomalies in negative or positive direction from the CI value (Fig. 5.6, for the complete data set of REE composition in meteorites please refer to Appendix C.).

The only exceptions are the ordinary chondrite (H4) NWA 267 and the carbonaceous chondrite (CR2) Acfer 059, which are highly enriched in light REEs. This is consistent with chemical alteration and contamination processes during weathering occurring in hot desert environments [Crozaz et al., 2003]. As NWA 267 was found in Northwest Africa and Acfer 059 was found in Algeria this explanation is viable if the samples have high terrestrial residence ages, or have been exposed to fluids like rain. As light REE enrichment often presents with Sr, Ba, and most importantly U contamination, the uranium isotope compositions of these two samples have to be interpreted with caution.

Enstatite chondrites have the lowest REE_{sample}/REE_{CI} ratios of <1 throughout, indic-

ating an origin in a region of the solar nebula that was depleted in refractory elements. Carbonaceous chondrites (other than Acfer 059) have ratios varying from just under 1 to just above 2 and the ordinary chondrites show the widest range of normalized REE abundances of about 0.5-2.5, not taking NWA 267 into account. These deviations can either indicate regions in the solar nebula with differing refractory element abundances or be caused by an increasing depletion of the solar nebula in refractory elements with time, as suggested by the condensation model.

No inconsistencies were found comparing the REE patterns of ordinary chondrites, showing that the digestions of the samples are complete and cannot have caused the inconsistencies within the isotope ratios analyzed for this meteorite group (section 5.2.1).

5.2.5 Chronology of the oldest solids in the solar system

All uranium and lead data of Allende and its inclusions as well as the implications for the timeline of the events of the early solar system were published in the co-authored publication of Amelin et al. [2010]. The data were analyzed during visits of Dr. Y. Amelin to Otago University (U isotopic and concentration data) and of myself to the ANU (Pb isotopic and concentration data).

The Allende CAI SJ101 formed in several condensation stages and was disturbed by at least two flash heating events during its accretion time before being removed from its source in the early solar nebula [Petaev and Jacobsen, 2009]. It is classified as a forsterite-bearing group II CAI, which is clearly displayed in its REE pattern (Fig. 5.7) showing an enrichment in light REEs and Tm up to 17 times of the CI concentration and a depletion in ultra-refractory elements as REEs between Gd and Er, and Lu. This pattern possibly indicates that the precursors of CAI SJ101 could have formed by a non-equilibrium condensation in a closed system [Petaev and Jacobsen, 2009, Ireland and Fegley, Jr., 2000]. As uranium is a refractory element as well, it would also have been partially removed during this process, possibly yielding lighter uranium in the condensate in respect to heavier uranium in the vapor residue.

The CAI NWA 4502-01a shows an enrichment in REEs up to 19 times with respect to CI concentration, consistent with most CAIs [Ireland and Fegley, Jr., 2000]. The generally flat REE pattern shows a slight depletion in light REEs and a positive Eu anomaly, classifying this CAI as a group I CAI [Ireland and Fegley, Jr., 2000]. The slightly uneven REE pattern is probably caused by incomplete back-reactions of the CAI with the solar nebula and its parent body, including partial evaporation and re-condensation [Ireland and Fegley, Jr., 2000]. The REE pattern of the Allende chondrules is flat with abundances only slightly higher than the CI composition and the bulk rock samples of Allende and NWA

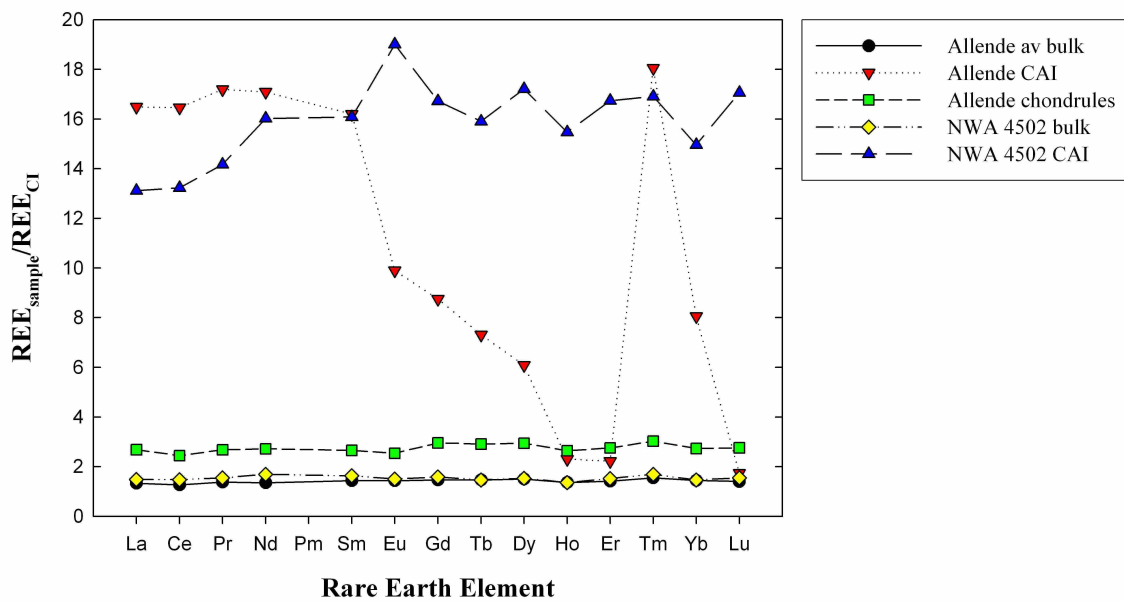


Figure 5.7: Rare earth element patterns for the CV3 chondrites Allende and NWA 4502 and their inclusions.

4502. This indicates that the chondrules are unfractionated and therefore undisturbed by partial reactions with the solar nebula or the host rock and that a complete condensation of elements took place during the chondrule formation.

Establishing a consistent timescale for the formation of the early solar system based on isotopic dating of CAIs and chondrules is one of the most important subjects in cosmochemistry, as these inclusions represent the first solids that accreted in the solar system. Until very recently it seemed confirmed that CAIs formed shortly before chondrules, which completed their accretion 3-5 Myr after the formation of the CAIs [e.g. Amelin et al., 2002, Jacobsen et al., 2008, Krot et al., 2009]. However, Connelly et al. [2012] utilizing revised Pb-Pb dating based on combined U and Pb isotopic measurement on the same sample found that chondrule and CAI formation started simultaneously and chondrule formation lasted for approximately 3 Myr. This would close the age gap between CAI and chondrule formation. The uranium isotopic data for the CAIs and chondrules presented in this study also have an important bearing on this issue.

As shown in Fig. 5.8, the $^{238}\text{U}/^{235}\text{U}$ ratios of the two CAIs of this study deviate from the uranium isotopic compositions of their parent meteorites, with differences from NWA 4502 (bulk) to NWA 4502-01a of 0.025 and Allende (bulk) to Allende SJ101 of -0.124.

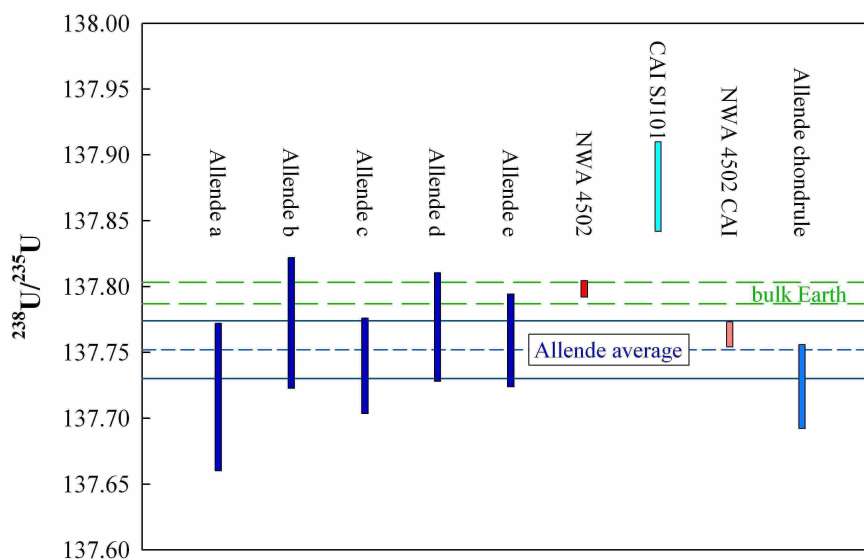


Figure 5.8: Uranium isotopic data for the carbonaceous chondrites Allende and NWA 4502 and their inclusions. Allende average and 2SE lines (in blue) are for bulk Allende a-e samples only, BSE values (with 2SE lines, in green) are discussed earlier (Chapter 3.1).

This will be reflected in the Pb-Pb ages of both CAIs, as was shown on the example of the angrites in Chapter 4. To date, Pb-Pb ages have been derived for the Allende chondrite and its inclusions, based on analyses acquired in this study and in collaboration with Dr. Y. Amelin (ANU, Australia). The $^{238}\text{U}/^{235}\text{U}$ value for bulk Allende obtained in this study is 137.752 ± 0.022 . This is in very good agreement with the compositions obtained from other studies, including $^{238}\text{U}/^{235}\text{U}$ values of 137.774 ± 0.012 [Brennecka et al., 2010b], 137.783 ± 0.011 [Connelly et al., 2012], 137.768 ± 0.019 [Stirling et al., 2006] and 137.789 ± 0.026 [Stirling et al., 2006]. It should be noted that Brennecka et al. [2010b] published values in reference to the standard SRM950a with $^{238}\text{U}/^{235}\text{U}$ of 137.88, Connelly et al. [2012] in reference to the CRM145 standard with $^{238}\text{U}/^{235}\text{U}$ of 137.44 and the values of Stirling et al. [2006] were re-calculated to the reference used in this study.

Three out of the five Allende subsamples have uranium isotopic compositions that agree, within error, with the BSE value of 137.795 ± 0.008 of this study. However, the Allende bulk average is lighter with respect to the BSE value while the $^{238}\text{U}/^{235}\text{U}$ value for NWA 4502 is identical with the BSE value. This finding is in agreement with the heterogeneity in values shown in chondrites throughout this study, yielding average $^{238}\text{U}/^{235}\text{U}$ values of 137.763 ± 0.005 (ordinary chondrites), 137.778 ± 0.016 (carbonaceous chondrites) and 137.759 ± 0.017 (enstatite chondrites). It is also consistent with the high abundance

of >80% chondrules in Allende and lower chondrule abundance of <50% in NWA 4502 as chondrules yield lighter $^{238}\text{U}/^{235}\text{U}$ values in respect to bulk chondrites. The possible fractionation of $^{238}\text{U}/^{235}\text{U}$ in terrestrial samples by different geochemical mechanisms, as shown in Chapter 3 and references therein, is also a factor.

However, the two CAIs extracted from Allende and NWA 4502 show statistically different uranium isotopic compositions from those of their host rocks. To this end, CAI SJ101 has a heavier $^{238}\text{U}/^{235}\text{U}$ composition than bulk Allende and BSE while the NWA 4502-01a shows a lighter ratio in respect to bulk NWA 4502 and BSE. This underlines the findings of Brennecka et al. [2010b] and Connelly et al. [2012], reporting $^{238}\text{U}/^{235}\text{U}$ ratios for CAIs spanning over a wide range of compositions from 137.409 to 137.885, which might cause the corresponding Pb-Pb ages to shift up to ~5 Myr. Despite their wide range in $^{238}\text{U}/^{235}\text{U}$ values, the Allende CAI SJ101 and three CAIs analyzed by Connelly et al. [2012] yield identical Pb-Pb ages of 4567.18 ± 0.50 Myr, 4567.35 ± 0.28 Myr, 4567.23 ± 0.29 and 4567.38 ± 0.31 Myr, giving a mean CAI age of 4567.30 ± 0.16 Myr. This finding supports the hypothesis of a single CAI-forming event, possibly lasting as short as 160,000 years [Connelly et al., 2012]. It is also in agreement with the suggestion of Jacobsen et al. [2008] of the presence of heterogeneous chemical reservoirs in the early solar system nebula, as the data suggest that the $^{238}\text{U}/^{235}\text{U}$ variability in CAIs was inherited from the solar nebula during accretion and does not represent secondary alteration. This is supported by the deviating $^{232}\text{Th}/^{238}\text{U}$ and $^{144}\text{Nd}/^{238}\text{U}$ abundance ratios between the two CAIs in this study, representing two different CAI groups. Specifically, these ratios correspond to $^{232}\text{Th}/^{238}\text{U}$ of 4.6 and 2.9 and $^{144}\text{Nd}/^{238}\text{U}$ of 16.8 and 8.4 for the CAIs SJ101 and the NWA 4502-01a. The elevated $^{144}\text{Nd}/^{238}\text{U}$ ratio of the group II CAI SJ101 against the group I CAI is consistent with their formation model as Nd is more volatile than U, causing a fractionation to higher abundances of Nd in respect to U during condensation processes that involve non-equilibrium condensation in the early solar system [Ireland and Fegley, Jr., 2000].

Lighter $^{238}\text{U}/^{235}\text{U}$ values in inclusions in respect to their host meteorites might be influenced by the decay of the now extinct, short-lived isotope ^{247}Cm to ^{235}U , building an excess of ^{235}U against ^{238}U , as will be discussed in detail in section 5.4. This effect is in agreement with the heavier uranium isotopic compositions of NWA 4502 against its extracted CAI. However, the chondrite Allende shows a lighter uranium isotopic composition than CAI SJ101. Therefore, the mechanism controlling uranium isotopic fractionation in this chondrite must be a different one, possibly isotope fractionation through redox processes occurring during secondary chemical processing, or an inheritance from a nucleosynthetic anomaly in the early solar system.

The interval between the timing of CAI (4567.18 ± 0.50 Myr) and chondrule formation

Table 5.4: Uranium isotope and concentration data for bulk samples of five eucrites and the ungrouped achondrite NWA 5400. Averages are weighted depending on ng U used per analysis (reflected by intensity and length of analysis). Subsamples are marked as sample name + a, b, averages of which are weighted over all measurements of the subsamples.

Sample	Type	find/ FALL	$^{238}\text{U}/^{235}\text{U}$	2SE	n	U conc. [ppb]
Agoult	Eucrite	find	137.708	0.016	3	79
Camel Donga a	Eucrite	find	137.785	0.038	2	138
Camel Donga b	Eucrite	find	137.780	0.020	3	106
<i>Camel Donga av.</i>	<i>Eucrite</i>	<i>find</i>	<i>137.783</i>	<i>0.009</i>	5	
Ibitira a	Eucrite	FALL	137.792	0.088	1	44
Ibitira b	Eucrite	FALL	137.778	0.005	2	305
<i>Ibitira av.</i>	<i>Eucrite</i>	<i>FALL</i>	<i>137.778</i>	<i>0.013</i>	3	
Millbillillie	Eucrite	FALL	137.775	0.022	1	95
NWA 2362	Eucrite	find	137.794	0.028	1	34
Average	Eucrites		137.768	0.008	5	
NWA 5400	ungr. achondrite	find	137.719	0.028	1	72

according to this study is 1.97 ± 1.13 Myr. While this interval shows a definitive age gap between CAI and chondrule formation it is still within the 3 Myr formation limit of chondrules as proposed by Connelly et al. [2012], as well as being in agreement with the formation intervals of 1.5-3.0 Myr derived using the Al-Mg short-lived relative chronometer [Villeneuve et al., 2009] and 1.7 ± 0.7 Myr determined utilizing the Hf-W short-lived relative chronometer [Kleine et al., 2009].

5.3 Eucrites

Four different eucrites and one eucrite-like meteorite, Ibitira, were sampled in the present study, giving an average $^{238}\text{U}/^{235}\text{U}$ ratio of 137.768 ± 0.008 (Table 5.4). This is within uncertainty of the uranium isotopic composition of each of the other meteorite groups analyzed throughout this study, being 137.783 ± 0.011 for angrites, 137.763 ± 0.005 for ordinary chondrites, 137.778 ± 0.016 for carbonaceous chondrites and 137.759 ± 0.017 for enstatite chondrites. The average $^{238}\text{U}/^{235}\text{U}$ composition over all five meteorite groups is therefore 137.770 ± 0.009 and shows a uniformity throughout the early solar nebula for the timespan of accretion of all meteorites.

Four of the five eucrite/eucrite-like samples show uranium isotopic compositions that

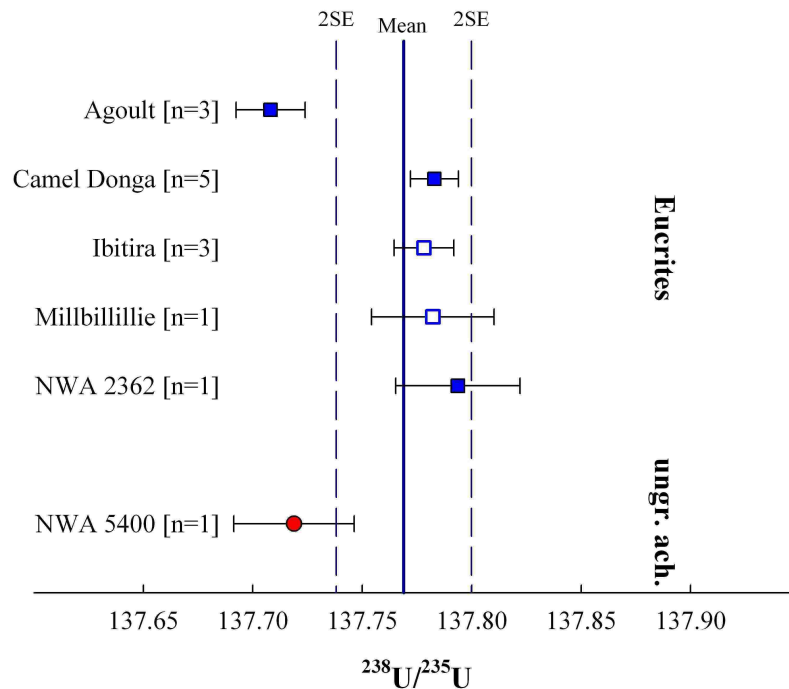


Figure 5.9: $^{238}\text{U}/^{235}\text{U}$ ratios for the eucrites and the ungrouped achondrite NWA 5400. Filled symbols represent 'finds', open symbols 'falls'.

agree within the 2SE uncertainty of all measurements. However, Agoult deviates from the other samples and is slightly enriched in ^{235}U (Fig. 5.9). This results in Agoult's $^{238}\text{U}/^{235}\text{U}$ composition being 0.5‰ lower than the other eucrites. The ungrouped achondrite NWA 5400 shows a similar uranium isotopic composition to the eucrite Agoult, with a $^{238}\text{U}/^{235}\text{U}$ ratio of 137.719 ± 0.029 . The eucrites Camel Donga and Millbillillie are monomict² breccia, while Agoult and NWA 2362 are unbrecciated. Ibitira is classified as a monomict achondrite. The consequently different formation histories of these eucrite groups, including partial melting and impact melting, might have caused an isotopic fractionation of uranium in the eucrite Agoult.

The REE patterns of the eucrites (Fig. 5.10, for the complete data set of REE composition in meteorites please refer to Appendix C) show a range of influences according to their different melting and metamorphism history. The depletion in light REEs of Agoult and NWA 2362 and their positive Eu anomalies are most likely explained by partial melt formation and removal of the crust of the eucrite parent body. This leaves the deeper situated residue enriched in refractory elements and is consistent with the mineralogical evidence for high temperature metamorphism in these eucrites [Yamaguchi et al., 2009]. Camel

²Monomict: all clasts of the breccia have identical lithologies with the matrix.

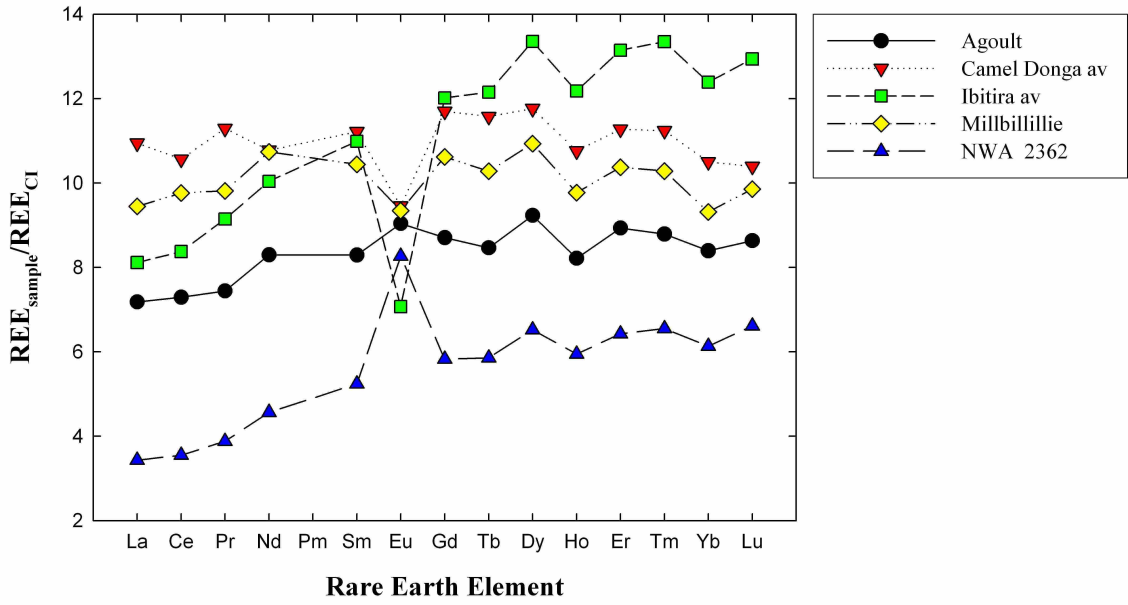


Figure 5.10: REE patterns for eucrites.

Donga and Millbillillie have similar, flat REE patterns with large negative Eu anomalies, indicating a mantle source for the initial magma. According to Mittlefehldt [2005] Ibitira originated from a different parent body than the other eucrites, due to its oxygen isotopic composition and the unusual presence of vesicles. The REE composition indicates that it derived from a partial melt, but with a negative Eu anomaly.

5.4 Implications for the ^{247}Cm chronometer

As briefly discussed in Chapter 1.4.2, the initial $(^{247}\text{Cm}/^{235}\text{U})_{t+\Delta}$ ratio at the beginning of the solar system, where t = the age of the solar system defined by the timing of CAI formation, determined as 4567.18 Myr in this study, and Δ = time span between the last r-process event and the timing of CAI formation, can be calculated using Nd or Th as a proxy for Cm. As outlined in Stirling et al. [2005], the abundance of present $^{235}\text{U}_p$, can be formulated as

$$^{235}\text{U}_p = ^{247}\text{Cm}_{t+\Delta} * \frac{\lambda_{247}}{\lambda_{235} - \lambda_{247}} * (e^{-\lambda_{247}t} - e^{-\lambda_{235}t}) + ^{235}\text{U}_{t+\Delta} * e^{-\lambda_{235}t} \quad (5.1)$$

where λ_{247} and λ_{235} are the respective decay constants of ^{247}Cm and ^{235}U . As $\lambda_{235} \gg \lambda_{247}$, Equation 5.1 becomes

$$^{235}\text{U}_p = (^{247}\text{Cm}_{t+\Delta} + ^{235}\text{U}_{t+\Delta}) * e^{-\lambda_{235}t}. \quad (5.2)$$

Dividing Equation 5.2 by ^{238}U to transform the isotope abundances into isotopic ratios gives

$$\left(\frac{^{235}\text{U}}{^{238}\text{U}}\right)_p = \frac{^{247}\text{Cm}_{t+\Delta}}{^{238}\text{U}_p} * e^{-\lambda_{235}t} + \left(\frac{^{235}\text{U}}{^{238}\text{U}}\right)_{t+\Delta} * e^{(\lambda_{238}-\lambda_{235})t}. \quad (5.3)$$

Utilizing ^{144}Nd as a proxy for ^{247}Cm , Equation 5.3 can be reformulated to

$$\left(\frac{^{235}\text{U}}{^{238}\text{U}}\right)_p = \left(\frac{^{247}\text{Cm}}{^{144}\text{Nd}}\right)_{t+\Delta} * e^{-\lambda_{235}t} * \left(\frac{^{144}\text{Nd}}{^{238}\text{U}}\right)_p + \left(\frac{^{235}\text{U}}{^{238}\text{U}}\right)_{t+\Delta} * e^{(\lambda_{238}-\lambda_{235})t}. \quad (5.4)$$

Equation 5.4 can be reformulated accordingly if utilizing ^{232}Th as an alternative proxy for ^{247}Cm .

It follows from equation 5.4 that plotting $^{144}\text{Nd}/^{238}\text{U}$ or $^{232}\text{Th}/^{238}\text{U}$ against $^{235}\text{U}/^{238}\text{U}$ as shown in Fig. 5.11 and Fig. 5.12 will give a linear relationship. The resulting interception points of the linear regression lines with the $^{235}\text{U}/^{238}\text{U}$ -axes are equivalent to $(^{235}\text{U}/^{238}\text{U})_{t+\Delta}$, while the slopes of the linear regression lines represent $(^{144}\text{Nd}/^{238}\text{U})_p$ and $(^{232}\text{Th}/^{238}\text{U})_p$, respectively.

Implementing decay constants of $\lambda_{247} = 4.39 \times 10^{-8}$, $\lambda_{238} = 1.56 \times 10^{-10}$ and $\lambda_{235} = 9.86 \times 10^{-10}$ [Jaffey et al., 1971, Mattinson, 2010], a maximum initial $^{247}\text{Cm}/^{235}\text{U}$ ratio at $t+\Delta$ of $\sim 2.9 \times 10^{-4}$ is calculated using Nd as a proxy for Cm and taking into account the possible 2SE errors on the interception point and the slope of the regression line. In contrast, a maximal initial $^{247}\text{Cm}/^{235}\text{U}$ ratio of $\sim 1.5 \times 10^{-3}$ is calculated utilizing Th as a proxy for Cm.

Assuming a present day ratio of Nd/U of 60.26 [Barrat et al., 2012] and Th/U of 3.68 [Barrat et al., 2012] and an $^{247}\text{Cm}/^{238}\text{U}$ production ratio at $t = T$ of 0.138 [Nittler and Dauphas, 2006] during the last r-process, Δ is equivalent to ~ 165 -195 Myr, using Nd as proxy for Cm, and ~ 140 -155 Myr utilizing Th as a proxy for Cm.

The Nd/U and Th/U datasets of this study give rise to values ranging from 0.2-17 for $^{144}\text{Nd}/^{238}\text{U}$ and from 0.08-6 for $^{232}\text{Th}/^{238}\text{U}$. No apparent trend is resolvable for these fractionations. This is consistent with the findings of several other studies [Stirling et al., 2005, 2006, Connelly et al., 2012]. To date, only the study by Brennecka et al. [2010b] has documented larger (10-100% levels) Nd/U and Th/U fractionations in meteorites. These highly fractionated compositions appear to be quite unusual in early solar system material. The data of this study are in agreement with the data of Blake and Schramm [1973],

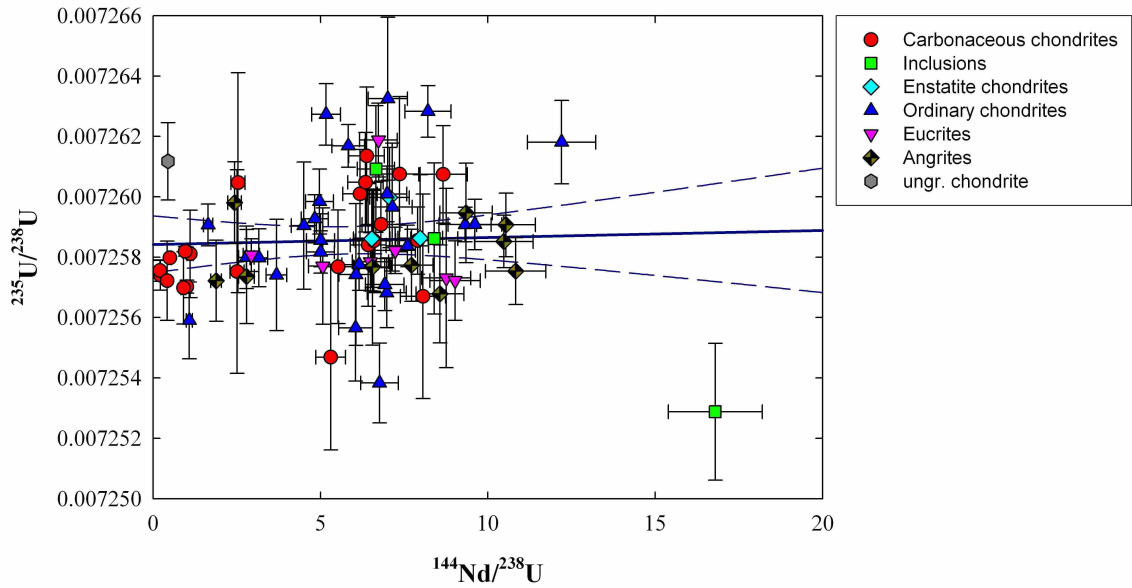


Figure 5.11: $^{144}\text{Nd}/^{238}\text{U}$ against $^{235}\text{U}/^{238}\text{U}$, the linear regression line (solid dark blue) gives the slope and the interception point for the calculations of the initial abundance of ^{247}Cm at $t+\Delta$. The dashed lines represent the 95% confidence intervals of the linear regression. Error bars on the x-axis represent 2% uncertainties of Nd, in agreement with the q-ICP-MS measurements of this element.

Chen and Wasserburg [1981], Stirling et al. [2005, 2006] and Brennecka et al. [2010b], who reported upper limits on the initial $^{247}\text{Cm}/^{235}\text{U}$ value of 9×10^{-4} , 4×10^{-3} , 1×10^{-4} , 8×10^{-5} and $1.1\text{-}2.4 \times 10^{-4}$, respectively. The calculated time intervals of free decay Δ correspond well to the published data of 100-200 Myr [Stirling et al., 2005], 230 Myr [Stirling et al., 2006] and 110-140 Myr [Brennecka et al., 2010b].

The differences in the inferred results for the initial $^{247}\text{Cm}/^{235}\text{U}$ ratio and the time interval of free decay Δ , depending on whether Nd or Th is used as a proxy for Cm, might be caused by slightly different chemical attributes of Nd and Th interfering with their use as a proxy for Cm.

In conclusion, the time between the last r-process and the formation of the first solids in the solar system can be estimated to 100-230 Myr (140-200 Myr in this study). Due to the low $^{247}\text{Cm}/^{235}\text{U}$ ratios at $t+\Delta$, with a maximum of 4×10^{-3} , and the lack of fractionation of Nd/U and Th/U and, hence, Cm/U, it can be assumed that the decay of ^{247}Cm does not have a significant effect on the U-Pb chronometer.

Several short-lived chronometers utilize short-lived, now extinct isotopes that are thought to be synthesized during r-processes only. For example, these isotopic systems include

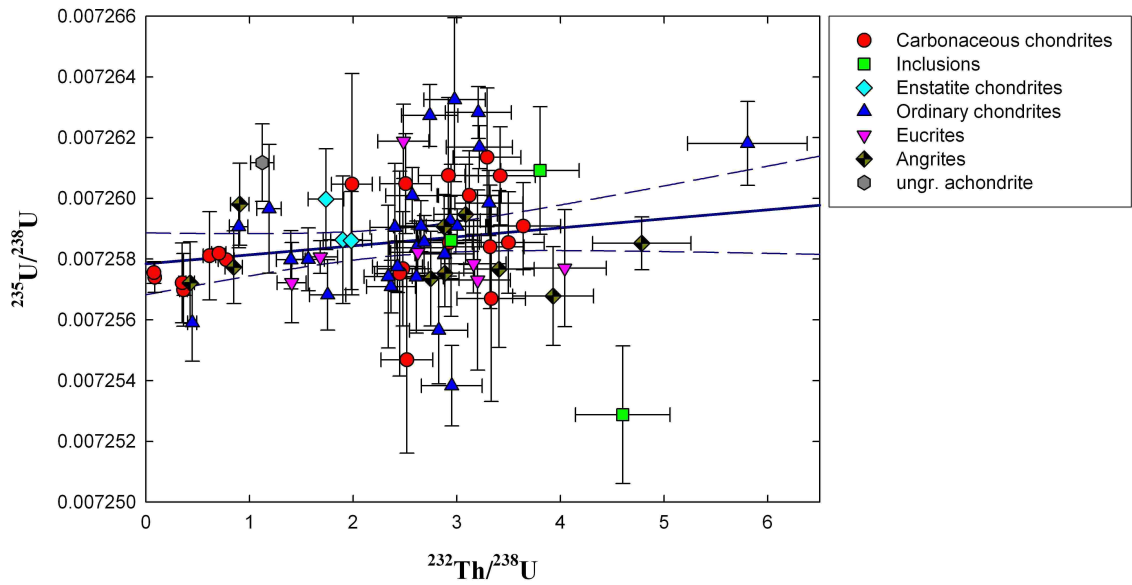


Figure 5.12: $^{232}\text{Th}/^{238}\text{U}$ ratios plotted against $^{235}\text{U}/^{238}\text{U}$, the linear regression line (solid dark blue) gives the slope and the interception point for the calculations of the initial abundance of ^{247}Cm at $t+\Delta$. The dashed lines represent the 95% confidence intervals of the linear regression. Error bars on the x-axis represent 10% uncertainties of Th, in agreement with the q-ICP-MS measurements for this element.

^{244}Pu - $^{134,136}\text{Xe}$, ^{182}Hf - ^{182}W and ^{129}I - ^{129}Xe , with half-lives of ~ 82 Myr [Croaz et al., 1989], 8.9 Myr [Kleine et al., 2009] and 15.7 Myr [Brazzle et al., 1999], respectively. The ^{247}Cm - ^{235}U and the ^{244}Pu - $^{134,136}\text{Xe}$ short-lived chronometers are similar two ways: both parent nuclides are actinides only produced during r-process events, and neither Pu nor Cm comprise a long-lived isotope. Therefore both of these short-lived chronometers are based on the assumption that (a) their parent isotopes were synthesized during a single r-process event shortly before the formation of the solar system and (b) a chemical proxy, for example Nd, is sufficient to determine the fractionation of the parent and the daughter nuclides. Both of these assumptions are reasons for the extreme unreliability of these possible chronometers. Nonetheless, Dauphas [2005] estimated an interval of free decay for ^{244}Pu of 158 ± 85 Myr, utilizing a production ratio for $^{244}\text{Pu}/^{238}\text{U}$ at $t = T$ of 0.53 ± 0.36 , while Wasserburg [1987] reported a Δ of ~ 160 Myr for ^{129}I . Both of these values are in very good agreement with Δ values for ^{247}Cm of 140-195 Myr of this study, indicating a single r-process event as nucleosynthetic source for the both actinides and ^{129}I . However, the Δ for ^{182}Hf of ~ 30 Myr [Dauphas, 2005, Nittler and Dauphas, 2006] is significantly shorter than the free decay intervals for the other r-process derived parent nuclides. As mentioned before (Chapter 1.4), Meyer and Clayton [2000] suggested a ‘fast’ s-process of

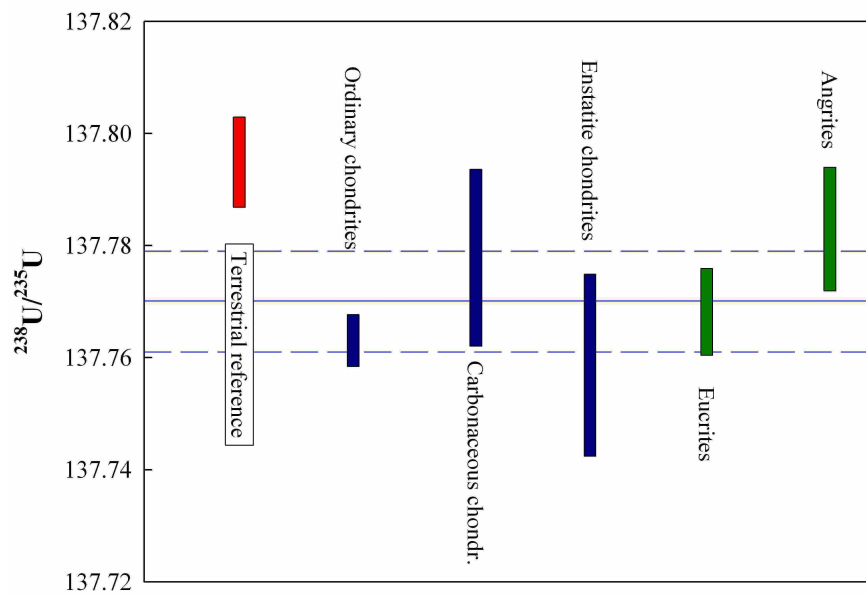


Figure 5.13: Summary of the average $^{238}\text{U}/^{235}\text{U}$ ratios of all meteorite groups analyzed in this study, in comparison with the terrestrial reference of this study. The dark blue solid line represents the mean of all meteorite groups, the dashed lines the 2SE uncertainty of this average.

a massive star as additional source of ^{182}Hf to the solar nebula, explaining the discrepancy in the longer free decay intervals of ^{247}Cm , ^{244}Pu , ^{129}I in respect to ^{182}Hf .

5.5 Conclusions

Fig. 5.13 summarizes the average uranium isotopic compositions of the five large groups of meteorites analyzed throughout this study. It is obvious that only the least metamorphic groups, the angrites and the carbonaceous chondrites, overlap with the terrestrial reference value, while the enstatite chondrites, ordinary chondrites and eucrites plot clearly below the BSE value of 137.795 ± 0.008 . The enstatite chondrites have the lightest $^{238}\text{U}/^{235}\text{U}$ average ratio at 137.759 ± 0.017 , while the least metamorphic angrites have the heaviest ratio at 137.783 ± 0.011 . The ordinary chondrites and the angrites are the only meteorite groups in this study with clearly deviating uranium isotopic compositions. This indicates that thermal metamorphism might fractionate uranium isotopes in chondrites. Additionally, CAI data show that the early solar system consist of heterogeneous reservoirs.

The combined CAI data of this study and data reported by Connelly et al. [2012] suggest that CAI formation took place in a single event 4567.30 ± 0.16 Myr ago, coinciding with

the beginning of chondrule formation, which continued for ~ 3 Myr.

The heterogeneity of $^{238}\text{U}/^{235}\text{U}$ in the early solar system together with the possibility of 'live' Cm in the solar nebula are consistent with a supernova explosion near the solar system close to its time of formation. A shockwave originating from a nearby supernova explosion could therefore have triggered the collapse of the molecular cloud. However, a supernova explosion cannot account for the range in $^{238}\text{U}/^{235}\text{U}$ ratios and Nd/U fractionation in CAIs reported by Brennecka et al. [2010b]. According to Connelly et al. [2012] these fractionations might be a relict of the CAI formation process and do not represent a secondary process, which is supported by the narrow age span of the CAIs, despite their highly variable $^{238}\text{U}/^{235}\text{U}$ ratios.

Chapter 6

Conclusions and future work

6.1 Summary and conclusions

For several decades the $^{238}\text{U}/^{235}\text{U}$ ratio has been considered invariant, equalling a value of 137.88 throughout the solar system. Recent studies with highly improved analytical precision have since refuted this assumption and show sizable 0.1%-level variations in $^{238}\text{U}/^{235}\text{U}$ in terrestrial as well as extraterrestrial samples. These variations show shifts towards both heavier and lighter isotope compositions. However, the mechanisms causing these fractionations are not well understood. Mass-dependent effects cause the lighter ^{235}U isotope to be preferentially removed from the system, while volume-dependent effects result in the heavier ^{238}U isotope being preferentially removed instead.

The first part of this study explored possible mechanisms controlling uranium isotope fractionations by analyzing various samples from different aqueous environments. These included the influence of redox controlled environments, aggregation, flocculation and complexation processes during the mixing of oceanic and riverine water masses, and adsorption on the $^{238}\text{U}/^{235}\text{U}$ isotopic composition, contributing significantly to the general knowledge base concerning the direction and magnitude of fractionation effects on the ^{238}U - ^{235}U system.

Isotope fractionations aside, in extraterrestrial samples natural variability in uranium isotopic compositions has a direct bearing on the U-Pb chronometer and the timescale of events in the early solar system. While the timescale of events is generally consistent, inconsistencies between the absolute U-Pb chronometer and the short-lived nuclide chronometers of up to ~1.5 Myr, more than a factor larger than the resolution of these systems, have been reported. This study explored whether natural deviations in $^{238}\text{U}/^{235}\text{U}$ away from the previously assumed value of 137.88 can explain these discrepancies. In this context, several angrites were analyzed for their U and Pb isotopic compositions to examine

these inconsistencies. A wide range of other meteorites were also analyzed to examine the extent to which uranium isotopes are homogeneously or heterogeneously distributed in the early solar system. This would be reflected as $^{238}\text{U}/^{235}\text{U}$ variations within and between meteoritic classes. Importantly, ^{235}U is the daughter isotope of the nowadays extinct, short-lived ^{247}Cm . Therefore, measurements of uranium isotopes in meteorites also offer the potential to identify if ^{247}Cm was ‘live’ at the formation of the solar system, providing constraints on the timeframe between the last r-process and the formation of the solar system. The former presence of ^{247}Cm would be reflected as an elevated abundance of ^{235}U in the oldest solids of the solar system.

Chapter 1 gave an overview of the nucleosynthesis of the elements during stellar evolution. While uranium, curium, and other heavy elements can only form during r-process nucleosynthesis in a massive supernova, other elements can have several different stellar sources. This chapter also provided a brief description of the meteorite classification, describing the mineralogical background of the extraterrestrial samples analyzed in this study. This was followed by the theory of isotopic dating and the use of the absolute U-Pb chronometer, in conjunction with short-lived nuclide relative chronometers that have to be anchored to the absolute ages of key meteoritic samples, typically CAIs or angrites. Further, the possible events that triggered the collapse of the molecular cloud leading to the formation the solar system were described. A supernova shockwave is favoured as a trigger and as source for uranium and curium, if the existence of ‘live’ Cm during the formation of the solar system can be proven. Lastly, the different theories of uranium isotopic fractionation, especially during reduction processes, were explained. Mass-dependent effects preferentially remove ^{235}U from the substrate while nuclear field shift effects preferentially remove ^{238}U .

Chapter 2 described the samples analyzed in this study as well as the sample preparation, chemical purification, and mass spectrometric procedures utilized. Fragmented samples of meteorites were powdered prior to digestion and large volume water samples were co-precipitated prior to chemical purification. Uranium was extracted from each sample and purified using a two-stage ion exchange chemical procedure. Pb was extracted and purified by adopting a three-step ion exchange procedure. Elemental abundances were quantified using q-ICP-MS. Uranium isotopic and concentration measurements were conducted using MC-ICPMS, utilizing a ^{233}U - ^{236}U double-spike procedure for instrumental mass fractionation correction. Meteorite samples were analyzed in time resolved mode while most water samples were analyzed utilizing a programmed analysis. Pb isotopic analysis was conducted using TIMS.

Chapter 3 established a ‘Bulk Silicate Earth’ $^{238}\text{U}/^{235}\text{U}$ value of 137.795 ± 0.008 , used as a terrestrial reference value throughout this study. The examination of ^{238}U - ^{235}U fractionation in an anoxic basin, Framvaren Fjord, showed that the reduction of U(VI) to U(IV) mediated by sulfate reducing bacteria is most likely the controlling mechanism for uranium fractionation in this environment. Specifically, uranium removal from the water column coincided with a shift of 0.35‰ towards isotopically lighter uranium isotopic ratios in the residual aqueous phase. The observed fractionation is in agreement with the nuclear volume dependent nuclear field shift effect and a Rayleigh fractionation model, corresponding to a fractionation factor α of 0.9985. The analysis of $^{238}\text{U}/^{235}\text{U}$ and uranium concentration in a depth profile of the Peruvian OMZ showed constant uranium isotopic compositions and concentrations.

Neither the conservative nor the non-conservative behaviour of uranium in the Amazon River and the Lena River estuaries led to resolvable $^{238}\text{U}/^{235}\text{U}$ isotopic fractionation, giving rise to the assumption that aggregation, flocculation, and complexation processes during riverine and seawater mixing do not result in resolvable uranium isotopic fractionation. In contrast, the examination of uranium isotopic behaviour in the Mojave freshwater aquifer concluded that isotopic fractionation is primarily influenced by adsorption processes. The $^{238}\text{U}/^{235}\text{U}$ composition of the aqueous phase shifts towards heavier values induced by mass-dependent effects. These findings fulfill one of the main objectives of this study by enhancing our general knowledge of fractionation mechanisms controlling natural variability in $^{238}\text{U}/^{235}\text{U}$.

Chapter 4 examined the $^{238}\text{U}/^{235}\text{U}$ compositions, uranium concentrations, and REE patterns of angrites. This resulted in a revision of the Pb-Pb ages of the angrites by ~1 Myr, resolving discrepancies between ages calculated utilizing the absolute U-Pb chronometer and the ^{26}Al - ^{26}Mg , ^{53}Mn - ^{53}Cr and ^{182}Hf - ^{182}W short-lived nuclide chronometers. These findings demonstrate that the $^{238}\text{U}/^{235}\text{U}$ ratios of all samples have to be analyzed parallel to Pb isotopic compositions to obtain accurate Pb-Pb ages. The revision of Pb-Pb ages of angrites is an important step towards establishing a high-resolution timescale of events in the early solar system.

Chapter 5 analyzed the $^{238}\text{U}/^{235}\text{U}$ compositions, uranium concentrations, and REE patterns of the three different chondrite groups and the eucrites. No resolvable variations in the $^{238}\text{U}/^{235}\text{U}$ average values could be detected between the different meteorite groups (Fig. 6.1), although some deviations are present between individual samples. These differences are possibly due to the variation of chondrule abundances and the differences in the mineral compositions of these samples. No evidence was found for a correlation

between uranium isotopic composition and uranium concentration or different redox conditions during the time of accretion of the chondrites.

Four ordinary chondrite samples showed highly fractionated $^{238}\text{U}/^{235}\text{U}$ compositions, possibly related to unusual mineral assemblages in these chondrites. However, the further mineralogical investigation of this hypothesis is beyond the scope of this thesis.

Combining the CAI data of this study with observations by Connelly et al. [2012] confirms that CAIs were probably formed during a single event in the early solar system 4567.30 ± 0.16 Myr ago. According to Connelly et al. [2012] this timing also coincides with the beginning of the formation of chondrules, which continued for ~ 3 Myr. This is in agreement with data collected for a chondrule sample in this study, showing an age 1.97 ± 1.13 Myr younger than those obtained for CAIs.

Deviations in the $^{238}\text{U}/^{235}\text{U}$ values of the two analyzed CAIs towards compositions that are both heavier and lighter than their host meteorites were observed. While lighter $^{238}\text{U}/^{235}\text{U}$ values in these inclusions might be caused by the decay of the nowadays extinct short-lived nuclide ^{247}Cm to ^{235}U , the heavier values must be controlled by a different fractionation mechanism, possibly stable isotope fractionation of uranium during accretion processes or secondary chemical processing. Nonetheless, the combination of $^{238}\text{U}/^{235}\text{U}$ data with Nd/U and Th/U elemental ratios yielded a possible initial abundance ratio of $^{247}\text{Cm}/^{235}\text{U}$ at the time of solar system formation of $< 2.9 \times 10^{-4}$ and $< 1.5 \times 10^{-3}$, respectively, and a time of free decay between the timing of the last r-process event and the formation of the solar system of 140-195 Myr. This is in excellent agreement with previously published data and warrants further investigation of the ^{247}Cm - ^{235}U system as a potential short-lived nuclide chronometer for early solar system events.

A comparison of the uranium isotopic compositions of all datasets in this study is shown in Fig. 6.1. Most datasets of the different aqueous environments and meteorite groups do not show resolvable uranium isotopic deviations. The most distinct deviation is determined between the isotopically heavy Mojave aquifer samples in comparison with all other datasets. The composition of these samples only marginally overlaps with the value for BSE. This isotopic shift is in agreement with mass-dependent fractionation caused by uranium adsorption processes. The $^{238}\text{U}/^{235}\text{U}$ ratios of the angrites and the carbonaceous chondrites are identical, within uncertainty, with the BSE values. As angrites are non-metamorphic igneous rocks their resemblance to BSE is expected. The marine and riverine aqueous systems have $^{238}\text{U}/^{235}\text{U}$ signatures that are isotopically lighter than BSE. For example, Framvaren Fjord is controlled by nuclear field shift effects during microbially mediated uranium reduction, resulting in lighter $^{238}\text{U}/^{235}\text{U}$ ratios in the aqueous phase. The light uranium isotopic ratios of the Peru OMZ and the estuaries can be ex-

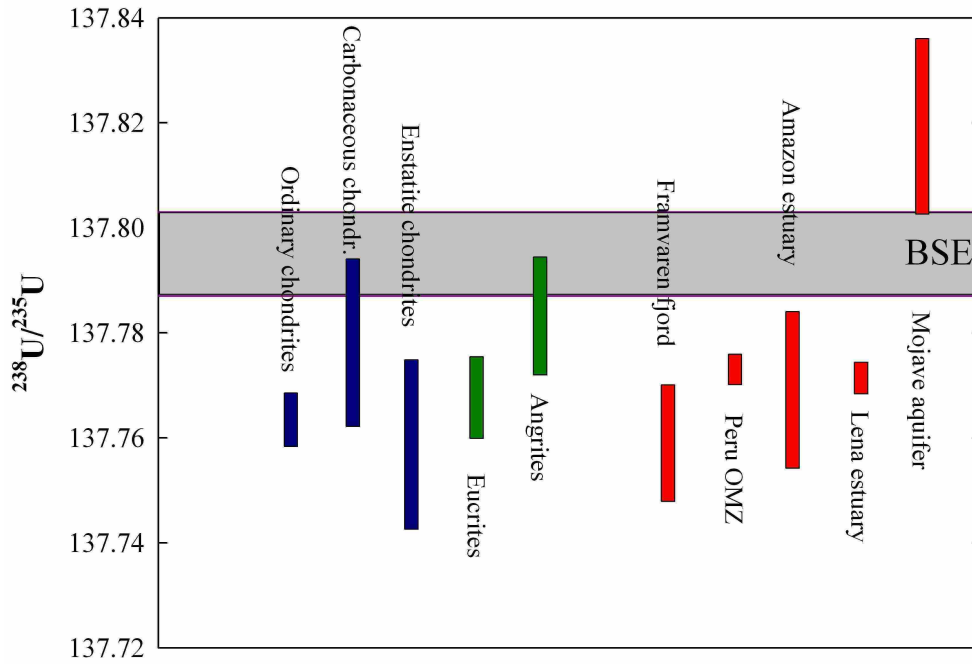


Figure 6.1: Comparison of averaged $^{238}\text{U}/^{235}\text{U}$ values, with their 2SE errors, of the different datasets analyzed in this study. Chondrite data are plotted in blue, achondrite data in green and terrestrial aqueous data in red. The grey bar represents the BSE value, including its 2SE errors.

plained by an enrichment of ^{235}U in the aqueous phase caused by the preferential leaching of the lighter ^{235}U during silicate weathering processes. However, the controlling mechanism causing the isotopically lighter $^{238}\text{U}/^{235}\text{U}$ ratio of the ordinary chondrites, enstatite chondrites, and eucrites compared to BSE remains unclear.

The weighted average of all bulk chondrites apart from the four 'anomalous' ordinary chondrites of $^{238}\text{U}/^{235}\text{U}$ is 137.768 ± 0.010 . This value changes only slightly to $^{238}\text{U}/^{235}\text{U} = 137.770 \pm 0.025$ if all analyzed solar system material but the 'anomalous' bulk meteorites presented in this study is taken into account. These values therefore represent the best estimates of the bulk $^{238}\text{U}/^{235}\text{U}$ of the solar system and the Sun. They are in agreement, within uncertainty, with the published value of Connelly et al. [2012] of 137.786 ± 0.013 for solar system material including Allende chondrules, bulk chondrites, and bulk achondrites. However, the value of all solar system material is only just within error of the presented BSE value of $^{238}\text{U}/^{235}\text{U}$ of 137.795 ± 0.008 . This discrepancy might be resolved once a larger suit of terrestrial material is used to re-define the BSE, consisting of more pristine mantle compositions than used in this study. Using for example ocean

island basalts might limit any effects of mantle recycling or mantle-crust segregation on $^{238}\text{U}/^{235}\text{U}$ and hence lower the value of the BSE estimate.

6.2 Future work

High-resolution $^{238}\text{U}/^{235}\text{U}$ measurements are still in their infancy. Since the pioneering work of Stirling et al. [2005] an increasing number of studies on this subject have been reported.

- Following the findings of this study further investigations of the mechanisms controlling adsorption processes of U onto particles and surface minerals would be advisable as it remains underconstrained, although the first field studies have been reported [Brennecka et al., 2011b].
- The fractionation mechanisms caused by nuclear field shift effects in Framvaren Fjord should be further examined to confirm if microbially mediated reduction of U(VI) to U(IV) by sulfate reducing bacteria is indeed controlling uranium isotopic fractionation at this location. A second study area could, for example, be the Black Sea, comprising a similar redox environment to Framvaren Fjord.
- A second study of the Amazon River estuary or another estuary showing non-conservative uranium behaviour with higher resolution might result in a resolvable fractionation of uranium isotopes and shed further light on the role of complexation and flocculation processes.
- The study of redox controlled fractionation in uranium ore deposits is ongoing [Murphy et al., 2012], although further studies are required to explore the use of uranium stable isotopes as a tool in mineral exploration.
- Although a large dataset of extraterrestrial samples was investigated in the present study, some questions could not be answered. Although the analysis of CAIs and chondrules is ongoing, further studies should be conducted to complete the $^{238}\text{U}/^{235}\text{U}$ dataset for angrites and expand the dataset for CAIs, as both angrite and CAI Pb-Pb ages are used to anchor the short-lived nuclide chronometers to an absolute timescale.
- The mechanisms controlling uranium isotopic fractionation in chondrites is still unresolved. The present study did not find conclusive evidence for a redox related fractionation mechanism, although the possibility still exists that uranium isotopic

fractionation is controlled by redox related processes during accretion and metamorphism processes.

- The possible contamination of the ordinary chondrites with anomalous $^{238}\text{U}/^{235}\text{U}$ should be further investigated. Leaching experiments of the affected meteorites are one way to test for possible contamination. The uranium isotopic composition of each leachate would be closer to ‘normal’ values if a contamination is indeed present.
- The detailed analysis of mineral separates extracted from bulk meteorites containing a concentrated amount of the phosphates apatite or merrillite could give insight into the possibility of highly isotopically fractionated uranium being present in these mineral phases.
- A combined investigation of uranium and xenon isotopic abundances in meteoritic samples could give further insight in the probability in utilizing both isotopic systems ^{247}Cm - ^{235}U and ^{244}Pu - $^{134,136}\text{Xe}$ as short-lived nuclide chronometers to investigate the timeframe between the last r-process and the formation of the solar system.

References

- A. Abdelouas, W. Lutze, W. Gong, E. H. Nuttall, B. A. Strietelmeier, and B. J. Travis. Biological reduction of uranium in groundwater and subsurface soil. *The Science of The Total Environment*, 250(1-3):21–35, 2000.
- Y. Amelin. The U-Pb systematics of angrite Sahara 99555. *Geochimica et Cosmochimica Acta*, 72(19):4874–4885, 2008a.
- Y. Amelin. U-Pb ages of angrites. *Geochimica et Cosmochimica Acta*, 72(1):221–232, 2008b.
- Y. Amelin and A. J. Irving. Seven million years of evolution on the angrite parent body from Pb-isotopic data. *Workshop on Chronology of Meteorites*, Abstract #A4061, 2007.
- Y. Amelin and A. J. Irving. Lead isotopic age of the quenched angrite Northwest Africa 1296. *Meteoritics & Planetary Science Supplementary*, 46:A9, 2011.
- Y. Amelin and E. Rotenberg. Sm-Nd systematics of chondrites. *Earth and Planetary Science Letters*, 223(3-4):267–282, 2004.
- Y. Amelin, L. Neymark, E. Ritsk, and A. Nemchin. Enriched Nd-Sr-Pb isotopic signatures in the Dovyren layered intrusion (eastern Siberia, Russia): evidence for source contamination by ancient upper-crustal material. *Chemical Geology*, 129(1-2):39–69, 1996.
- Y. Amelin, A. N. Krot, I. D. Hutcheon, and A. A. Ulyanov. Lead isotopic ages of chondrules and calcium-aluminum-rich inclusions. *Science*, 297(5587):1678–1683, 2002.
- Y. Amelin, A. Ghosh, and E. Rotenberg. Unraveling the evolution of chondrite parent asteroids by precise U-Pb dating and thermal modeling. *Geochimica et Cosmochimica Acta*, 69(2):505–518, 2005.
- Y. Amelin, M. Wadhwa, and G. W. Lugmair. Pb isotopic dating of meteorites using ^{202}Pb - ^{205}Pb double-spike: comparison with other high-resolution chronometers. *Lunar and Planetary Science Conference XXXVII*, Abstract #1970, 2006.
- Y. Amelin, J. Connelly, R. E. Zartman, J. H. Chen, C. Göpel, and L. A. Neymark. Modern U-Pb chronometry of meteorites: Advancing to higher time resolution reveals new problems. *Geochimica et Cosmochimica Acta*, 73(17):5212–5223, 2009.

- Y. Amelin, A. Kaltenbach, T. Iizuka, C. H. Stirling, T. R. Ireland, M. Petaev, and S. B. Jacobsen. U-Pb chronology of the solar system's oldest solids with variable $^{238}\text{U}/^{235}\text{U}$. *Earth and Planetary Science Letters*, 300(3-4):343–350, 2010.
- Y. Amelin, A. Kaltenbach, and C. H. Stirling. The U-Pb systematics and cooling rate of plutonic angrite NWA 4590. *42nd Lunar and Planetary Science Conference*, Abstract #1682, 2011.
- A. D. Anbar. Iron stable isotopes: beyond biosignatures. *Earth and Planetary Science Letters*, 217(3-4):223–236, 2004.
- E. Anders and N. Grevesse. Abundances of the elements: Meteoritic and solar. *Geochimica et Cosmochimica Acta*, 53(1):197–214, 1989.
- M. Andersen and T. Elliott. The influence of recycling on mantle $^{238}\text{U}/^{235}\text{U}$. *American Geophysical Union, Fall Meeting*, Abstract #V43E-07, 2011.
- M. B. Andersen, C. H. Stirling, D. Porcelli, A. N. Halliday, P. S. Andersson, and M. Bas-karan. The tracing of riverine U in Arctic seawater with very precise $^{234}\text{U}/^{238}\text{U}$ measurements. *Earth and Planetary Science Letters*, 259(1-2):171 – 185, 2007.
- L. G. Anderson, D. Dyrssen, and P. O. J. Hall. On the sulphur chemistry of a super-anoxic fjord, Framvaren, South Norway. *Marine Chemistry*, 23(3-4):283–293, 1988.
- R. F. Anderson, M. Q. Fleisher, and A. P. LeHuray. Concentration, oxidation state, and particulate flux of uranium in the Black Sea. *Geochimica et Cosmochimica Acta*, 53: 2215–2224, 1989.
- P. S. Andersson, D. Porcelli, Ö. Gustafsson, J. Ingri, and G. J. Wasserburg. The importance of colloids for the behavior of uranium isotopes in the low-salinity zone of a stable estuary. *Geochimica et Cosmochimica Acta*, 65(1):13–25, 2001.
- J. W. Arden. Isotopic composition of uranium in chondritic meteorites. *Nature*, 269: 788–789, 1977.
- M. A. Arthur, S. O. Schlanger, and H. C. Jenkyns. The Cenomanian-Turonian Oceanic Anoxic Event, II. palaeoceanographic controls on organic-matter production and preservation. *Geological Society, London, Special Publications*, 26:401–420, 1987.
- J. A. Barrat, B. Zanda, F. Moynier, C. Bollinger, C. Liorzou, and G. Bayon. Geochemistry of CI chondrites: Major and trace elements, and Cu and Zn isotopes. *Geochimica et Cosmochimica Acta*, 83:79–92, 2012.
- A. W. R. Bevan. *Developments in Precambrian Geology*, volume 15, chapter 2.2 Early Solar System Materials, Processes, and Chronology, pages 31–59. Elsevier, 2007.
- J. Bigeleisen. Nuclear size and shape effects in chemical reactions. isotope chemistry of the heavy elements. *Journal of the American Chemical Society*, 118(15):3676–3680, 1996.

- R. P. Binzel and S. Xu. Chips off of asteroid 4 vesta: Evidence for the parent body of basaltic achondrite meteorites. *Science*, 260(5105):186–191, 1993.
- J.-L. Birck and C. J. Allègre. Evidence for the presence of ^{53}Mn in the Early Solar System. *Geophysical Research Letters*, 12(11):745–748, 1985.
- J. B. Blake and D. N. Schramm. ^{247}Cm as a short-lived r-process chronometer. *Nature*, 243:138–140, 1973.
- C. J. Bopp, C. C. Lundstrom, T. M. Johnson, and J. J. G. Glessner. Variations in $^{238}\text{U}/^{235}\text{U}$ in uranium ore deposits: Isotopic signatures of the U reduction process? *Geology*, 37(7):611–614, 2009.
- C. J. Bopp, C. C. Lundstrom, T. M. Johnson, R. A. Sanford, P. E. Long, and K. H. Williams. Uranium $^{238}\text{U}/^{235}\text{U}$ isotope ratios as indicators of reduction: Results from an in situ biostimulation experiment at Rifle, Colorado, U.S.A. *Environmental Science & Technology*, 44(15):5927–5933, 2010.
- W. V. Boynton. Fractionation in the solar nebula: condensation of yttrium and the rare earth elements. *Geochimica et Cosmochimica Acta*, 39:569–584, 1975.
- W. V. Boynton. *Rare earth element geochemistry*, volume 2 of *Developments in Geochemistry*, chapter 3: Cosmochemistry of the rare earth elements: Meteorite studies. Elsevier Science Publishers B. V., 1984.
- R. H. Brazzle, O. V. Pravdivtseva, A. P. Meshik, and C. M. Hohenberg. Verification and interpretation of the I-Xe chronometer. *Geochimica et Cosmochimica Acta*, 63(5):739–760, 1999.
- A. J. Brearley and R. H. Jones. *Planetary Materials*, volume 36 of *Reviews in Mineralogy*, chapter 3: Chondritic Meteorites, pages 3.01–3.398. Mineralogical Society of America, Washington, D.C., USA, 1998.
- G. A. Brennecka and M. Wadhwa. Uranium isotope compositions of the basaltic angrite meteorites and the chronological implications for the early Solar System. *Proceedings of the National Academy of Sciences*, 109(24):9299–9303, 2012.
- G. A. Brennecka, L. E. Borg, I. D. Hutcheon, M. A. Sharp, and A. D. Anbar. Natural variations in uranium isotope ratios of uranium ore concentrates: Understanding the $^{238}\text{U}/^{235}\text{U}$ fractionation mechanism. *Earth and Planetary Science Letters*, 291(1-4):228–233, 2010a.
- G. A. Brennecka, S. Weyer, M. Wadhwa, P. E. Janney, J. Zipfel, and A. D. Anbar. $^{238}\text{U}/^{235}\text{U}$ variations in meteorites: Extant ^{247}Cm and implications for Pb-Pb dating. *Science*, 327(5964):449–451, 2010b.
- G. A. Brennecka, A. D. Herrmann, T. J. Algeo, and A. D. Anbar. Rapid expansion of oceanic anoxia immediately before the end-Permian mass extinction. *Proceedings of the National Academy of Sciences*, 108(43):17631–17634, 2011a.

- G. A. Brennecke, L. E. Wasylenko, J. R. Bargar, S. Weyer, and A. D. Anbar. Uranium isotope fractionation during adsorption to Mn-oxyhydroxides. *Environmental Science & Technology*, 45(4):1370–1375, 2011b.
- D. Brownlee, P. Tsou, J. Aléon, C. M. O. Alexander, T. Araki, S. Bajt, G. A. Baratta, R. Bastien, P. Bland, P. Bleuett, J. Borg, J. P. Bradley, A. Brearley, F. Brenker, S. Brennan, J. C. Bridges, N. D. Browning, J. R. Brucato, E. Bullock, M. J. Burchell, H. Busemann, A. Butterworth, M. Chaussidon, A. Chevront, M. Chi, M. J. Cintala, B. C. Clark, S. J. Clemett, G. Cody, L. Colangeli, G. Cooper, P. Cordier, C. Daghlain, Z. Dai, L. D'Hendecourt, Z. Djouadi, G. Dominguez, T. Duxbury, J. P. Dworkin, D. S. Ebel, T. E. Economou, S. Fakra, S. A. J. Fairey, S. Fallon, G. Ferrini, T. Ferroir, H. Fleckenstein, C. Floss, G. Flynn, I. A. Franchi, M. Fries, Z. Gainsforth, J.-P. Gallien, M. Genge, M. K. Gilles, P. Gillet, J. Gilmour, D. P. Glavin, M. Gounelle, M. M. Grady, G. A. Graham, P. G. Grant, S. F. Green, F. Grossemy, L. Grossman, J. N. Grossman, Y. Guan, K. Hagiya, R. Harvey, P. Heck, G. F. Herzog, P. Hoppe, F. Hörz, J. Huth, I. D. Hutcheon, K. Ignatyev, H. Ishii, M. Ito, D. Jacob, C. Jacobsen, S. Jacobsen, S. Jones, D. Joswiak, A. Jurewicz, A. T. Kearsley, L. P. Keller, H. Khodja, A. D. Kilcoyne, J. Kissel, A. Krot, F. Langenhorst, A. Lanzirrotti, L. Le, L. A. Leshin, J. Leitner, L. Lemelle, H. Leroux, M.-C. Liu, K. Luening, I. Lyon, G. MacPherson, M. A. Marcus, K. Marhas, B. Marty, G. Matrajt, K. McKeegan, A. Meibom, V. Mennella, K. Messenger, S. Messenger, T. Mikouchi, S. Mostefaoui, T. Nakamura, T. Nakano, M. Newville, L. R. Nittler, I. Ohnishi, K. Ohsumi, K. Okudaira, D. A. Papanastassiou, R. Palma, M. E. Palumbo, R. O. Pepin, D. Perkins, M. Perronnet, P. Pianetta, W. Rao, F. J. M. Rietmeijer, F. Robert, D. Rost, A. Rotundi, R. Ryan, S. A. Sandford, C. S. Schwandt, T. H. See, D. Schlutter, J. Sheffield-Parker, A. Simionovici, S. Simon, I. Sinitisky, C. J. Snead, M. K. Spencer, F. J. Stadermann, A. Steele, T. Stephan, R. Stroud, J. Susini, S. R. Sutton, Y. Suzuki, M. Taheri, S. Taylor, N. Teslich, K. Tomeoka, N. Tomioka, A. Toppani, J. M. Trigo-Rodríguez, D. Troadec, A. Tsuchiyama, A. J. Tuzzolino, T. Tyliszczak, K. Uesugi, M. Velbel, J. Vellenga, E. Vicenzi, L. Vincze, J. Warren, I. Weber, M. Weisberg, A. J. Westphal, S. Wirick, D. Wooden, B. Wopenka, P. Wozniakiewicz, I. Wright, H. Yabuta, H. Yano, E. D. Young, R. N. Zare, T. Zega, K. Ziegler, L. Zimmerman, E. Zinner, and M. Zolensky. Comet 81P/Wild 2 under a microscope. *Science*, 314(5806):1711–1716, 2006.
- J. Bruno, J. D. Pablo, L. Duro, and E. Figuerola. Experimental study and modeling of the U(VI)-Fe(OH)₃ surface precipitation/coprecipitation equilibria. *Geochimica et Cosmochimica Acta*, 59(20):4113–4123, 1995.
- C. Burkhardt, T. Kleine, B. Bourdon, H. Palme, J. Zipfel, J. M. Friedrich, and D. S. Ebel. Hf-W mineral isochron for Ca,Al-rich inclusions: Age of the solar system and the timing of core formation in planetesimals. *Geochimica et Cosmochimica Acta*, 72(24):6177–6197, 2008.
- M. Busso. *Astronomy with radioactivities*, volume 812 of *Lecture Notes in physics*, chapter 6: The early Solar System, pages 309–344. Springer Verlag, Berlin Heidelberg, 2011.

- A. Cameron and J. Truran. The supernova trigger for formation of the solar system. *Icarus*, 30(3):447–461, 1977.
- D. E. Canfield, F. J. Stewart, B. Thamdrup, L. D. Brabandere, T. Dalsgaard, E. F. Delong, N. P. Revsbech, and O. Ulloa. A cryptic sulfur cycle in Oxygen-Minimum-Zone water off the Chilean coast. *Science*, 330:1375–1378, 2010.
- J. Carroll and W. S. Moore. Uranium removal during low discharge in the Ganges-Brahmaputra mixing zone. *Geochimica et Cosmochimica Acta*, 58:4987 – 4995, 1994.
- G. Cauwet and I. Sidorov. The biogeochemistry of Lena River: organic carbon and nutrients distribution. *Marine Chemistry*, 53(3-4):211 – 227, 1996.
- F. P. Chavez, A. Bertrand, R. Guevara-Carrasco, P. Soler, and J. Csirke. The northern Humboldt Current System: Brief history, present status and a view towards the future. *Progress In Oceanography*, 79(2-4):95–105, 2008.
- J. Chen and G. Wasserburg. The isotopic composition of uranium and lead in Allende inclusions and meteoritic phosphates. *Earth and Planetary Science Letters*, 52(1):1–15, 1981.
- J. H. Chen and G. J. Wasserburg. A search for isotopic anomalies in uranium. *Geophysical Research Letters*, 7(4):275–278, 1980.
- C. L. Chou and J. D. Moffatt. A simple co-precipitation inductively coupled plasma mass spectrometric method for the determination of uranium in seawater. *Fresenius Journal of Analytical Chemistry*, 368(1):59–61, 2000.
- A. Chrysostomou and P. W. Lucas. The formation of stars. *Contemporary Physics*, 46(1): 29–40, 2005.
- F. J. Ciesla and L. L. Hood. The nebular shock wave model for chondrule formation: Shock processing in a particle–gas suspension. *Icarus*, 158(2):281–293, 2002.
- R. N. Clayton, T. K. Mayeda, J. N. Goswami, and E. J. Olsen. Oxygen isotope studies of ordinary chondrites. *Geochimica et Cosmochimica Acta*, 55:2317–2337, 1991.
- D. J. Condon, N. McLean, S. R. Noble, and S. A. Bowring. Isotopic composition ($^{238}\text{U}/^{235}\text{U}$) of some commonly used uranium reference materials. *Geochimica et Cosmochimica Acta*, 74(24):7127–7143, 2010.
- J. N. Connelly, M. Bizzarro, K. Thrane, and J. A. Baker. The Pb-Pb age of angrite SAH99555 revisited. *Geochimica et Cosmochimica Acta*, 72(19):4813–4824, 2008.
- J. N. Connelly, M. Bizzarro, A. N. Krot, Å. Nordlund, D. Wielandt, and M. A. Ivanova. The absolute chronology and thermal processing of solids in the protoplanetary disk. *Science*, in press, 2012.
- G. A. Cowan and H. H. Adler. The variability of the natural abundance of ^{235}U . *Geochimica et Cosmochimica Acta*, 40(12):1487–1490, 1976.

- G. Crozaz, P. Pellas, M. Bourot-Denise, S. M. d. Chazal, C. Fieni, L. L. Lundberg, and E. Zinner. Plutonium, uranium and rare earths in the phosphates of ordinary chondrites - the quest for a chronometer. *Earth and Planetary Science Letters*, 93:157–169, 1989.
- G. Crozaz, C. Floss, and M. Wadhwa. Chemical alteration and REE mobilization in meteorites from hot and cold deserts. *Geochimica et Cosmochimica Acta*, 67(24):4727–4741, 2003.
- N. Dauphas. Multiple sources or late injection of short-lived r-nuclides in the early solar system? *Nuclear Physics A*, 758:757–760, 2005.
- S. J. Desch and H. C. Connolly. A model of the thermal processing of particles in solar nebula shocks: Application to the cooling rates of chondrules. *Meteoritics & Planetary Science*, 37(2):183–207, 2002.
- L. A. Dietz, C. F. Paghugki, and G. A. Land. Internal standard technique for precise isotopic abundance measurements in thermal ionization mass spectrometry. *Analytical Chemistry*, 34(6):709–710, 1962.
- T. Dittmar and G. Kattner. The biogeochemistry of the river and shelf ecosystem of the Arctic Ocean: a review. *Marine Chemistry*, 83(3-4):103–120, 2003.
- D. L. Donohue, D. H. Smith, J. P. Young, H. S. McKown, and C. A. Pritchard. Isotopic analysis of uranium and plutonium mixtures by resonance ionization mass spectrometry. *Analytical Chemistry*, 56(3):379–381, 1984.
- M. J. Drake. Presidential address: Presented 2000 August 28, Chicago, Illinois, USA the eucrite/Vesta story. *Meteoritics & Planetary Science*, 36(4):501–513, 2001.
- M. C. Duff, J. U. Coughlin, and D. B. Hunter. Uranium co-precipitation with iron oxide minerals. *Geochimica et Cosmochimica Acta*, 66(20):3533–3547, 2002.
- M. Ebihara and M. Honda. Rare earth abundances in chondritic phosphates and their implications for early stage chronologies. *Earth and Planetary Science Letters*, 63(3): 433–445, 1983. ISSN 0012-821X.
- P. K. Egeberg, M. Schaanning, and K. Næs. Modelling the manganese cycling in two stratified fjords. *Marine Chemistry*, 23(3-4):383–391, 1988.
- T. J. Fagan, A. N. Krot, K. Keil, and H. Yurimoto. Oxygen isotopic evolution of amoeboid olvine aggregates in the reduced CV3 chondrites Efremovka, Vigarano and Leoville. *Geochimica et Cosmochimica Acta*, 68(11):2591–2611, 2004.
- C. Floss, G. Crozaz, G. McKay, T. Mikouchi, and M. Killgore. Petrogenesis of angrites. *Geochimica et Cosmochimica Acta*, 67(24):4775–4789, 2003.
- T. Fujii, F. Moynier, and F. Albarède. Nuclear field vs. nucleosynthetic effects as cause of isotopic anomalies in the early solar system. *Earth and Planetary Science Letters*, 247 (1-2):1–9, 2006.

- M. Gault-Ringold and C. H. Stirling. Anomalous isotopic shifts associated with organic resin residues during cadmium isotopic analysis by double spike MC-ICPMS. *Journal of Analytical Atomic Spectrometry*, 27:449–459, 2012.
- F. Gauthier-Lafaye, P. Holliger, and P.-L. Blanc. Natural fission reactors in the Franceville basin, Gabon: A review of the conditions and results of a “critical event” in a geologic system. *Geochimica et Cosmochimica Acta*, 60(23):4831–4852, 1996.
- M. Gellissen, H. Palme, R. L. Korotev, and A. J. Irving. NWA 2999, a unique angrite with a large chondritic component. *Lunar and Planetary Science Conference XXXVIII*, Abstract #1612, 2007.
- D. P. Glavin, A. Kubny, E. Jagoutz, and G. W. Lugmair. Mn-Cr isotope systematics of the D’Orbigny angrite. *Meteoritics & Planetary Science*, 39(5):693–700, 2004.
- V. Gordeev and I. Sidorov. Concentrations of major elements and their outflow into the Laptev Sea by the Lena River. *Marine Chemistry*, 43(1-4):33–45, 1993.
- J. N. Goswami, K. K. Marhas, M. Chaussidon, M. Gounelle, and B. S. Meyer. Origin of short-lived nuclides in the early solar system. In A. N. Krot, E. R. D. Scott, and B. Reipurth, editors, *Chondrites and the Protoplanetary Disk*, volume 341 of *ASP conference series*, pages 485–514, San Francisco, USA, 2005. Astronomical Society of the Pacific.
- M. Gounelle and S. S. Russell. On early solar system chronology: Implications of an heterogeneous spatial distribution of ^{26}Al and ^{53}Mn . *Geochimica et Cosmochimica Acta*, 69(12):3129–3144, 2005.
- Y. Guan, K. D. McKeegan, and G. J. MacPherson. Oxygen isotopes in calcium-aluminum-rich inclusions from enstatite chondrites: new evidence for a single CAI source in the solar nebula. *Earth and Planetary Science Letters*, 181(3):271–277, 2000.
- C. Guieu, W. W. Huang, J.-M. Martin, and Y. Y. Yong. Outflow of trace metals into the Laptev Sea by the Lena River. *Marine Chemistry*, 53(3-4):255–267, 1996.
- A. N. Halliday, D.-C. Lee, J. N. Christensen, A. J. Walder, P. A. Freedman, C. E. Jones, C. M. Hall, W. Yi, and D. Teagle. Recent developments in inductively coupled plasma magnetic sector multiple collector mass spectrometry. *International Journal of Mass Spectrometry and Ion Processes*, 146-147(0):21–33, 1995.
- A. N. Halliday, D.-C. Lee, J. N. Christensen, M. Rehkämper, W. Yi, X. Luo, C. M. Hall, C. J. Ballentine, T. Pettke, and C. Stirling. Applications of multiple collector-ICPMS to cosmochemistry, geochemistry, and paleoceanography. *Geochimica et Cosmochimica Acta*, 62(6):919–940, 1998.
- E. I. Hamilton. What is geochronology? II: Methods in geochronology. *Physics Education*, 2:188–194, 1967.
- C. Haraldsson and S. Westerlund. Trace metals in the water columns of the Black Sea and Framvaren Fjord. *Marine Chemistry*, 23(3-4):417–424, 1988.

- A. Heger, S. E. Woosley, K. Langanke, E. Kolbe, T. Rauscher, and R. D. Hoffman. Nucleosynthesis of heavy elements in massive stars. *Nuclear Physics*, A718:159c–166c, 2003.
- F. Herwig. Evolution of Asymptotic Giant Branch stars. *Annual Review of Astronomy and Astrophysics*, 43:435–479, 2005.
- J. Hiess, D. J. Condon, N. McLean, and S. R. Noble. $^{238}\text{U}/^{235}\text{U}$ systematics in terrestrial uranium-bearing minerals. *Science*, 335(6076):1610–1614, 2012.
- J. A. Hölemann, M. Schirmacher, and A. Prange. Seasonal variability of trace metals in the Lena River and the southeastern Laptev Sea: Impact of the spring freshet. *Global and Planetary Change*, 48(1-3):112–125, 2005.
- K. Horie, H. Hidaka, and F. Gauthier-Lafaye. Isotopic evidence for trapped fissiogenic REE and nucleogenic Pu in apatite and Pb evolution at the Oklo natural reactor. *Geochimica et Cosmochimica Acta*, 68(1):115–125, 2004.
- A. Hubert, B. Bourdon, E. Pili, and L. Meynadier. Transport of radionuclides in an unconfined chalk aquifer inferred from U-series disequilibria. *Geochimica et Cosmochimica Acta*, 70(22):5437–5454, 2006.
- T. R. Ireland and B. Fegley, Jr. The solar system’s earliest chemistry: Systematics of refractory inclusions. *International Geology Review*, 42(10):865–894, 2000.
- L. Jacobs, S. Emerson, and J. Skei. Partitioning and transport of metals across the interface in a permanently anoxic basin: Framvaren Fjord, Norway. *Geochimica et Cosmochimica Acta*, 49(6):1433–1444, 1985.
- B. Jacobsen, Q.-Z. Yin, F. Moynier, Y. Amelin, A. N. Krot, K. Nagashima, I. D. Hutcheon, and H. Palme. ^{26}Al - ^{26}Mg and ^{207}Pb - ^{206}Pb systematics of allende CAIs: Canonical solar initial $^{26}\text{Al}/^{27}\text{Al}$ ratio reinstated. *Earth and Planetary Science Letters*, 272(1-2):353–364, 2008.
- A. H. Jaffey, K. F. Flynn, L. E. Glendenin, W. C. Bentley, and A. M. Essling. Precision measurement of half-lives and specific activities of ^{235}U and ^{238}U . *Physical Review*, 4(5):1889–1906, 1971.
- M. Javoy, E. Kaminski, F. Guyot, D. Andrault, C. Sanloup, M. Moreira, S. Labrosse, A. Jambon, A. Agrinier, A. Davaille, and C. Jaupart. The chemical composition of the Earth: Enstatite chondrite models. *Earth and Planetary Science Letters*, 293(3-4):259–268, 2010.
- B. L. Jolliff, L. A. Haskin, R. O. Colson, and M. Wadhwa. Partitioning in REE-saturating minerals: Theory, experiment, and modelling of whitlockite, apatite, and evolution of lunar residual magmas. *Geochimica et Cosmochimica Acta*, 57:4069–4094, 1993.
- J. H. Jones and D. S. Burnett. Experimental geochemistry of Pu and Sm and the of trace element partitioning. *Geochimica et Cosmochimica acta*, 51(4):769–782, 1987.

- G. W. Kallemeyn and J. T. Wasson. Composition of enstatite (EH3, EH4,5 and EL6) chondrites: Implications regarding their formation. *Geochimica et Cosmochimica Acta*, 50:2153–2164, 1986.
- G. W. Kallemeyn, A. E. Rubin, D. Wang, and J. T. Wasson. Ordinary chondrites: Bulk compositions, classification, lithophile-element fractionations and composition-petrographic type relationships. *Geochimica et Cosmochimica Acta*, 53(10):2747–2767, 1989.
- A. Kaltenbach, Y. Amelin, and C. H. Stirling. Uranium isotopic composition in meteorites, and the origin of the solar system. *9th Australian Space Science Conference*, 2009.
- A. Kaltenbach, C. H. Stirling, D. Porcelli, and J. T. Kulongoski. The effect of redox mechanisms on the fractionation of uranium 'stable' isotopes. *American Physical Union, Fall Meeting*, Abstract #V21B-2335, 2010.
- A. Kaltenbach, C. H. Stirling, and Y. Amelin. Revised ages of angrites. *Mineralogical Magazine*, 75(3):1137, 2011.
- A. Kaltenbach, C. H. Stirling, and Y. Amelin. Uranium isotopic composition of carbonaceous chondrites. *43rd Lunar and Planetary Science Conference*, Abstract #1691, 2012.
- J. H. Kastner and P. C. Myers. An observational estimate of the probability of encounters between mass-losing evolved stars and molecular clouds. *The Astrophysical Journal*, 421(2):605–614, 1994.
- K. Keil. Thermal alteration of asteroids: evidence from meteorites. *Planetary and Space Science*, 48(10):887–903, 2000.
- K. Keil. Angrites, a small but diverse suite of ancient, silica-undersaturated volcanic-plutonic mafic meteorites, and the history of their parent asteroid. *Chemie der Erde - Geochemistry*, (in press), 2012. doi: 10.1016/j.chemer.2012.06.002.
- M. Kikuchi, H. Hidaka, and F. Gauthier-Lafaye. Formation and geochemical significance of micrometallic aggregates including fissiogenic platinum group elements in the Oklo natural reactor, Gabon. *Geochimica et Cosmochimica Acta*, 74(16):4709–4722, 2010.
- T. Kleine, M. Touboul, J. A. V. Orman, B. Bourdon, C. Maden, K. Mezger, and A. N. Halliday. Hf-W thermochronometry: Closure temperature and constraints of the H chondrite parent body. *Earth and Planetary Science Letters*, 270(1-2):106–118, 2008.
- T. Kleine, M. Touboul, B. Bourdon, F. Nimmo, K. Mezger, H. Palme, S. B. Jacobsen, Q.-Z. Yin, and A. N. Halliday. Hf-W chronology of the accretion and early evolution of asteroids and terrestrial planets. *Geochimica et Cosmochimica Acta*, 73(17):5150–5188, 2009.
- T. Kleine, U. Hans, A. J. Irving, and B. Bourdon. Chronology of the angrite parent body and implications for core formation in protoplanets. *Geochimica et Cosmochimica Acta*, 84:186–203, 2012.

- J. Komlos, A. Peacock, R. K. Kukkadapu, and P. R. Jaffé. Long-term dynamics of uranium reduction/reoxidation under low sulfate conditions. *Geochimica et Cosmochimica Acta*, 72(15):3603–3615, 2008.
- A. Krot, K. Keil, E. Scott, C. Goodrich, and M. Weisberg. *Meteorites, Comets and Planets*, volume 1 of *Treatise on Geochemistry*, chapter 1.05 Classification of Meteorites, pages 83–128. Elsevier-Pergamon, Oxford, 2003.
- A. N. Krot, Y. Amelin, P. Bland, F. J. Ciesla, J. Connelly, A. M. Davis, G. R. Huss, I. D. Hutcheon, K. Makide, K. Nagashima, L. E. Nyquist, S. S. Russell, E. R. D. Scott, K. Thrane, H. Yurimoto, and Q. Z. Yin. Origin and chronology of chondritic components: A review. *Geochimica et Cosmochimica Acta*, 73(17):4963–4997, 2009.
- T.-L. Ku, K. G. Knauss, and G. G. Mathieu. Uranium in open ocean: concentration and isotopic composition. *Deep Sea Research*, 24(11):1005–1017, 1977.
- J. T. Kulongoski, D. R. Hilton, and J. A. Izbicki. Helium isotope studies in the Mojave Desert, California: implications for groundwater chronology and regional seismicity. *Chemical Geology*, 202(1-2):95–113, 2003.
- G. Kurat, E. Zinner, and F. Brandstätter. A plagioclase-olivine-spinel-magnetite inclusion from Maralinga (CK): Evidence for sequential condensation and solid-gas exchange. *Geochimica et Cosmochimica Acta*, 66(16):2959–2979, 2002.
- G. Kurat, M. E. Varela, F. Brandstätter, G. Weckwerth, R. N. Clayton, H. W. Weber, L. Schultz, E. Wäsch, and M. A. Nazarov. D’Orbigny: A non-igneous angritic achondrite? *Geochimica et Cosmochimica Acta*, 68(8):1901–1921, 2004.
- P. K. Kuroda. On the isotopic constitution of radium (Ra-223/Ra-226) in uranium minerals and recent problems of geochronology. *Annals of the New York Academy of Science*, 62(8):179–207, 1955.
- J. R. Lancelot, A. Vitrac, and C. J. Allegre. The Oklo natural reactor: Age and evolution studies by U-Pb and Rb-Sr systematics. *Earth and Planetary Science Letters*, 25(2):189–196, 1975.
- D. Langmuir. Uranium solution-mineral equilibria at low temperatures with applications to sedimentary ore deposits. *Geochimica et Cosmochimica Acta*, 42(6):547–569, 1978.
- K. K. Larsen, A. Trinquier, C. Paton, M. Schiller, D. Wielandt, M. A. Ivanova, J. N. Connelly, Å. Nordlund, A. N. Krot, and M. Bizzarro. Evidence for magnesium isotope heterogeneity in the solar protoplanetary disk. *The Astrophysical Journal Letters*, 735(2):L37, 2011.
- D.-C. Lee and A. N. Halliday. Hafnium-tungsten chronometry and the timing of terrestrial core formation. *Nature*, 378:771–774, 1995.
- T. Lee, D. A. Papanastassiou, and G. J. Wasserburg. Demonstration of ^{26}Mg excess in Allende and evidence for ^{26}Al . *Geophysical Research Letters*, 3(1):41–44, 1976.

- I. Leya, A. N. Halliday, and R. Wieler. The predictable collateral consequences of nucleosynthesis by spallation reactions in the early solar system. *The Astrophysical Journal*, 594:605–616, 2003.
- K. R. Ludwig. Isoplot/Ex version 3.00/4.13. A geochronological toolkit for Microsoft Excel. Berkeley Geochronology Center Special Publication 4, 2003.
- M. Lugaro and A. Chieffi. *Astronomy with radioactivities*, volume 812 of *Lecture Notes in physics*, chapter 3: Radioactivities in low- and intermediate mass stars, pages 83–151. Springer Verlag, Berlin Heidelberg, 2011.
- G. W. Lugmair and K. Marti. Sm-Nd-Pu timepieces in the Angra dos Reis meteorite. *Earth and Planetary Science Letters*, 35(2):273–284, 1977.
- J. Luo, F.-A. Weber, O. A. Cirpka, W.-M. Wu, J. L. Nyman, J. Carley, P. M. Jardine, C. S. Criddle, and P. K. Kitanidis. Modeling in-situ uranium(VI) bioreduction by sulfate-reducing bacteria. *Journal of Contaminant Hydrology*, 92(1-2):129–148, 2007.
- X. Luo, M. Rehkämper, D.-C. Lee, and A. N. Halliday. High precision $^{230}\text{Th}/^{232}\text{Th}$ and $^{234}\text{U}/^{238}\text{U}$ measurements using energyfiltered ICP magnetic sector multiple collector mass spectrometry. *International Journal of Mass Spectrometry and Ion Processes*, 171(1-3):105–117, 1997.
- K. W. Mandernack and B. M. Tebo. In situ sulfide removal and CO_2 fixation rates at deep-sea hydrothermal vents and the oxic/anoxic interface in Framvaren Fjord, Norway. *Marine Chemistry*, 66(3-4):201–213, 1999.
- K. W. Mandernack, H. R. Krouse, and J. M. Skei. A stable sulfur and oxygen isotopic investigation of sulfur cycling in an anoxic marine basin, Framvaren Fjord, Norway. *Chemical Geology*, 195(1-4):181–200, 2003.
- G. Manhes, J. Minster, and C. Allègre. Comparative uranium-thorium-lead and rubidium-strontium study of the Saint Sèverin amphoterite: consequences for early solar system chronology. *Earth and Planetary Science Letters*, 39(1):14–24, 1978.
- C. Maréchal and F. Albarède. Ion-exchange fractionation of copper and zinc isotopes. *Geochimica et Cosmochimica Acta*, 66(9):1499–1509, 2002.
- A. Markowski, G. Quitté, T. Kleine, A. N. Halliday, M. Bizzarro, and A. J. Irving. Hafnium-tungsten chronometry of angrites and the earliest evolution of planetary objects. *Earth and Planetary Science Letters*, 262(1-2):214–229, 2007.
- J.-M. Martin, M. Meybeck, and M. Pusset. Uranium behaviour in the Zaire estuary. *Netherlands Journal of Sea Research*, 12(3/4):338–344, 1978.
- J. M. Martin, D. M. Guan, F. Elbaz-Poulichet, A. J. Thomas, and V. V. Gordeev. Preliminary assessment of the distributions of some trace elements (As, Cd, Cu, Fe, Ni, Pb and Zn) in a pristine aquatic environment: The Lena River estuary (Russia). *Marine Chemistry*, 43(1-4):185–199, 1993.

- J. M. Mattinson. Analysis of the relative decay constants of ^{235}U and ^{238}U by multi-step ca-tims measurements of closed-system natural zircon samples. *Chemical Geology*, 275(3-4):186–198, 2010. ISSN 0009-2541.
- T. J. McCoy, K. Keil, D. W. Muenow, and L. Wilson. Partial melting and melt migration in the acapulcoite-lodranite parent body. *Geochimica et Cosmochimica Acta*, 61(3): 639–650, 1997.
- B. McKee and J. Skei. Framvaren Fjord as a natural laboratory for examining biogeochemical processes in anoxic environments. *Marine Chemistry*, 67(3-4):147–148, 1999.
- B. A. McKee and J. F. Todd. Uranium behavior in a permanently anoxic fjord: Microbial control? *Limnology and Oceanography*, 38(2):408–414, 1993.
- B. A. McKee, D. J. DeMaster, and C. A. Nittrouer. Uranium geochemistry on the Amazon shelf: Evidence for uranium release from bottom sediments. *Geochimica et Cosmochimica Acta*, 51(10):2779–2786, 1987.
- K. Metzler, K. D. Bobe, H. Palme, B. Spettel, and D. Stöffler. Thermal and impact metamorphism on the HED parent asteroid. *Planetary and Space Science*, 43(3-4): 499–525, 1995.
- B. S. Meyer and D. D. Clayton. Short-lived radioactivities and the birth of the sun. *Space Science Review*, 92:133–152, 2000.
- K. Misawa, A. Yamaguchi, and H. Kaiden. U-Pb and ^{207}Pb - ^{206}Pb ages of zircons from basaltic eucrites: Implications for early basaltic volcanism on the eucrite parent body. *Geochimica et Cosmochimica Acta*, 69(24):5847–5861, 2005.
- D. W. Mittlefehldt. Ibitira: A basaltic achondrite from a distinct parent asteroid and implications for the Dawn mission. *Meteoritics & Planetary Science*, 40(5):665–677, 2005.
- D. W. Mittlefehldt, M. Killgore, and M. T. Lee. Petrology and geochemistry of D’Orbigny, geochemistry of Sahara 99555, and the origin of angrites. *Meteoritics & Planetary Science*, 37(3):345–369, 2002.
- C. Montoya-Pino, S. Weyer, A. D. Anbar, J. Pross, W. Oschmann, B. van de Schootbrugge, and H. W. Arz. Global enhancement of ocean anoxia during Oceanic Anoxic Event 2: A quantitative approach using U isotopes. *Geology*, 38(4):315–318, 2010.
- M. J. Murphy, C. H. Stirling, S. P. Turner, B. F. Schaefer, and A. Kaltenbach. Redox-controlled fractionation of $^{238}\text{U}/^{235}\text{U}$ during low temperature uranium mineralisation. *Earth and Planetary Science Letters*, submitted, 2012.
- M. T. Murrell and D. S. Burnett. The behavior of actinides, phosphorus, and rare earth elements during chondrite metamorphism. *Geochimica et Cosmochimica Acta*, 47(11): 1999–2014, 1983.

- K. Newman, P. A. Freedman, J. Williams, N. S. Belshaw, and A. N. Halliday. High sensitivity skimmers and non-linear mass dependent fractionation in ICP-MS. *Journal of Analytical Atomic Spectrometry*, 24(6):742–751, 2009.
- A. O. Nier. The isotopic constitution of uranium and the half-lives of uranium isotopes. *Physical Review*, 55(2):150–153, 1939.
- L. R. Nittler and N. Dauphas. *Meteorites and the early solar system II*, chapter Meteorites and the chemical evolution of the Milky Way, pages 127–146. The University of Arizona Press, Tuscon, 2006.
- C. A. Nittrouer and D. J. DeMaster. The Amazon shelf setting: tropical, energetic, and influenced by a large river. *Continental Shelf Research*, 16(5-6):553–573, 1996.
- J. Noordmann, S. Weyer, M. Sharma, and R. B. Georg. Variations of the $^{238}\text{U}/^{235}\text{U}$ isotope composition in rivers. *Geochimica et Cosmochimica Acta Supplement*, 73, Abstract #A951, 2009.
- J. Noordmann, S. Weyer, M. Sharma, R. Georg, S. Rausch, and W. Bach. Fractionations of $^{238}\text{U}/^{235}\text{U}$ in rivers and hydrothermal systems: Constraints for the oceanic U cycle. *American Geophysical Union, Fall Meeting*, Abstract #V31B-2330, 2010.
- Nu-Instruments. Nu plasma HR operating manual. edited by N.I Limited, U.K., 2005.
- L. E. Nyquist, H. Takeda, B. M. Bansal, C. Y. Shih, H. Wiesmann, and J. L. Wooden. Rb-Sr and Sm-Nd internal isochron ages of a subophitic basalt clast and a matrix sample from the Y75011 eucrite. *Journal of Geophysical Research*, 91(B8):8137–8150, 1986.
- L. E. Nyquist, T. Kleine, C. Y. Shih, and Y. D. Reese. The distribution of short-lived radioisotopes in the early solar system and the chronology of asteroid accretion, differentiation, and secondary mineralization. *Geochimica et Cosmochimica Acta*, 73(17):5115–5136, 2009.
- K. S. Ormerod. Distribution of some non-phototrophic bacteria and active biomass (ATP) in the permanently anoxic fjord Framvaren. *Marine Chemistry*, 23(3-4):243–256, 1988.
- N. Ouellette, S. J. Desch, J. J. Hester, and L. A. Leshin. A nearby supernova injected short-lived radionuclides into our protoplanetary disk. In A. N. Krot, E. R. D. Scott, and B. Reipurth, editors, *Chondrites and the Protoplanetary Disk*, volume 341 of *ASP conference series*, pages 527–538, San Francisco, USA, 2005. Astronomical Society of the Pacific.
- N. Ouellette, S. J. Desch, and J. J. Hester. Interaction of supernova ejecta with nearby protoplanetary disks. *The Astrophysical Journal*, 662(2):1268–1281, 2007.
- A. Paulmier and D. Ruiz-Pino. Oxygen minimum zones (OMZs) in the modern ocean. *Progress In Oceanography*, 80(3-4):113–128, 2009.
- M. I. Petaev and S. B. Jacobsen. Petrologic study of SJ101, a new forsterite-bearing CAI from the Allende CV3 chondrite. *Geochimica et Cosmochimica acta*, 73(17):5100–5114, 2009.

- D. Z. Piper. The distribution of Co, Cr, Cu, Fe, Mn, Ni and Zn in Framvaren, a norwegian anoxic fjord. *Geochimica et Cosmochimica Acta*, 35(6):531–550, 1971.
- D. Porcelli and P. W. Swarzenski. The behavior of U- and Th-series nuclides in ground-water. *Reviews in Mineralogy and Geochemistry*, 52(1):317–361, 2003.
- D. Porcelli, P. S. Andersson, G. J. Wasserburg, J. Ingri, and M. Baskaran. The importance of colloids and mires for the transport of uranium isotopes through the Kalix River watershed and Baltic Sea. *Geochimica et Cosmochimica Acta*, 61(19):4095–4113, 1997.
- E.-K. Potter, C. H. Stirling, M. B. Andersen, and A. N. Halliday. High precision faraday collector MC-ICPMS thorium isotope ratio determination. *International Journal of Mass Spectrometry*, 247(1-3):10–17, 2005.
- Y. Z. Qian, P. Vogel, and G. J. Wasserburg. Diverse supernova sources for the r-process. *The Astrophysical Journal*, 494:285–296, 1998.
- L. K. Rademacher, C. C. Lundstrom, T. M. Johnson, R. A. Sanford, J. Zhao, and Z. Zhang. Experimentally determined uranium isotope fractionation during reduction of hexavalent U by bacteria and zero valent iron. *Environmental Science & Technology*, 40(22):6943–6948, 2006.
- T. Rauscher. Modeling the nucleosynthesis of massive stars. *New Astronomy Reviews*, 48(1-4):3–6, 2004.
- J. H. Reynolds. Isotopic composition of primordial xenon. *Physical Review Letters*, 4(7):351–354, 1960a.
- J. H. Reynolds. Determination of the age of the elements. *Physical Review Letters*, 4(1):8–10, 1960b.
- S. Richter, R. Eykens, H. Kühn, Y. Aregbe, A. Verbruggen, and S. Weyer. New average values for the $n(^{238}\text{U})/n(^{235}\text{U})$ isotope ratios of natural uranium standards. *International Journal of Mass Spectrometry*, 295(1-2):94–97, 2010.
- D. J. Rokop, R. E. Perrin, G. W. Knobeloch, V. M. Armijo, and W. R. Shields. Thermal ionization mass spectrometry of uranium with electrodeposition as a loading technique. *Analytical Chemistry*, 54(6):957–960, 1982.
- A. E. Rubin. Relationships among intrinsic properties of ordinary chondrites: Oxidation state, bulk chemistry, oxygen-isotopic composition, petrologic type, and chondrule size. *Geochimica et Cosmochimica Acta*, 69(20):4907–4918, 2005.
- R. D. Russell, W. F. Slawson, T. J. Ulrych, and P. H. Reynolds. Further applications of concordia plots to rock lead isotope abundances. *Earth and Planetary Science Letters*, 3:284–288, 1967.
- E. Ryabenko, A. Kock, H. W. Bange, M. A. Altabet, and D. W. R. Wallace. Contrasting biogeochemistry of nitrogen in the Atlantic and Pacific Oxygen Minimum Zones. *Biogeosciences*, 9:203–215, 2012.

- M. E. Sanborn and M. Wadhwa. Rare earth element geochemistry of quenched angrites Northwest Africa 1296 and Northwest Africa 1670. *41st Lunar and Planetary Science Conference*, Abstract #1490, 2010.
- E. A. Schauble. Role of nuclear volume in driving equilibrium stable isotope fractionation of mercury, thallium, and other very heavy elements. *Geochimica et Cosmochimica Acta*, 71(9):2170–2189, 2007.
- M. Schiller, J. A. Baker, and M. Bizzarro. ^{26}Al - ^{26}Mg dating of asteroidal magmatism in the young solar system. *Geochimica et Cosmochimica Acta*, 74(16):4844–4864, 2010a.
- M. Schiller, M. R. Handler, and J. A. Baker. High-precision Mg isotopic systematics of bulk chondrites. *Earth and Planetary Science Letters*, 297(1-2):165–173, 2010b.
- S. O. Schlanger and H. C. Jenkyns. Cretaceous oceanic anoxic events: causes and consequences. *Geologie en Mijnbouw*, 55:179–194, 1976.
- F. Scholz, C. Hensen, A. Noffke, A. Rohde, V. Liebetrau, and K. Wallmann. Early diagenesis of redox-sensitive trace metals in the Peru upwelling area - response to ENSO-related oxygen fluctuations in the water column. *Geochimica et Cosmochimica Acta*, 75:7257–7276, 2011.
- E. R. D. Scott and A. N. Krot. *Meteorites, Comets and Planets*, volume 1 of *Treatise on Geochemistry*, chapter 1.07 Chondrites and their components, pages 143–200. Elsevier-Pergamon, Oxford, 2003.
- E. R. D. Scott and I. S. Sanders. Implications of the carbonaceous chondrite Mn-Cr isochron for the formation of early refractory planetesimals and chondrules. *Geochimica et Cosmochimica Acta*, 73(17):5137–5149, 2009.
- K. M. Scott, X. Lu, C. M. Cavanaugh, and J. S. Liu. Optimal methods for estimating kinetic isotope effects from different forms of the Rayleigh distillation equation. *Geochimica et Cosmochimica Acta*, 68(3):433–442, 2004.
- F. E. Senftle, L. Stieff, F. Cuttitta, and P. K. Kuroda. Comparison of the isotopic abundance of U235 and U238 and the radium activity ratios in Colorado Plateau uranium ores. *Geochimica et Cosmochimica Acta*, 11(3):189–193, 1957.
- T. Shimamura and G. W. Lugmair. U-isotopic abundances. *Lunar and Planetary Science Conference XII*, Abstract:976–978, 1981.
- T. Shimamura and G. W. Lugmair. Uranium isotopic abundance in Allende residue. *Lunar and Planetary Science Conference XV*, Abstract:776–777, 1984.
- E. R. Sholkovitz. The geochemistry of rare earth elements in the Amazon River estuary. *Geochimica et Cosmochimica Acta*, 57(10):2181–2190, 1993.
- F. H. Shu, H. Shang, A. E. Glassgold, and T. Lee. X-rays and fluctuating X-winds from protostars. *Science*, 277(5331):1475–1479, 1997.

- F. H. Shu, H. Shang, M. Gounelle, A. E. Glassgold, and T. Lee. The origin of chondrules and refractory inclusions in chondritic meteorites. *The Astrophysical Journal*, 548: 1029–1050, 2001.
- A. Shukolyukov and G. W. Lugmair. ^{60}Fe in eucrites. *Earth and Planetary Science Letters*, 119(1-2):159–166, 1993. ISSN 0012-821X.
- A. Shukolyukov and G. W. Lugmair. Mn-Cr chronology of eucrite CMS 04049 and angrite NWA 2999. *Lunar and Planetary Science Conference XXXIX*, Abstract #2094, 2008.
- A. Shukolyukov, G. W. Lugmair, and A. J. Irving. Mn-Cr systematics of angrite Northwest Africa 4801. *40th Lunar and Planetary Science Conference*, Abstract #1381, 2009.
- J. Skei. Geochemical and sedimentological considerations of a permanently anoxic fjord – Framvaren, south Norway. *Sedimentary Geology*, 36(2-4):131–145, 1983.
- J. M. Skei. Framvaren - environmental setting. *Marine Chemistry*, 23(3-4):209–218, 1988.
- L. Spivak-Birndorf, M. Wadhwa, and P. Janney. ^{26}Al - ^{26}Mg systematics in D’Orbigny and Sahara 99555 angrites: Implications for high-resolution chronology using extinct chronometers. *Geochimica et Cosmochimica Acta*, 73(17):5202–5211, 2009.
- C. L. Stamos, P. Martin, T. Nishikawa, and B. F. Cox. *Simulation of ground-water flow in the Mojave River basin, California*. Number 2001-4002. U.S. Dept. of the Interior, U.S. Geological Survey ; Information Services [distributor], 2001.
- R. H. Steiger and E. Jäger. Subcommission on geochronology: Convention on the use of decay constants in geo- and cosmochemistry. *Earth and Planetary Science Letters*, 36:359–362, 1977.
- A. Stigebrandt and J. Molvær. On the water exchange of Framvaren. *Marine Chemistry*, 23(3-4):219–228, 1988.
- C. H. Stirling, A. N. Halliday, and D. Porcelli. In search of live ^{247}Cm in the early solar system. *Geochimica et Cosmochimica Acta*, 69(4):1059–1071, 2005.
- C. H. Stirling, A. N. Halliday, E.-K. Potter, M. B. Andersen, and B. Zanda. A low initial abundance of ^{247}Cm in the early solar system and implications for r-process nucleosynthesis. *Earth and Planetary Science Letters*, 251(3-4):386–397, 2006.
- C. H. Stirling, M. B. Andersen, E.-K. Potter, and A. N. Halliday. Low-temperature isotopic fractionation of uranium. *Earth and Planetary Science Letters*, 264(1-2):208–225, 2007.
- D. Stöffler, K. Keil, and E. R. D. Scott. Shock metamorphism of ordinary chondrites. *Geochimica et Cosmochimica Acta*, 55(12):3845–3867, 1991.
- H. E. Suess, H. Wänke, and F. Wlotzka. On the origin of gas-rich meteorites. *Geochimica et Cosmochimica Acta*, 28(5):595–607, 1964.

- N. Sugiura, A. Miyazaki, and K. Yanai. Widespread magmatic activities on the angrite parent body at 4562 ma ago. *Earth Planets Space*, 57:4, 2005.
- P. W. Swarzenski, B. A. McKee, and J. G. Booth. Uranium geochemistry on the Amazon shelf: Chemical phase partitioning and cycling across a salinity gradient. *Geochimica et Cosmochimica Acta*, 59(1):7–18, 1995.
- P. W. Swarzenski, B. A. McKee, J. M. Skei, and J. F. Todd. Uranium biogeochemistry across the redox transition zone of a permanently stratified fjord: Framvaren, Norway. *Marine Chemistry*, 67(3-4):181–198, 1999.
- P. W. Swarzenski, P. Campbell, D. Porcelli, and B. A. McKee. The estuarine chemistry and isotope systematics of $^{234,238}\text{U}$ in the Amazon and Fly Rivers. *Continental Shelf Research*, 24(19):2357–2372, 2004.
- T. D. Swindle, A. M. Davis, C. M. Hohenberg, G. J. MacPherson, and L. E. Nyquist. *Chondrules and the protoplanetary disk*, chapter Formation times of chondrules and Ca-Al-rich inclusions: constraints from short-lived radionuclides, pages 77–86. Cambridge University Press, 1996.
- S. Tachibana, G. R. Huss, N. T. Kita, G. Shimoda, and Y. Morishita. ^{60}Fe in chondrites: Debris from a nearby supernova in the early solar system? *The Astrophysical Journal Letters*, 639(2):L87–L90, 2006.
- M. Tatsumoto and T. Shimamura. Evidence for live ^{247}Cm in the early solar system. *Nature*, 286(5769):118–122, 1980.
- F. Tera, R. W. Carlson, and N. Z. Boctor. Radiometric ages of basaltic achondrites and their relation to the early history of the solar system. *Geochimica et Cosmochimica Acta*, 61(8):1713–1731, 1997.
- B. Thamdrup, T. Dalsgaard, and N. P. Revsbech. Widespread functional anoxia in the oxygen minimum zone of the Eastern South Pacific. *Deep Sea Research Part I: Oceanographic Research Papers*, 65(0):36–45, 2012.
- F.-K. Thielemann, R. Hirschi, M. Liebendörfer, and R. Diehl. *Astronomy with radioactivities*, volume 812 of *Lecture Notes in physics*, chapter 4: Massive stars and their supernovae, pages 153–231. Springer Verlag, Berlin Heidelberg, 2011.
- J. F. Todd, R. J. Elsinger, and W. S. Moore. The distributions of uranium, radium and thorium isotopes in two anoxic fjords: Framvaren Fjord (Norway) and Saanich Inlet (British Columbia). *Marine Chemistry*, 23(3-4):393–415, 1988.
- J. Toole, M. S. Baxter, and J. Thomson. The behaviour of uranium isotopes with salinity change in three U.K. estuaries. *Estuarine, Coastal and Shelf Science*, 25:283–297, 1987.
- A. Trinquier, J. L. Birck, C. J. Allègre, C. Göpel, and D. Ulfbeck. ^{53}Mn - ^{53}Cr systematics of the early solar system revisited. *Geochimica et Cosmochimica Acta*, 72(20):5146–5163, 2008.

- J. W. Truran. Nucleosynthesis. *Annual Review of Nuclear and Particle Science*, 34(1): 53–97, 1984.
- J. W. Truran, Jr. and A. Heger. *Meteorites, Comets and Planets*, volume 1 of *Treatise in Geochemistry*, chapter Origin of the elements, pages 1–16. Elsevier-Pergamon, Oxford, 2003.
- O. Ulloa and S. Pantoja. The oxygen minimum zone of the eastern South Pacific. *Deep Sea Research Part II: Topical Studies in Oceanography*, 56(16):987–991, 2009.
- T. J. Ulrych. Oceanic basalt leads: A new interpretation and an independent age for the Earth. *Science*, 158(3798):252–256, 1967.
- W. van Schmus and J. Wood. A chemical-petrologic classification for the chondritic meteorites. *Geochimica et Cosmochimica Acta*, 31(5):747–765, 1967.
- D. J. Velinsky and M. L. Fogel. Cycling of dissolved and particulate nitrogen and carbon in the Framvaren Fjord, Norway: stable isotopic variations. *Marine Chemistry*, 67 (3-4):161–180, 1999.
- J. Villeneuve, M. Chaussidon, and G. Libourel. Homogeneous distribution of ^{26}Al in the solar system from the Mg isotopic composition of chondrules. *Science*, 325(5943): 985–988, 2009.
- C. Vockenhuber, F. Oberli, M. Bichler, I. Ahmad, G. Quitté, M. Meier, A. N. Halliday, D.-C. Lee, W. Kutschera, P. Steier, R. J. Gehrke, and R. G. Helmer. New half-life measurement of ^{182}Hf : Improved chronometer for the early solar system. *Physical Review Letters*, 93(17):172501–1–4, 2004.
- M. Wadhwa, Y. Amelin, O. Bogdanovski, A. Shukolyukov, G. W. Lugmair, and P. Janney. Ancient relative and absolute ages for a basaltic meteorite: Implications for timescales of planetesimal accretion and differentiation. *Geochimica et Cosmochimica Acta*, 73 (17):5189–5201, 2009.
- G. J. Wasserburg. Isotopic abundances: interferences on solar system and planetary evolution. *Earth and Planetary Science Letters*, 86:129–173, 1987.
- K. S. Weeks and D. W. Sears. Chemical and physical studies of type 3 chondrites - V: The enstatite chondrites. *Geochimica et Cosmochimica Acta*, 49(7):1525 – 1536, 1985.
- B. P. Weiss, J. S. Berdahl, L. Elkins-Tanton, S. Stanley, E. A. Lima, and L. Carporzen. Magnetism on the angrite parent body and the early differentiation of planetesimals. *Science*, 322(5902):713–716, 2008.
- G. W. Wetherill. Discordant uranium-lead ages, I. *Transactions, American Physical Union*, 37(3):320–326, 1956.
- S. Weyer, A. D. Anbar, A. Gerdes, G. W. Gordon, T. J. Algeo, and E. A. Boyle. Natural fractionation of $^{238}\text{U}/^{235}\text{U}$. *Geochimica et Cosmochimica Acta*, 72(2):345–359, 2008.

- W. M. White. *Geochemistry*, chapter 10: The Big Picture: Cosmochemistry. <http://www.imwa.info/white-geochemistry.html>, 2009.
- P. B. Wignall and R. J. Twitchett. Oceanic anoxia and the end Permian mass extinction. *Science*, 272(5265):1155–1158, 1996.
- A. Yamaguchi, J. A. Barrat, R. C. Greenwood, N. Shirai, C. Okamoto, T. Setoyanagi, M. Ebihara, I. A. Franchi, and M. Bohn. Crustal partial melting on Vesta: Evidence from highly metamorphosed eucrites. *Geochimica et Cosmochimica Acta*, 73(23):7162–7182, 2009.
- Q.-Z. Yin, B. Jacobsen, F. Moynier, and I. D. Hutcheon. Toward consistent chronology in the early solar system: High-resolution ^{53}Mn - ^{53}Cr chronometry for chondrules. *The Astrophysical Journal*, 662:L43–L46, 2007.
- E. D. Young, A. Galy, and H. Nagahara. Kinetic and equilibrium mass-dependent isotope fractionation laws in nature and their geochemical and cosmochemical significance. *Geochimica et Cosmochimica Acta*, 66(6):1095–1104, 2002.
- B. Zanda. Chondrules. *Earth and Planetary Science Letters*, 224(1-2):1–17, 2004.
- E. Zinner. Stellar nucleosynthesis and the isotopic composition of presolar grains from primitive meteorites. *Annual Review of Earth and Planetary Sciences*, 26:147–188, 1998.

Appendix A: Cleaning procedures

Centrifuge tubes and micro-centrifuge tubes were rinsed 6 times with Milli-Q water and were left in a 1 M AR HCl bath at room temperature until needed, but a minimum of two weeks. Afterwards they were rinsed again, filled with quartz-distilled 6 M HCl (centrifuge tubes) or double-distilled 6 M HCl (micro-centrifuge tubes) overnight, rinsed with Milli-Q water and air dried in a laminar flow bench.

Sample and skimmer cones of the MC-ICPMS were cleaned before the analysis of each set of samples. For this, the cones were alternatingly sonicated in Milli-Q water for 15 min each and cleaned with stainless steel cleaner and Milli-Q water using Kimwipes/cotton tips until no deposits were visible anymore. A dust mask was worn during this procedure to avoid inhaling uranium dust coming of the cones.

Cleaning of PFA vials and columns took place on a hotplate at 120°C. The cleaning protocols can be found in Table 1 and Table 2, respectively.

HDPE bottles were cleaned prior to filling them with water samples. All acid baths were contained in sealed plastic buckets at room temperature. The cleaning procedure can be found in Table 4.

Resins were cleaned with every acid later used during the ion exchange column chemistry (Table 3).

Table 1: PFA cleaning

Acid	Time
distilled water	rinse 4 times
Ethanol	wipeout
distilled water	rinse 6 times
6 M AR HCl	reflux overnight
distilled water	rinse 6 times
5% Citranox [®] bath	overnight
distilled water	rinse 6 times
6 M AR HCl	2 weeks in acid bath
distilled water	rinse 6 times
7 M AR HNO ₃	2 weeks in acid bath
distilled water	rinse 4 times
Milli-Q water	rinse single vials 4 times
6 M quartz-distilled HCl + trace HF	reflux overnight
Milli-Q water	rinse 6 times
7 M quartz-distilled HNO ₃	reflux overnight
Milli-Q water	rinse 6 times
air dry in laminar flow bench	

Table 2: Column cleaning

Acid	Time
Frits were soaked in 6 M quartz-distilled HCl for one week before first use	
distilled water	rinse until all resin removed
Ethanol	rinse 4 times
distilled water	rinse 6 times
6 M AR HCl	3 days in acid bath
Milli-Q water	rinse 6 times
6 M quartz-distilled HCl	until needed in Teflon beaker minimum 3 days
Milli-Q water	rinse 6 times

Table 3: Resin cleaning

Acid	Time
TRU resin, in 50 ml centrifuge tube	
fill up with Milli-Q water	centrifuge for 10 min at 1500 G, discard water
10 ml 0.2 M HCl	centrifuge, discard acid
fill up with 0.2 M HCl	let sit for 3 days, shake every day
Milli-Q water	5 times full, centrifuge, discard water
10 ml 0.1 M HCl - 0.3 M HF	centrifuge, discard acid
fill up with 0.1 M HCl - 0.3 M HF	let sit for 3 days, shake every day
Milli-Q water	5 times full, centrifuge, discard water
10 ml 3 M HCl	centrifuge, discard acid
fill up with 3 M HCl	let sit for 3 days, shake every day
Milli-Q water	5 times full, centrifuge, discard water
10 ml 1.5 M HNO ₃	centrifuge, discard acid
fill up with 1.5 M HNO ₃	let sit for 3 days, shake every day
Milli-Q water	5 times full, centrifuge, discard water
store in Milli-Q water until needed	
UTEVA resin, in 50 ml centrifuge tube	
fill up with Milli-Q water	centrifuge for 10 min at 1500 G, discard water
10 ml 0.2 M HCl	centrifuge, discard acid
fill up with 0.2 M HCl	let sit for 3 days, shake every day
Milli-Q water	5 times full, centrifuge, discard water
10 ml 0.1 M HCl - 0.3 M HF	centrifuge, discard acid
fill up with 0.1 M HCl - 0.3 M HF	let sit for 3 days, shake every day
Milli-Q water	5 times full, centrifuge, discard water
10 ml 3 M HCl	centrifuge, discard acid
fill up with 3 M HCl	let sit for 3 days, shake every day
Milli-Q water	5 times full, centrifuge, discard water
10 ml 3 M HNO ₃	centrifuge, discard acid
fill up with 3 M HNO ₃	let sit for 3 days, shake every day
Milli-Q water	5 times full, centrifuge, discard water
store in Milli-Q water until needed	

Table 4: HDPE bottle cleaning

Acid	Time
distilled water	rinse 6 times
Citranox [®]	bath one week
distilled water	rinse 6 times
filled with 6 M AR HCl	minimum 4 weeks in 0.6 M HCl acid bath
Milli-Q water	rinse 6 times
6 M quartz-distilled HCl	reflux 3 days on hotplate at 80°C
Milli-Q water	rinse 6 times
	air dry in laminar flow bench

Appendix B: Chemicals

In the following Table 5, q-distilled refers to sub-boiling distillation in a quartz still and double distilled refers to quartz-distillation, followed by sub-boiling distillation in a teflon still.

Table 5: Chemicals used during this project

Chemical	Formula	Strength	Brand/Cleaning
Hydrochloric acid	HCl	37%	AR grade Merck q-distilled double-distilled
Nitric acid	HNO ₃	65-70%	AR grade Merck/BDH q-distilled double-distilled
Ammonium hydroxide	NH ₃	25%	TraceSelect Ultra Sigma-Aldrich
Iron(III) chloride	FeCl ₃	20%	in-house cleaned
Hydrogen peroxide	H ₂ O ₂	31%	Ultrapur Merck
Hydrofluoric acid	HF	48%	Optima Fisher Scientific double-teflon-distilled
Perchloric acid	HClO ₄	68%	Optima Fisher Scientific
Milli-Q water	H ₂ O	18 MΩ	Milli-Q Element
Quartz sand	SiO ₂	99.995%pure	Alfa Aesar

Appendix C: REE data for meteoritic samples

Table 6: REE data from La to Lu, normalized to CI values by Barrat et al. [2012], and Th concentrations in ppb for meteoritic samples. The raw data can be found in the electronic appendix.

Sample	Type	La	Ce	Pr	Nd	Sm	Eu	Gd	Tb	Dy	Ho	Er	Tm	Yb	Lu	Th
Barrat et al. [2012]	in ng/g	235	600	91	464	153	58.6	206	37.5	254	56.6	166	26.2	168	24.6	28.3
DaG 430	C3 (ungr.)	1.7	1.6	1.7	1.9	1.8	1.7	1.9	1.8	1.9	1.7	1.8	1.9	1.6	1.8	49
Allende a	CV3	1.2	1.1	1.2	1.2	1.3	1.3	1.4	1.5	1.6	1.4	1.4	1.5	1.3	1.3	41
Allende b	CV3	1.2	1.2	1.3	1.3	1.3	1.3	1.3	1.3	1.3	1.2	1.3	1.4	1.4	1.2	42
Allende c	CV3	1.4	1.3	1.5	1.5	1.5	1.5	1.5	1.5	1.6	1.4	1.5	1.6	1.6	1.5	48
Allende d	CV3	1.3	1.2	1.3	1.3	1.4	1.3	1.4	1.4	1.4	1.3	1.4	1.5	1.4	1.3	44
Allende e	CV3	1.5	1.4	1.5	1.5	1.6	1.7	1.7	1.6	1.6	1.5	1.5	1.7	1.6	1.6	53
Allende av	CV3	1.3	1.3	1.4	1.4	1.4	1.4	1.5	1.5	1.5	1.4	1.4	1.5	1.5	1.4	46
DaG 521 a	CV3	1.4	1.4	1.4	1.5	1.5	2.6	1.4	1.3	1.4	1.3	1.4	1.5	1.3	1.5	39
DaG 521 b	CV3	1.5	1.5	1.5	1.5	1.6	2.4	1.4	1.3	1.4	1.2	1.3	1.5	1.3	1.3	38
DaG 521 av	CV3	1.5	1.5	1.5	1.5	1.5	2.5	1.4	1.3	1.4	1.2	1.3	1.5	1.3	1.4	38
Leoville	CV3	2.2	1.9	2.1	2.2	2.1	1.6	2.0	1.9	1.8	1.4	1.5	2.1	1.5	1.5	61
NWA 2140	CV3	1.6	1.6	1.7	1.8	1.7	1.7	1.6	1.6	1.7	1.5	1.5	1.8	1.7	1.7	47
NWA 4818 a	CV3	1.4	1.4	1.4	1.6	1.6	1.4	1.4	1.4	1.5	1.3	1.4	1.5	1.4	1.5	38
NWA 4818 b	CV3	1.6	1.5	1.6	1.7	1.7	1.6	1.6	1.5	1.6	1.4	1.5	1.7	1.5	1.5	44
NWA 4818 av	CV3	1.5	1.4	1.5	1.6	1.6	1.5	1.5	1.5	1.6	1.4	1.4	1.6	1.5	1.5	41
NWA 4502	CV3	1.5	1.5	1.5	1.7	1.6	1.5	1.6	1.5	1.5	1.4	1.5	1.7	1.5	1.5	40
Vigarano a	CV3	1.3	1.3	1.3	1.3	1.4	1.3	1.4	1.4	1.4	1.2	1.3	1.5	1.3	1.2	45
Vigarano b	CV3	1.3	1.3	1.4	1.3	1.4	1.6	1.4	1.3	1.4	1.2	1.3	1.5	1.6	1.3	39
Vigarano c -1	CV3	1.3	1.4	1.4	1.4	1.5	1.7	1.4	1.4	1.4	1.2	1.3	1.6	1.7	1.2	45
Vigarano c -2	CV3	1.7	1.7	1.8	1.9	1.9	1.7	1.9	1.8	1.9	1.7	1.8	2.0	1.7	1.9	50
Vigarano av	CV3	1.4	1.4	1.5	1.5	1.5	1.6	1.5	1.5	1.5	1.3	1.4	1.7	1.6	1.4	45
NWA 4502 CAI	CV3 CAI	13.1	13.2	14.2	16.0	16.1	19.0	16.7	15.9	17.2	15.5	16.7	16.9	15.0	17.1	366
Allende CAISJ101	CV3 CAI	16.5	16.5	17.2	17.1	16.2	9.9	8.8	7.3	6.1	2.3	2.2	18.0	8.1	1.7	305
Allende chondrules	CV3 ch.	2.7	2.4	2.7	2.7	2.7	2.5	3.0	2.9	2.9	2.6	2.8	3.0	2.7	2.8	101
Orgueil a -1	CI1	1.2	1.0	1.0	0.9	0.9	0.8	0.8	0.8	0.8	0.8	0.8	0.9	0.8	0.8	56

Continued on next page...

Table 6 continued from previous page...

Sample	Type	La	Ce	Pr	Nd	Sm	Eu	Gd	Tb	Dy	Ho	Er	Tm	Yb	Lu	Th
Orgueil a -2	CI1	1.3	1.2	1.1	1.0	1.0	0.9	0.9	0.9	0.9	0.9	0.9	0.9	0.9	0.9	70
Orgueil b -1	CI1	1.0	0.9	0.9	0.9	0.9	0.9	0.9	0.9	0.9	0.8	0.9	0.9	0.9	0.8	45
Orgueil b -2	CI1	1.0	1.0	0.9	1.0	0.9	0.9	0.9	0.9	0.9	0.8	0.9	0.9	0.9	0.9	48
Orgueil av	CI1	1.1	1.0	1.0	1.0	0.9	0.8	0.9	0.9	0.9	0.8	0.9	0.9	0.9	0.9	55
Acfer059 a	CR2	2.1	1.7	1.8	1.6	1.5	1.6	1.5	1.5	1.5	1.3	1.4	1.5	1.4	1.4	89
Acfer059 b	CR2	7.5	5.5	4.6	3.9	2.8	2.8	2.4	2.2	2.0	1.8	2.0	2.1	1.9	1.9	388
Acfer 059 av	CR2	4.8	3.6	3.2	2.7	2.1	2.2	1.9	1.8	1.7	1.6	1.7	1.8	1.6	1.7	238
NWA721	CR2	1.3	1.1	1.2	1.2	1.2	1.4	1.2	1.2	1.2	1.1	1.2	1.3	1.2	1.2	43
NWA801	CR2	1.9	1.7	1.7	1.6	1.5	1.5	1.5	1.4	1.4	1.3	1.4	1.4	1.3	1.4	74
Mighei -1	CM2	1.1	1.0	1.1	1.1	1.1	1.1	1.1	1.1	1.1	1.0	1.1	1.2	1.1	1.1	32
Mighei -2	CM2	1.1	1.1	1.1	1.1	1.2	1.2	1.2	1.1	1.2	1.1	1.1	1.2	1.1	1.1	38
Mighei av	CM2	1.1	1.1	1.1	1.1	1.1	1.1	1.1	1.1	1.1	1.0	1.1	1.2	1.1	1.1	35
SAH 97096	EH3	0.8	0.8	0.8	0.9	0.8	0.8	0.9	0.8	0.9	0.9	0.9	0.9	0.9	1.0	14
Abee	EH4	0.7	0.7	0.8	0.8	0.9	0.7	0.9	0.9	0.9	0.9	0.9	0.9	0.8	0.8	13
Indarch	EH4	0.7	0.7	0.8	0.8	0.7	0.7	0.9	0.8	0.8	0.8	0.9	0.9	0.8	0.9	15
Tulia(a) -1	H3-4	1.4	1.3	1.3	1.3	1.2	1.2	1.3	1.2	1.2	1.2	1.2	1.2	1.2	1.3	50
Tulia(a) -2	H3-4	1.5	1.3	1.3	1.3	1.2	1.2	1.2	1.2	1.2	1.1	1.2	1.2	1.2	1.2	49
Tulia(a) av	H3-4	1.4	1.3	1.3	1.3	1.2	1.2	1.2	1.2	1.2	1.1	1.2	1.2	1.2	1.2	50
NWA 267 a	H4	5.2	2.9	3.8	3.5	2.8	2.5	2.6	2.2	2.0	1.8	1.8	1.7	1.6	1.6	123
NWA 267 b	H4	6.1	3.8	4.5	4.5	3.3	2.7	3.0	2.5	2.4	2.1	2.1	2.0	1.8	1.9	139
NWA 267 av	H4	5.7	3.3	4.1	4.0	3.1	2.6	2.8	2.3	2.2	1.9	1.9	1.9	1.7	1.8	131
Kunashak	H5	1.2	1.2	1.3	1.4	1.3	1.4	1.4	1.3	1.4	1.4	1.4	1.5	1.4	1.5	37
Orlovka	H5	1.5	1.4	1.5	1.5	1.4	1.4	1.5	1.5	1.5	1.4	1.5	1.6	1.4	1.5	40
Richardton	H5	0.9	0.9	1.0	1.0	1.0	0.9	1.1	1.0	1.1	1.0	1.1	1.1	1.0	1.0	11
Estacado	H6	2.3	2.3	2.3	2.4	2.4	2.3	2.4	2.3	2.5	2.2	2.3	2.3	2.0	2.1	47
Great Bend	H6	2.0	2.0	2.0	2.0	2.0	1.4	2.0	1.9	2.0	1.8	1.9	1.8	1.7	1.6	34
Kidairat	H6	0.7	0.6	0.7	0.7	0.8	1.0	0.8	0.9	0.9	0.8	0.9	0.9	0.9	1.0	31
Mt. Browne	H6	2.0	1.9	2.0	2.1	1.9	1.5	2.1	2.0	2.1	1.9	2.1	2.1	1.9	2.0	44

Continued on next page...

Table 6 continued from previous page...

Sample	Type	La	Ce	Pr	Nd	Sm	Eu	Gd	Tb	Dy	Ho	Er	Tm	Yb	Lu	Th
Krymka a	LL3.1	1.1	1.1	1.2	1.1	1.2	1.1	1.3	1.3	1.3	1.2	1.3	1.3	1.3	1.3	39
Krymka b	LL3.1	1.2	1.2	1.3	1.3	1.2	1.2	1.3	1.3	1.4	1.2	1.4	1.4	1.3	1.4	37
Krymka av	LL3.1	1.2	1.2	1.2	1.2	1.2	1.2	1.3	1.3	1.3	1.2	1.3	1.3	1.3	1.3	38
Krymka 0.2-0.4IF	LL3.2	1.3	1.3	1.3	1.4	1.4	1.5	1.6	1.4	1.5	1.4	1.5	1.6	1.5	1.5	38
EET 87544.4	LL4	1.3	1.3	1.3	1.4	1.4	1.2	1.4	1.3	1.4	1.3	1.4	1.4	1.3	1.4	30
Holbrook	L/LL6	0.9	0.9	1.0	1.0	1.0	1.2	1.1	1.0	1.1	1.1	1.1	1.2	1.1	1.2	34
Dhofar 008	L3.3	1.0	1.1	1.1	1.2	1.2	1.2	1.2	1.2	1.3	1.2	1.3	1.3	1.2	1.3	32
Bjurboele	L4	1.1	1.0	1.1	1.1	1.2	1.2	1.2	1.2	1.3	1.2	1.2	1.3	1.2	1.3	38
NWA 869 a	L4	1.2	1.1	1.2	1.2	1.2	1.2	1.3	1.3	1.4	1.2	1.3	1.4	1.2	1.4	44
NWA 869 b	L4	1.2	1.2	1.2	1.3	1.3	1.2	1.3	1.3	1.4	1.2	1.3	1.4	1.3	1.4	38
NWA 869 av	L4	1.2	1.2	1.2	1.3	1.3	1.2	1.3	1.3	1.4	1.2	1.3	1.4	1.3	1.4	41
Saratov a	L4	1.3	1.2	1.3	1.2	1.3	1.3	1.4	1.4	1.4	1.3	1.4	1.4	1.3	1.4	42
Saratov b	L4	1.1	1.1	1.2	1.2	1.2	1.1	1.2	1.2	1.3	1.2	1.3	1.3	1.2	1.3	27
Saratov c	L4	1.4	1.4	1.5	1.5	1.5	1.4	1.5	1.5	1.5	1.4	1.5	1.5	1.4	1.5	36
Saratov av	L4	1.3	1.2	1.3	1.3	1.3	1.3	1.4	1.4	1.4	1.3	1.4	1.4	1.3	1.4	35
Elenovka	L5	0.6	0.6	0.7	0.7	0.8	1.0	0.8	0.8	0.9	0.8	0.9	1.0	1.0	1.0	32
Elenovka 0.2IF	L5	0.7	0.7	0.8	0.8	0.8	0.9	0.8	0.9	0.9	0.8	0.9	1.0	1.0	1.0	25
Elenovka 0.3IF	L5	0.6	0.6	0.7	0.6	0.7	0.9	0.7	0.7	0.7	0.7	0.8	0.8	0.9	0.9	16
Elenovka 0.3IF	L5	0.6	0.6	0.7	0.7	0.7	0.9	0.7	0.7	0.7	0.7	0.8	0.8	0.9	0.9	16
Elenovka 0.4IF	L5	1.0	1.0	1.0	1.0	1.1	1.1	1.1	1.1	1.2	1.1	1.2	1.2	1.2	1.3	29
QUE 90201.5	L5	1.1	1.1	1.1	1.2	1.2	1.3	1.3	1.2	1.3	1.2	1.2	1.2	1.2	1.3	29
QUE 90218.4 -1	L5	0.9	0.9	1.0	1.0	1.0	1.2	1.1	1.1	1.2	1.1	1.2	1.2	1.2	1.3	40
QUE 90218.4 -2	L5	0.9	0.9	1.0	1.0	1.0	1.3	1.1	1.0	1.1	1.1	1.2	1.2	1.2	1.3	34
QUE 90218.4 -3	L5	0.9	0.9	1.0	1.0	1.0	1.3	1.1	1.0	1.2	1.1	1.2	1.2	1.2	1.3	37
QUE 90218.4 av	L5	0.9	0.9	1.0	1.0	1.0	1.3	1.1	1.0	1.2	1.1	1.2	1.2	1.2	1.3	37
ALH 77297.4	L6	1.2	1.3	1.3	1.4	1.3	1.3	1.4	1.3	1.5	1.3	1.4	1.4	1.4	1.4	25
EET 87541.2	L6	1.4	1.4	1.4	1.5	1.5	1.3	1.6	1.5	1.6	1.5	1.6	1.5	1.5	1.5	32
Agout	Eucrite	7.2	7.3	7.4	8.3	8.3	9.0	8.7	8.5	9.2	8.2	8.9	8.8	8.4	8.6	200

Continued on next page...

Table 6 continued from previous page...

Sample	Type	La	Ce	Pr	Nd	Sm	Eu	Gd	Tb	Dy	Ho	Er	Tm	Yb	Lu	Th
Camel Donga a	Eucrite	11.6	11.2	11.5	10.9	11.2	9.8	11.5	11.4	11.5	10.5	11.1	11.1	10.3	10.3	569
Camel Donga b	Eucrite	10.3	9.9	11.0	10.6	11.2	9.1	11.9	11.8	12.0	11.0	11.5	11.4	10.7	10.5	337
Camel Donga av	Eucrite	10.9	10.6	11.3	10.8	11.2	9.5	11.7	11.6	11.8	10.8	11.3	11.2	10.5	10.4	453
Ibitira a	Eucrite	4.8	4.9	5.6	6.1	7.3	3.6	8.5	9.3	10.4	10.0	11.0	11.5	11.2	11.7	145
Ibitira b	Eucrite	11.4	11.8	12.7	14.0	14.7	10.6	15.6	15.0	16.4	14.3	15.3	15.2	13.6	14.2	523
Ibitira av	Eucrite	8.1	8.4	9.1	10.0	11.0	7.1	12.0	12.2	13.4	12.2	13.1	13.3	12.4	12.9	334
Millbillillie	Eucrite	9.4	9.8	9.8	10.7	10.4	9.3	10.6	10.3	10.9	9.8	10.4	10.3	9.3	9.9	254
NWA 2362	Eucrite	3.4	3.5	3.9	4.6	5.2	8.3	5.8	5.9	6.5	5.9	6.4	6.6	6.1	6.6	46
AdoR	Plutonic angrite	21.6	25.1	29.3	33.4	34.3	28.6	35.5	33.6	34.7	30.9	31.5	29.7	26.5	25.3	580
NWA 4590 a	Plutonic angrite	13.3	12.9	13.3	13.2	12.9	11.6	13.2	13.3	13.8	13.1	14.3	14.9	14.0	14.5	845
NWA 4590 b	Plutonic angrite	14.1	14.7	15.5	17.1	17.2	14.5	17.7	16.7	18.0	15.9	17.1	17.4	16.2	17.1	367
NWA 4590 av	Plutonic angrite	13.7	13.8	14.4	15.1	15.1	13.0	15.5	15.0	15.9	14.5	15.7	16.2	15.1	15.8	606
NWA 4801	Plutonic angrite	11.3	12.6	14.4	15.3	15.9	15.7	16.5	16.2	16.4	14.4	14.7	14.2	12.6	12.7	272
NWA 2999 -a-	Plutonic angrite	4.2	4.0	4.7	5.0	5.4	6.2	6.1	6.0	6.1	5.5	5.7	5.6	5.5	5.9	75
NWA 2999 -b-	Plutonic angrite	3.7	4.0	4.6	5.3	5.7	6.7	6.4	6.3	6.3	5.6	5.9	6.0	5.6	6.1	128
NWA 2999 -c-	Plutonic angrite	1.8	2.4	3.0	3.6	4.1	3.9	4.5	4.5	4.9	4.3	4.7	4.7	4.6	5.1	26
NWA 2999 av	Plutonic angrite	3.2	3.5	4.1	4.7	5.1	5.6	5.7	5.6	5.8	5.1	5.4	5.4	5.2	5.7	76
D'Orbigny	Quenched angrite	8.9	8.9	9.3	9.6	9.6	9.8	10.0	9.8	9.9	8.7	9.5	9.7	8.9	9.3	286
NWA 1296	Quenched angrite	10.3	10.4	10.6	10.9	10.8	10.4	11.0	10.8	10.9	10.1	10.5	10.4	9.7	9.3	325
SAH 99555	Quenched angrite	9.9	10.3	10.8	10.6	11.0	10.9	11.5	11.3	11.4	10.1	10.9	11.0	10.5	10.6	359
NWA 5400	Achondrite (ungr.)	0.8	0.6	0.5	0.5	0.4	0.3	0.4	0.3	0.4	0.3	0.4	0.4	0.4	0.6	82

Appendix D: q-ICP-MS instrument settings

Table 7: q-ICP-MS instrument settings

Setting	Mode
Plasma Power	1550 W
Nebuliser	Micro concentric
Carrier gas (Argon)	0.75 ml/min
Makeup gas (Argon)	0.3 ml/min
Spray chamber temperature	12°C
Collision gas mode	He 4.5 ml/min

Table 8: Internal standard concentrations

Element	Conc [ppb]
Be	40.26
Rh	1.97798
Ge	19.54
In	1.7232
Bi	1.6456

Table 9: q-ICP-MS: Isotopes and integration times.

Dilution factor <50			Dilution factor ~500		
Element	Isotope mass	Integration time	Element	Isotope mass	Integration time
Y	89	0.1 sec	Li	7	0.1 sec
Pd	105	0.1 sec	Na	23	0.05 sec
La	139	0.1 sec	Mg	24	0.05 sec
Ce	140	0.1 sec	Al	27	0.05 sec
Pr	141	0.1 sec	K	39	0.05 sec
Nd	146	0.1 sec	Ca	44	0.05 sec
Sm	147	0.1 sec	V	51	0.1 sec
Eu	153	0.1 sec	Cr	53	0.1 sec
Gd	157	0.1 sec	Mn	55	0.1 sec
Tb	159	0.1 sec	Fe	57	0.05 sec
Dy	163	0.1 sec	Co	59	0.1 sec
Ho	165	0.1 sec	Ni	60	0.1 sec
Er	166	0.1sec	Cu	63	0.1 sec
Tm	169	0.1 sec	Zn	66	0.1 sec
Yb	172	0.1 sec	Ga	69	0.1 sec
Lu	175	0.1 sec	As	75	0.1 sec
Th	232	0.1 sec	Se	82	0.1 sec
U	238	0.3 sec	Rb	85	0.1 sec
			Sr	88	0.1 sec
			Mo	95	0.1 sec
			Ag	107	0.1 sec
			Cd	111	0.1 sec
			Ba	137	0.1 sec